CR175046
FEBRUARY 1986



National Aeronautics and Space Administration

# THE DESIGN OF A TURBOSHAFT SPEED GOVERNOR USING MODERN CONTROL TECHNIQUES

BY

G. DE LOS REYES AND D. R. GOUCHOE

GENERAL ELECTRIC COMPANY
AIRCRAFT ENGINE BUSINESS GROUP
LYNN, MASSACHUSETTS



PREPARED FOR

NATIONAL AERONAUTICS AND SPACE ADMINISTRATION
NASA LEWIS RESEARCH CENTER

CONTRACT

NAS3-22763

# FOREWORD

The following engineers made a significant technical contribution to this project: WH Pfeil designed the preliminary LQR power turbine speed governor on which the final LQR design was based; WL Miller did the research on off-schedule variable geometry effects; DR Gilmore, Senior Engineer, provided technical supervision for the entire project.

TABLE OF CONTENTS

TABLE OF CONTENTS - Continued

TABLE OF CONTENTS - Continued

TABLE OF CONTENTS - Continued

List of Figures

TABLE OF CONTENTS - Continued

List of Figures

List of Figures

## List of Figures

## List of Figures

## List of Figures

## List of Figures

## List of Figures

## List of Figures

List of Figures

## List of Tables

## 1.0 Summary

Advances in digital hardware design allows engineers to take advantage of research results in modern control theory that provide a systematic approach for improved control system design. Such designs require accurate linear and nonlinear models for synthesis and evaluation of the control laws. The purpose of this research was to design a high performance power-turbine governor for a recent technology turboshaft engine and articulated rotor system, and concurrently to evaluate the linear and nonlinear models using engine test data.

The governor was designed using the Linear Quadratic Regulator (LQR) approach with a Kalman Filter (KF) observer. The LQR governor regulates power turbine speed by summing the product of calculated gains and system states. The system states characterize the dynamics of interest at every time. There exists one state for each independent energy storage element, and the states are chosen by the engineer. The LQR gains are calculated from a linear state space model of the engine and helicopter rotor system. This model is a system of first order differential equations that are functions of the state variables and the inputs. The LQR is designed as though all the states are measured. The helicopter main-rotor blade angular velocity cannot be measured in flight and was estimated using a Kalman Filter observer. This observer is a closed-loop system that contains a simplified linear model of the helicopter rotor system. The Kalman Filter design parallels the LQR design. The estimated rotor-blade angular velocity is used in place of a measured value with no change in the LQR gains. The resulting governor has a bandwidth of about 6 rad/sec compared to a bandwidth of about 3 rad/sec for current controllers.

The linear and nonlinear models were evaluated using engine test data. The model of off-schedule variable geometry effects in the nonlinear model was evaluated by using steady state and transient engine data recorded with the variable geometry off schedule. This analysis did not indicate that a change was necessary in the current model.

Research also focused on evaluating a more efficient frequency response method than the sinusoidal input technique. A Pseudo Random Binary Noise (PRBN) signal containing all frequencies in a range of interest was superimposed on a steady state input. A maximum likelihood analysis was used to compute the frequency responses from fuel flow input to power turbine speed and gas generator speed outputs. The results were compared to results of the standard sinusoidal input response and the linear design model response. The PRBN method was shown to be effective in computing frequency response, and the results indicate the need for further analysis of frequencies where there are discrepancies between the actual engine response and the model response.

## 2.0 Introduction: Modern Control Power Turbine Governor

The maneuverability requirements of successive generations of helicopters have increased dramatically, yet only recently have the important relationships between engine controller characteristics and helicopter handling qualities begun to be explored (Ref. 1, 2). A continued emphasis on nap-of-the-earth flying capability and reduction of pilot workload has initiated further investigation into this critical relationship. The NASA/Army Small Turboshaft Engine Research (STER) program has aided this research by providing the opportunity to evaluate the Linear Quadratic Regulator (LQR) control of a recent-technology turboshaft engine (Ref. 11). The STER program consists of a series of joint Army Propulsion Lab and NASA Lewis Research Center tasks to investigate advanced technology on a complete engine system.

The control of turbine engines based on optimization techniques has received significant attention in the past decade (Ref. 3, 4). LQR controllers have been designed for the F401 (Ref. 5) and F100 (Ref. 6) turbofan engines. Although some preliminary work was done on an LQR for the T700 turboshaft engine (Ref. 7), most of the work has focused on turbofan and turbojet engines. The current research applies LQR techniques to the design of a power-turbine governor for a turboshaft engine. The resulting control law, now facilitated by the continuing emergence of digital technology, promises to provide a system with increased capabilities.

The purpose of a power turbine governor for a helicopter application is to maintain constant power turbine speed in the presence of load changes to the helicopter rotor system. These changes can come about by pilot initiated actions or by wind gusts. When the power turbine speed is constant, the main rotor speed is also constant (for nonautorotation), and the pilot modulates horsepower by changing the collective pitch angle of the main rotor blades.

The power turbine governor is a regulator: a controller that functions to maintain a system parameter (NP) equal to a setpoint. The torsional dynamic interaction between the helicopter rotors and the power turbine shows up as resonant peaks on a frequency response plot. The first peak is due to the interaction of the main rotor with the power turbine, and the second peak is due to the interaction of the tail rotor with the power turbine. The frequency range and height of the resonant peaks vary with helicopter rotor inertia, damping, and spring constant. These peaks are at high frequency compared to engine dynamics and are in the range where the system dynamics are not accurately known. For this reason, each resonant peak must be attenuated at least 6dB. This requirement has limited the bandwidth of existing controllers to about 3 rad/sec.

A power turbine governor designed using the Linear Quadratic Regulator technique attenuates the main rotor resonance such that the bandwidth of the system can be increased. This is indicative of a more responsive power turbine governor that will better attenuate disturbances to the power turbine coming from the helicopter rotor system.

The Linear Quadratic Regulator (LQR) is a regulator that computes the input to the system (in this case, WF) as a sum of the product of gains and the system states. The system states are those parameters that fully characterize the system at any point in time. That is, when the values of the state variables and the inputs to the system are known, all other system parameters can be calculated. There is one state variable for each independent energy storage element in a system. The design engineer makes the choice of state variables which are not unique for a system. The state variables are chosen from a lumped-parameter, linearized model of the system that retains the significant dynamics.

An observer was used in conjunction with the LQR governor. An observer is a closed-loop system containing a model of part or all of the system and is used to calculate a state variable that is not measured by sensors. This estimated state-variable is then used by the LQR as though the state were measured. The observer was used to calculate helicopter main-rotor tip velocity.

## 2.1 Linear Quadratic Regulator (LQR) Design Procedure

### 2.1.1 Engine-Rotor System Model

The LQR design process begins with a linearized, state-space model of the system; in this case, the engine and helicopter-rotor system. The model was linearized at six engine power settings from flight idle (FI) to intermediate rated power (IRP). A model for autorotation was not done for this study. The model of the engine is based on partial derivatives calculated from an accurate nonlinear model. The linear model of the rotor system is a generic model of an articulated rotor system that has been used successfully at General Electric for power turbine governor design. Figure 2.1 shows the combined engine and rotor system model block diagram.

The engine model as shown has P3 and T45 effects and two inputs - WF and variable geometry (VG). The P3 and T45 dynamics were neglected as they are assumed fast compared to the other dynamics. The VG input was investigated as a way of improving power turbine governing, but was shown to make no improvement. This is discussed in Section 2.5. This simplified model, which is used for calculating the LQR gains, is shown in Figure 2.2. The tail rotor dynamics were neglected because they are at high frequency compared to the main rotor dynamics. Note that this engine-rotor model is valid only for small deviations around the point at which it was linearized.

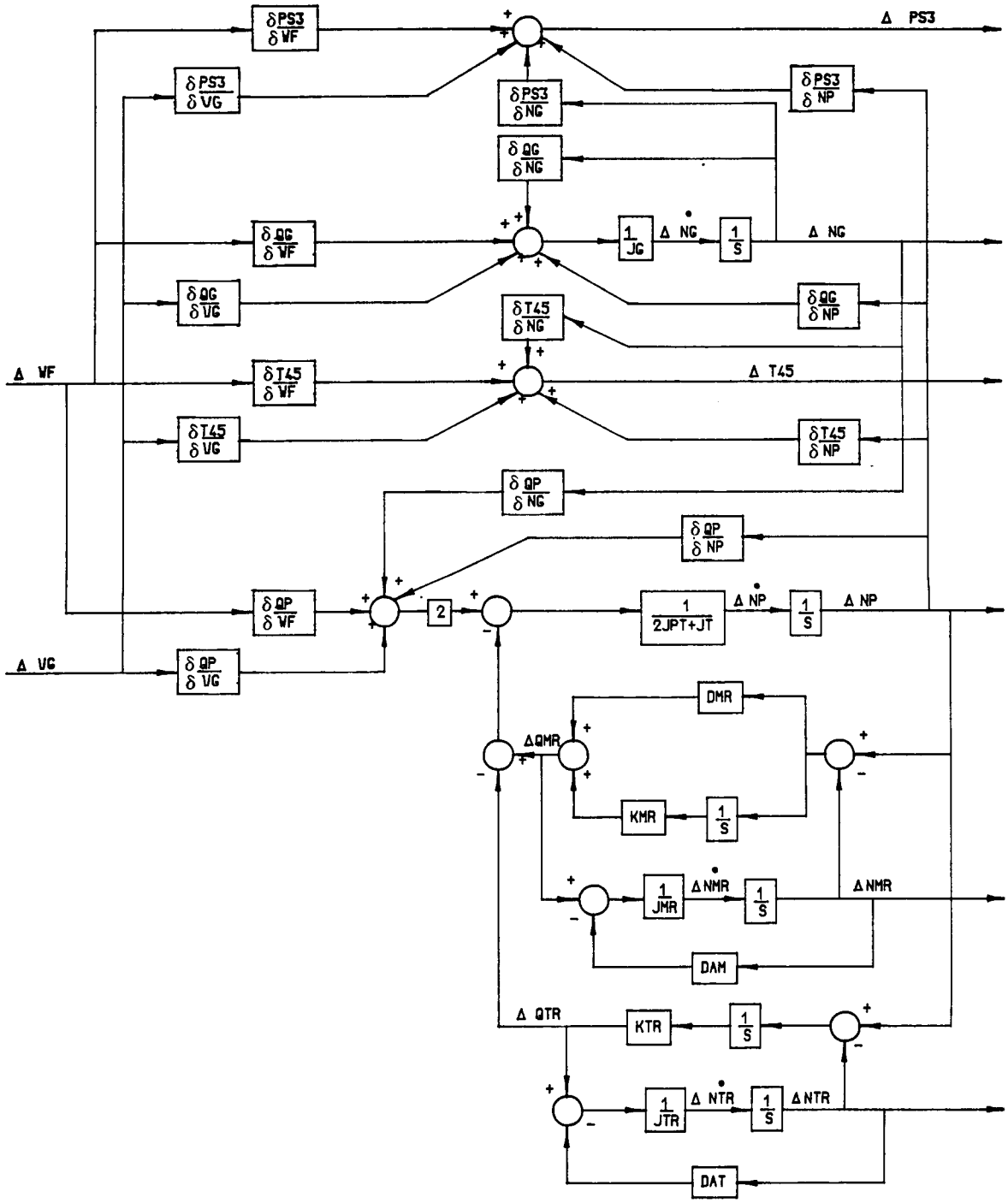


Figure 2.1 Engine and Helicopter Rotor System Linear Block Diagram.

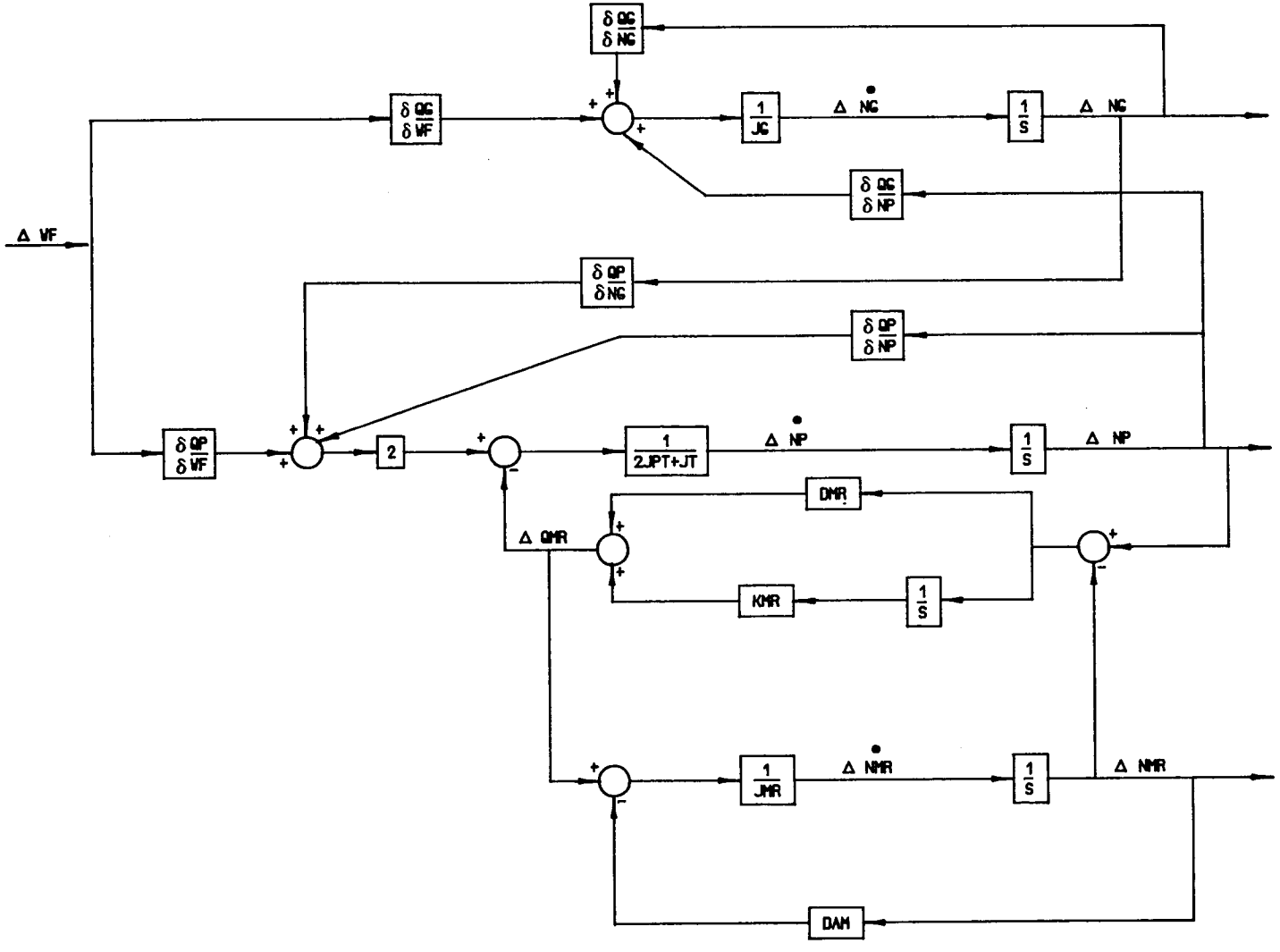


Figure 2.2 Simplified, Linear, Engine and Helicopter Rotor System Block Diagram.

### 2.1.2 Rotor Model

The full, linear rotor model is shown in Figure 2.3. This lumped-parameter model is used for frequency response testing, but is unnecessarily complex for the LQR design. This model was simplified to the model shown in Figure 2.4. It accurately retains the dynamic characteristics of the rotor through the main rotor frequency. The engine-rotor model of Figure 2.2 with the simplified helicopter rotor system was compared to the model with the more complex rotor system by comparing the frequency response of each system from WF input (more correctly d (WF)/dt input - see Section 2.1.3) to NP output. The Bode plots comparing the simplified and complex rotor systems as mentioned above are included in Appendix I. For rotor systems that do not have a large frequency separation between the main and tail rotor resonances, the tail rotor dynamics may need to be included in the model used for LQR design. The nonlinear engine model used for transient testing has this simplified helicopter rotor model with simplified tail rotor dynamics. This model is shown in Figure 2.5.

The rotor model parameters were maintained constant for all power levels. The aerodynamic damping varies with power level, but this was maintained constant for frequency response analysis. The centrifugal spring constant arises from the rotation of the rotor. If the constitutive relationship for a torsional spring is

$$Q = K\theta \tag{2.1}$$

where Q is the torque caused by the centripetal acceleration on the main rotor blade and $\theta$ is the lag angle as defined in Figure 2.6, K is known as the centrifugal spring constant. This constant actually varies proportionally to the square of the main rotor angular blade velocity (Ref. 14). Nominally, the blade angular velocity is constant at all power levels. This velocity changes during rotor droop. For frequency response analysis, to assure adequate stability margins, this spring constant was varied about the nominal corresponding to a $\pm$ 10% change in rotor speed. All rotor models assume rigid blades.

### 2.1.3 Integral Augmentation

The LQR design does not add any dynamics to the system. If isochronous NP governing is required, an integrator must be appended to the engine model. This integrator is added to the system input, as shown in Figure 2.7. The system is later transformed such that the input to the integrator is the difference between the power turbine speed reference and the actual speed, as required to have isochronous governing. The integrator is actually part of the controller, but for the LQR design, it is considered part of the plant. Several design iterations were tried with the integrator appended directly to NP, but the results were not as good as for the integrator added to the WF input.

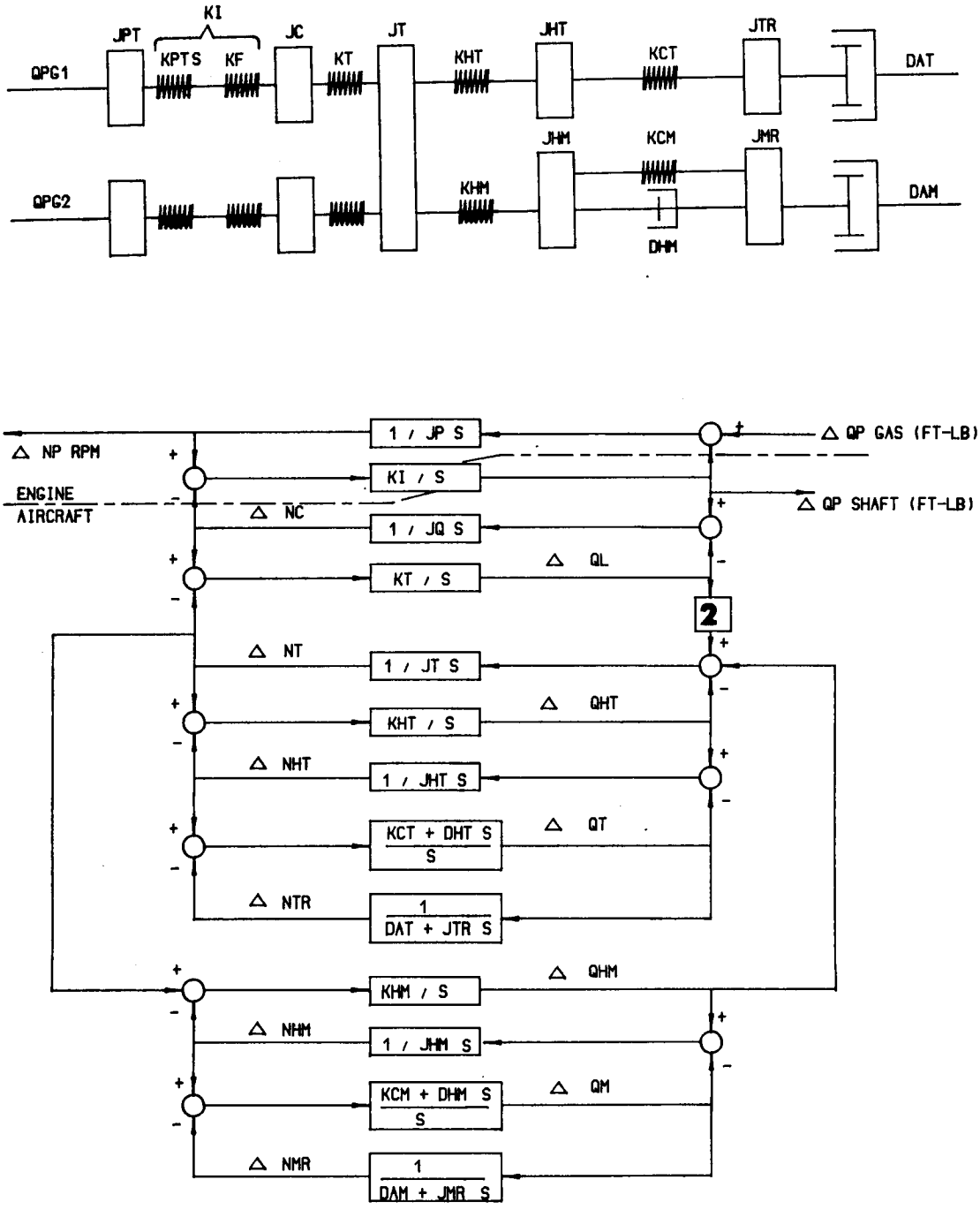


Figure 2.3 Full, Linear, Helicopter Rotor System.
a. Schematic
b. Block Diagram

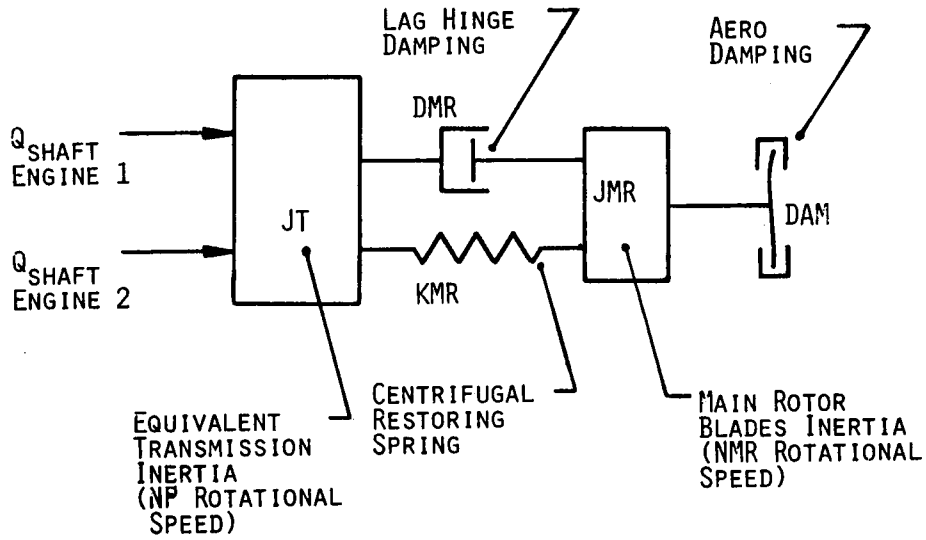


Figure 2.4 Simplified, Linear, Helicopter Main-Rotor Model.

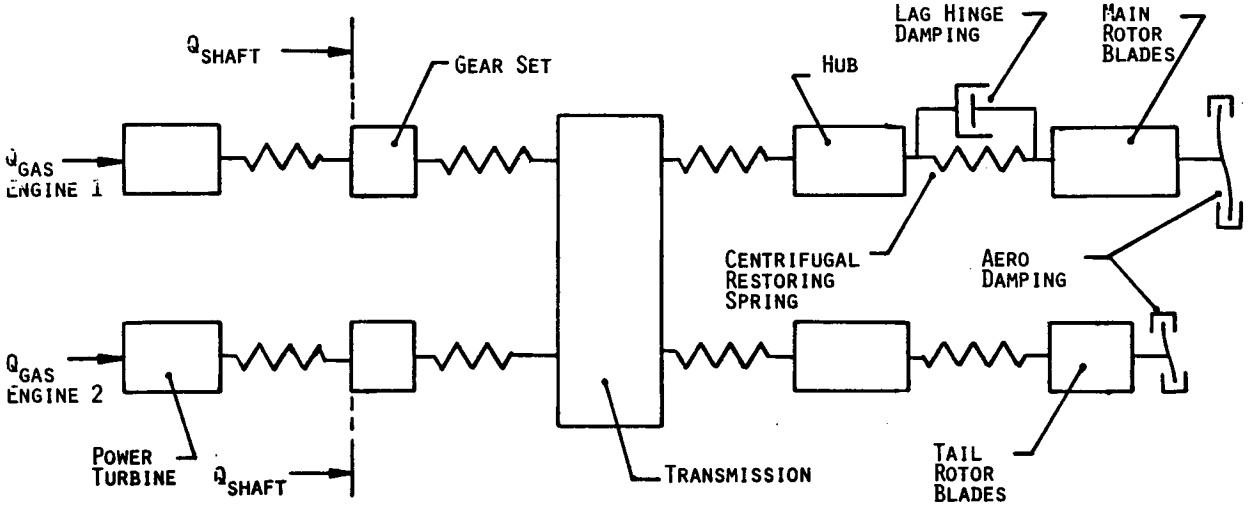


Figure 2.5 Simplified, Linear, Helicopter Rotor Model for Time Simulations.

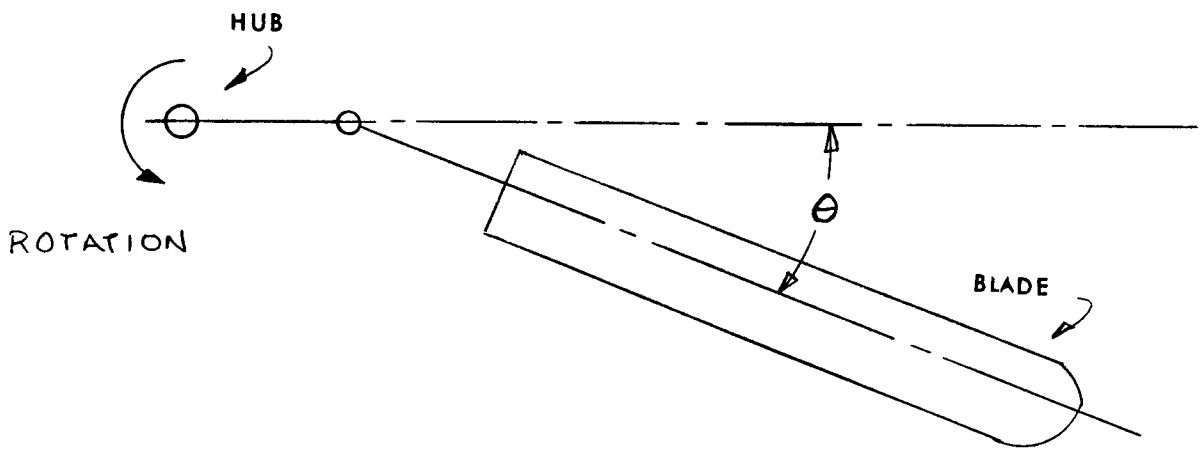


Figure 2.6 Geometrical Definition of Helicopter Main Rotor Lag Angle.

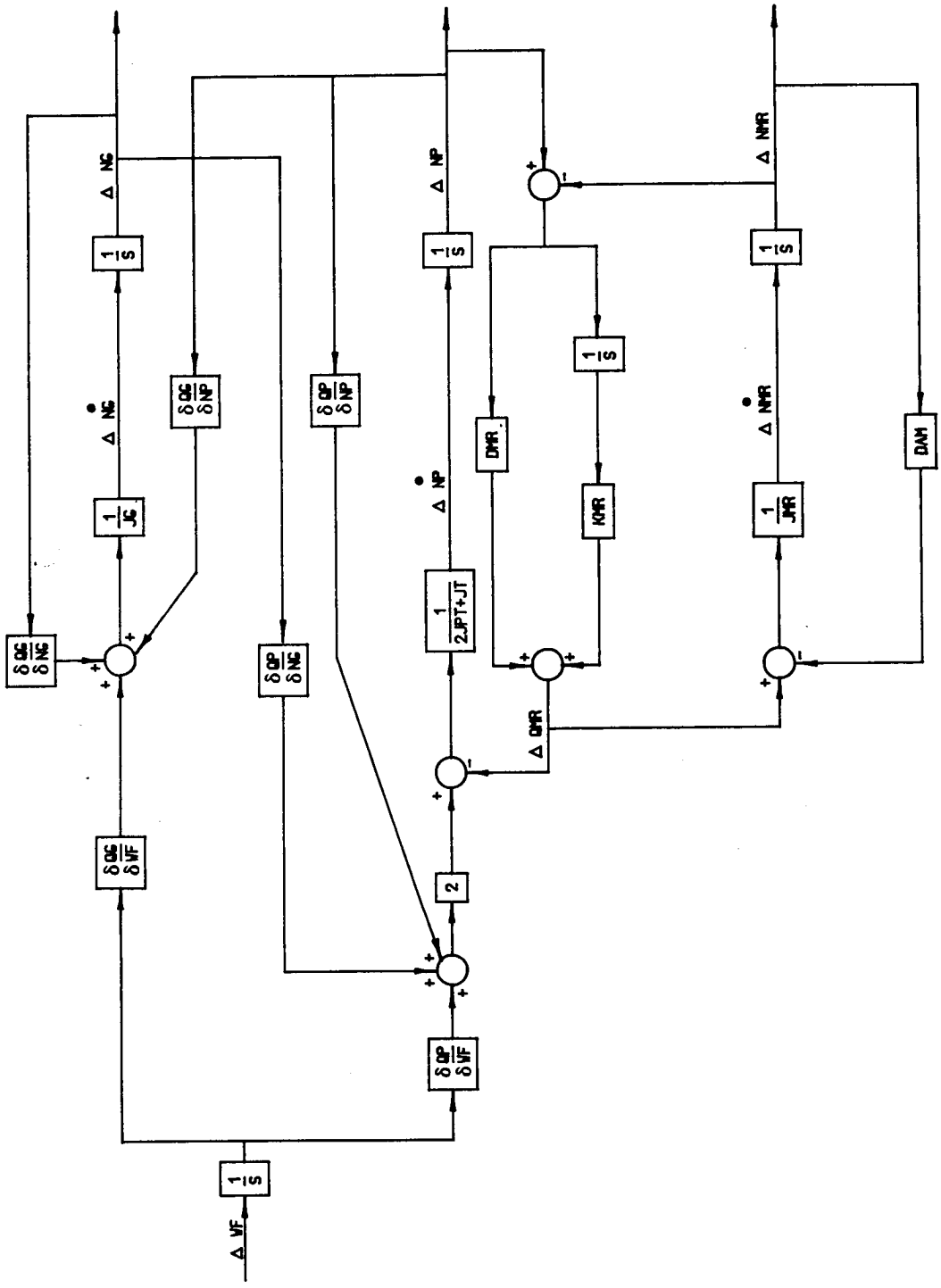


Figure 2.7 Simplified, Linear, Engine and Helicopter Rotor System with Appended WF Integrator.

### 2.1.4 State Variables

The state variables of a system are not unique, but often the system dictates a particular set. This is the case with the engine-rotor system. The engine states were chosen to be gas generator speed, NG, and power turbine speed, NP. These states are already measured in the real engine. The main rotor angular velocity (recall the models assume rigid blades) was also chosen as a state. This state is not practically measurable and was estimated using an observer. This will be discussed more fully starting in Section 2.2. The other state associated with the rotor is the rotor torque arising from the lag-hinge damper and the centrifugal spring. This state is not measurable but is approximated by engine shaft torque. This approximation is at least in error by the torque absorbed by the tail rotor and the aerodynamic damping, and there is a noticeable adverse effect seen on frequency response results when the engine shaft torque is used instead of the actual main rotor torque state, as discussed in Section 2.3.2.1. The last state is the output of the appended integrator. This state is WF and thus the input to the integrator is dWF/dt. All of the states were chosen as the outputs of integrators with the slight variation of adding the lag-hinge damping to the rotor "spring" state.

For some rotor systems, it may be necessary to include the tail rotor dynamics in the design. This would add two more states to the system - a tail-rotor torque state and a tail-rotor speed state.

### 2.1.5 System Equations

The equations of the system are derived as a set of first order differential equations that are functions of the state variables and the inputs. Because of the appended integrator for isochronous governing, the input to the system is the derivative of WF (refer to Figure 2.7). This is only a mathematical input for use in deriving the LQR gains. The first order differential equations are then put into the general matrix state-space form:

$$\Delta \dot{\underline{x}} = \underline{A}\ \Delta \underline{x} + \underline{B}\ \Delta \underline{u} \qquad (2.2a)$$

$$\Delta \underline{y} = \underline{C}\ \Delta \underline{x} \qquad (2.2b)$$

where $\Delta \underline{x}$ is a vector (column matrix) of states, $\Delta \dot{\underline{x}}$ is the first derivative of the states with respect to time ($d\Delta \underline{x}/dt$), $\Delta \underline{u}$ is the input (WF), and $\underline{A}$, $\underline{B}$ and $\underline{C}$ are matrices of coefficients. $\Delta \underline{y}$ is a matrix of outputs, and each element of $\Delta \underline{y}$ is a linear combination of the states, $\Delta \underline{x}$. $\underline{A}$ and $\underline{B}$ vary with power level from FI to IRP, but are constant at each power level. $\Delta \underline{x}$ and $\Delta \underline{u}$ generally vary with time. A block-diagram representation of the system in matrix state-space form is shown in Figure 2.8. The $\Delta$'s emphasize that the model is only valid around the steady state point.

The equations are put into matrix form rather than the more traditional and equivalent transfer function representation to facilitate the application of the LQR design. Transformation from transfer function to state-space form is possible by replacing the Laplace operator s by d/dt and transforming the

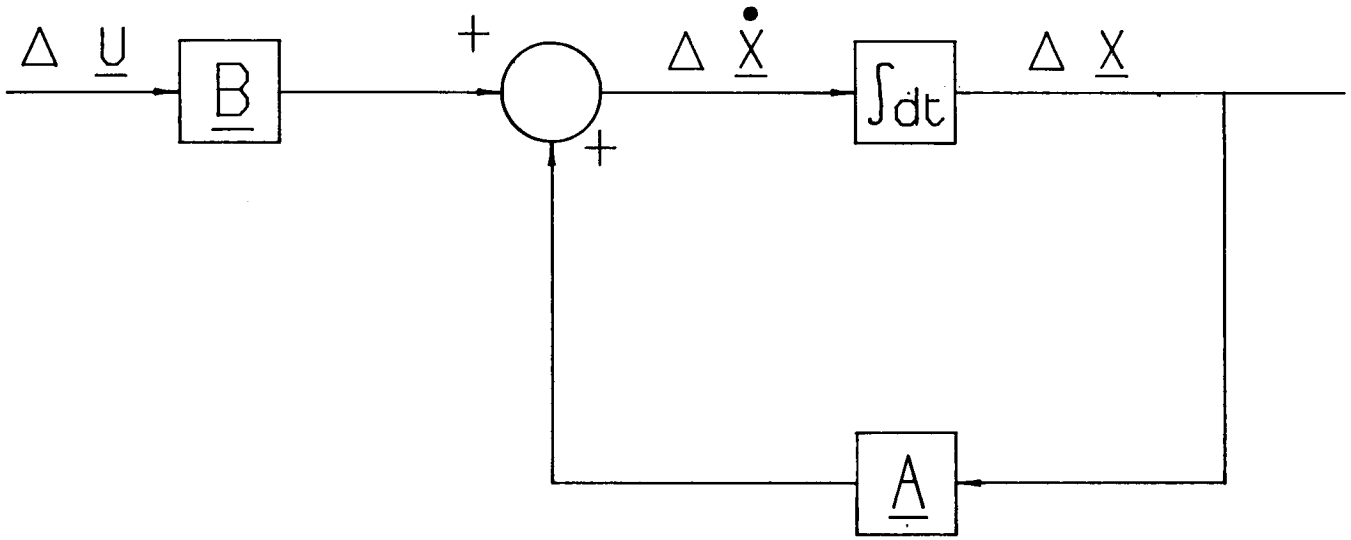


Figure 2.8 Matrix Block Diagram Representation of Engine and Helicopter Rotor with No Control.

resulting n'th order differential equation into a system of n first-order differential equations.

The state space equations for the engine-rotor system of Figure 2.7 are given in Figure 2.9. The equations can be derived from the block diagram of Figure 2.7 by starting at the input to each integrator ($\Delta \dot{\underline{x}}$) and working back through the diagram until $\Delta \dot{\underline{x}}$ is only a function of constants, state variables, or the input. A little more algebraic manipulation is necessary to get the equation for the rotor torque state.

### 2.1.6 LQR Design

The Linear Quadratic Regulator (LQR) computes the input, WF, to the system as a sum of the product of gain and the system states. The form of the regulator is shown in Figure 2.10. Figure 2.10 shows the compact matrix block diagram that compares with the uncompensated system of Figure 2.8. This controller is a perturbational controller in that it calculates an incremental WF needed to regulate the system based on the deviations of the states from reference values. Except for the reference value of power turbine speed, NP, the references only need to be approximations of the values at steady state. The WF reference is added to the incremental WF to get the total WF demanded by the controller. The integrator on NP error assures convergence of the actual NP to the reference NP, and makes up for approximations in the other reference values.

The LQR design is different than the standard governor design because the only dynamic element added is the integrator. Also, the internal makeup of the system (the states) are used for compensation rather than the input-output characteristics (transfer function) as used in standard compensation design.

The compensation shown in Figure 2.10 is called linear, state-feedback control because each of the states is fed back and combined linearly to calculate the WF input to the system. For controllable systems, it is possible to calculate the gains, $\underline{G}$, such that the poles of the system can be placed anywhere in the s-plane with the restriction that complex poles be placed as complex conjugate pairs. A system is loosely defined as controllable if the control can affect all of the natural modes of a system. Power turbine speed in the T700 engine is controllable from fuel flow. More discussion on controllability can be found in Ref. 9. The Linear Quadratic Regulator method places the poles in a way that minimizes a certain cost functional chosen by the control engineer.

### 2.1.7 LQR Theory

The LQR method calculates the matrix of gains, $\underline{G}$, such that a cost functional, J, is minimized. In general, the gains, $\underline{G}$, vary with time, but for the special case where the system of Equation 2.2 is asymptotically stable (all poles are in the left-half plane), the gains, $\underline{G}$, reach a steady state value as

$$\begin{bmatrix} \dot{NG} \\ \dot{NP} \\ \dot{QMR} \\ \dot{NMR} \\ \dot{Wf} \end{bmatrix} = \begin{bmatrix} \frac{1}{JG}\frac{\delta Qg}{\delta NG} & 0 & 0 & 0 & \frac{1}{JG}\frac{\delta Qg}{\delta Wf} \\ \frac{2}{(2JP+JT)}\frac{\delta QP}{\delta NG} & \frac{2}{(2JP+JT)}\frac{\delta QP}{\delta NP} & -\frac{1}{(2JP+JT)} & 0 & \frac{2}{(2JP+JT)}\frac{\delta QP}{\delta Wf} \\ \frac{2\ DMR}{(2JP+JT)}\frac{\delta QP}{\delta NG} & KMR + \frac{2\ DMR}{(2JP+JT)}\frac{\delta QP}{\delta NP} & \frac{-DMR}{(2JP+JT)} - \frac{DMR}{JMR} & -KMR + \frac{DAM\ DMR}{JMR} & \frac{2\ DMR}{(2JP+JT)}\frac{\delta QP}{\delta Wf} \\ 0 & 0 & \frac{1}{JMR} & \frac{-DAM}{JMR} & 0 \\ 0 & 0 & 0 & 0 & 0 \end{bmatrix} \begin{bmatrix} NG \\ NP \\ QMR \\ NMR \\ Wf \end{bmatrix}$$

$$+ \begin{bmatrix} 0 \\ 0 \\ 0 \\ 0 \\ 1 \end{bmatrix} \dot{Wf}$$

Figure 2.9 State-Space Equations of Simplified, Linear, Engine and Helicopter Rotor with Integral Augmentation.

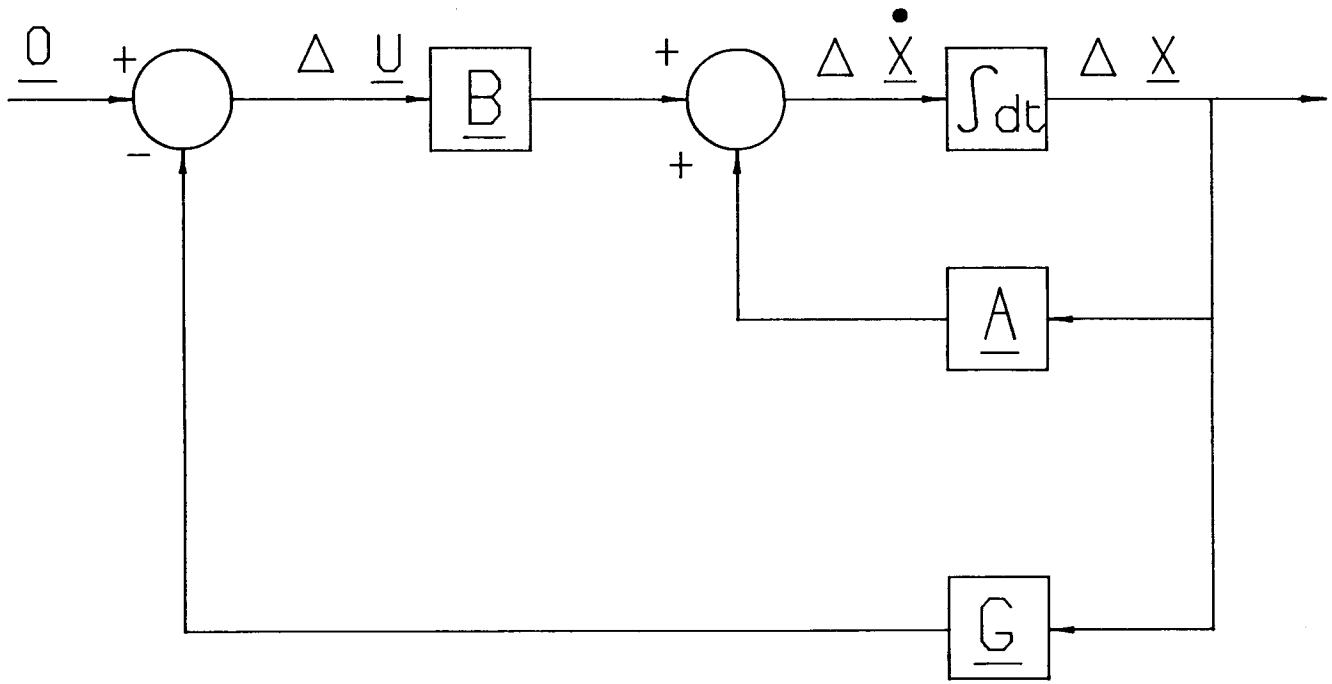


Figure 2.10 Matrix Block Diagram Representation of Engine and Helicopter Rotor with Linear State Feedback.

time approaches $\infty$. These steady-state gains can be used in place of the time-varying gains, and the resulting closed-loop system will remain asymptotically stable, generally with no loss in performance.

The cost functional, J, has the form:

$$J = \int_{t_0}^{\infty} [\underline{x}^T(t)\ \underline{Q}\ \underline{x}\ (t) + \underline{u}^T(t)\ \underline{R}\ \underline{u}\ (t)]\ dt \qquad (2.3)$$

where $\underline{x}(t)$ is the state vector, $\underline{u}(t)$ is the input vector, $x^T$ denotes the transpose of $\underline{x}$, and $\underline{Q}$ and $\underline{R}$ are weighting matrices chosen by the design engineer. Choosing $\underline{Q}$ and $\underline{R}$ will be discussed in Section 2.1.12. The $\Delta$'s have been dropped from the notation, although the small-perturbation restriction still applies.

The cost, J, is a functional because it is a function of functions $\underline{x}(t)$ and $\underline{u}(t)$, however, J has a scalar value.

The closed-loop control law is:

$$\underline{u}(t) = -\underline{G}\ \underline{x}\ (t) \qquad (2.4)$$

The cost, J, is minimized for the system of Equation 2.2 and the weighting matrices $\underline{Q}$ and $\underline{R}$ when the gains, $\underline{G}$, are calculated by:

$$\underline{G} = \underline{R}^{-1}\ \underline{B}^T\ \underline{S} \qquad (2.5)$$

where $\underline{R}$ is the weighting on the control, $\underline{B}$ comes from the system differential equation, and $\underline{S}$ is the solution to the algebraic Ricatti Equation:

$$\underline{0} = \underline{Q} - \underline{S}\ \underline{B}\ \underline{R}^{-1}\ \underline{B}^T\ \underline{S} + \underline{S}\ \underline{A} + \underline{A}^T\ \underline{S} \qquad (2.6)$$

$\underline{Q}$ is the state weighting, and $\underline{A}$ and $\underline{B}$ are the coefficient matrices from the system differential equation. $\underline{0}$ is a square matrix of zeros.

Calculating the gains, $\underline{G}$, consists of choosing nonnegative, symmetric $\underline{Q}$ and $\underline{R}$ matrices (to assure a unique solution), solving the algebraic Ricatti Equation to get $\underline{S}$, and then computing $\underline{G}$ from Equation 2.5. The difficulty in the procedure comes in choosing $\underline{Q}$ and $\underline{R}$ to get the desired performance results. Many software packages exist that will compute $\underline{G}$ given the matrices $\underline{A}$, $\underline{B}$, $\underline{Q}$, and $\underline{R}$.

### 2.1.8 Properties of the LQR

Several characteristics of a closed-loop system designed via the LQR method are mentioned here. A continuous LQR system has guaranteed 60° of phase margin and -1/2 to $\infty$ gain margin when the loop is broken at the system input. The system input is not WF when an integrator is added to a system, it is the input

to the integrator. In Section 2.1.10 it will be shown that this can be transformed such that the guaranteed phase and gain margins are at the WF input to the plant. These guaranteed margins do not hold for systems that are sampled by a computer, or for systems where one or several states cannot be measured, and an observer must be used to estimate states. For a single-input-single -output system, these restrictions do not present a problem since the system can be analyzed using standard frequency response techniques. For multi-input-multi-output systems, analysis techniques based on singular values have been developed, but they must be used with caution when a system does not meet the assumptions of the techniques. Another property of the LQR system is that it has a high-frequency roll-off in the frequency domain of -20 dB/decade. Generally, a steeper roll-off is desired to attenuate noise, and this was achieved using analog anti-alias filters.

### 2.1.9 LQR Theory Applied to the T700 Engine

The LQR method requires that all states be available for feedback to compute the input to the system. The five states of the engine and rotor system are summarized below:

| | |
|---|---|
| NG | Gas generator speed |
| NP | Power turbine speed |
| WF | Output of appended integrator |
| NMR | Helicopter main-rotor velocity |
| QMR | Helicopter main-rotor torque due to centrifugal spring and lag-hinge damper |

The first two states are currently measured on the T700 engine. The third state is computed in the control and is, therefore, available. The last two states are rotor states and are not measured. Engine shaft torque is used to estimate QMR. This will be discussed in more detail in Section 2.3.2.1. NMR cannot be estimated accurately with currently measured signals, so it was calculated, or reconstructed, using an observer of the rotor system. The observer is a closed-loop system that contains a model of the rotor system to estimate the rotor system states. The estimated main-rotor velocity, NMR, is then fed back in place of the actual state, NMR, to calculate the WF input. The LQR gain matrix, $\underline{G}$, remains the same.

The observer system is designed as a separate control loop independent of the main LQR loop. Note that the entire system that includes the observer no longer has guaranteed phase and gain margins. The system has to be analyzed in the frequency domain to determine actual stability margins. The observer is discussed in detail starting with Section 2.2.

### 2.1.10 Transforming LQR Gains for Isochronous Np Governing

The LQR method for this system with integral augmentation produced the best performance results when the integrator was appended to the input. This system is shown schematically in Figure 2.11. For isochronous NP governing, the system must be configured as shown in Figure 2.12. The gains, $\underline{G}_1$ and $\underline{G}_2$, calculated for the format of Figure 2.11 can be transformed to the gains, $\underline{L}$ and $\underline{H}$, of Figure 2.12 using a transformation derived in Ref. 12. The guaranteed gain and phase margins mentioned in Section 2.1.8 are now at the point in the loop where WF enters the engine. Figure 2.13 is a more detailed schematic that compares with Figure 2.12. The LQR system, with the observer, is shown in Figure 2.14, where shaft torque has been substituted for QMR as described in the previous section.

The transformed gains, $\underline{L}$ $\underline{H}$, are calculated as follows:

$$[\underline{L}\ \underline{H}] = \begin{bmatrix} \underline{A} & \underline{B} \\ \underline{C} & \underline{0} \end{bmatrix}^{-1} [\underline{G}] \qquad (2.7)$$

where $\underline{L}$ $\underline{H}$ are the transformed gains, $\underline{G}$ are the original gains $[\underline{G}_1\ \underline{G}_2]$, and $\underline{A}$, $\underline{B}$, and $\underline{C}$ are the system matrices defined by Equations 2.2 and do not include the integral state.

### 2.1.11 LQR Perturbational Controller

The LQR power turbine governor, like the current T700 governor, is designed as a perturbational controller and the design is strictly only valid for small deviations from the steady-state design point. This means that stability or good performance is not guaranteed if the engine operates at some condition that was not analyzed. A standard design procedure is to analyze the system at several representative operating points and do time simulations to exercise the system with large deviations from steady state. Then, the engineer can become confident that the system will be stable and perform adequately across the engine envelope.

The LQR governor controls NP based on the deviations of the states from their steady-state values. When a new load demand is made and a transient is initiated, the steady-state values from which the deviations are computed are the values at the demanded steady state. These are the variables labeled as references (REF) in Figure 2.13. The steady-state references are scheduled as a function of the load demand spindle (LDS) and approximate steady state values of a standard engine as a function of the load on the engine. The load demand spindle is a signal that is proportional to collective pitch angle and is an indication of pilot load demand through the collective pitch. The LDS is used as a feed-forward compensation in the baseline T700 Control System (Ref. 8) to reduce power turbine speed droop. Transients that used the LDS are referred to as compensated transients. Wind gusts or maneuvers that are not initiated by changing the collective pitch angle are referred to as

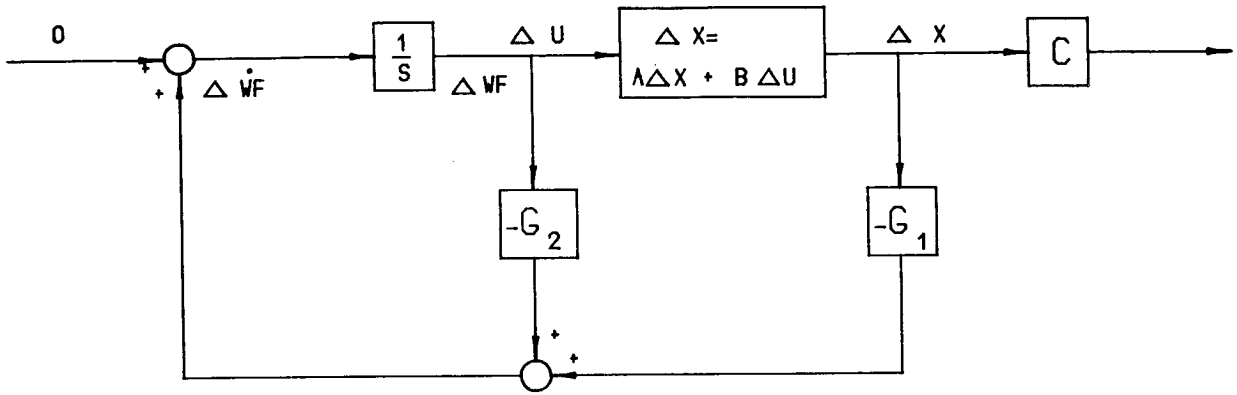


Figure 2.11 Matrix Block Diagram Representation of Standard LQR System with Integral Augmentation



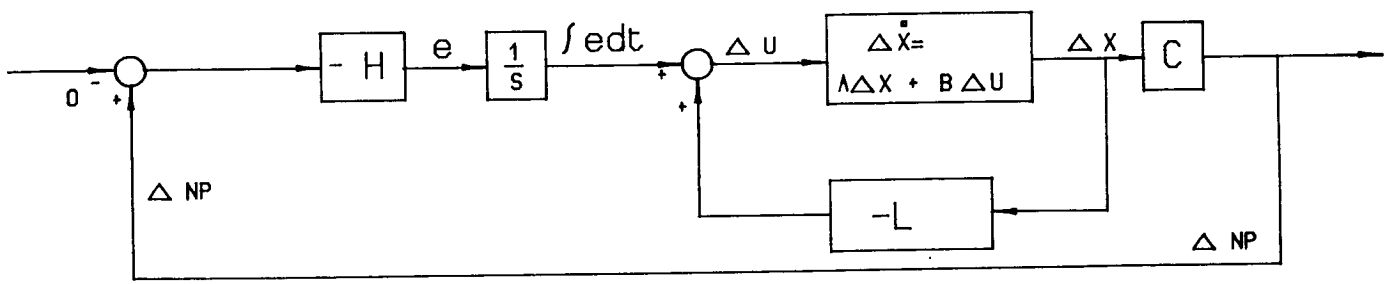


Figure 2.12 Matrix Block Diagram Representation of LQR System Transformed for Isochronous Np Governing.

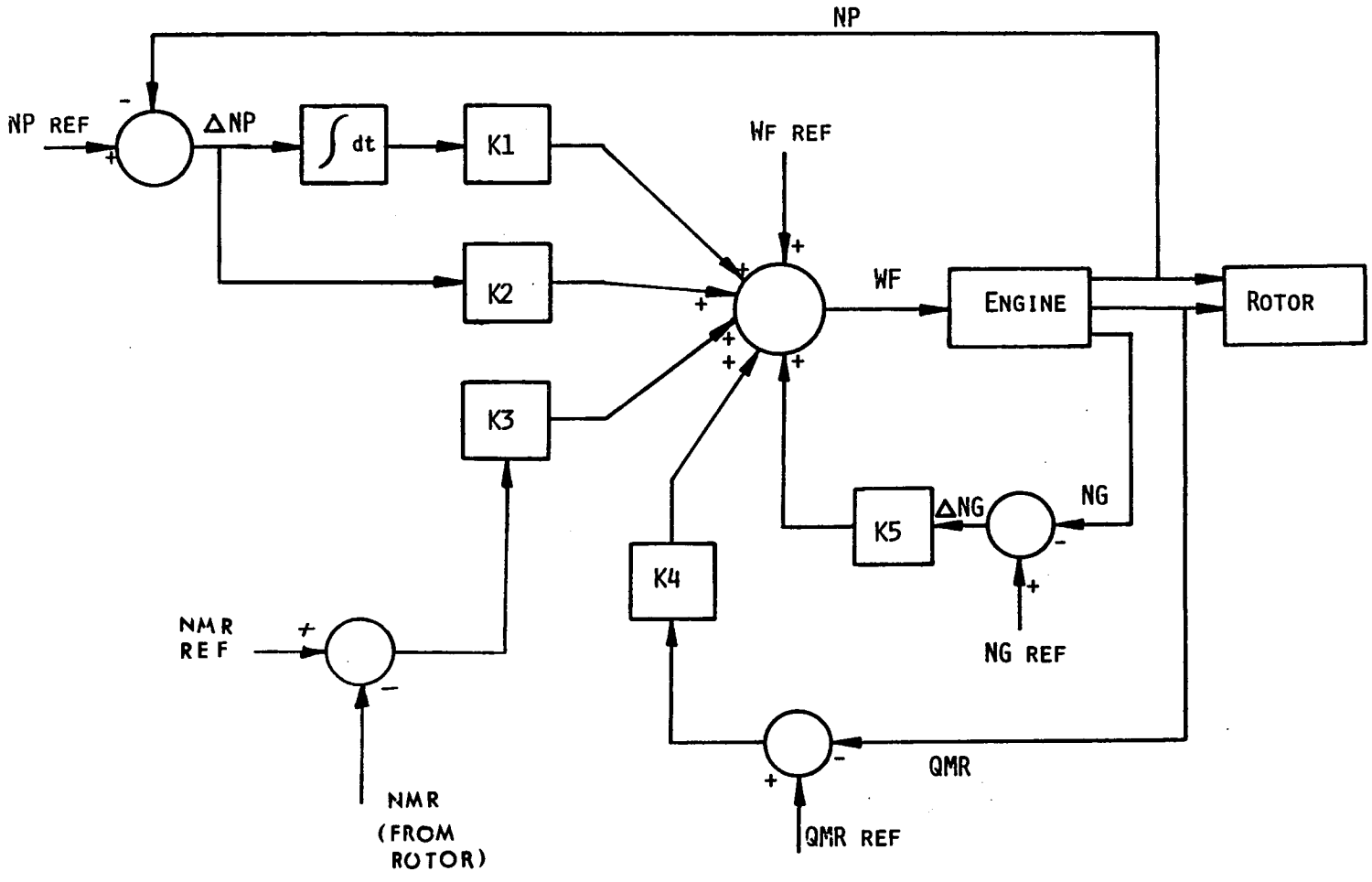


Figure 2.13 Detailed Block Diagram Representation of Engine and Helicopter Rotor with Linear State Feedback.

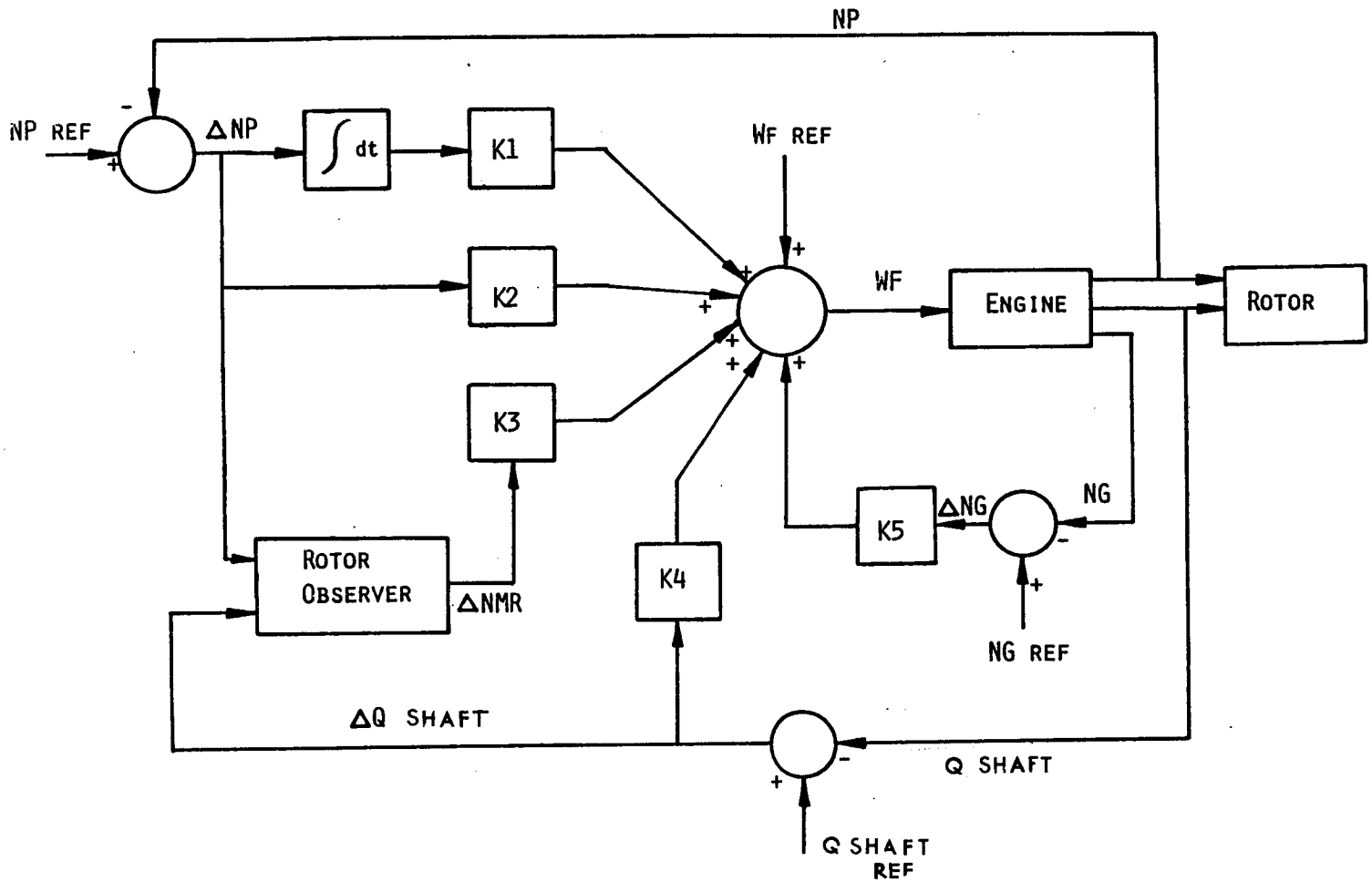


Figure 2.14 Detailed Block Diagram Representation of Engine and Helicopter Rotor with Linear State Feedback and Observer.

uncompensated since the load demand spindle remains constant as does the collective pitch angle. In this case, the steady-state references remain at the original steady-state value.

### 2.1.12 Calculating LQR Gains

To calculate the LQR gain matrix, $\underline{G}$, the engineer can vary the state weighting matrix, $\underline{Q}$, and the control weighting matrix, $\underline{R}$, in the cost functional of Equation 2.3. The matrix, $\underline{Q}$, changes the shape of the Bode plot in the frequency domain, and if $\underline{R}$ is chosen as the diagonal matrix:

$$\underline{R} = \rho \underline{I} \tag{2.8}$$

with $\rho$ a scalar and $\underline{I}$ the identity matrix, then $\rho$ has the effect of moving the magnitude of the Bode plot up and down like a gain. Generally, choosing $\underline{Q}$ and $\rho$ is an iterative procedure.

The state weighting matrix, $\underline{Q}$, was chosen to be unity weight on the helicopter main rotor velocity, NMR, and on fuel flow, WF. This is given in matrix form as:

$$\text{diag} [\ 0 \quad 0 \quad 1 \quad 0 \quad 1\ ] \tag{2.9}$$

where "diag" means a square matrix with the elements in the brackets along the diagonal, and zeros everywhere else. Recall that the state matrix, $\underline{x}$, is:

$$\underline{x} = [\ \text{NG} \quad \text{NP} \quad \text{NMR} \quad \text{QMR} \quad \text{WF}\ ]^T \tag{2.10}$$

as described in Section 2.1.9. For each model at the six power levels, $\rho$ was varied to give a crossover of about 10 rad/sec. A crossover of 10 rad/sec was chosen to give a fast governor response without exciting the helicopter main rotor resonance at about 18 rad/sec. Also, the engine dynamics are not very well known above about 10 rad/sec. A different set of gains was calculated for each power level for a total of six sets of gains. Each set of gains, $\underline{G}$, was then transformed to the set of gains, $\underline{L}$ $\underline{H}$, as described in Section 2.1.10. The design model and the gains $\underline{L}$ $\underline{H}$ are included in Appendix II for each power level.

It is desirable to simplify the control logic by having a constant set of LQR gains independent of power level. The set of gains having elements with the lowest magnitudes was chosen, and the frequency response of the six engine models was calculated with this constant set of gains. The results are discussed in Section 2.3.3. The lowest magnitude gains were computed for the system model at 95% NG and are given as:

$$\underline{L}\ \underline{H} = [0.0726,\ 0.25,\ 0.94,\ -0.67,\ 4.3] \qquad (2.11)$$

These gains correspond to the state vector:

$$\underline{x}' = [\ NG \quad NP \quad NMR \quad QMR \quad \int NP]^T \qquad (2.12)$$

where $\underline{x}'$ is the transformed state vector (Section 2.1.10), and $\int NP$ is the integral of the NP error. The NP error is defined as the NP reference minus the measured NP.

### 2.1.13 Use of Continuous versus Discrete LQR Gains

The sampling and zero-order hold process in a process controlled by a digital computer introduces phase lag not introduced by a continuous or analog controller. The system design can be done with an equivalent discrete model that includes the effects of sampling and the zero-order hold. The LQR gains can then be calculated using the discrete model. The dynamic behavior of the sampled system with the discrete - model LQR gains should be a close approximation to the analog - controlled system with analog - model LQR gains. As the sampling period approaches zero, the discrete gains approach the continuous gains in magnitude.

In order to evaluate this effect, the LQR gains were calculated at the 90% NG power setting using a discrete - model equivalent to the continuous engine - rotor model. The continuous state weighting and control weighting matrices were converted to equivalent discrete weighting matrices. The LQR gains were also calculated for the continuous system. The continuous and equivalent discrete gains are given below:

Continuous gains: (2.13)

$$[0.0783 \quad 0.1123 \quad 0.0037 \quad 0.7261 \quad 9.0050]$$

Discrete gains: (2.14)

$$[0.0753 \quad 0.1067 \quad 0.0025 \quad 0.6926 \quad 8.8078]$$

The gains correspond to the untransformed states:

$$\underline{x} = [\ NG \quad NP \quad NMR \quad QMR \quad WF]^T \qquad (2.10)$$

The continuous values vary by less than 5% for all gains except the gain or NMR. For a sampled system, a small change in the value of coefficients can have a big effect on the location of the system poles, but frequency response analysis showed adequate stability margins. The continuous gains were used because the transformation described in Section 2.1.10 could not be adapted for use with the discrete - equivalent model.

## 2.2 Observer (Kalman Filter)

### 2.2.1 Introduction

An observer is a closed loop system that contains a model of all or part of the system and estimates system states when driven by known inputs and measurements. A schematic of an observer is shown in Figure 2.15. The observer system must meet the usual requirements of stability and performance with the added requirement that it calculate the estimated states of interest fast enough so that the performance of the main loop is not affected. If the model of the system used in the observer is observable, all of its poles can be placed arbitrarily in the s-place, with the restriction that complex poles be placed as complex conjugate pairs. Main rotor blade velocity is observable in the T700 system from power turbine speed. More discussion on observability can be found in Ref. 9. The Kalman Filter algorithm places the system poles in a specific manner.

### 2.2.2 Rotor Model for Observer

The rotor model used for the observer is the simplified model of Figure 2.4 that neglects the tail-rotor dynamics. The power turbine inertia is not lumped as part of the transmission as is done for the complete engine and rotor system. The rotor model was put into state-space form given generically as:

$$\underline{\dot{X}}_R(t) = \underline{A}_R \underline{X}_R(t) + \underline{B}_R \underline{u}_R(t) \qquad (2.15a)$$

$$\underline{Y}_R(t) = \underline{C}_R \underline{X}_R(t) \qquad (2.15b)$$

where $\underline{X}_R(t)$ is the rotor state vector, $\underline{u}_R(t)$ is the input to the rotor, $\underline{Y}_R$ is the output vector, and $\underline{A}_R$, $\underline{B}_R$, and $\underline{C}_R$, are the system coefficient matrices. Model validity around a steady-state value is implied.

The states for this system are main rotor angular velocity, $\hat{NMR}$, a main rotor torque state, $\hat{QMR}$, and transmission speed, $\hat{NP}$. The transmission speed is approximated as power turbine speed, NP, because for this simple model, the coupling between the power turbine and transmission is assumed rigid. The caret ($\hat{}$) above the state variables indicates that these are estimated states from the observer rather than measured states. The input, $\underline{u}_R(t)$, to this system is engine shaft torque, Q shaft. The output vector, $\underline{Y}$ consists of $\hat{NP}$ and $\hat{QMR}$. An assumption was made that Q shaft was a good approximation to QMR. This is discussed more in Section 2.3.2.1.

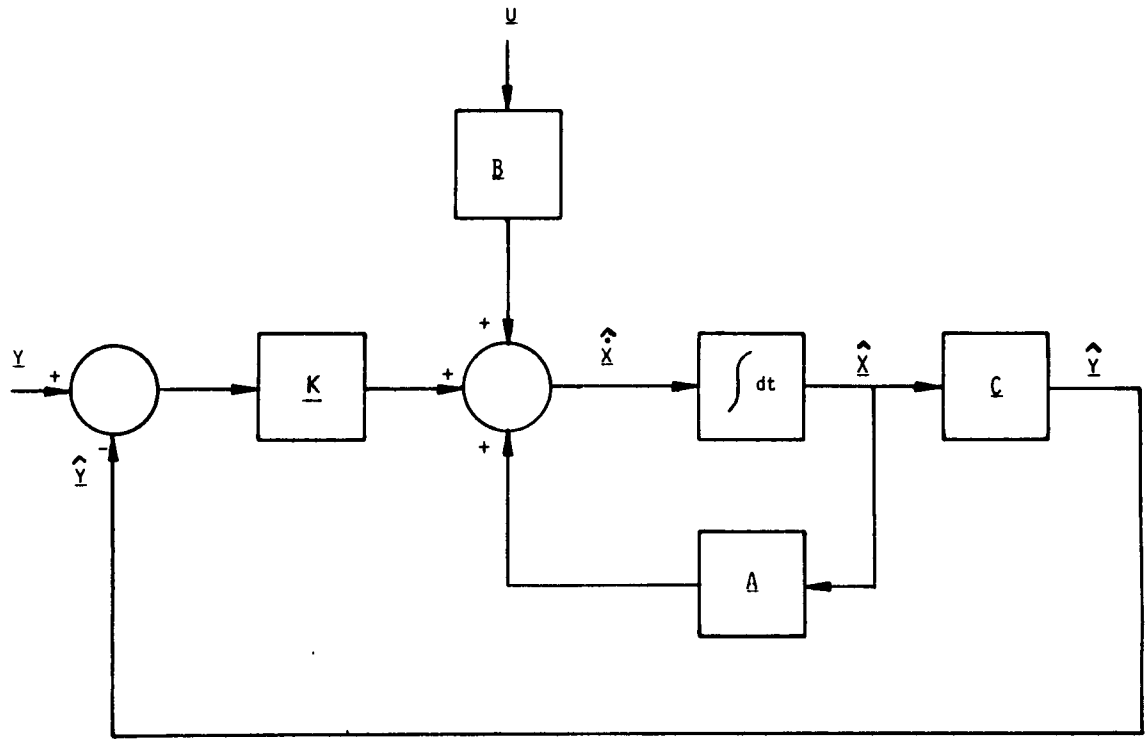


Figure 2.15 Matrix Block Diagram Representation of Observer.

The Kalman Filter of the helicopter rotor system was designed using an equivalent discrete model of the system given by Equations 2.15. The discrete model is a set of first order difference equations that approximates the behavior of the continuous model driven by a zero order hold input. In reality, the rotor is driven by the continuous torque from the engine, so the zero-order hold assumption is a further approximation. This assumption only affects the system $\underline{B}_R$ matrix, however, which does not enter into the Kalman Filter gain calculations and should not have a major impact on system performance.

The generic form of the system difference equations is:

$$\underline{X}(i + 1) = \underline{A}_d\underline{X}\ (i) + \underline{B}_d\ u(i) \tag{2.16a}$$

$$\underline{Y}(i) = \underline{C}_d\underline{X}(i) \tag{2.16b}$$

where i is the time step at which measurements are sampled and control action is possible on the plant. Here it is assumed that the measurements and control action occur at the same time, and there is a full-interval processing delay from the time the measurements are taken to the time the new control action is taken. More discussion on the sequencing of events in the control is included in Section 2.6. The transformations from the continuous system matrices to the discrete system matrices are:

$$\underline{A}_d = \Phi\ [t(i + 1),\ t(i)] \tag{2.17a}$$

$$\underline{B}_d = \int_{t(i)}^{t(i+1)} \Phi\ [t(i + 1), \tau\ ]\ \underline{B}_R\ d\tau \tag{2.17b}$$

$$\underline{C}_d = \underline{C}_R \tag{2.17c}$$

where $\Phi$ is the state transition matrix, the solution to the unforced matrix differential equation of Equation 2.15a. Equations 2.17 are simplified based on the assumptions of constant input, u, over the interval between time steps and full-interval processing delay from $\underline{Y}(i)$ to $u(i + 1)$. The continuous simplified state-space description of the rotor system in terms of system variables is given in Equation 2.18. The variables are defined in Figure 2.4. The numerical values of the variables in included in Appendix II.

$$\begin{bmatrix} NP \\ NMR \\ QMR \end{bmatrix} = \begin{bmatrix} 0 & 0 & \frac{-1}{JT} \\ 0 & \frac{-DAM}{JMR} & \frac{1}{JMR} \\ KMR & \frac{DMR}{JMR}\frac{DAM}{-KMR} & \frac{-DMR}{JT} - \frac{DMR}{JMR} \end{bmatrix} \begin{bmatrix} NP \\ NMR \\ QMR \end{bmatrix}$$

$$+ \begin{bmatrix} \frac{2}{JT} \\ 0 \\ \frac{2DMR}{JT} \end{bmatrix} \text{ Q Shaft} \qquad (2.18)$$

### 2.2.3 Kalman Filter Formulation

The Kalman Filter formulation assumes the system of Equations 2.16 is corrupted by process noise and measurement noise as defined below:

$$\underline{X}(i+1) = \underline{A}_d \underline{X}(i) + \underline{B}_d u(i) + \underline{W}_1(i) \qquad (2.19a)$$

$$\underline{Y}(i) = \underline{C}_d \underline{X}(i) + \underline{W}_2(i) \qquad (2.19b)$$

where $\underline{W}_1(i)$ is the discrete process noise and $\underline{W}_2(i)$ is the discrete measurement noise. $\underline{W}_1(i)$ and $\underline{W}_2(i)$ have zero-mean, are uncorrelated, and have variance matrices $\underline{V}_1$ and $\underline{V}_2$, respectively.

The Kalman Filter places the closed-loop poles of the system to minimize the variance of the reconstruction error defined as:

$$E\left\{[(\underline{X}(i) - \hat{\underline{X}}(i)]\,[\underline{X}(i) - \hat{\underline{X}}(i)]^T\right\} \qquad (2.20)$$

where $\underline{X}(i)$ is the actual state value at sample i, and $\hat{\underline{X}}(i)$ is the estimated state value at sample i.

This variance is minimized for the variances of the process and measurement noises chosen, $\underline{V}_1$ and $\underline{V}_2$, respectively.

For a system that is asymptotically stable, the gains, $\underline{K}$, reach a constant value as the time step $i \longrightarrow \infty$. The discrete gains are computed from:

$$\underline{K} = \underline{A}_d \, \underline{P} \, \underline{C}_d^T \, (\underline{V}_2 + \underline{C}_d \, \underline{P} \, \underline{C}_d^T)^{-1} \tag{2.21}$$

when $\underline{P}$ is calculated from:

$$\underline{P} = (\underline{A}_d - \underline{K} \, \underline{C}_d) \, \underline{P} \, \underline{A}_d^T + \underline{V}_1 \tag{2.22}$$

The $\underline{V}_1$ and $\underline{V}_2$ matrices were treated as design variables to get good time and frequency domain results.

### 2.2.4 Kalman Filter Design Summary

This section summarizes the procedure used for designing the Kalman Filter used in the LQR power turbine governor. The first step was to formulate a continuous model of the rotor system. This model was then transformed to an equivalent discrete model using the transformations of Equations 2.17. The modeling steps are described in Section 2.2.2. A schematic of the rotor Kalman Filter is shown in Figure 2.16. Engine shaft torque, Q shaft, enters the system through the $\underline{B}_d$ matrix and also as a measured state. Using Q shaft as a measured state is an approximation to the actual main rotor state, QMR. Power turbine speed, NP, is also a measured state for this system.

The next task was to calculate the Kalman Filter gains, $\underline{K}$, by choosing suitable noise intensity matrices, $\underline{V}_1$ and $\underline{V}_2$, and solving Equations 2.21 and 2.22. For a given set of gains, $\underline{K}$, the Kalman Filter was analyzed as a separate system to determine if it met stability and performance criteria. Details of choosing the noise intensity matrices and analyzing the Kalman Filter are given in the following sections. The Kalman Filter was then included in the LQR power turbine governor, and the entire system was analyzed. This discussion begins with Section 2.3.

### 2.2.5 Calculating Kalman Filter Gains

#### 2.2.5.1 Choosing Noise Intensity Matrices

The process noise intensity matrix, $\underline{V}_1$, and the measurement noise intensity matrix, $\underline{V}_2$, determine the Kalman Filter gains, $\underline{K}$, for a given plant. These gains determine the shape of the Bode curves in the frequency domain, and thus the time response of the system. If $\underline{V}_2$ is chosen as:

$$\underline{V}_2 = \alpha \, \underline{I} \tag{2.23}$$

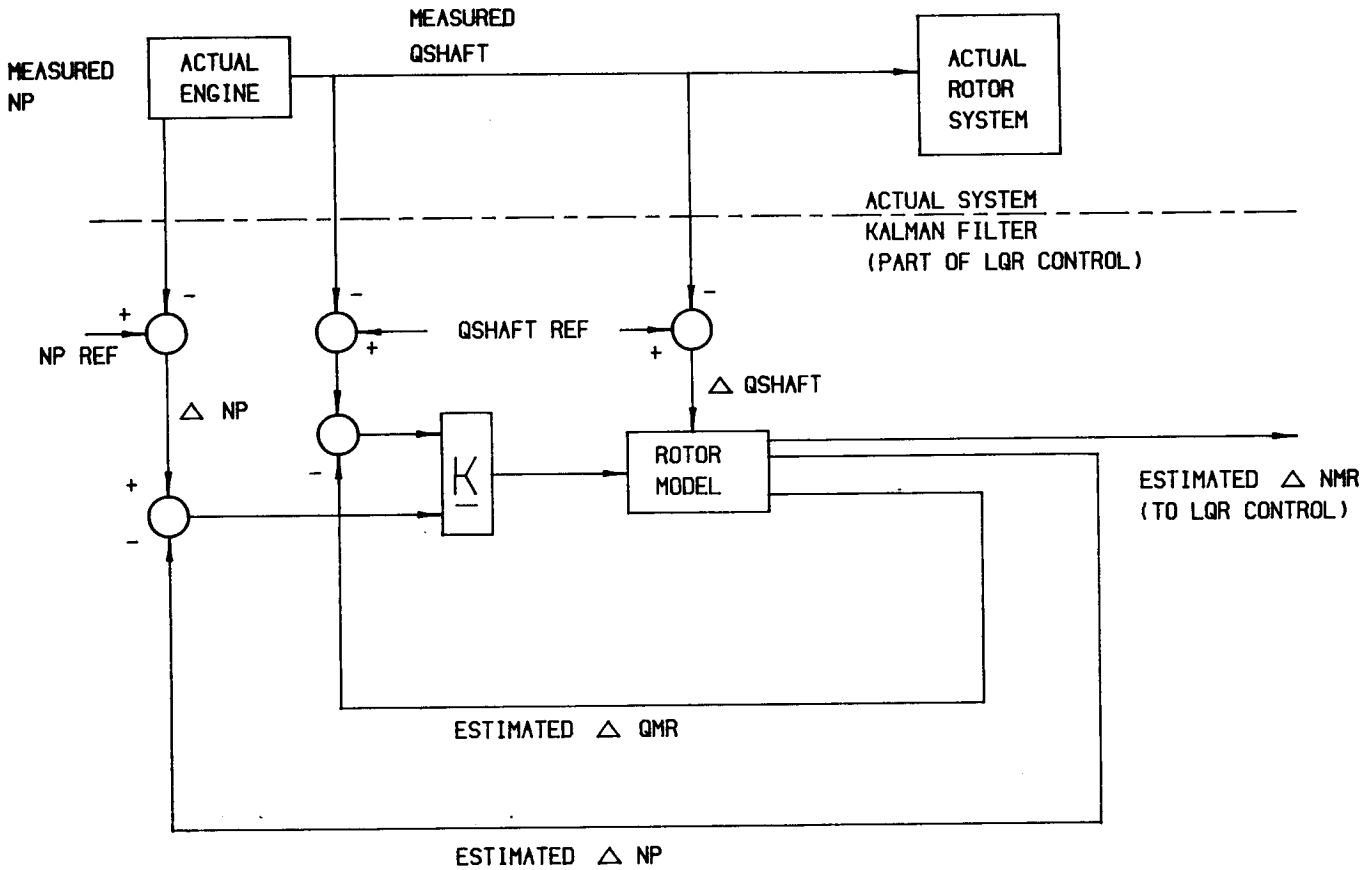


Figure 2.16 Schematic Block Diagram Representation of MIMO Observer with Np and Torque as References.

where $\alpha$ is a scalar and $\underline{I}$ is the identity matrix, then changing $\alpha$ has the effect of moving the magnitude Bode curves up and down like a gain while $\underline{V}_1$ changes the shape of the curve. Increasing the magnitude of $\underline{V}_1$ or decreasing the magnitude of $\underline{V}_2$ causes the Kalman Filter gains to increase in magnitude. This increases the filter bandwidth and indicates that the filter is relying more heavily on actual measurements to estimate the states and doing less filtering of the data. More discussion on this can be found in Ref. 10.

The $\underline{V}_1$ and $\underline{V}_2$ matrices were chosen without regard to actual noise representations, but rather to achieve good time and frequency domain results. Generally, choosing $\underline{V}_1$ and $\underline{V}_2$ is an iterative procedure. The matrix, $\underline{V}_1$, was chosen as:

$$\underline{V}_1 = \underline{B}_d \underline{B}_d^T \tag{2.24}$$

where $\underline{B}_d$ is the plant matrix from Equation 2.17b and $\underline{B}_d^T$ is the transpose of $\underline{B}_d$. The final value of $\alpha$ was chosen as:

$$\alpha = 5.6 \tag{2.25}$$

The gain matrix, $\underline{K}$, was calculated as:

$$\underline{K} = \begin{bmatrix} 0.31 & 0.022 \\ 0.013 & 0.0034 \\ 0.072 & 0.018 \end{bmatrix} \tag{2.26}$$

2.2.6 Analysis of Kalman Filter - Time Domain

The time response of the Kalman Filter alone was used initially as a qualitative measure of a set of Kalman Filter gains, $\underline{K}$. The continuous rotor model of Figure 2.5, including the tail rotor dynamics was used to represent the "real" plant. The estimated states of the Kalman Filter were compared to the states of this real plant. Time simulations were done to check the convergence of the estimated states to the actual, or real states. The simulations included starting the estimated states at some nonzero initial conditions with the actual states at zero initial conditions, starting the actual states at nonzero initial conditions with the estimated states at zero, and starting both the actual and estimated states at zero initial conditions and stepping the shaft torque input from zero to a positive value.

Figure 2.17 shows the responses of the actual states, $\underline{X}$, and the reconstructed states, $\hat{\underline{X}}$, when each estimated state is given an initial condition of 50 RPM for NP and NMR, and 50 ft-lbs torque for QMR. Figure 2.18 shows the responses of the actual states, $\underline{X}$, and the estimated states, $\hat{\underline{X}}$, when each actual state is given an initial condition of 50 (same units as above). The torque state for the real plant is QKMR which is the torque stored in the

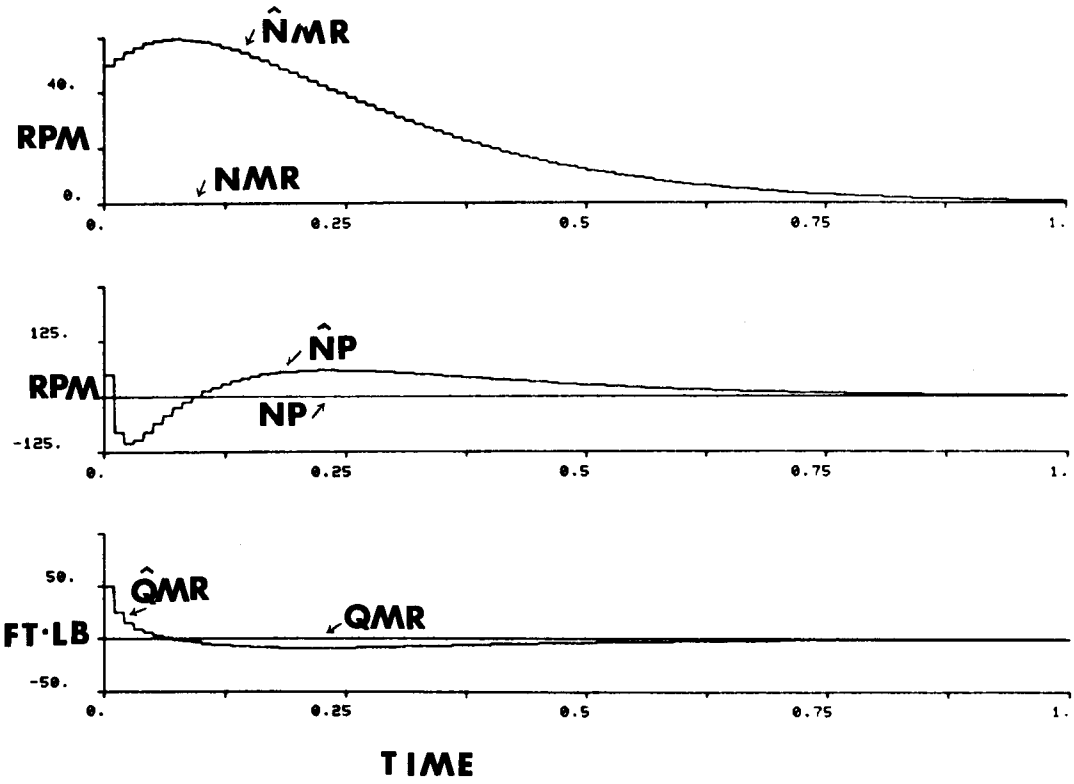


Figure 2.17 Kalman Filter Time Response with Initial Condition of Zero on Actual States and Initial Condition of 50 on Estimated States.

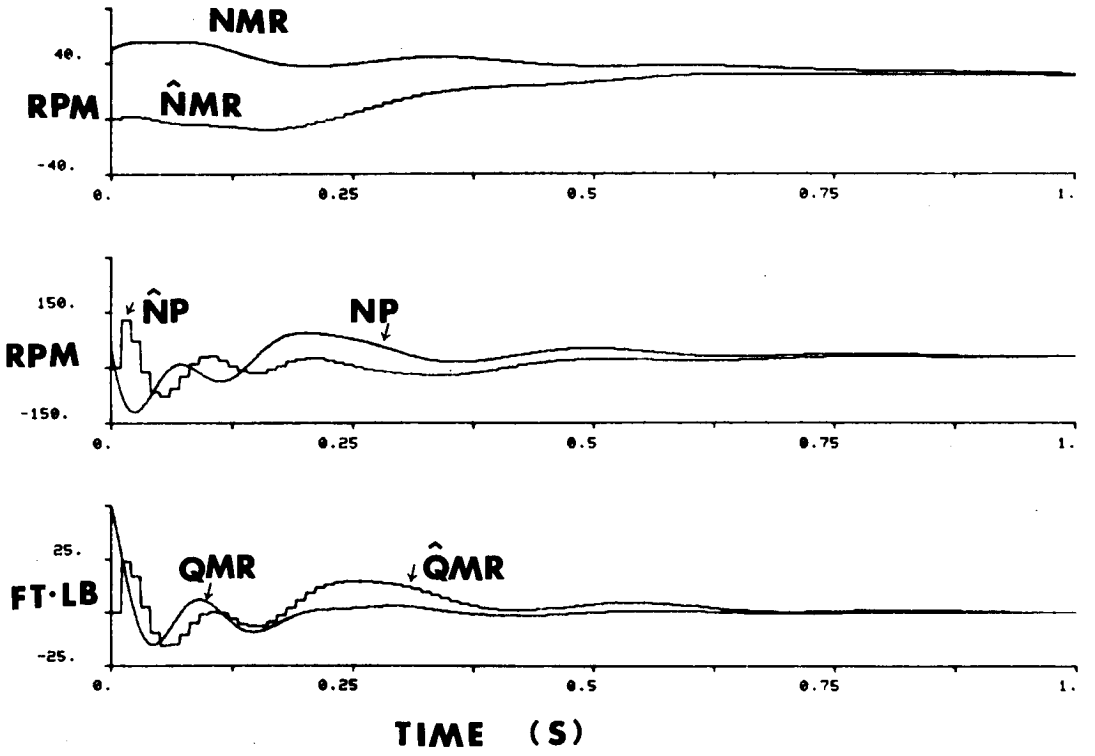


Figure 2.18 Kalman Filter Time Response with Initial Condition of 50 on Actual States and Initial Condition of Zero on Estimated States.

centrifugal spring only. Figure 2.19 shows the responses of the actual and estimated states, all with zero initial conditions, to a step in engine shaft torque, Q shaft. The zero-order-hold output of the Kalman Filter is evident in these figures. Figures 2.17 and 2.18 show that the estimated states converge to the actual states in about 1 sec. This agrees very well with the position of the closed-loop Kalman Filter poles. The poles are located in the z-plane on the real axis at:

$$\underline{z} = \begin{bmatrix} 0.333 \\ 0.9137 \\ 0.9453 \end{bmatrix} \tag{2.27}$$

This corresponds to s-plane pole positions

$$\underline{s} = \begin{bmatrix} -108.5 \\ -9.0 \\ -5.6 \end{bmatrix} \tag{2.23}$$

using the transformation of poles from s-plane to z-plane:

$$z = e^{sT} \tag{2.29a}$$

$$s = \frac{1}{T} (\ln z) \tag{2.29b}$$

where T is the sampling period, z is the pole position in the z-plane and s is the pole position in the s-plane. The slowest pole is at -5.6 rad/sec and corresponds to a time constant of

$$\tau = 0.18 \text{ sec} \tag{2.30}$$

Assuming convergence in 5 $\tau$, this corresponds to convergence in 0.9 sec, which is close to the 1 sec seen in the simulations.

Figure 2.17 shows the case where the estimated states were started with nonzero initial conditions and shows that there is no oscillation during the convergence as is expected from all real poles. The response of states to nonzero initial conditions on actual states, Figure 2.18, is oscillatory, but that is because the Kalman Filter does not converge to the actual states until 1 sec, and in the meantime, the actual states are oscillating. This same effect is seen in Figure 2.19.

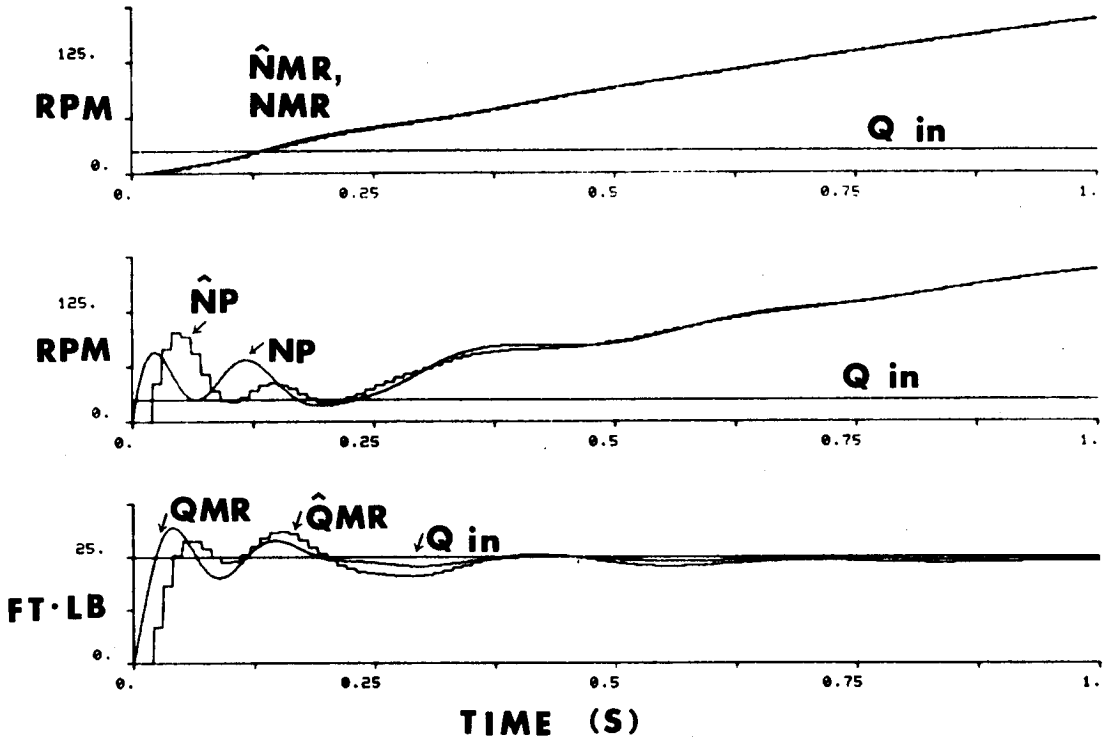


Figure 2.19 Kalman Filter Time Response to a 25 ft-lb Step in Engine Torque with Initial Conditions of Zero on Actual and Estimated States.

The criteria for acceptance of the Kalman Filter (KF) design based on these time simulations were qualitative. Excessive oscillations of the NMR estimated state for nonzero initial conditions of the actual states was undesirable. This condition was imposed because NMR directly affects fuel flow in the LQR power turbine governor, and oscillations would feed directly to the engine. [This situation would only occur during initialization of the control when the initial conditions of the Kalman Filter are different than the actual engine and helicopter parameter initial conditions. Therefore, this restriction placed on the Kalman Filter may not be necessary.]

### 2.2.7 Analysis of Kalman Filter - Frequency Domain

The Kalman Filter (KF) as a separate system was also analyzed in the frequency domain. Under the restriction of a continuous system, the KF has the same stability margin properties as the LQR as mentioned in Section 2.1.8. However, for a sampled system, as the rotor was modeled, these stability margins do not hold. Standard Bode analysis cannot be used with the usual confidence because this KF is not a single-input-single-output (SISO) system. Singular value techniques that have been developed for analyzing the absolute stability of multi-input-multi-output (MIMO) systems (Ref. 15) have not been developed for discrete systems. A standard method of analyzing a multiloop system in the frequency domain is to open one loop at a time while maintaining the other loops closed. This may give misleading results as is illustrated by an example in Ref. 15.

Despite these problems, frequency domain analysis can be useful if the results are used correctly. The KF was initially designed as a SISO loop with NP as the only measured state. This system was then used as a basis for comparison for the MIMO KF having NP and torque as measure states. The torque measurement was added to take advantage of available measurements of the engine parameters. The KF algorithm for calculating gains yields a system with good stability margins. As long as the gains and, therefore, the bandwidth are not driven too high, the phase lag introduced by sampling does not have a significant effect on stability. The gains on the NP error for the Kalman Filter with two measured states were the dominant gains, so the gains of the KF using only the NP error were used as a gauge for choosing the magnitude of the multi-input KF gains. Frequency response analysis was done to determine the stability margins of the system.

The SISO KF is shown schematically in Figure 2.20. This system can be analyzed using Bode techniques as applied to digital systems (Ref. 9). The gains, $\underline{K}$, were calculated for the SISO KF using $\underline{V}_1 = \underline{B}_d\underline{B}_d^T$ and $\underline{V}_2 = \alpha \underline{I}$ with $\alpha = 3.0$. The $\underline{B}_d$ matrix, and the $\underline{A}_d$ matrix are the same for the SISO case and the MIMO case. The frequency response analysis was done for a power turbine speed, NP, input and an estimated speed, NP, output. Figure 2.21 shows a Bode plot and Figure 2.22 shows a Nyquist plot. From these figures it can be seen that the KF is stable with 7.7dB gain margin and 71.6° phase margin. The Bode plot in Figure 2.21 shows amplification at around 40 rad/sec.

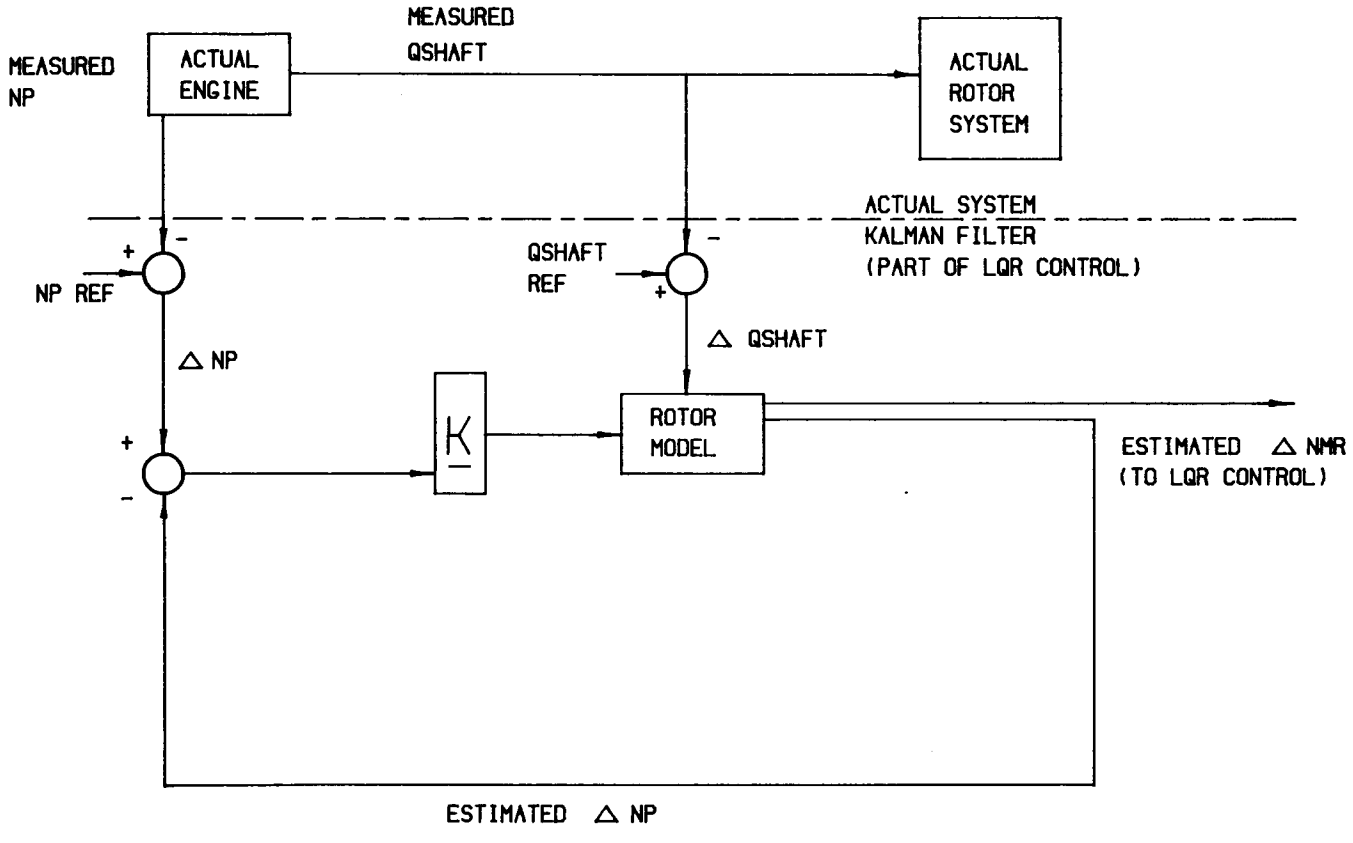


Figure 2.20 Schematic Block Diagram Representation of SISO Observer with Np as a Reference.

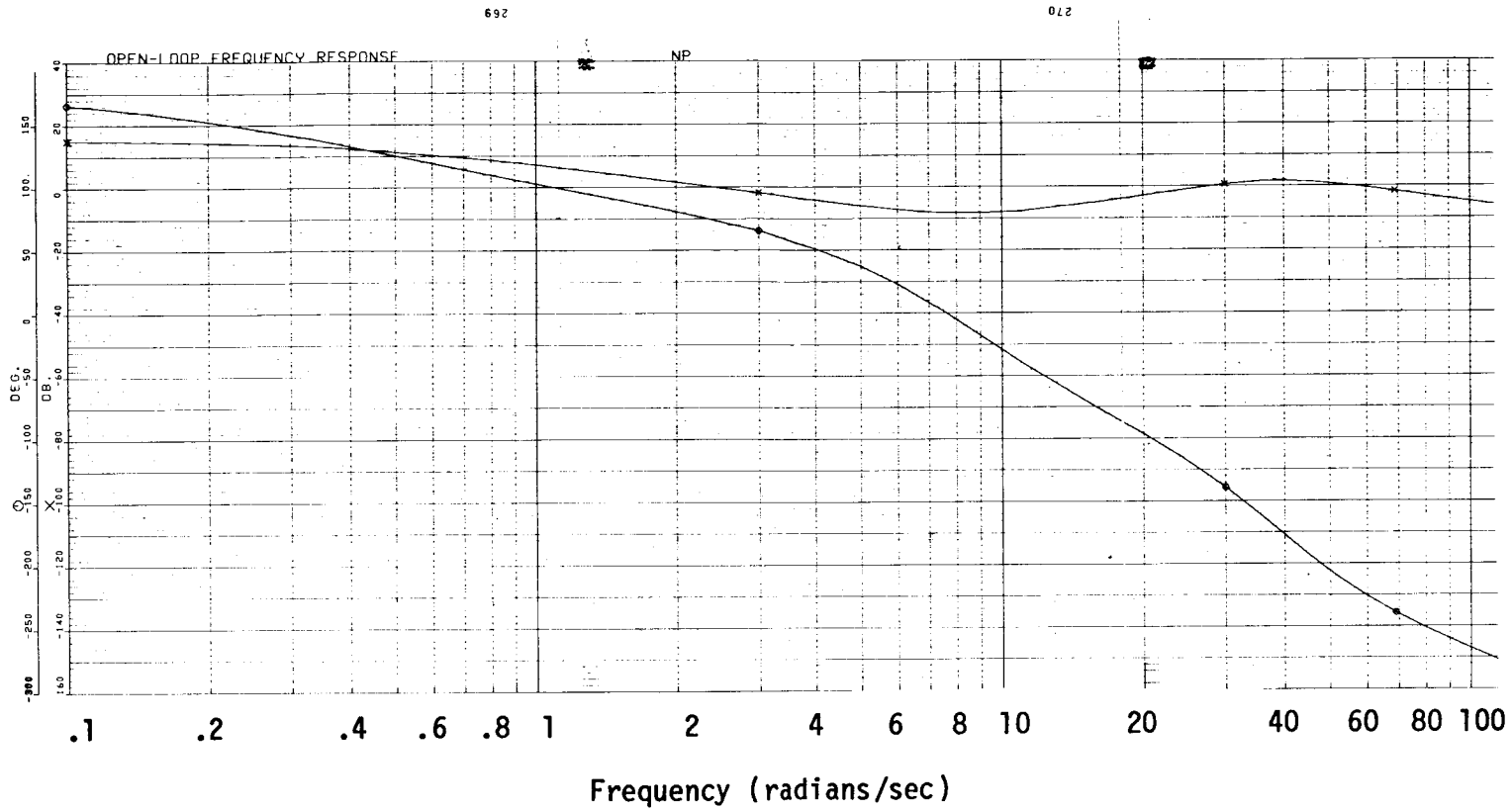


Figure 2.21 Bode Plot Frequency Response of SISO Kalman Filter with Loop Broken at Estimated Np Reference.

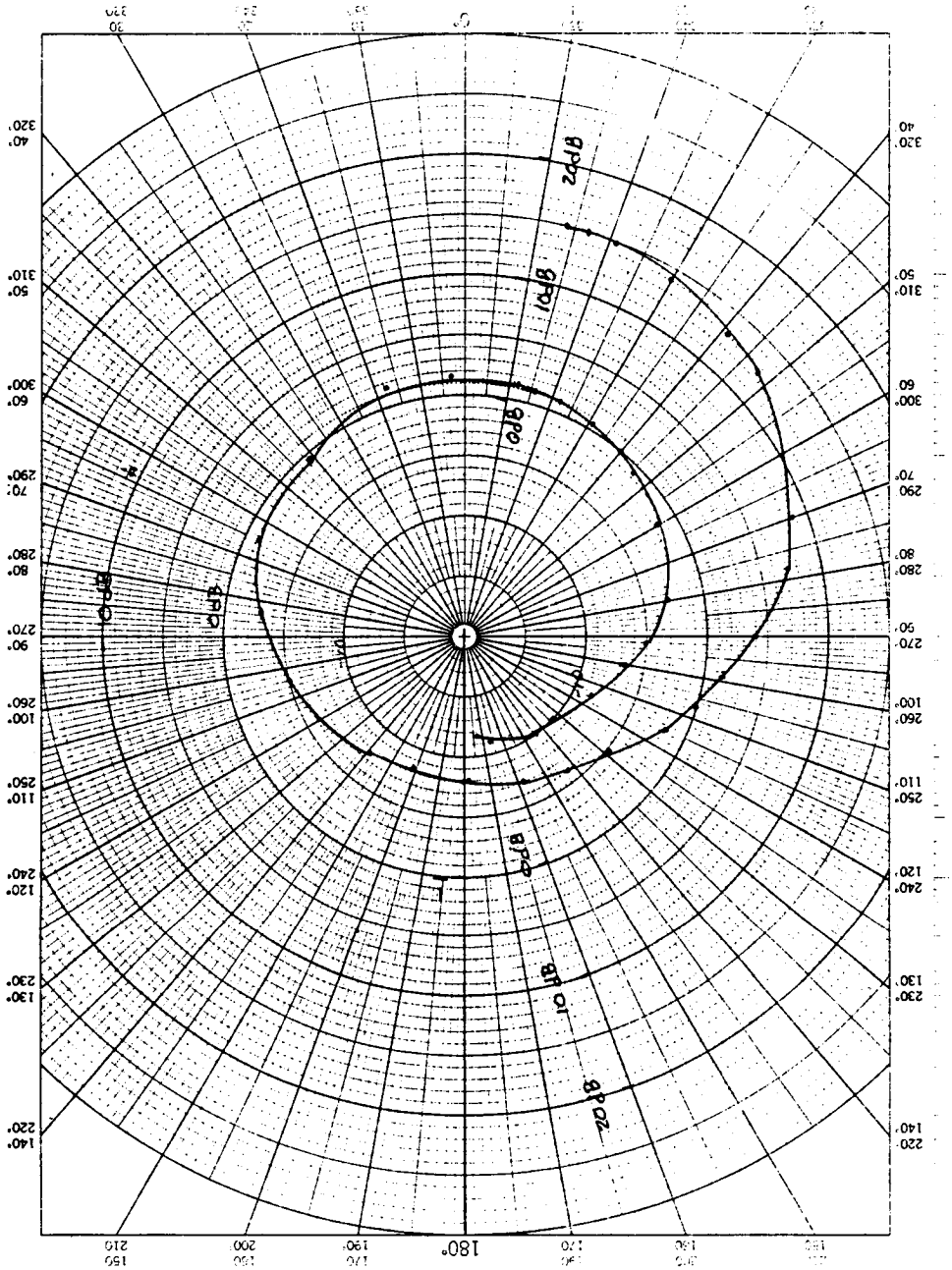


Figure 2.22 Nyquist Diagram of SISO Kalman Filter with Loop Broken at Estimated Np Reference.

This peak does not affect stability as is shown by the Nyquist plot of Figure 2.22 since the amplification occurs 180° away from the -1 point, which is the critical point for stability analysis. There is no danger of losing stability margin in the KF since the values of the KF coefficients will not change. This system allows +180° uncertainty in sampling effects. [There is a different risk of instability, however, if the model used by the KF does not accurately depict the rotor dynamics. In this case, the KF may not accurately calculate the estimated NMR.] There are no significant NP dynamics in the region of this high frequency peak, so a 20 rad/sec prefilter lag was added to the input of the KF where the NP measurement enters to attenuate any high frequency noise. The resulting Bode plot of the system from measured NP to estimated power turbine speed, NP, is shown in Figure 2.23.

## 2.3 Analysis of LQR - Frequency Domain

The LQR NP governor was analyzed in the frequency domain using standard Bode plot techniques to determine the system stability margins, speed of response, and disturbance-rejection characteristics. These techniques are valid since the final LQR design is single input (WF) and single output (NP). The primary stability analysis was done with the loop broken at the WF input to the engine. A sinusoidal WF was input to the engine model and the resulting WF feedback was measured. This is shown schematically in Figure 2.24. This point in the loop is important because WF is the main driver of the engine, and also it is affected by all the engine states by the definition of full-state feedback. WF is also affected by the Kalman Filter. The turbine governor is a regulator that functions to reject disturbances to the power turbine. The controller reacts to these disturbances through WF when the disturbances appear in power turbine speed or shaft torque. The greater the magnitude of WF in the frequency domain, the more disturbances are rejected. The magnitude of the open-loop transfer function at this point should be as large as possible over the frequency range where the disturbances occur. The crossover of the magnitude on a Bode plot should not exceed about 10 rad/sec, however, so that WF does not excite the helicopter main rotor resonance at about 18 rad/sec.

The system frequency response was calculated for sinusoidal inputs at the gas generator speed (NG), shaft torque, and power turbine speed (NP) sensors to determine the noise rejection characteristics of the system. The disturbance rejection characteristics of the system were analyzed by putting a sinusoidal torque disturbance input to the closed-loop system through the helicopter main and tail rotors.

Except where noted otherwise, the frequency response plots are for the engine at a power level of 90% NG and the LQR gains calculated for 95% NG. As described in Section 2.3.3, the LQR gains were maintained constant at the value of the gains calculated at 95% NG. The 90% NG power setting with these LQR gains often gave the lowest stability margin of the system, so this point was used for comparison.

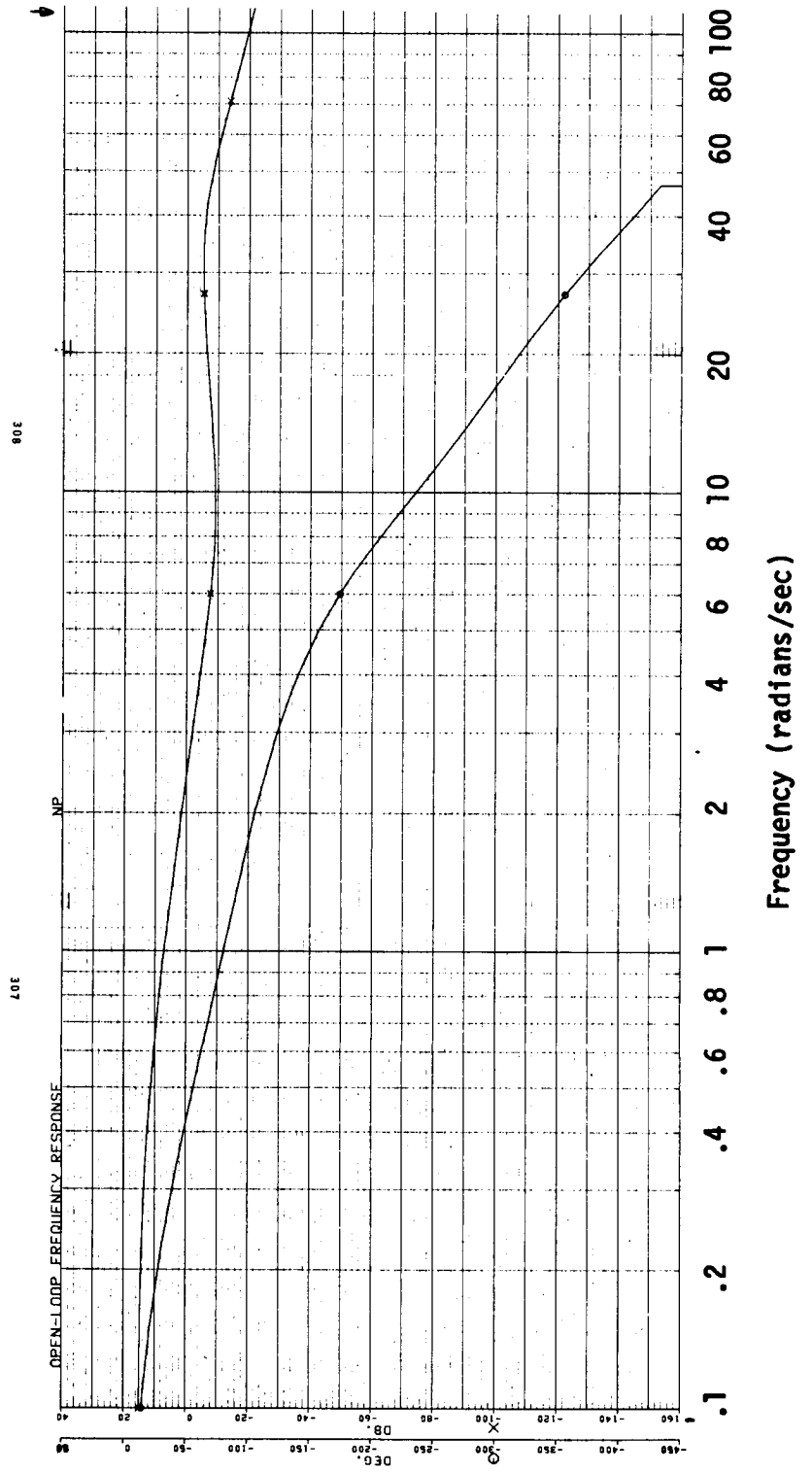


Figure 2.23 Bode Plot of SISO Kalman Filter with Prefilter on Measured Np, Loop Broken at Estimated Np.

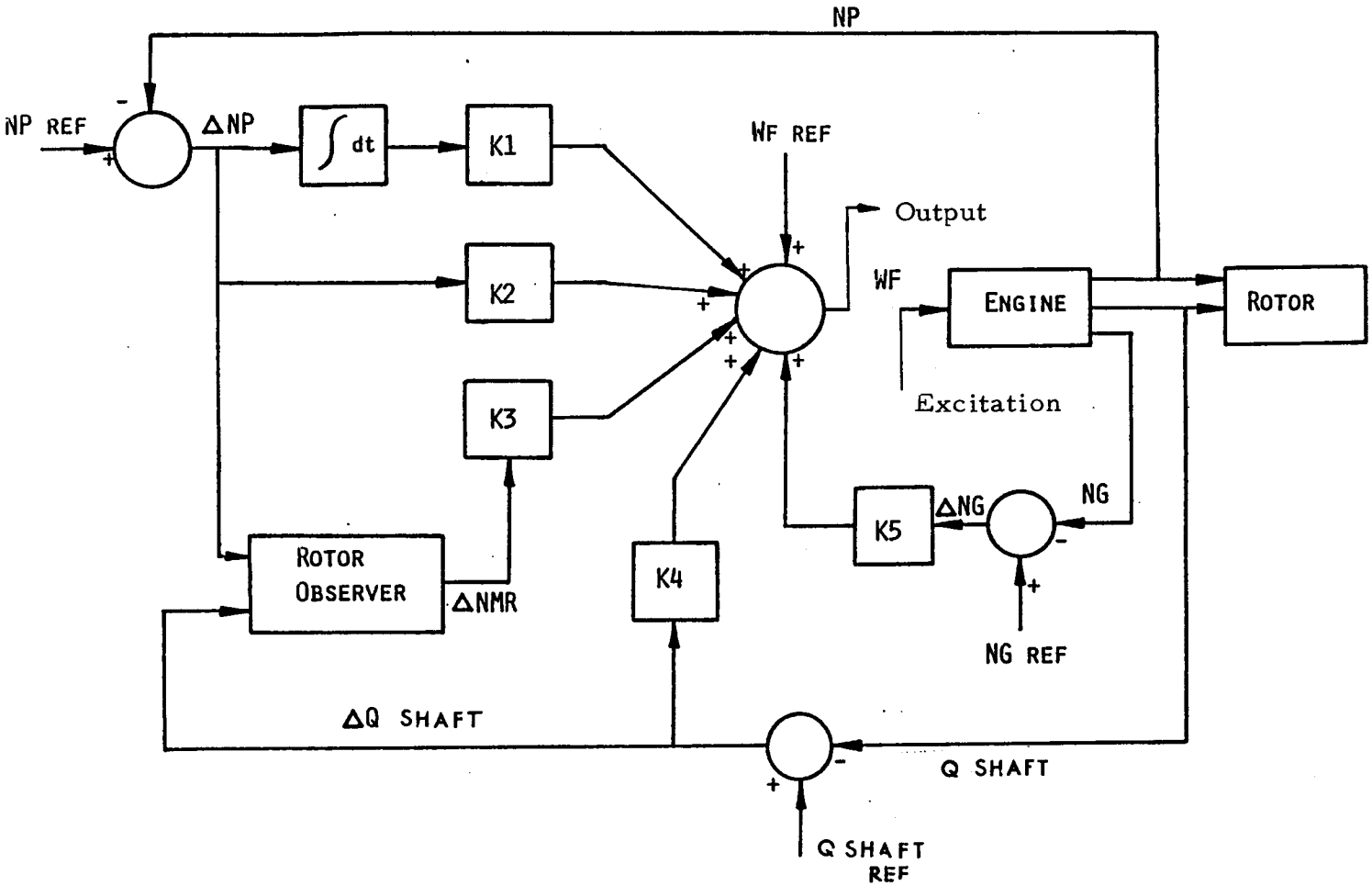


Figure 2.24 Schematic of Engine, Rotor, and Control System Showing Input and Output of WF Frequency Response.

### 2.3.1 Design Model with Controller

Using the simplified model of Figure 2.7, the LQR gains were calculated as described in Section 2.1.12. The frequency response of this system with the LQR gains is shown in Figure 2.25. This frequency response is for the open-loop system with the integrator appended to WF, no tail rotor dynamics, and the LQR gains before they are transformed for the integrator on NP error. The sinusoidal input to this system is at the input to the WF integrator. This point in the loop is where the desirable LQR properties are guaranteed. The engine is at the 95% power level. These same untransformed gains were used with the more accurate helicopter rotor model of Figure 2.3. This system also has the integrator appended to WF, and the sinusoidal input goes into the integrator. The frequency response is shown in Figure 2.26. The responses of the two systems are very similar even though the tail rotor dynamics are included in the more detailed model.

The LQR gains were transformed as described in Section 2.1.10, and the system was changed so that the integrator operated on the NP error, which is the difference between the NP reference and the measured NP. This frequency response is shown in Figure 2.27. This is the open-loop response with the sinusoidal input being WF to the engine. The transformation is such that the guaranteed LQR properties are now at this point in the system loop. This is a physically meaningful point in the system, while the untransformed system guarantees the LQR properties at a point inside the controller.

### 2.3.2 Deviations from the Design Model

The four state design model of Figure 2.2 is the simplest model that was judged acceptable for the LQR design. The model that was used for further analysis of the design in the frequency domain was more complex and included several known deviations from the design model. The changes and additions to the simple model are explained below. Refer to Section 2.7 for their effect on rotor droop.

#### 2.3.2.1 Shaft Torque

The two helicopter rotor states used in the three state model of Figure 2.4 were main rotor blade velocity, NMR, and a torque state, QMR, which is the sum of the torque in the lag-hinge damper and the centrifugal spring. Neither of these states is measured. The main rotor speed, NMR, was estimated using a Kalman Filter observer. This is discussed fully in the section on the observer.

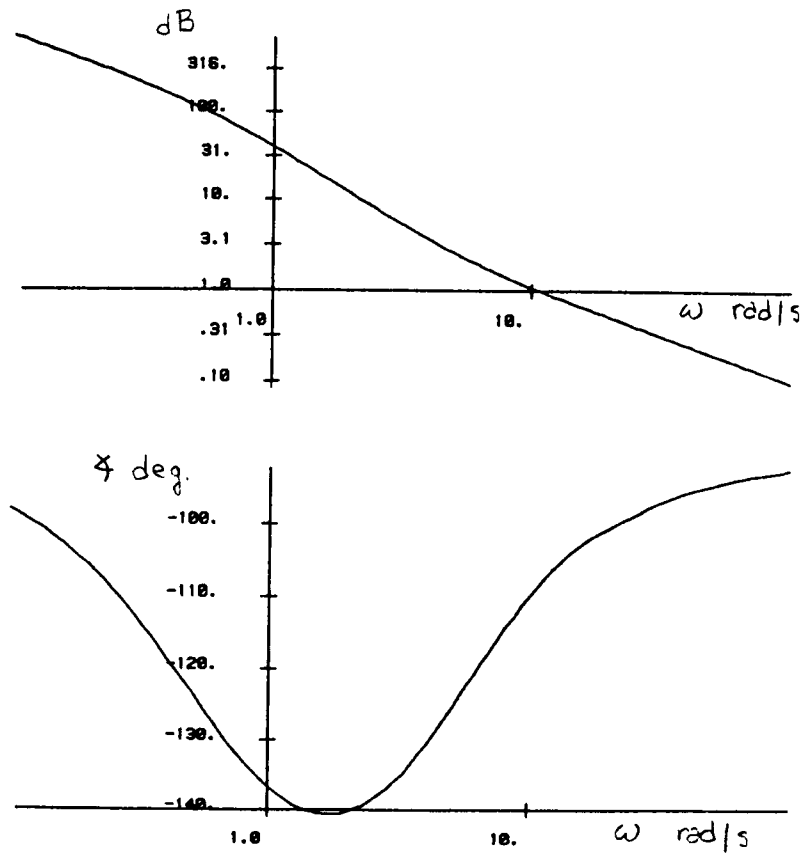


Figure 2.25 Bode Plot of LQR Np Governor with Integrator Appended to WF. No Tail Rotor is Included in Rotor System. 95% NG Power Level.

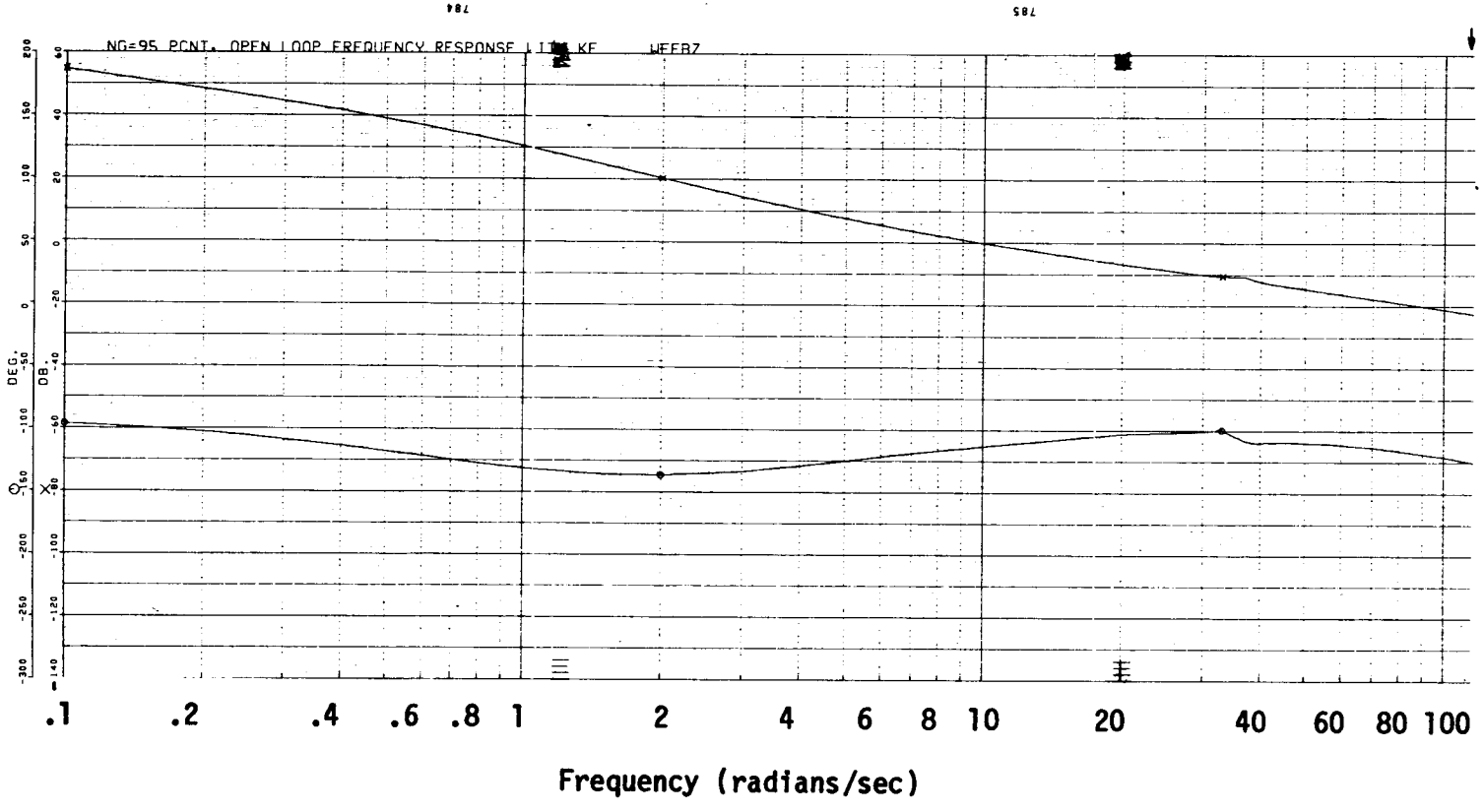


Figure 2.26 Bode Plot of LQR Np Governor Integrator Appended to WF. Tail Rotor Included in Rotor System. 95% NG Power Level.

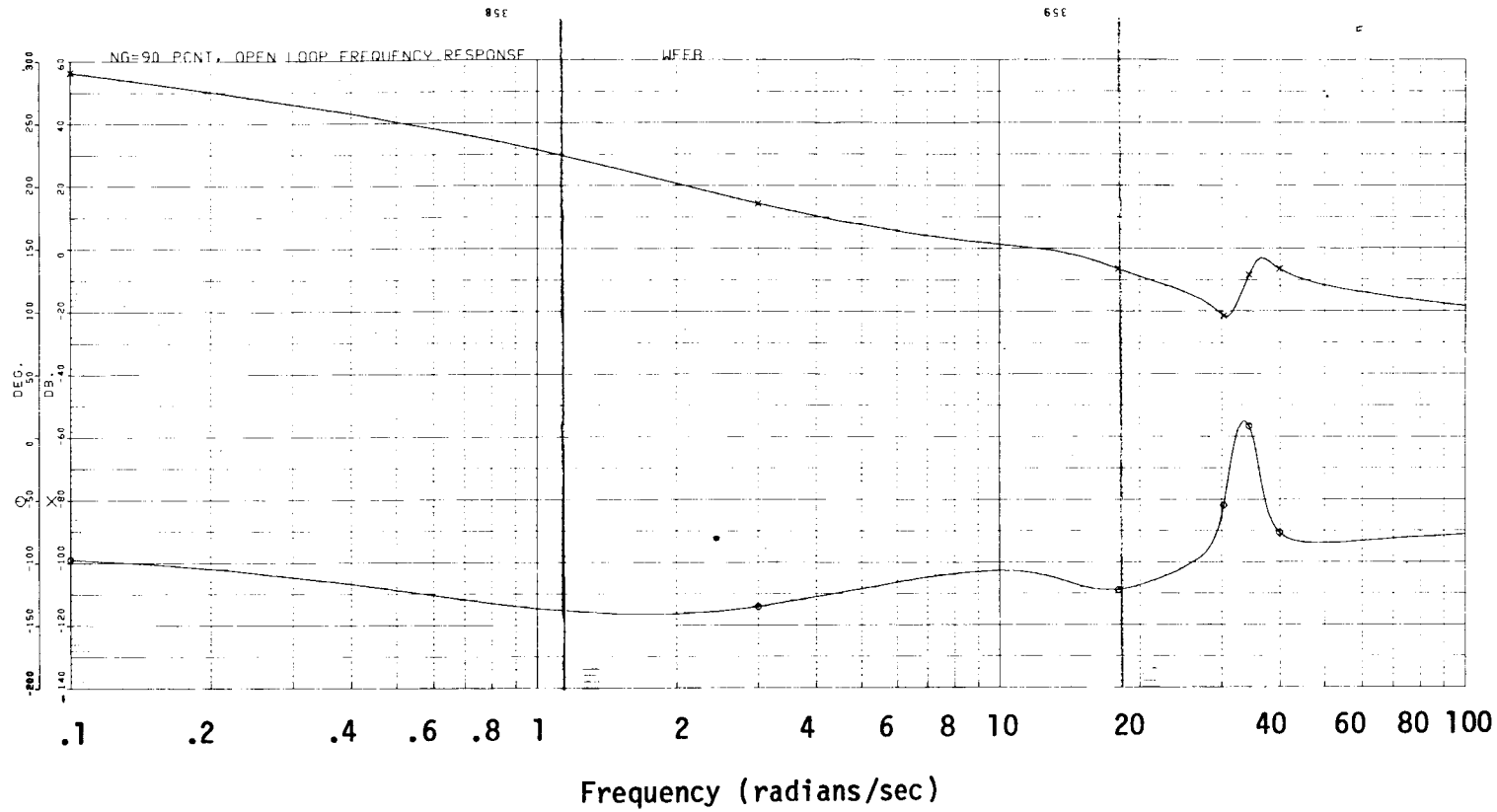


Figure 2.27 Bode Plot of LQR Np Governor with Integrator on Np Error. Tail Rotor Included in Rotor System. 90% NG Power Level. Actual QMR Used in LQR.

The torque state was approximated by engine shaft torque. This had a noticeable effect on the frequency response as can be seen in Figures 2.27 and 2.28. Figure 2.27 is the frequency response of the system having QMR as a state, and Figure 2.28 is the response of the system that has engine shaft torque as an approximation to QMR. The substitution of shaft torque for QMR has a lead effect on the system. This is not a desirable effect in this case because it raises the tail-rotor resonant peak and flattens the response at the crossover. A drop in gain is needed to attenuate the tail-rotor peak to -6dB, and this attenuation lowers the system bandwidth and speed of response. The main rotor torque estimated in the Kalman Filter was tried in place of the actual main rotor torque, QMR. This frequency response is shown in Figure 2.29. This response is worse than the response that uses engine shaft torque. A possible reason for this is that the estimate of QMR is not accurate enough. This can be due to many things including using shaft torque as an approximation to QMR in the observer, estimating QMR too slowly, and not having a sufficiently accurate model of the rotor system. The final system uses engine shaft torque.

#### 2.3.2.2 Anti-Alais Filters

This LQR power turbine governor was designed for implementation in a digital control. Anti-alias (analog) filters are used where gas generator speed, NG, power turbine speed, NP, and shaft torque, Q shaft, are sampled by the control. These filters are two single poles at 100 rad/sec. This provides at least 20dB attenuation at 314 rad/sec, which is half the sampling frequency of 628 rad/sec (0.01 sec sampling period). This amount of attenuation has been used successfully in General Electric digital controls. These filters contribute about 10 degrees phase lag at 10 rad/sec.

#### 2.3.2.3 Zero-Order-Hold Model

The digital WF signal from the control passes through a zero-order hold (ZOH) digital-to-analog (D/A) converter and then to the engine. The frequency response model used for the zero-order-hold is:

$$H_0(s) = \frac{1}{T}\left(\frac{1-\exp(-sT)}{s}\right) \qquad (2.31)$$

where $H_0(s)$ is the transfer function of the ZOH, T is the sampling period in sec, and s is the Laplace operator. The frequency response of this model is shown in Figure 2.30. The model is equivalent to a delay of half the update time. The ZOH model contributes 3 degrees of phase lag at 10 rad/sec with unity gain.

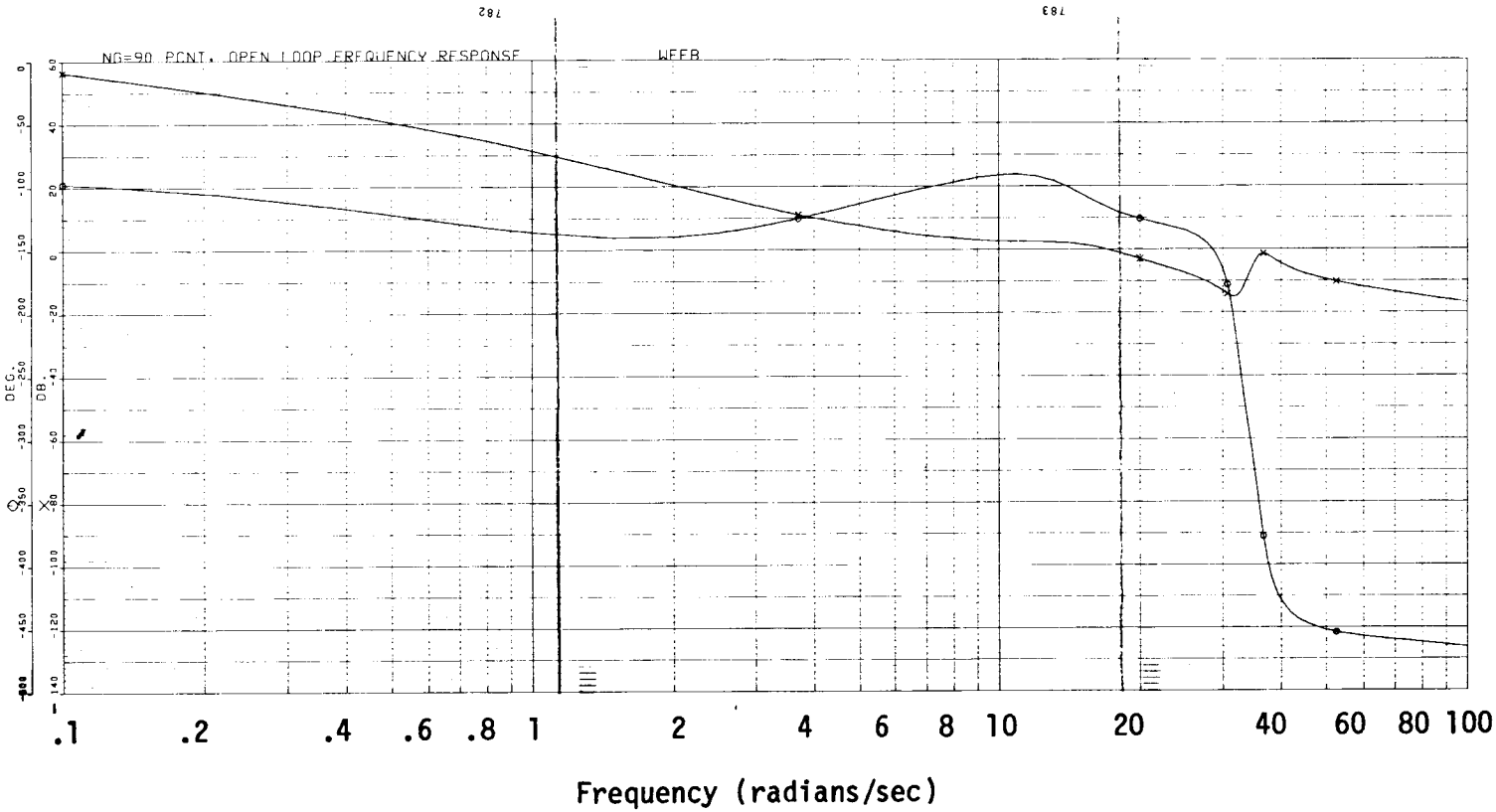


Figure 2.28 Bode Plot of LQR System Using Engine Shaft Torque as an Approximation to Actual QMR.

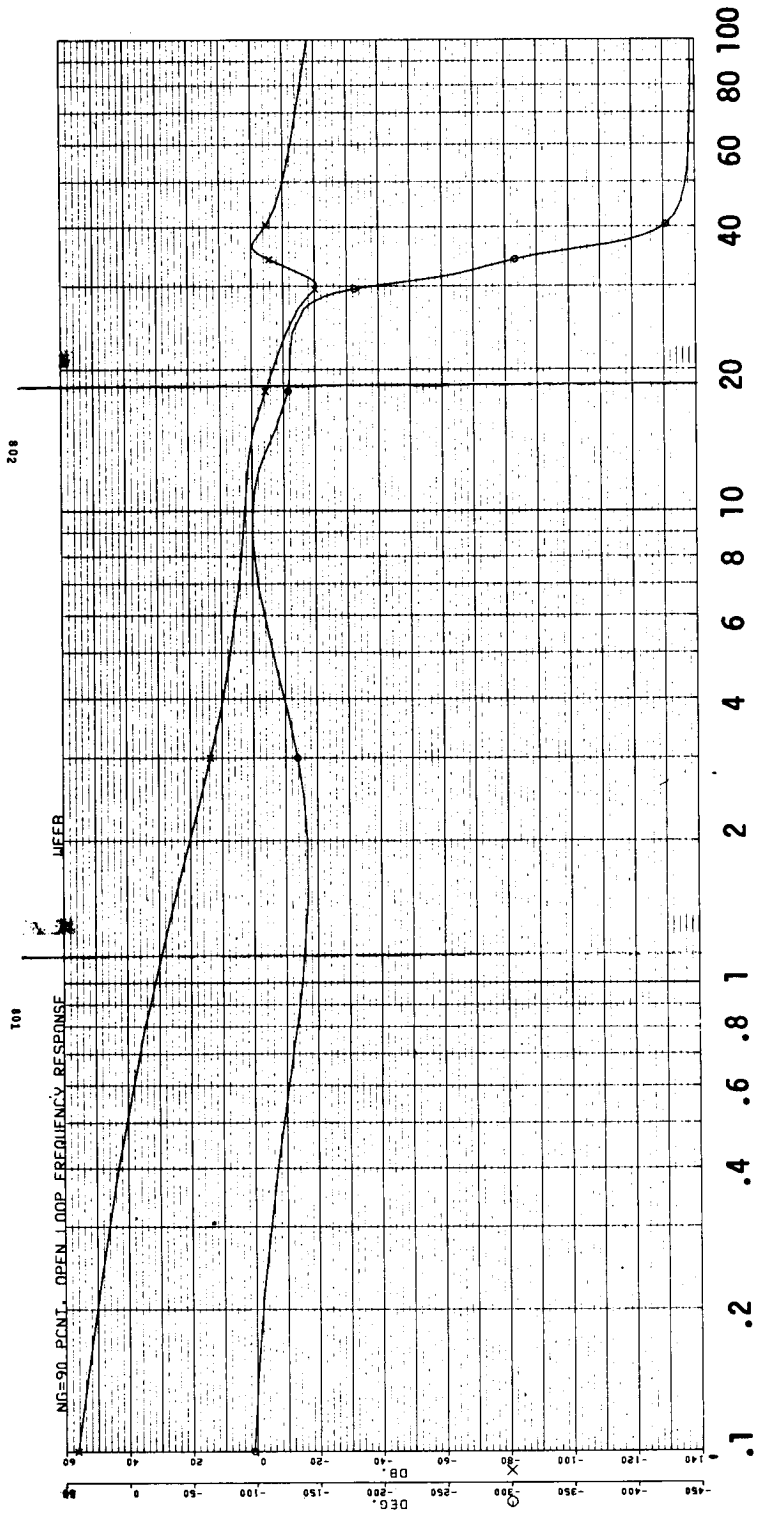


Figure 2.29 Bode Plot of LQR Np Governor Using Estimated QMR as an Approximation to Actual QMR.

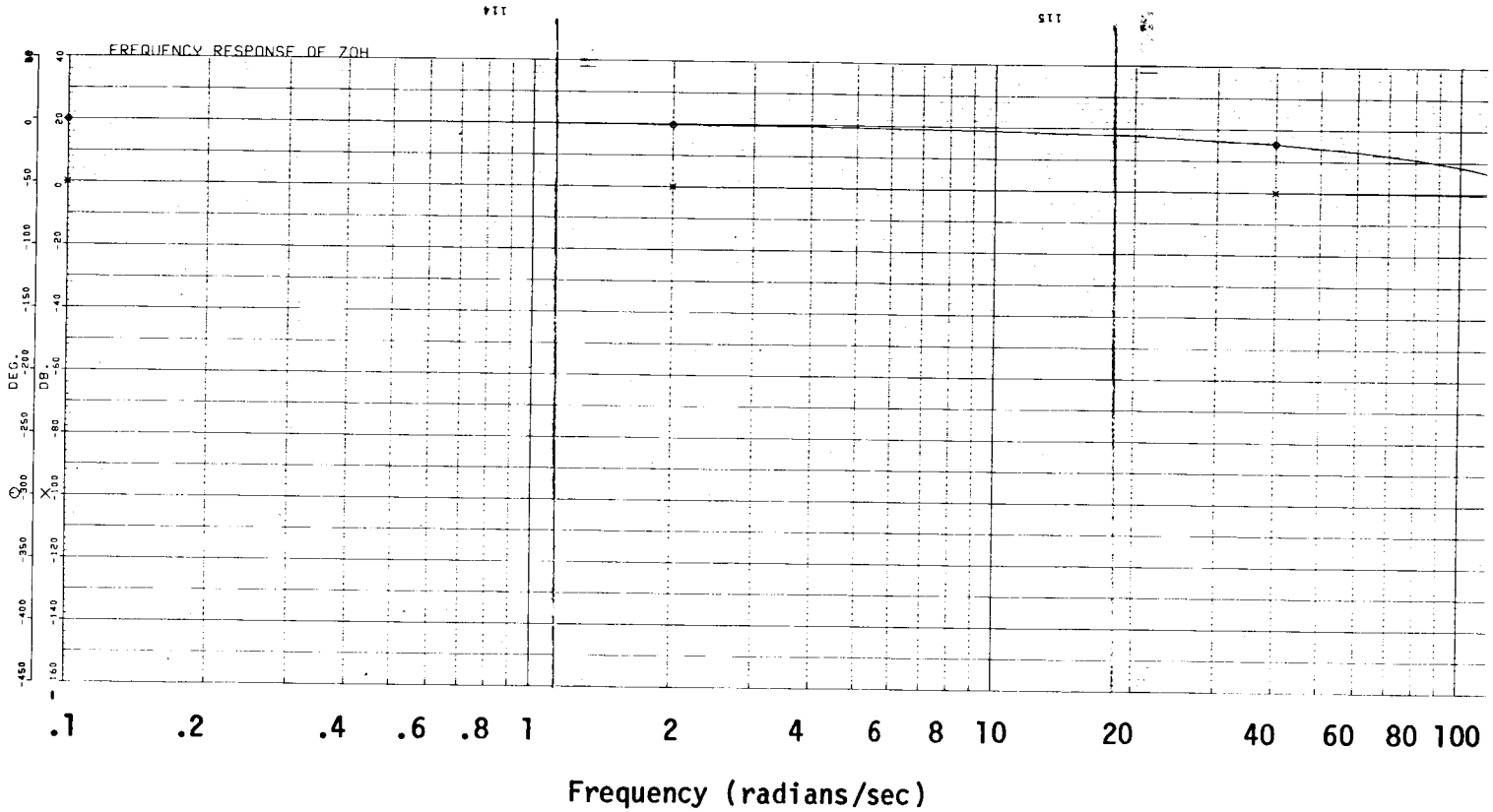


Figure 2.30 Bode Plot of Zero - Order Hold (ZOH) Model.

#### 2.3.2.4 Hydromechanical Fuel Control

The Hydromechanical Fuel Control (HMU) was modeled as a first order lag with a break frequency of 56 rad/sec. This model was based on test data of the HMU done by the manufacturer of the HMU. A sample frequency response of the hardware test is shown in Figure 2.31. This HMU differs from the standard T700 HMU because it is modified to allow WF and the compressor variable geometry (VG) to be manipulated directly by an outside signal. This allows the control laws to be computed in a digital computer and direct the normally hydromechanical WF and VG.

#### 2.3.2.5 Heat Soak Model

Transient simulations of the engine with the LQR controller showed that the system was stable as predicted for simulations without the heat soak model, but unstable when the heat soak model was included. The heat soak model accounts for the effects of heat absorption by the engine metal mass during bursts and chops. Analysis of the heat soak model revealed that it contributed 25 degrees of phase lag and 4.5 dB attenuation at 4 rad/sec. This lag combined with other lags unaccounted for in the design model was sufficient to drive the system unstable. Comparison of the frequency domain effects of this heat soak model with the effects of other similar models indicates that this phase lag is excessive. Until further evidence proves this result, a lead compensator was added to the WF output of the LQR controller to restore sufficient stability margins. This lead had a minimal effect on performance when the heat soak model was not included in the transient simulations. The lead contributed 60° phase angle at 0.5 rad/sec.

#### 2.3.2.6 Helicopter Rotor System

The detailed helicopter rotor system of Figure 2.3 was used for analysis in the frequency domain. For time domain analysis, the simpler model shown in Figure 2.1 was used. This model retains any dynamics that are significant for time simulations. The dynamics that were retained were those that had an effect on the frequency response of the system up to the tail rotor resonant frequency. The different rotor models are described in Section 2.3.9.

### 2.3.3 Effect of Constant LQR Gains

It is desirable to maintain the LQR gains constant with power level to simplify the control logic. The effect of constant gains on stability was analyzed in the frequency domain. The frequency response was calculated at the six power levels using the LQR gains computed for the 95% NG power level. This set of gains had the lowest magnitude of the gains computed at the six power levels. Each set of gains was calculated to give a crossover of about 10 rad/sec at each power level, so the lowest magnitude gains were chosen to not exceed this design criterion at any power level. The frequency response shows that sufficient stability margins were maintained. Time simulations

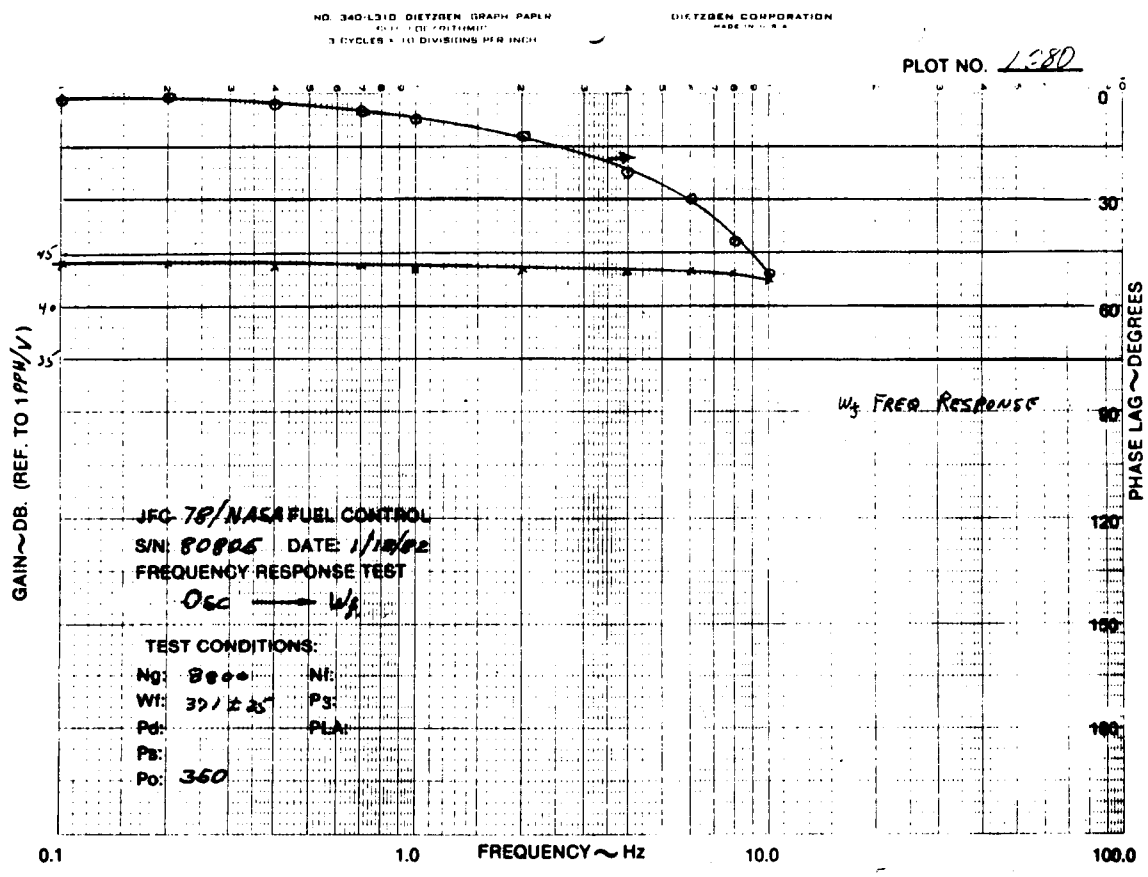


Figure 2.31 Experimental Bode Plot Frequency Response of Modified Hydromechanical Unit (HMU), WF Demand to WF Output.

reported in Section 2.7 show that acceptable time results were achieved. The gain and phase margins are compiled in Table 2.1, and the frequency responses are shown in Figures 2.32a-f. These frequency responses contain the lead compensation described previously. The gain of the final system was decreased 1 db to attenuate the tail rotor resonance a minimum of 6 db.

### 2.3.4 Effect of Variation of Helicopter Rotor Parameters

#### 2.3.4.1 Centrifugal Spring Constant

The helicopter main-rotor centrifugal spring constant can be considered proportional to main rotor speed squared as described in Section 2.1.2. For steady state operation, this variable was considered a constant because rotor speed is governed at 100% speed. During a transient, however, the rotor speed will vary from 100%, and the centrifugal spring constant will also vary. To assure that stability margins are maintained at extreme variations from 100%, the spring constant was varied up and down corresponding to a $\pm$ 10% change in helicopter rotor speed. The spring constant is proportional to speed squared, so the constant was increased 21% and decreased 19%. The frequency response results are shown for increased and decreased spring constant in Figures 2.33 and 2.34, respectively. Figure 2.33 shows that increasing the spring constant raises the tail rotor resonant peak compared to the nominal system. The system remains stable under both conditions. The gain and phase margins are included in Table 2.1.

#### 2.3.4.2 Aerodynamic Damping

Aerodynamic damping of the main and tail rotors was not varied with helicopter rotor speed.

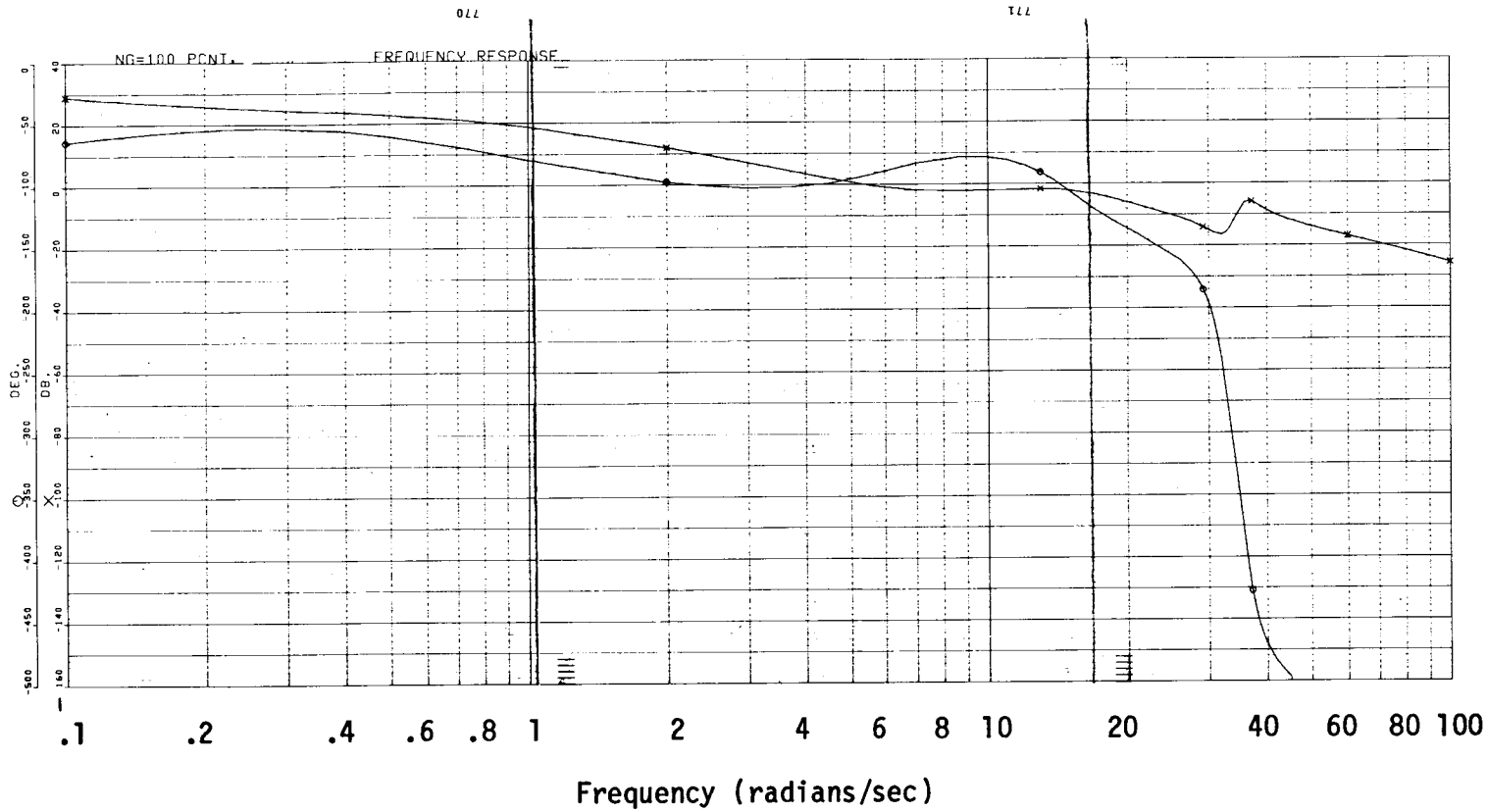


Figure 2.32a Effect of Constant LQR Gains on Frequency Response of LQR Np Governor. 100% NG Power Level.

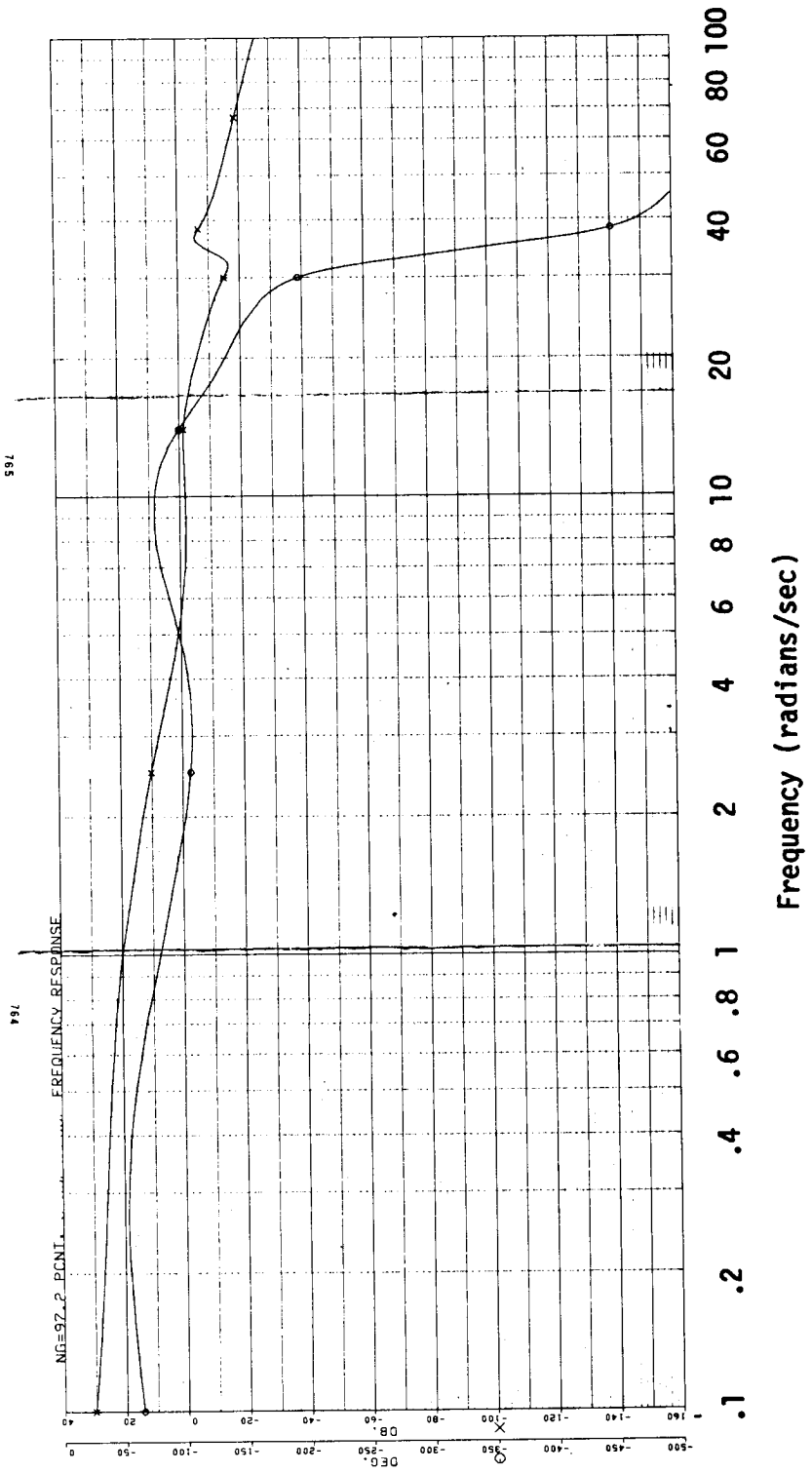


Figure 2.32b Effect of Constant LQR Gains on Frequency Response of LQR Np Governor. 97.2% NG Power Level.

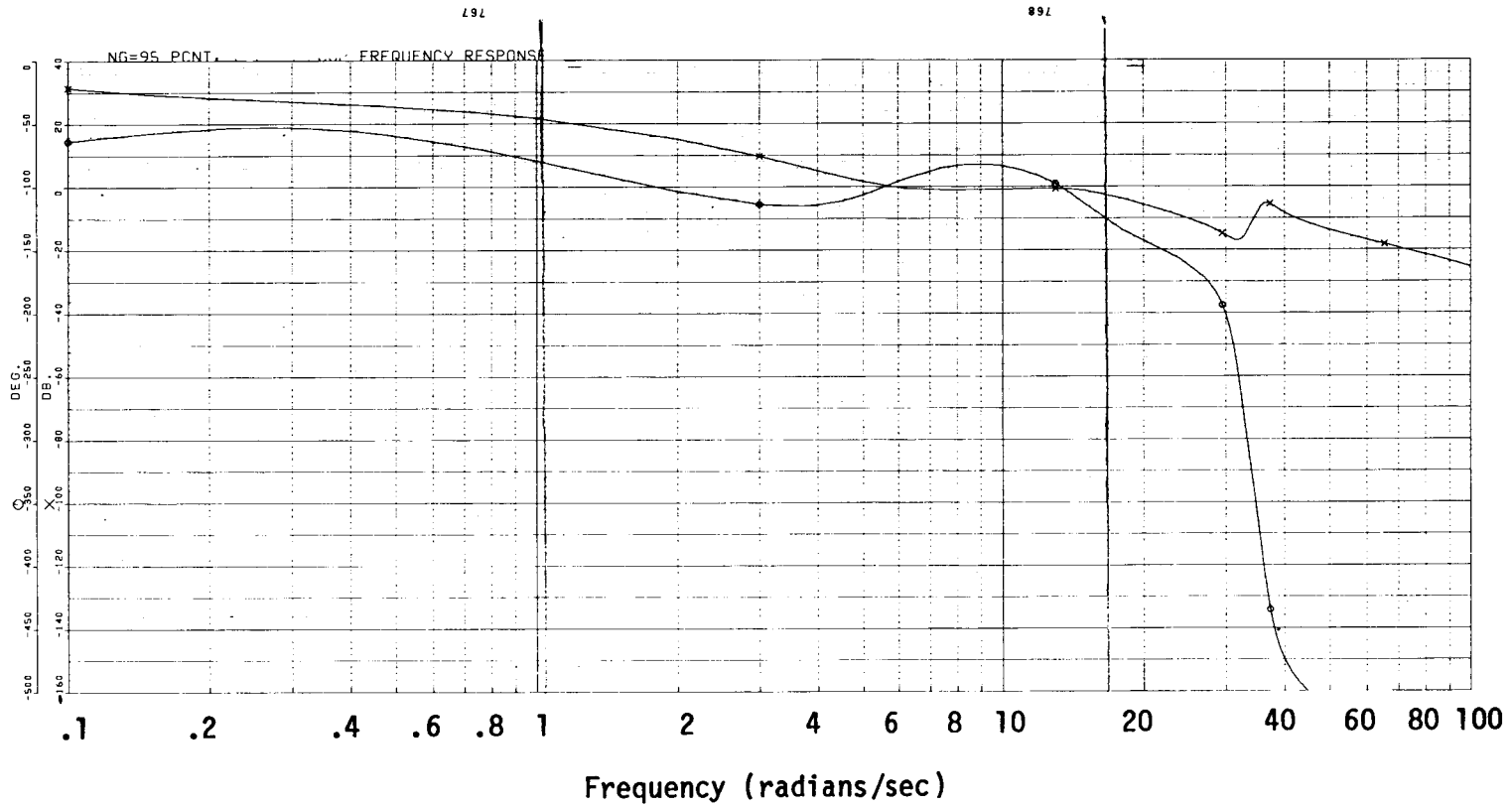


Figure 2.32c Effect of Constant LQR Gains on Frequency Response of LQR Np Governor. 95% NG Power Level.

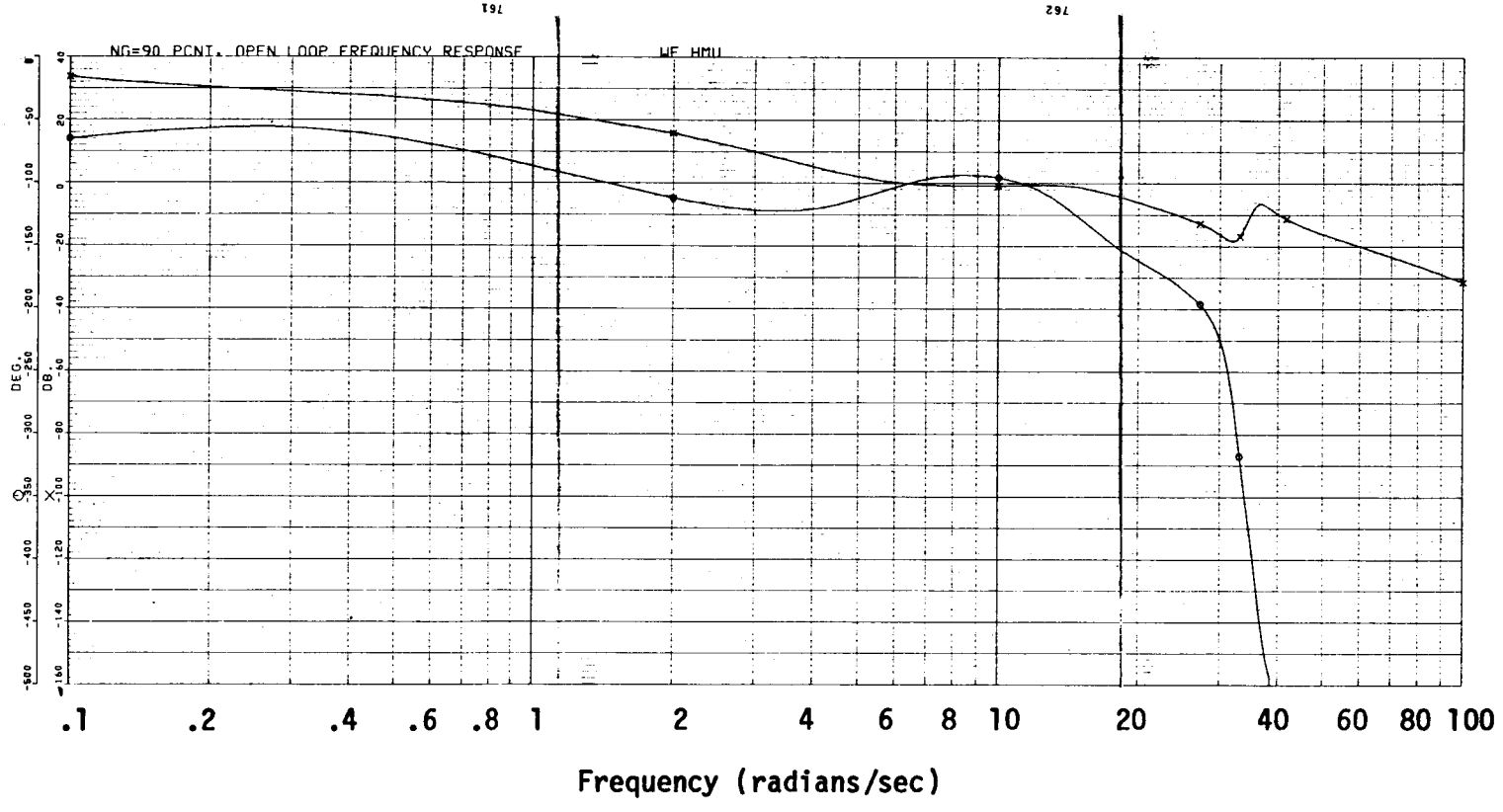


Figure 2.32d Effect of Constant LQR Gains on Frequency Response of LQR Np Governor. 90% NG Power Level.

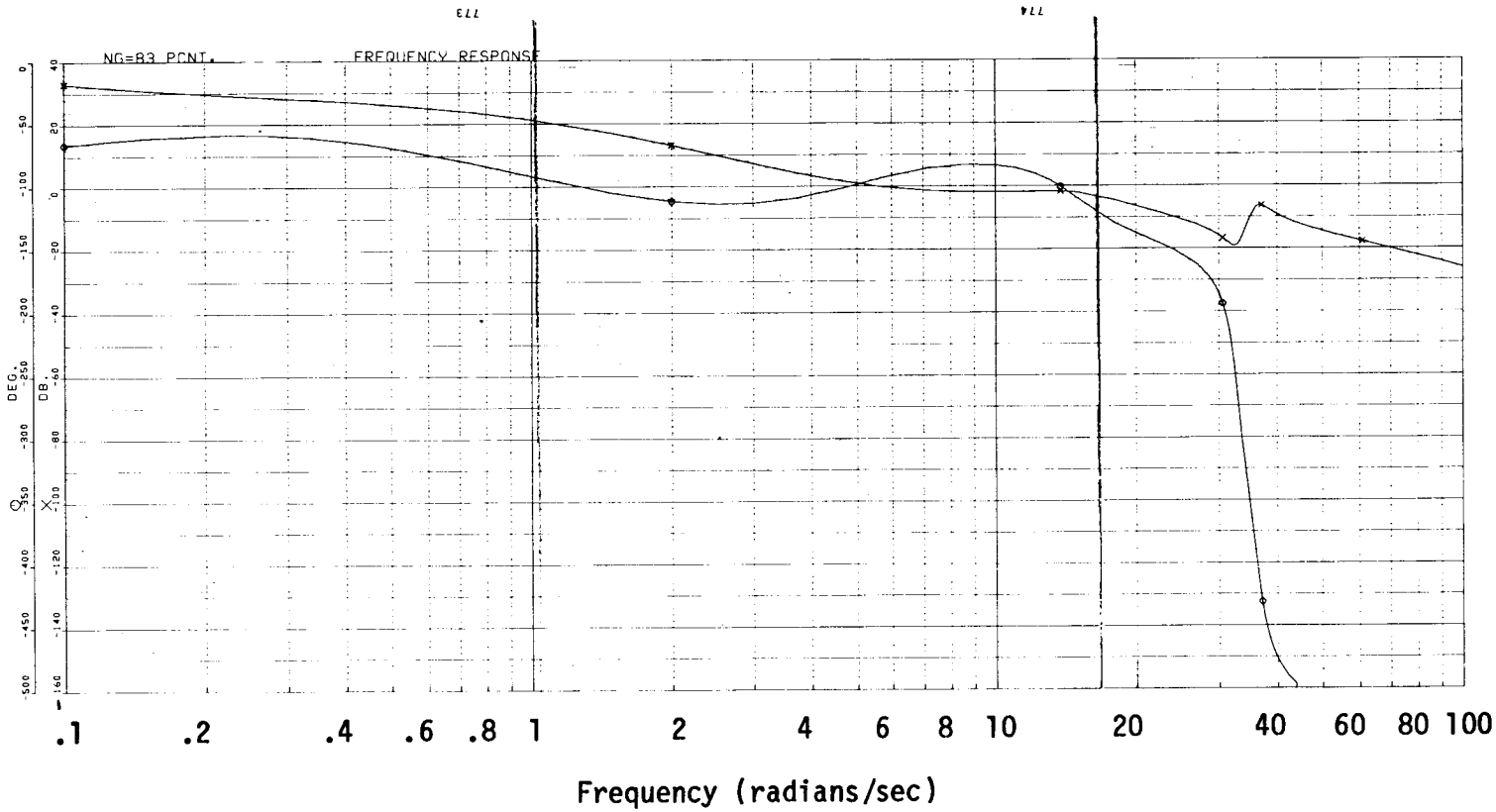


Figure 2.32e Effect of Constant LQR Gains on Frequency Response of LQR Np Governor. 83% NG Power Level.

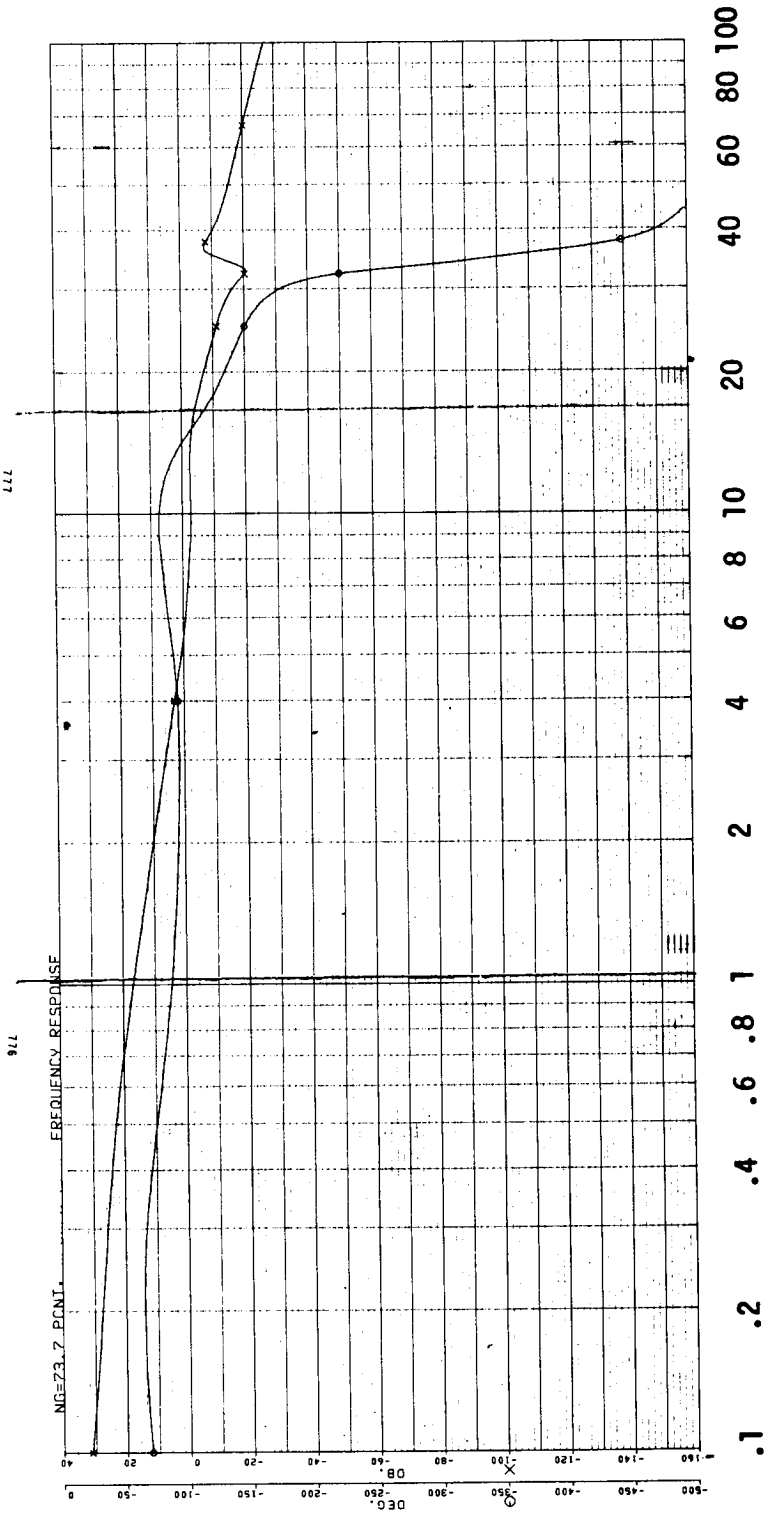


Figure 2.32f Effect of Constant LQR Gains on Frequency Response of LQR Np Governor. 73.7% NG Power Level.

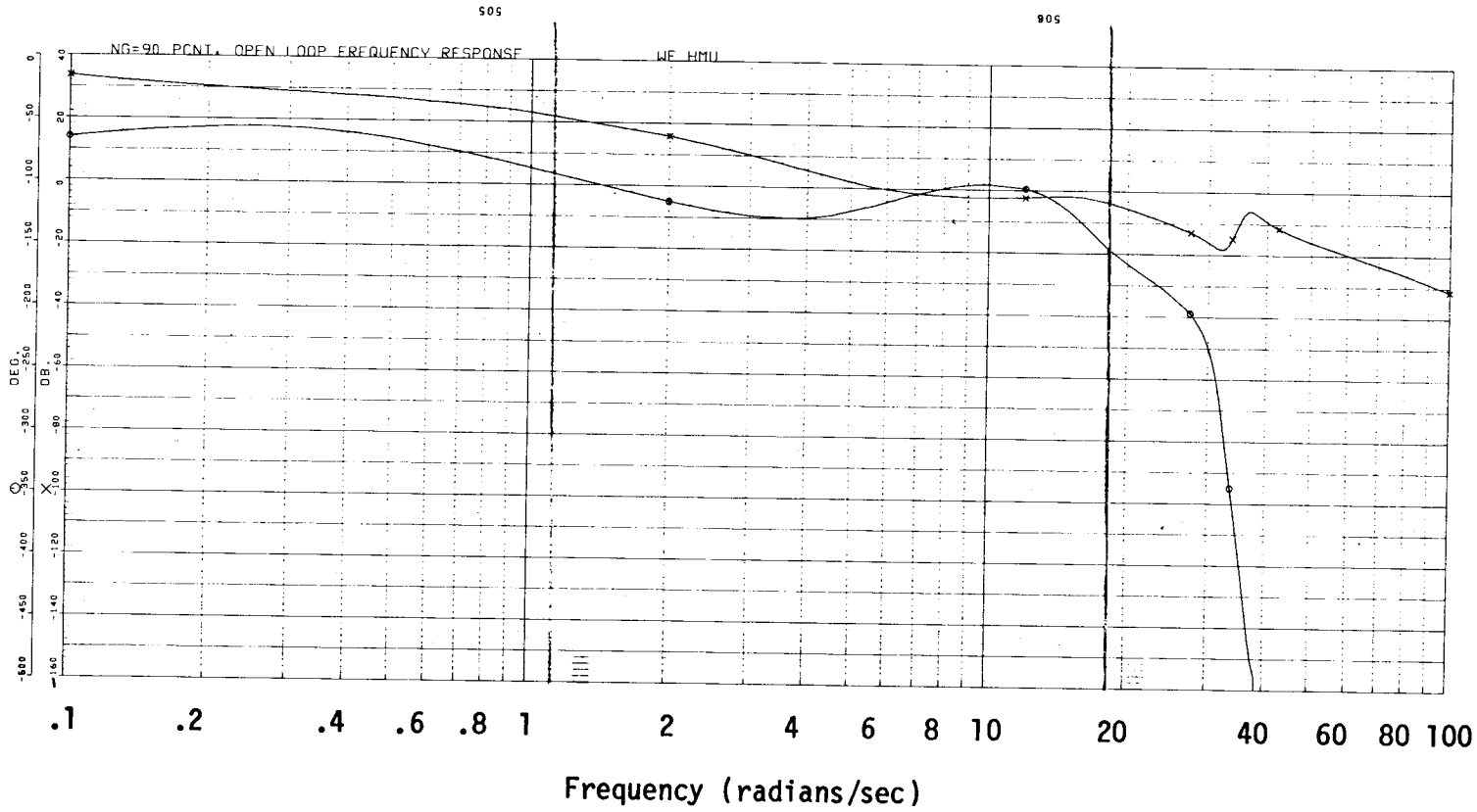


Figure 2.33 Bode Plot of LQR Np Governor with Centrifugal Spring Constant Increase 21% Corresponding to a 10% Increase in Rotor Speed.

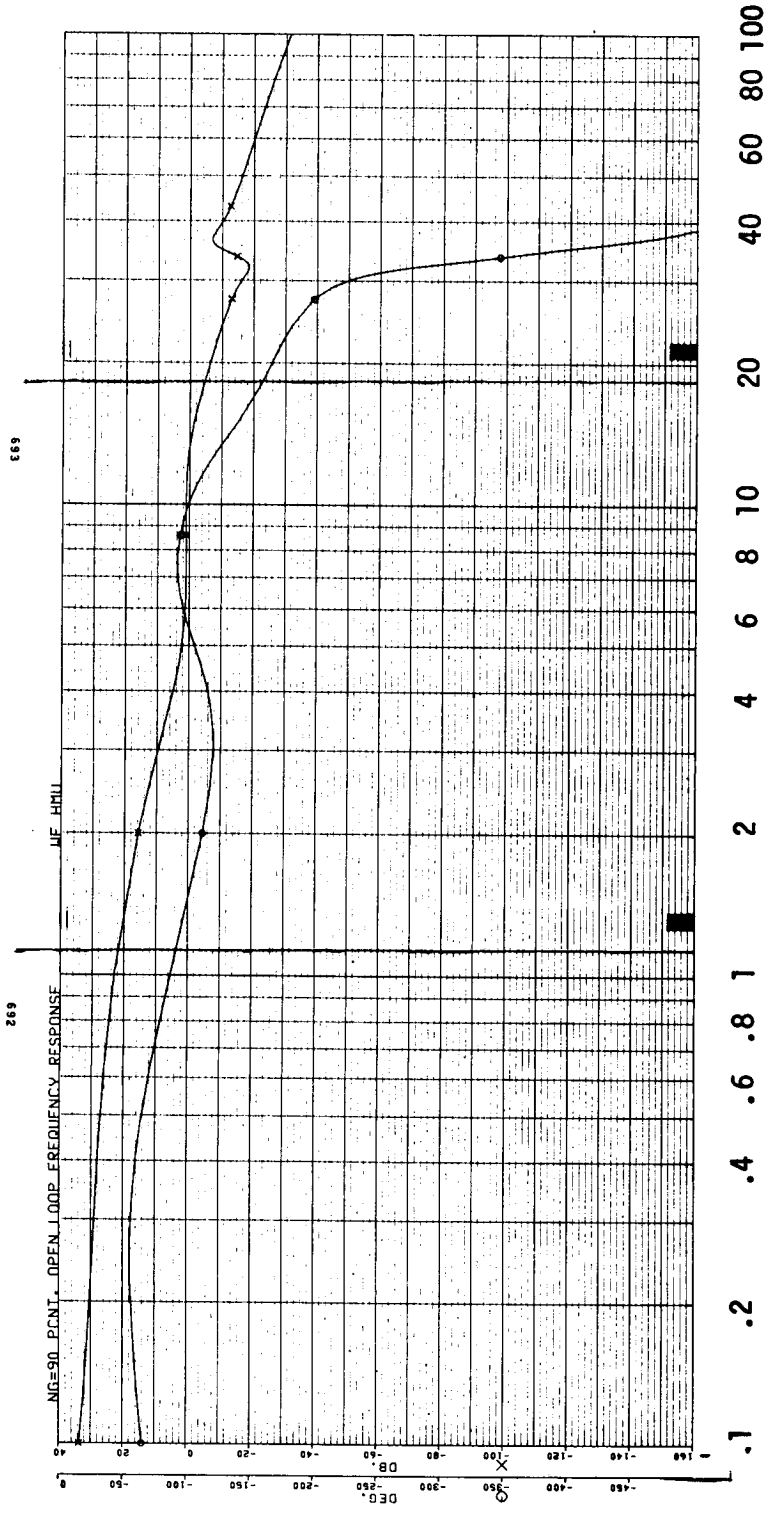


Figure 2.34 Bode Plot of LQR Np Governor with Centrifugal Spring Constant Decreased 19% Corresponding to a 10% Decrease in Rotor Speed.

Table 2.1 Compilation of Frequency Response Results

| | Power Level (% NG) | Phase Margin (degrees) | Gain Margin (dB) | Tail Rotor Attenuation (dB) |
|---|---|---|---|---|
| | | Standard LQR System | | |
| | 100% | 87° | 13.4 dB | 5.8 dB |
| | 97.2% | 85.6° | 13.3 dB | 5.5 dB |
| | 95% | 83° | 13.0 dB | 5.4 dB |
| | 90% | 79° | 10.0 dB | 6.5 dB |
| | 83% | 85.6° | 15.1 dB | 6.3 dB |
| | 73.7% | 90.2° | 16.5 dB | 7.5 dB |
| | | Centrifugal Spring Constant Variation | | |
| +21% KCM: | 90% | 68.2° | 10.0 dB | 6.0 dB |
| -19% KCM: | 90% | 55.4° | 9.9 dB | 6.9 dB |
| | | One Engine Inoperative (OEI) | | |
| | 90% | 79.6° | 11.3 dB | 11.9 dB |

#### 2.3.4.3 Helicopter Main Rotor Lag-Hinge Damping

The frequency response of the system with zero lag-hinge damping was computed. The Bode plot is shown in Figure 2.35 and shows the system will not be stable for zero lag-hinge damping. It is possible that a system can be designed that will be stable with no lag-hinge damping and will operate well with nominal damping.

### 2.3.5 Effect of One-Engine Inoperative (OEI)

The frequency response of the LQR Np governor was calculated with only one engine driving the helicopter rotor system. This simulates the loss of one engine. This response is shown in Figure 2.38. Stability was not adversely affected. These gain and phase margins are included in Table 2.1.

### 2.3.6 Frequency Response Comparison with T700 Baseline

#### 2.3.6.1 Open-Loop System at WF Input

The system loop was broken at the WF input to the engine as shown in Figure 2.24 and described in Section 2.3. The frequency response of the LQR NP governor is shown in Figure 2.32d, and the response of the baseline T700 governor is shown in Figure 2.36. The figures show that the LQR NP governor has 79° phase margin and 10.0 dB gain margin compared to the baseline T700 governor with 51° phase margin and 5.7 dB gain margin. The crossover of the T700 baseline governor is only 2.7 rad/sec compared to about 6 rad/sec for the LQR NP governor.

#### 2.3.6.2 Open-Loop System at Np Feedback

The system loop was broken at the power turbine speed feedback to the error junction as shown in Figure 2.39. The sinusoidal input to this system was the NP reference. Only the NP reference was oscillated. The NP signal from the engine to the LQR control was not oscillated directly. This frequency response was calculated for comparison with the baseline T700 Control System. This frequency response is not as meaningful as the disturbance rejection responses that follow, however, because the power turbine governor is not a reference following system, but a disturbance rejection system. Figure 2.40 shows the LQR governor response to a sinusoidal NP reference, and Figure 2.41 shows the baseline T700 response. Both systems have sufficient stability margins.

#### 2.3.6.3 Disturbance Rejection

The power turbine governor is a regulator that maintains power turbine speed constant in the presence of disturbances. The primary sources of disturbances are the helicopter main and tail rotors. The frequency response of the closed-loop LQR and T700 baseline systems was calculated for a main rotor

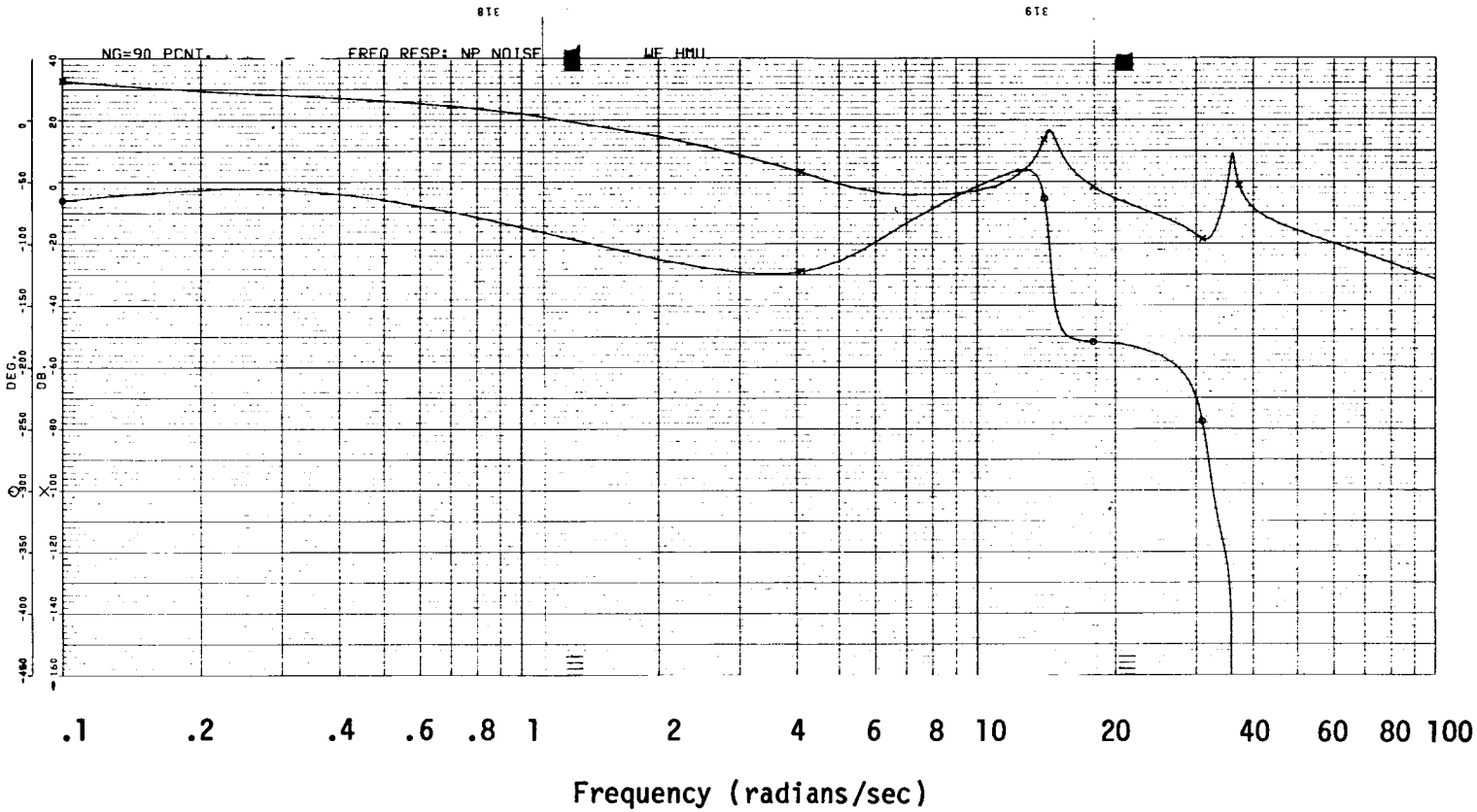


Figure 2.35 Bode Plot of LQR Np Governor with Zero Lag-Hinge Damping. LQR Gains Calculated for Minimum, but Nonzero, Lag-Hinge Damping.

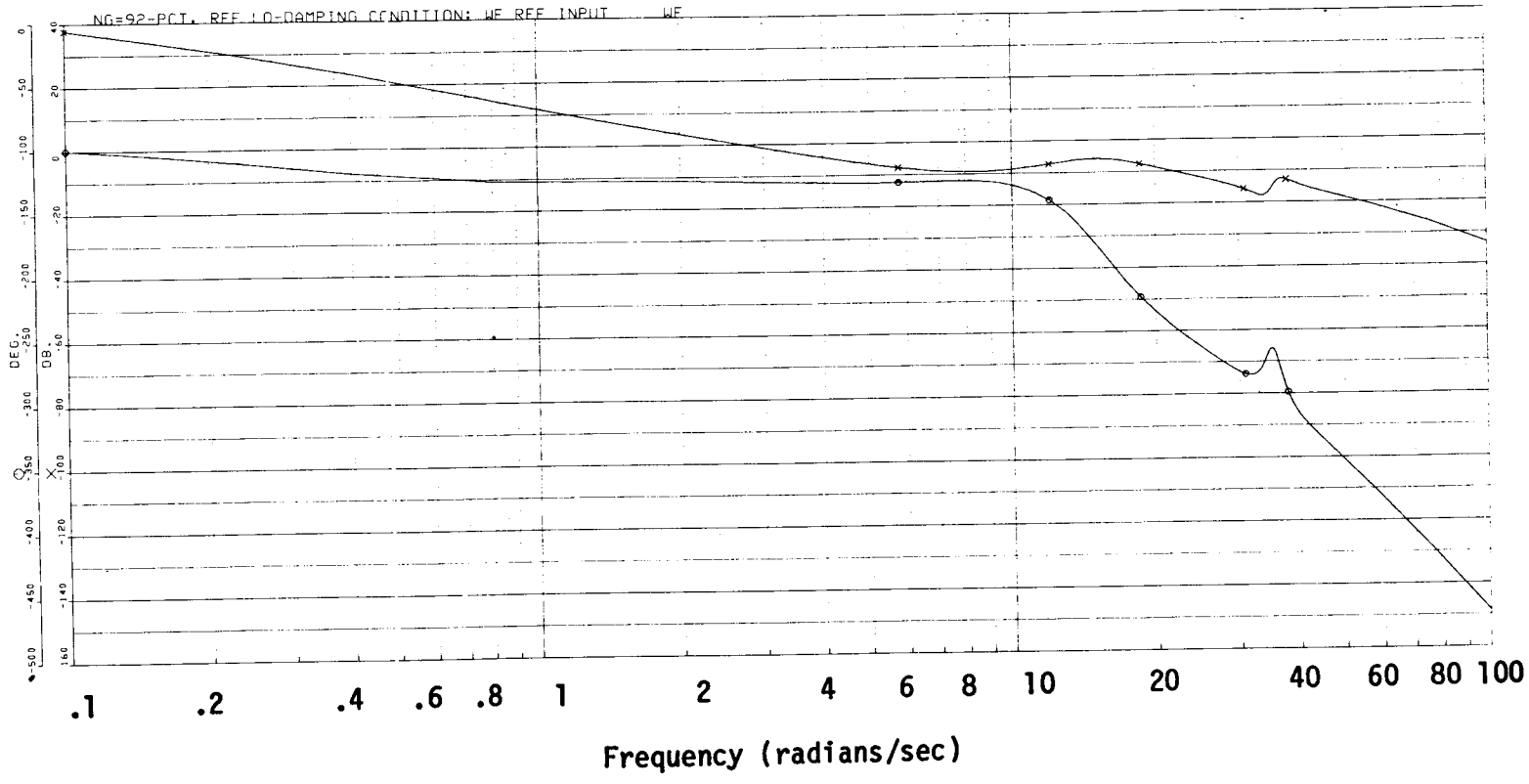




Figure 2.36 Bode Plot of T700 Baseline Np Governor with System Loop Broken at WF.

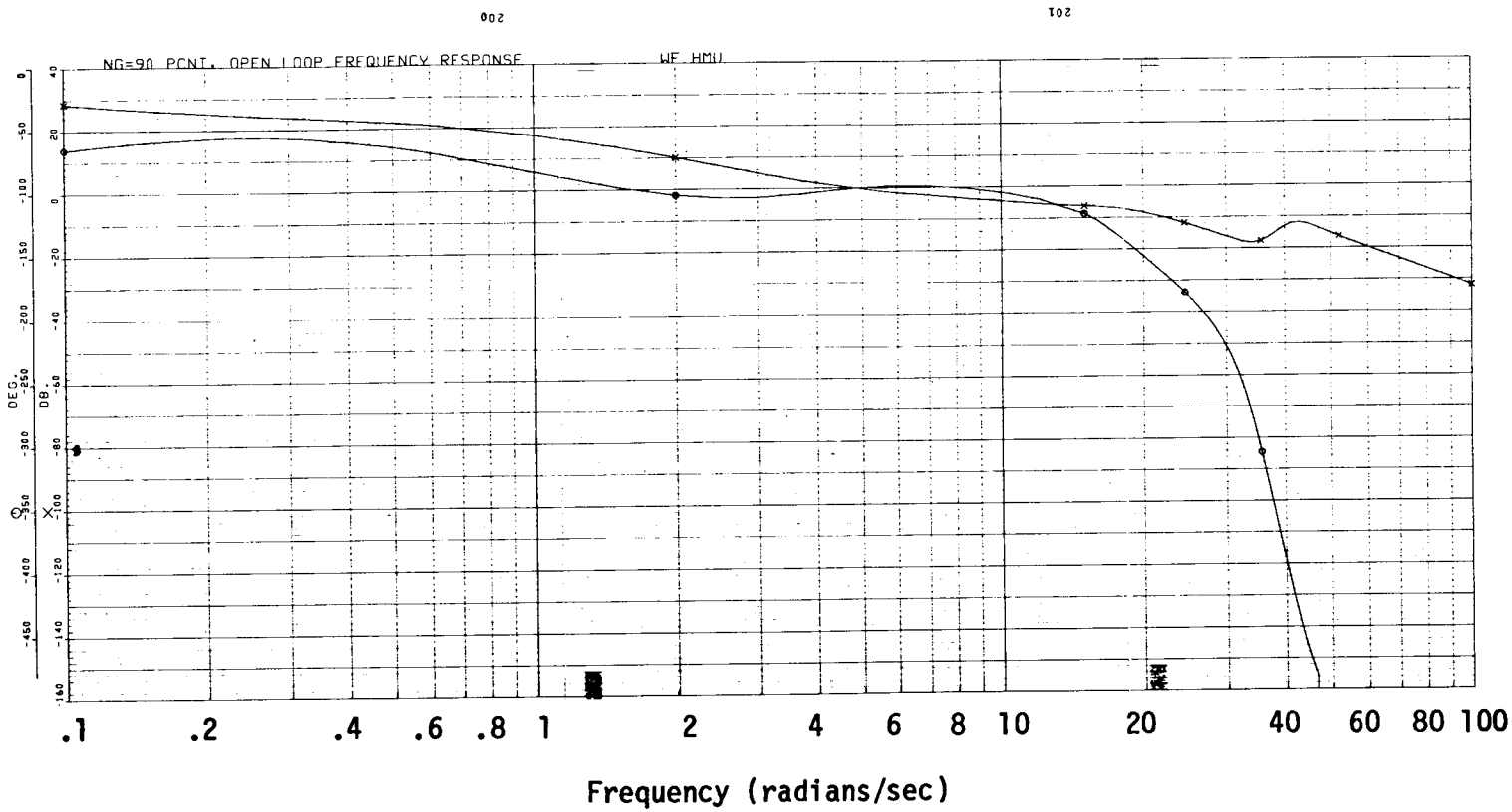


Figure 2.38 Bode Plot of LQR Governor with One Engine Inoperative (OEI).

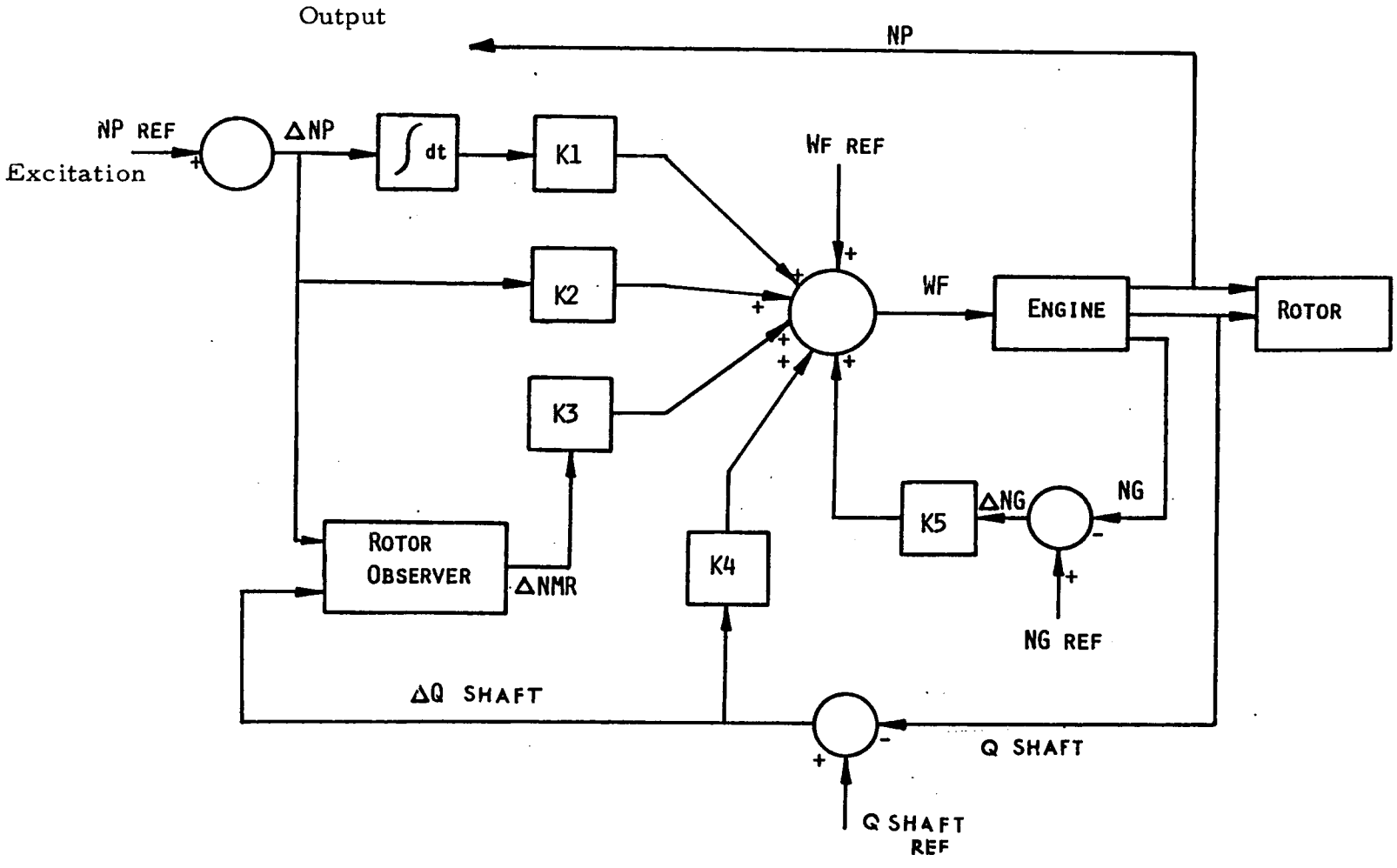


Figure 2.39 Schematic of Engine, Rotor, and Control System Showing Input and Output of Np Frequency Response.

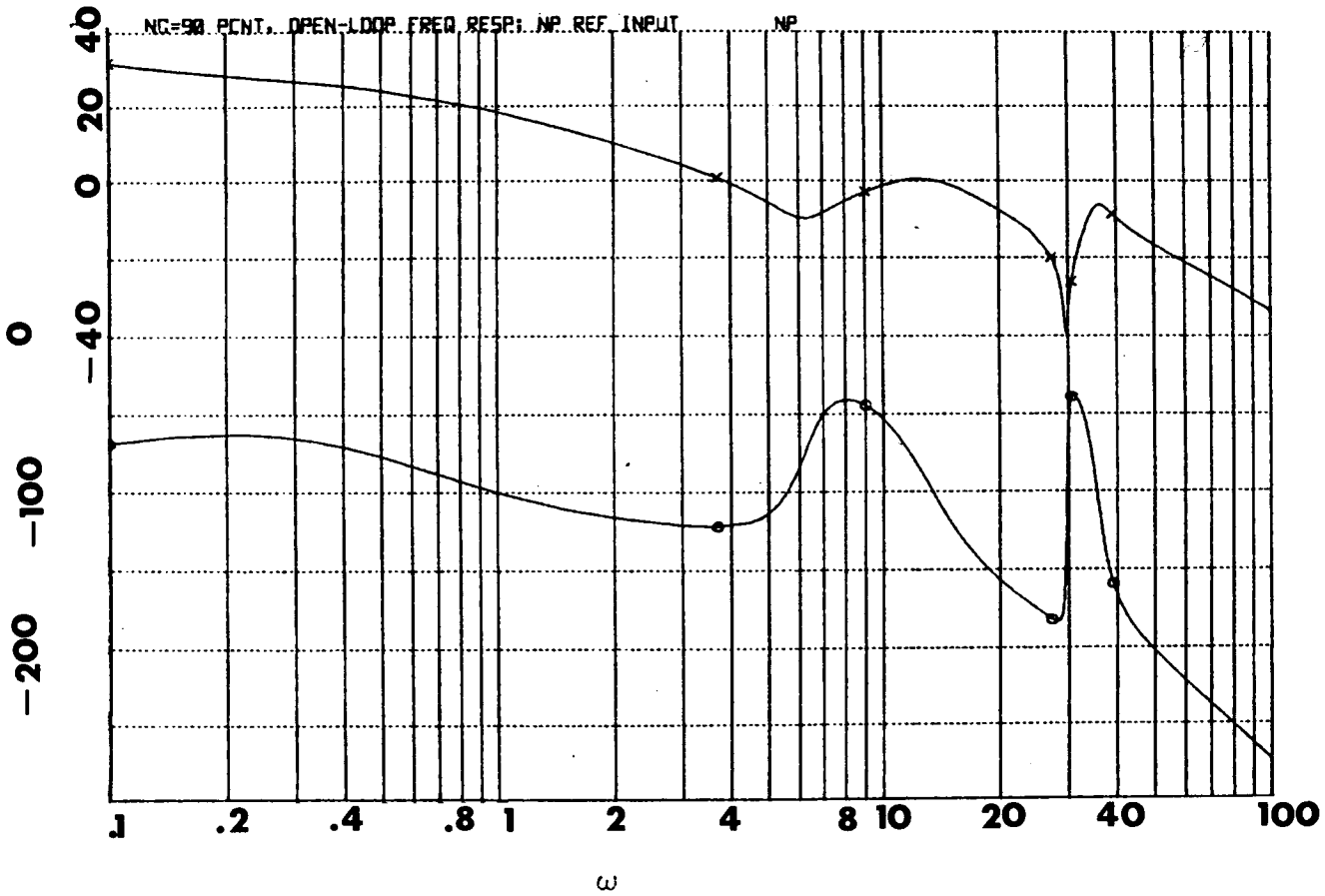


Figure 2.40 Bode Plot of LQR Np Governor to Np Reference Excitation.

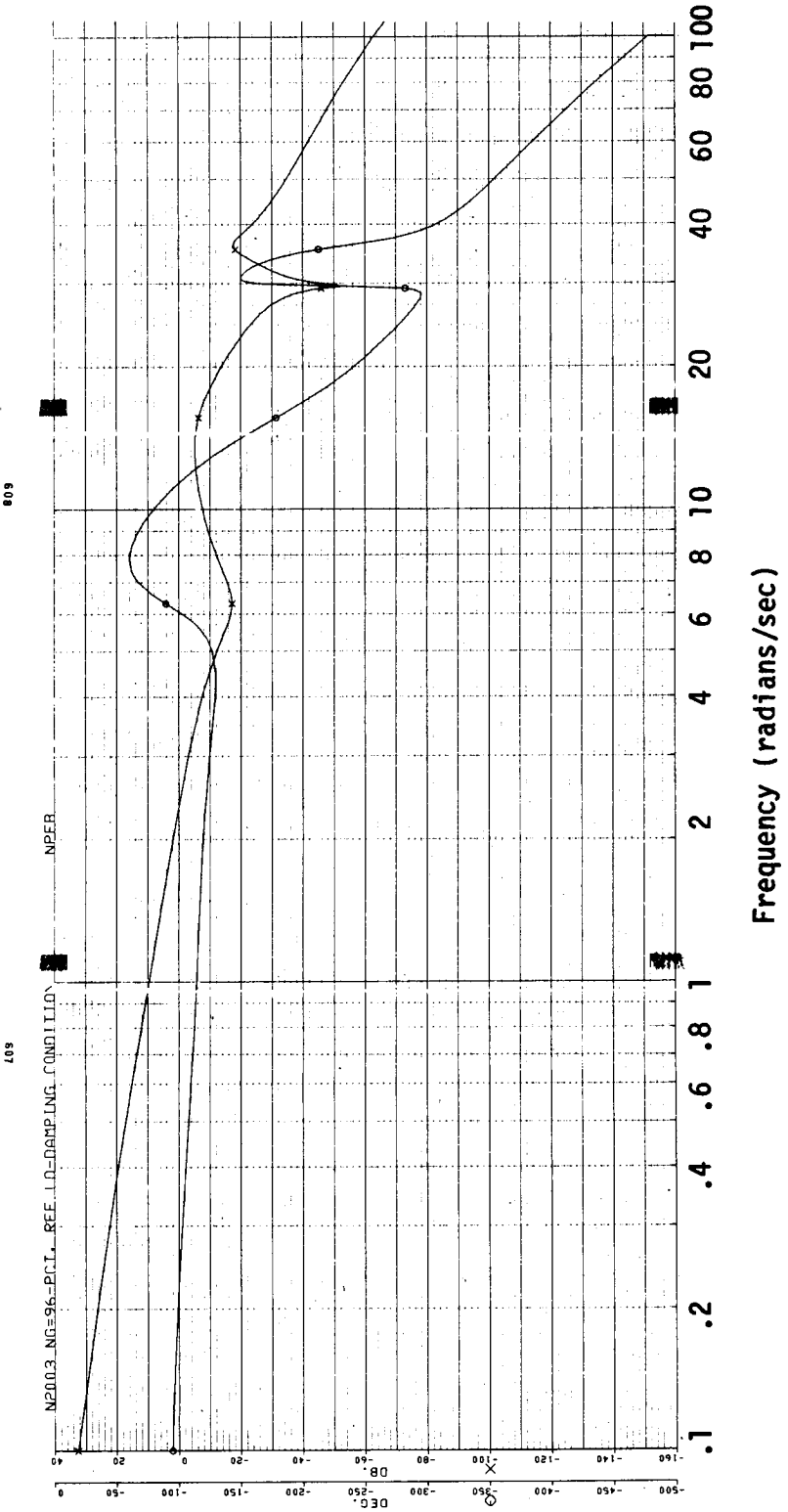


Figure 2.41 Bode Plot of Baseline T700 Np Governor to Np Reference Excitation.

torque disturbance and a tail rotor torque disturbance to analyze the effects on power turbine speed and helicopter main rotor speed. The simulated disturbance was a sinewave frequency sweep. The parts in the rotor system where the disturbances were input are shown in Figure 2.42. Each disturbance was input separately. The response of power turbine speed to a main rotor disturbance is shown in Figure 2.43 for the LQR governor and in Figure 2.44 for the T700 baseline governor. The response of helicopter main rotor speed to a main rotor torque disturbance is shown in Figure 2.45 for the LQR governor and in Figure 2.46 for the T700 baseline governor.

The closed-loop response of power turbine speed to tail rotor torque disturbances for the LQR governor is shown in Figure 2.47 and for the T700 baseline governor in Figure 2.48. The figures show that disturbances are rejected better by the LQR NP governor than by the T700 baseline governor. This better attenuation of disturbances is seen in the time responses, also.

### 2.3.7 Sensor Noise Rejection

Analysis was done in the frequency domain on the effect of sensor noise on the WF input to the engine and on power turbine speed. The three sensors measure gas generator speed, NG, power turbine speed, NP and engine shaft torque, Q shaft. For each sensor separately, a sinusoidal signal was superimposed on the sensor just before the antialias filters with the system operating closed loop. The disturbance rejection characteristics of WF and power turbine speed was assessed in the frequency domain by looking at the magnitude of the Bode plots of WF and power turbine speed. The response of power turbine speed to the NP sensor excitation is shown in Figure 2.49. This figure shows that noise on the NP sensor above the tail rotor resonance frequency will be attenuated. Figure 2.50 shows the response of WF to NP sensor noise. Noise is attenuated at all frequencies. The effects of NG sensor noise on NP and WF are shown in Figures 2.51 and 2.52, respectively. Noise is attenuated in both instances. Engine torque sensor noise effect on NP and WF are shown in Figures 2.53 and 2.54, respectively. The effect of noise on NP is attenuated except at the main rotor and tail rotor frequencies, and the effect of noise on WF is attenuated except at the main rotor frequency. This is not unexpected since the torque sensor measures main and tail rotor torque to the engine. The sensor should not see noise in this region, but rather a real signal. The figures show the LQR governor is insensitive to sensor noise.

### 2.3.8 Other Helicopter Rotor Systems

The LQR power turbine governor and observer that were designed for use on the Black Hawk were analyzed without changes with a Westland WG30 and a Hughes articulated rotor systems. The frequency response of the Black Hawk, Westland, and Hughes rotor systems were calculated for an input to WF integrator (see Figure 2.7) and an output of NP. This was done to compare the rotor system frequency domain characteristics. Figure 2.55 shows the Black Hawk response, Figure 2.56 shows the Westland, WG30 response, and Figure 2.57 shows the Hughes response. Each system exhibits a resonant peak at the main

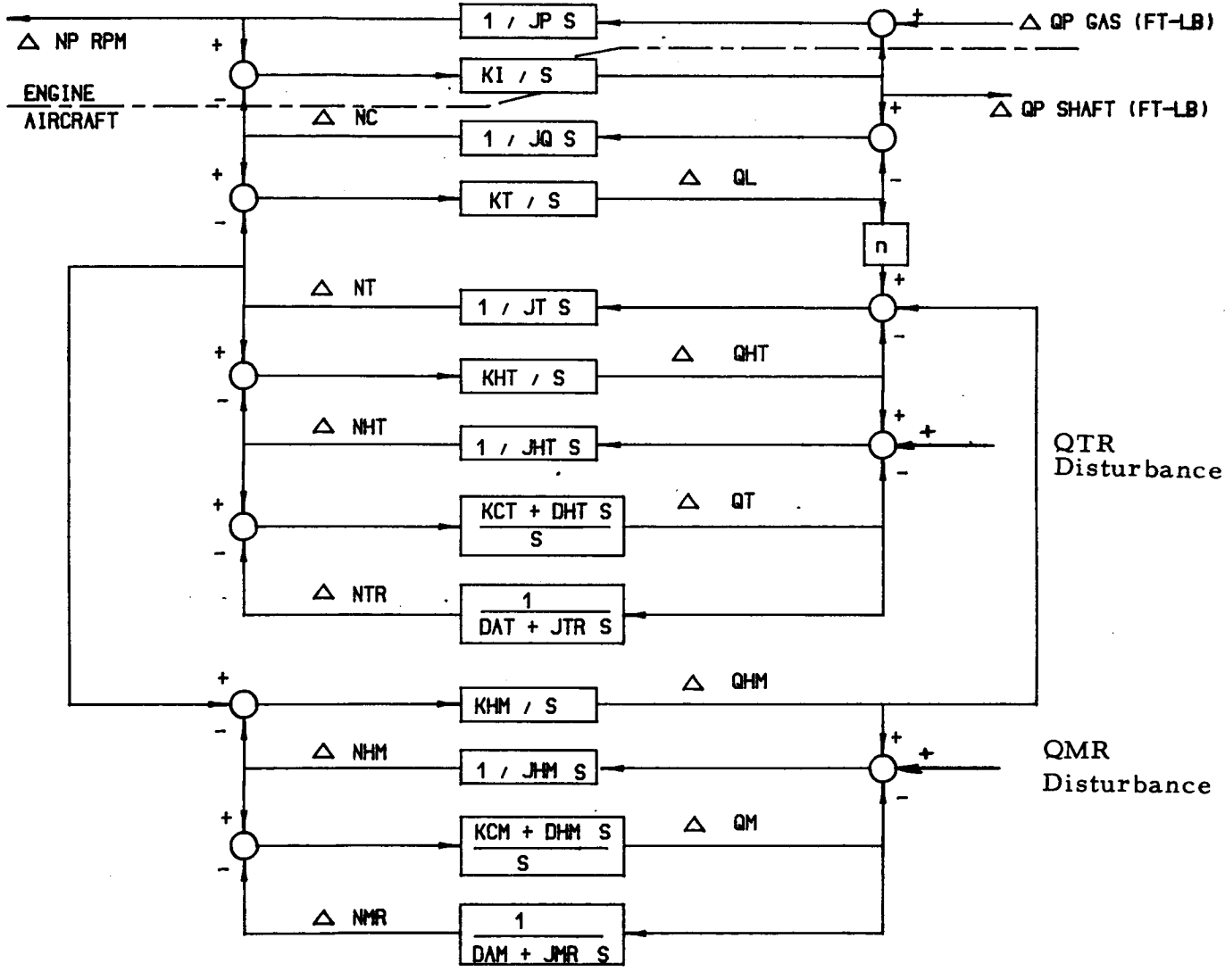


Figure 2.42 Schematic of Rotor System Showing where Main Rotor and Tail Rotor Disturbances are Introduced.

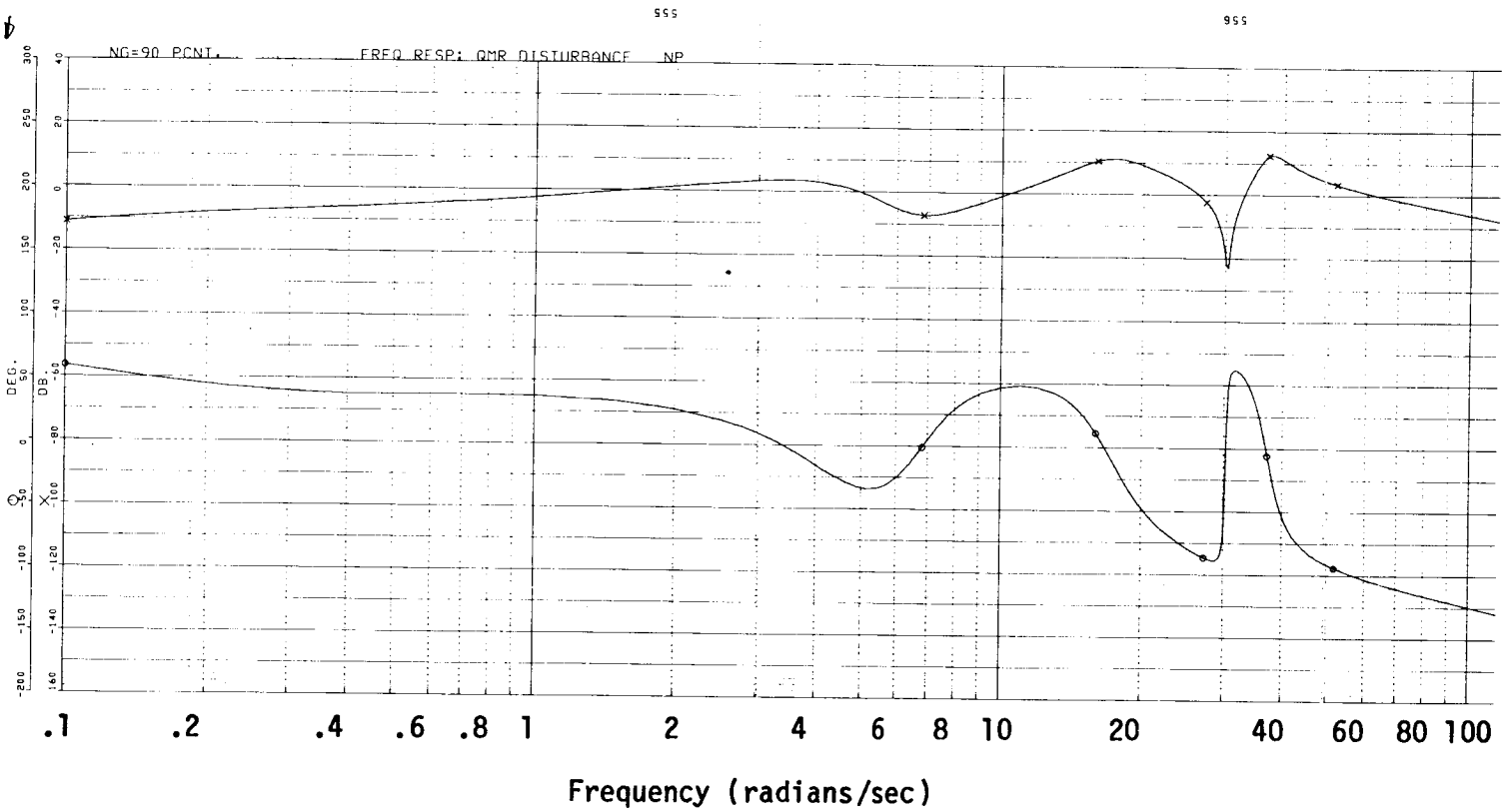


Figure 2.43 Bode Plot of Np Response of LQR Governor to Helicopter Main Rotor Torque Disturbance.

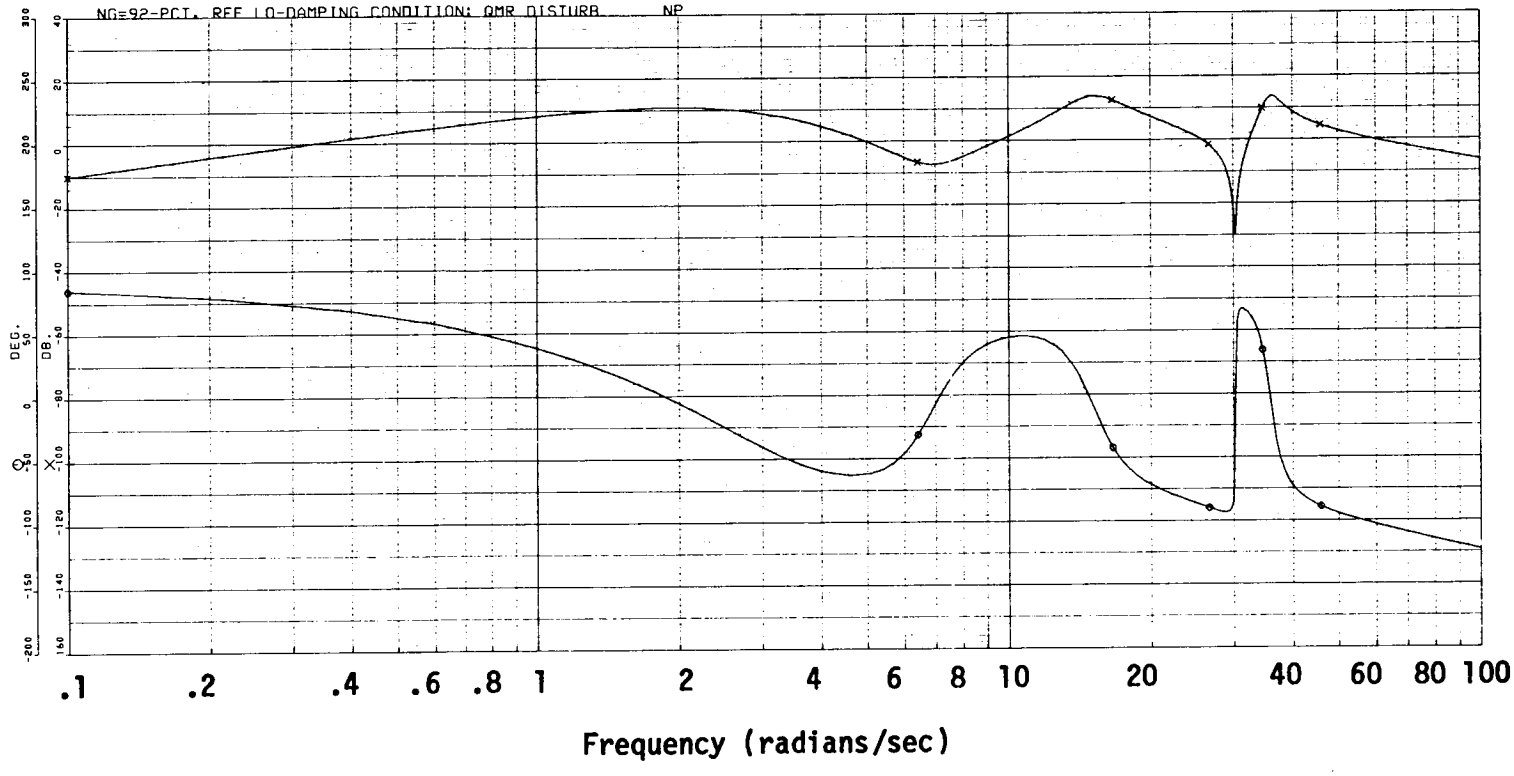




Figure 2.44 Bode Plot of Np Response of T700 Baseline Governor to Helicopter Main Rotor Torque Disturbance. NG = 92%.

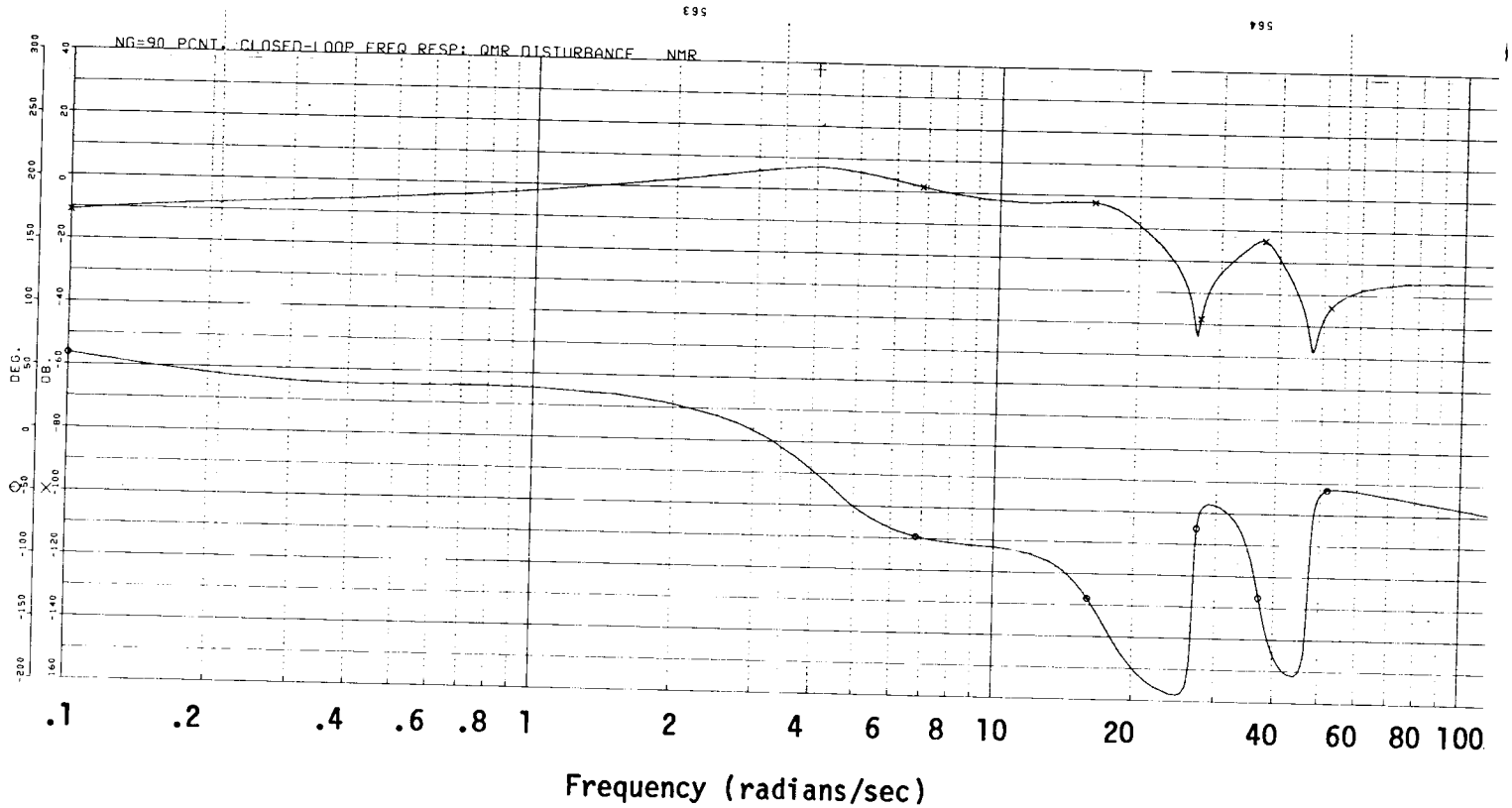


Figure 2.45 Bode Plot of Main Rotor Speed Response of LQR Governor to Helicopter Main Rotor Torque Disturbance.

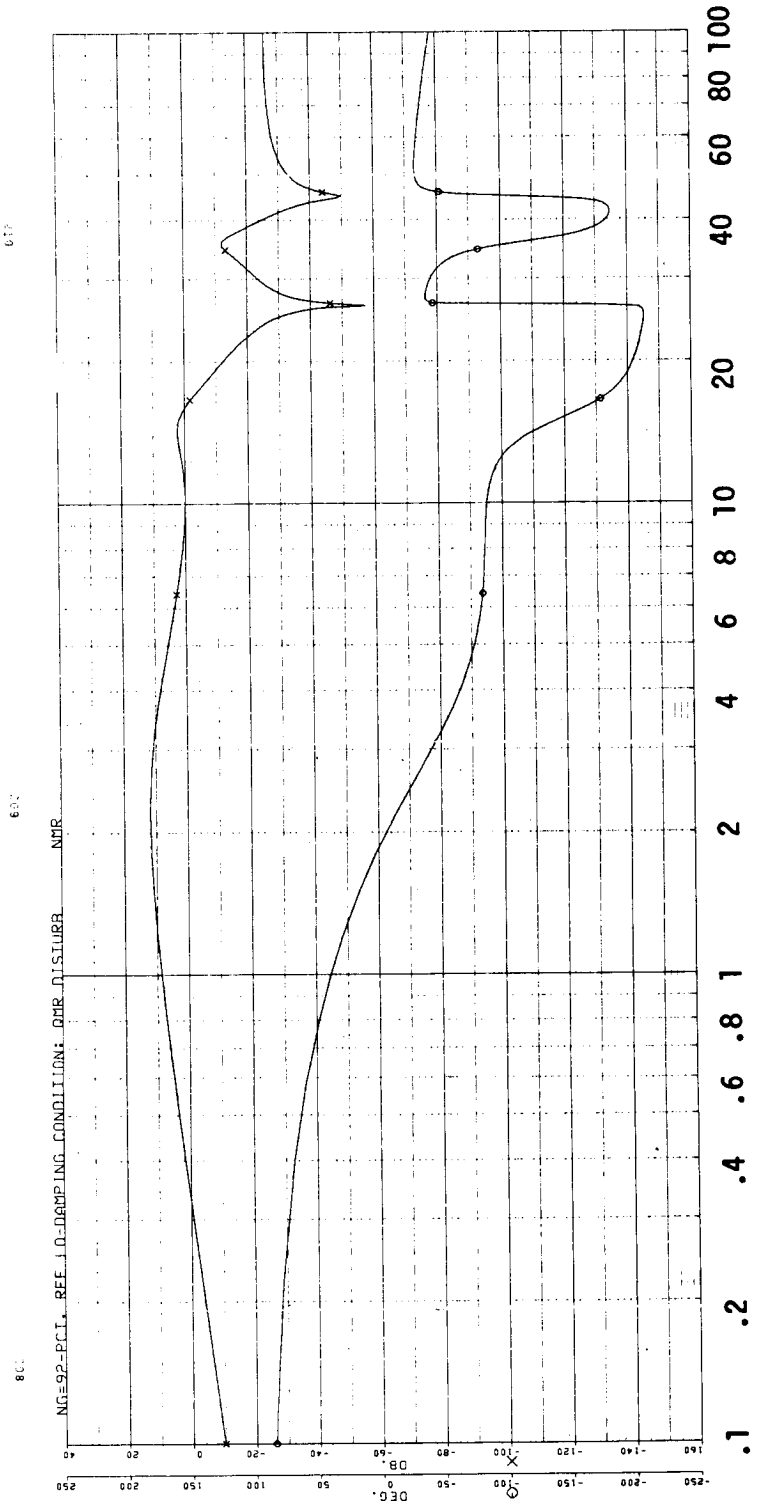


Figure 2.46 Bode Plot of Main Rotor Speed Response of T700 Baseline Governor to Helicopter Main Rotor Torque Disturbance. NG = 92%.

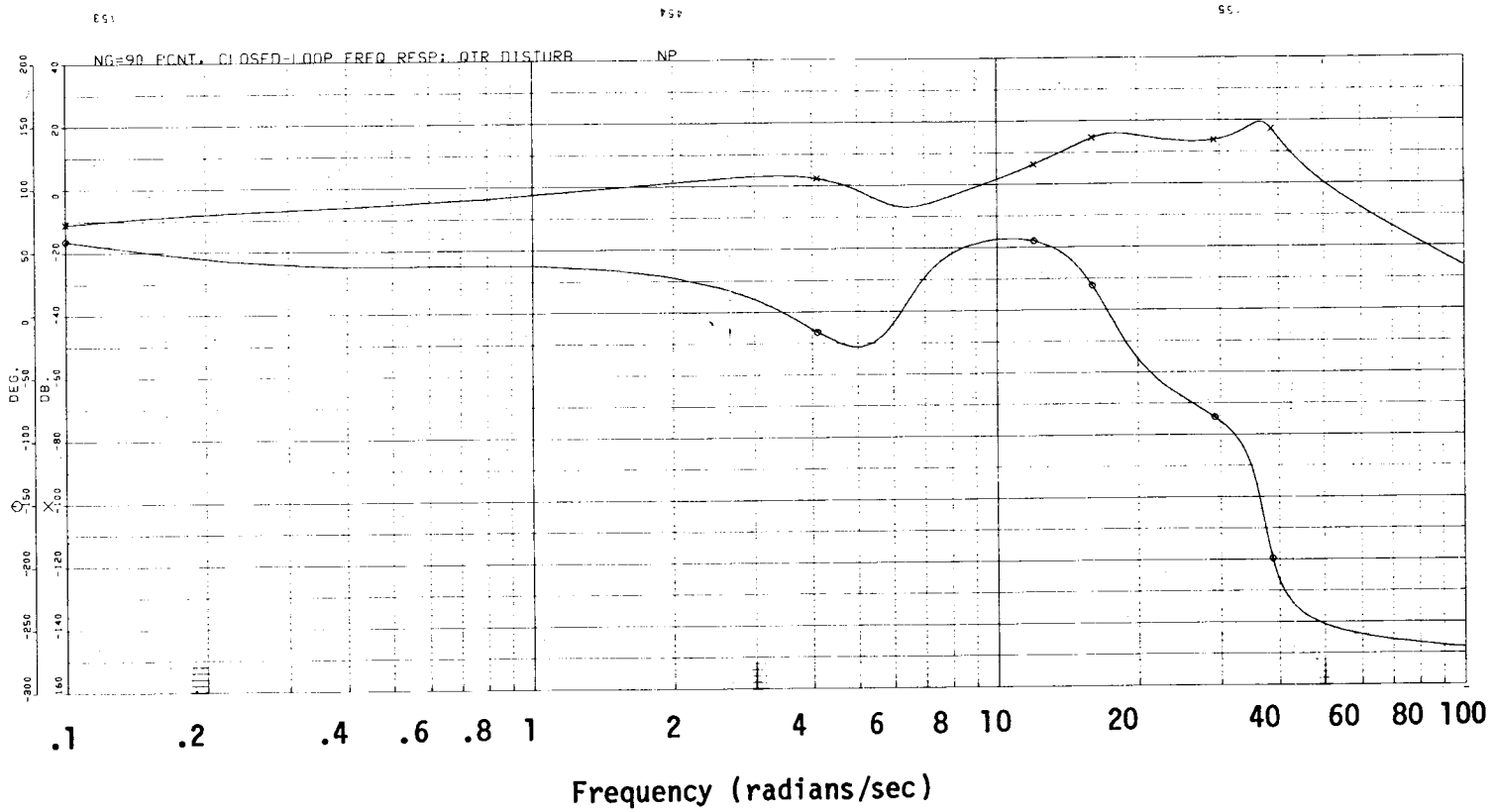


Figure 2.47 Bode Plot of Np Response of LQR Governor to Helicopter Tail Rotor Torque Disturbance.

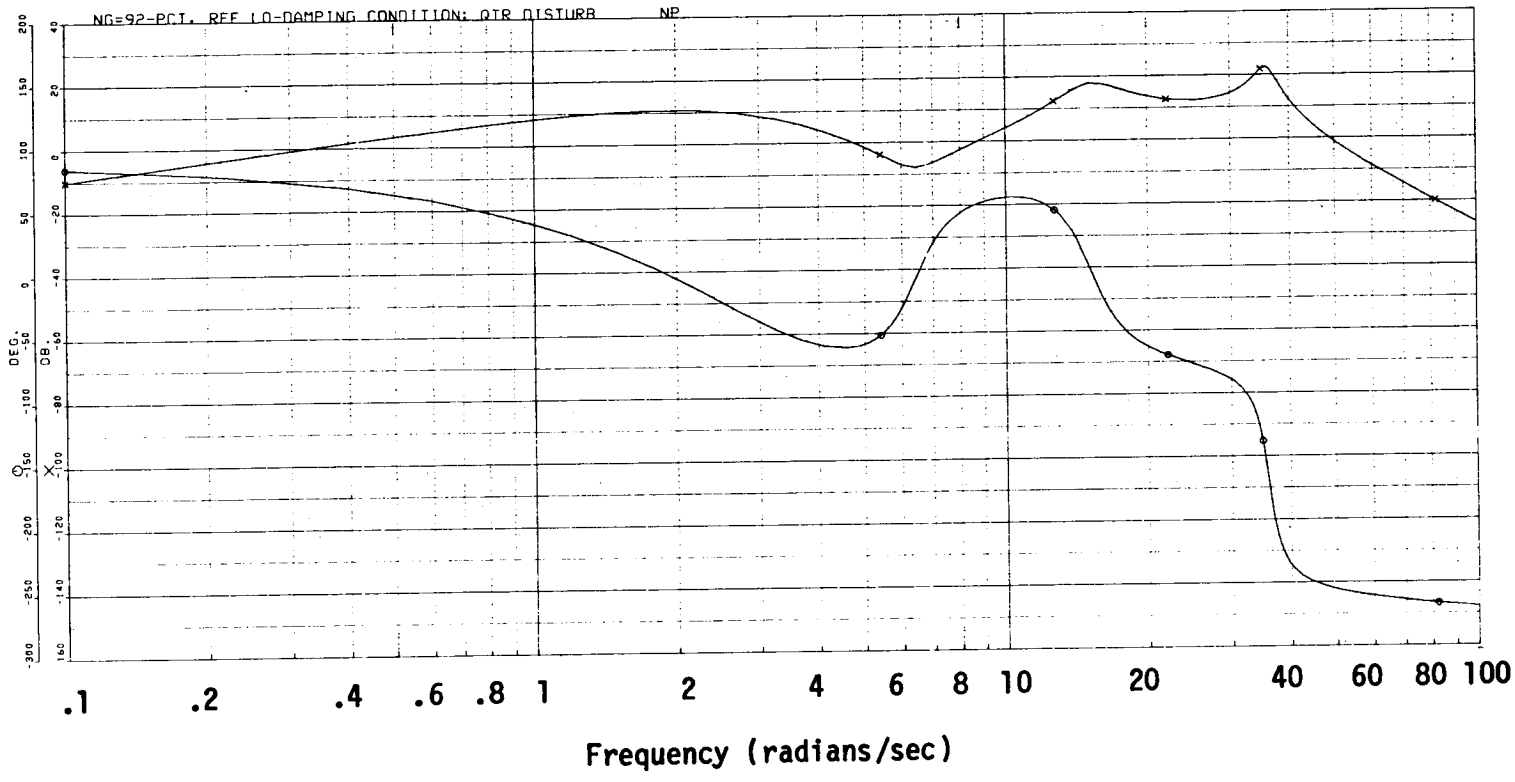


Figure 2.48 Bode Plot of Np Response of T700 Baseline Governor to Helicopter Tail Rotor Torque Disturbance. NG = 92%.

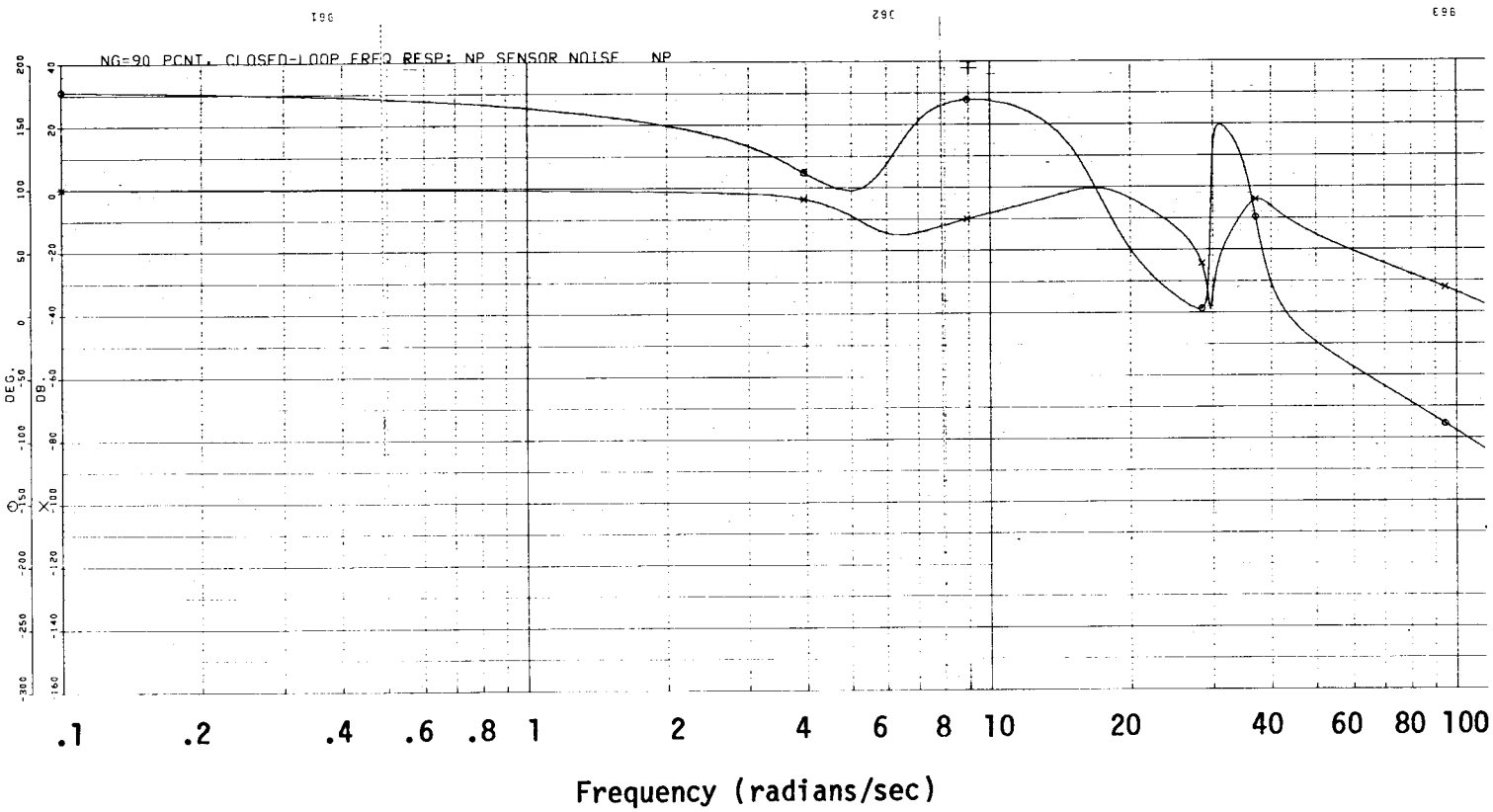


Figure 2.49 Bode Plot of Np Response to Np Sensor Noise.

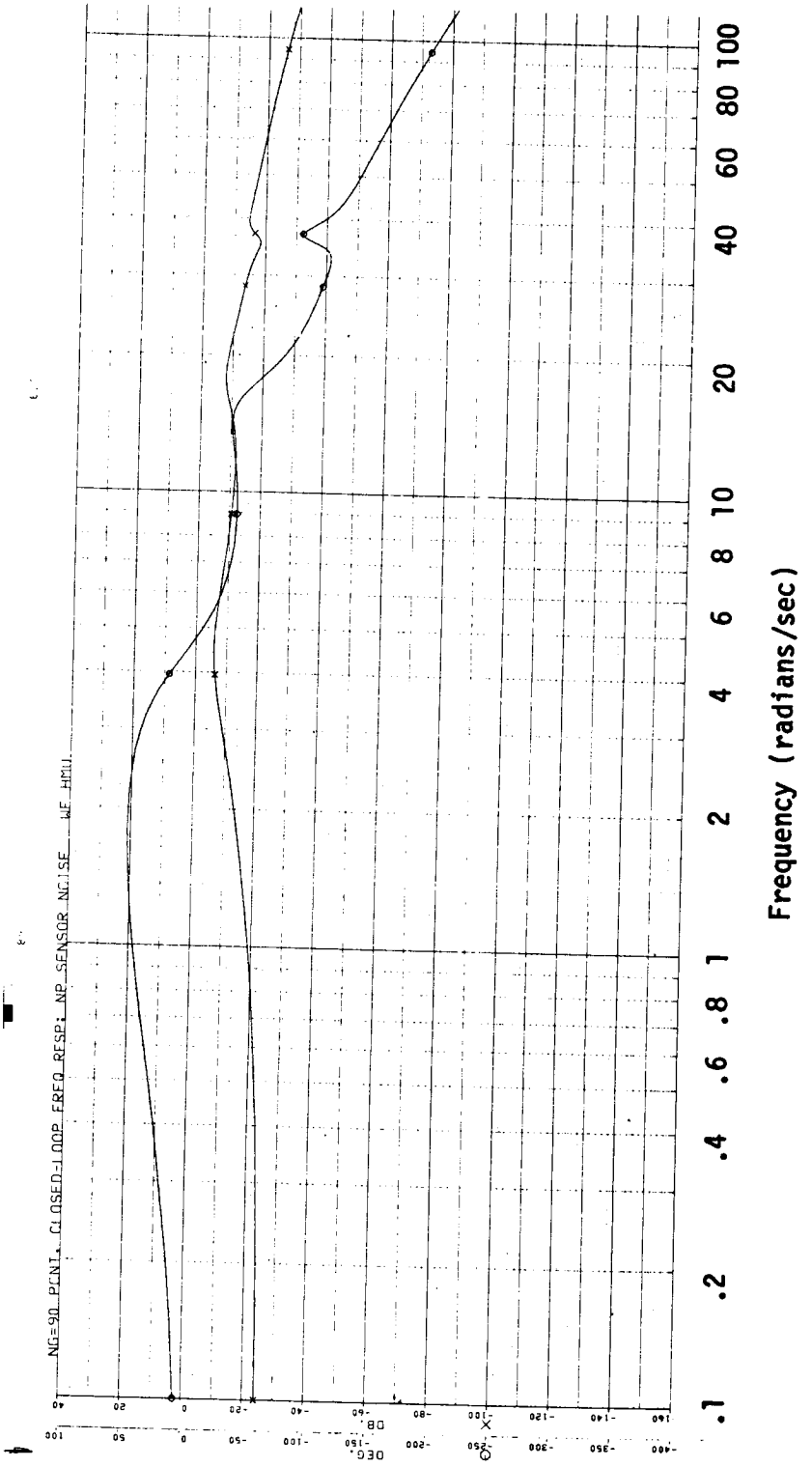


Figure 2.[illegible] Bode Plot of WF Response to Np Sensor Noise.

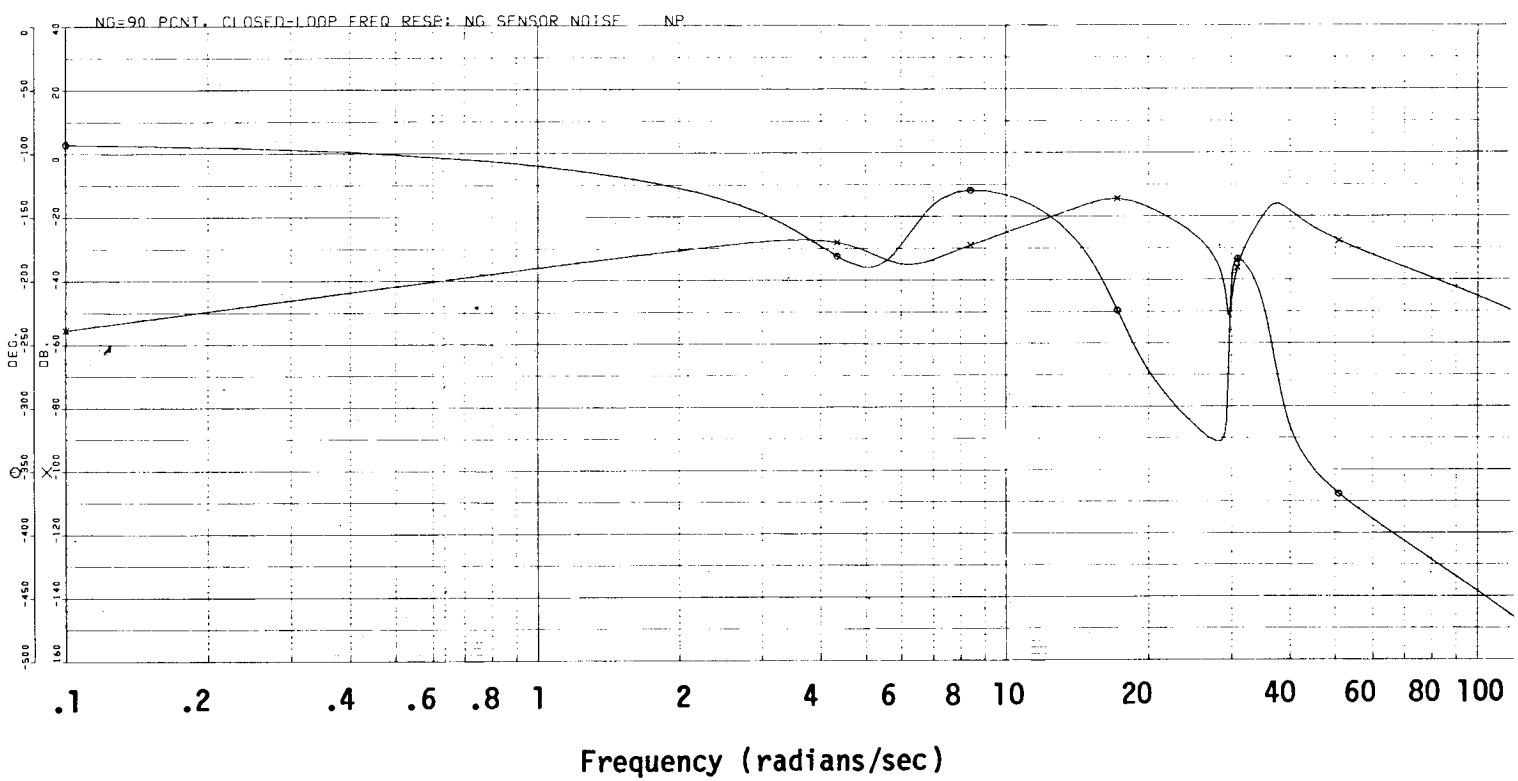


Figure 2.51 Bode Plot of Np Response to NG Sensor Noise.

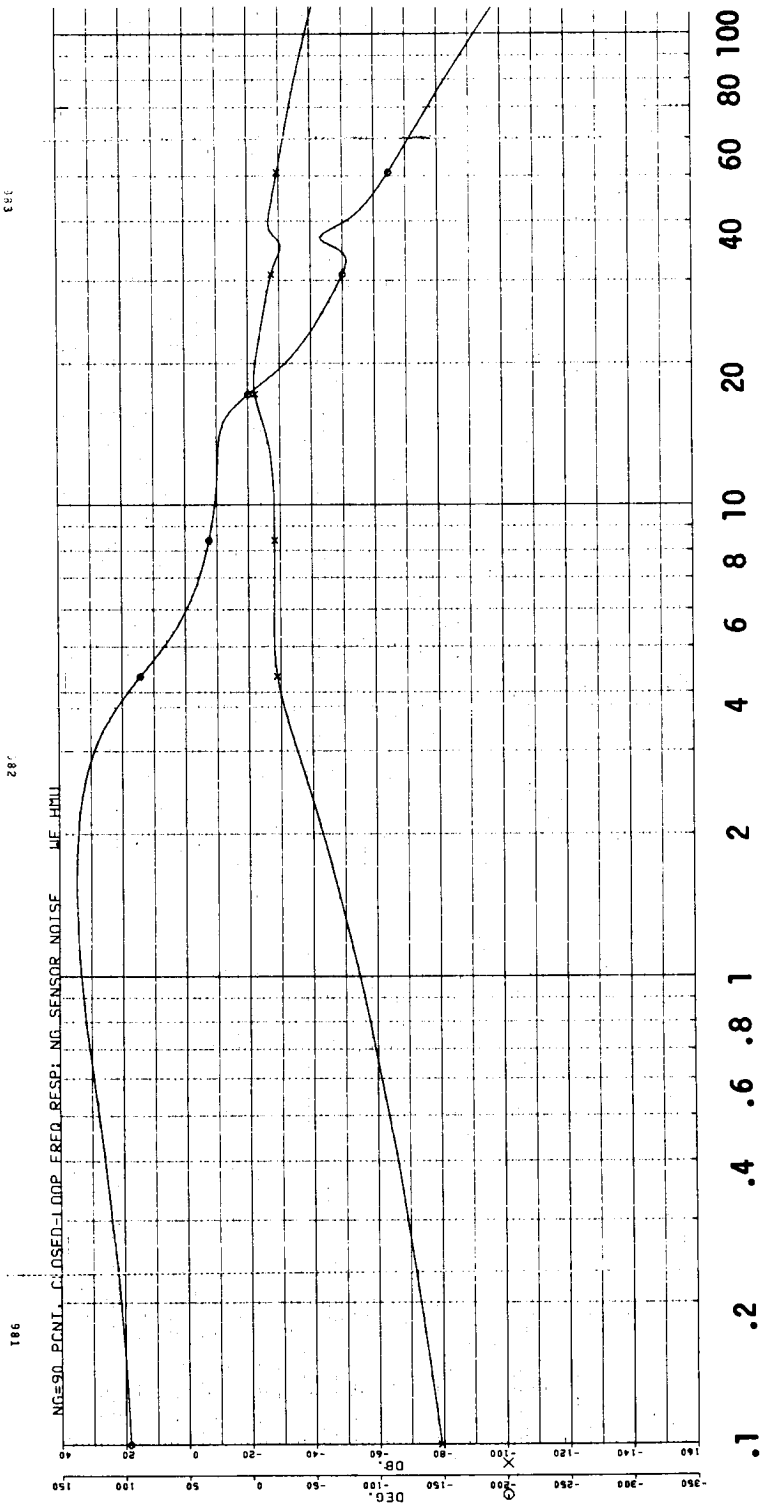


Figure 2.52 Bode Plot of WF Response to NG Sensor Noise.

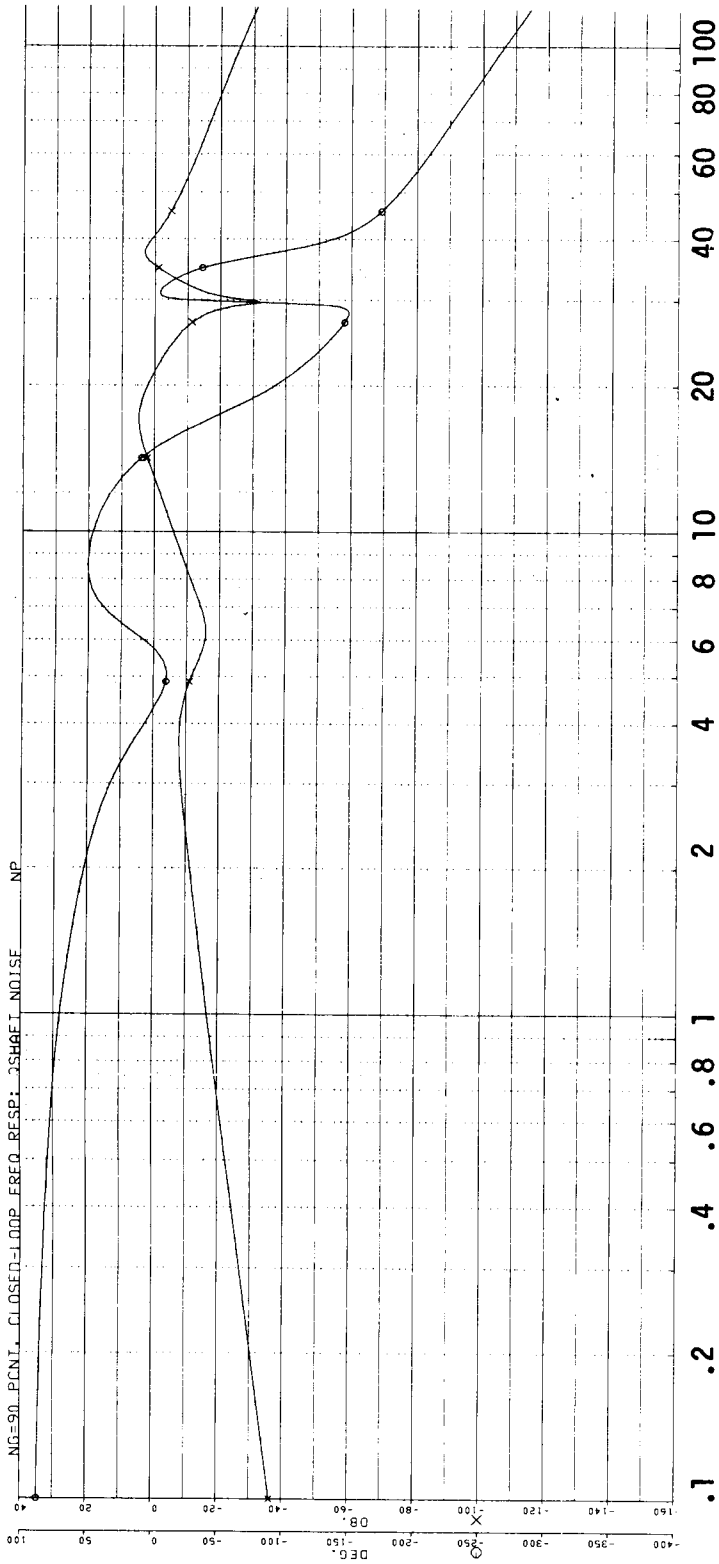


Figure 2.53 Bode Plot of Np Response to Engine Shaft Torque Sensor Noise.



C-2

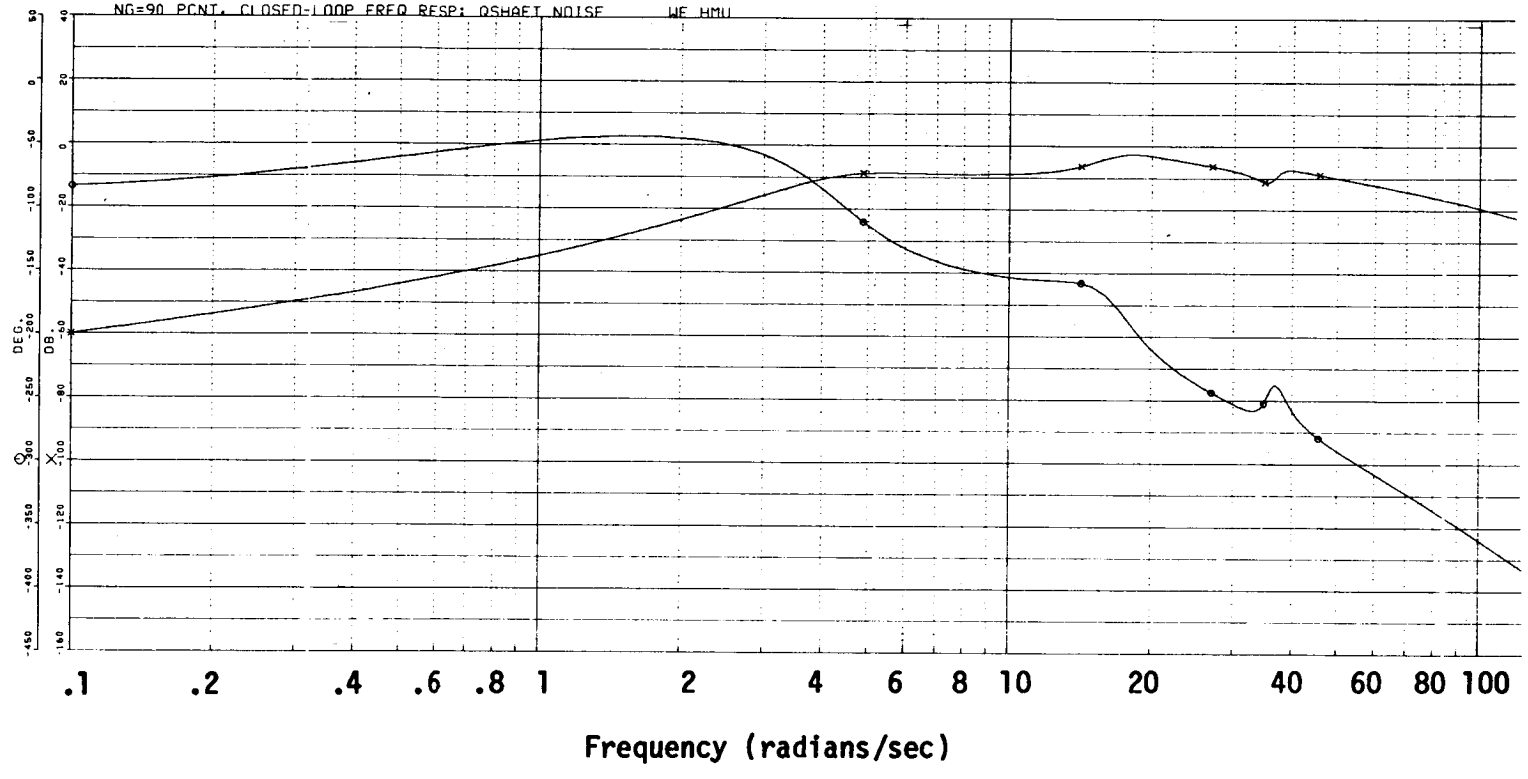


Figure 2.54 Bode Plot of WF Response to Engine Shaft Torque Sensor Noise.

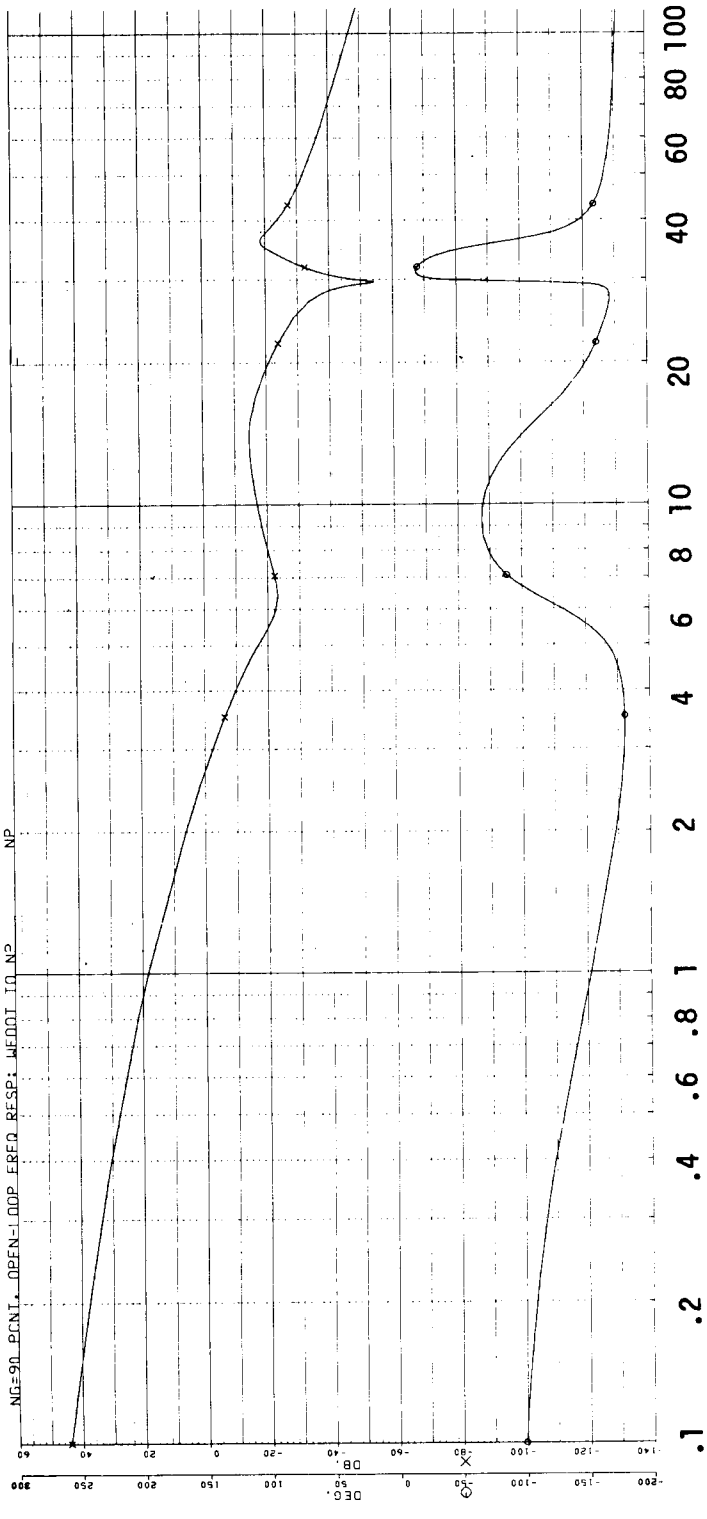


Figure 2.55 Bode of Black Hawk Rotor System Frequency Response from d(WF)/dt Input to Np Output.

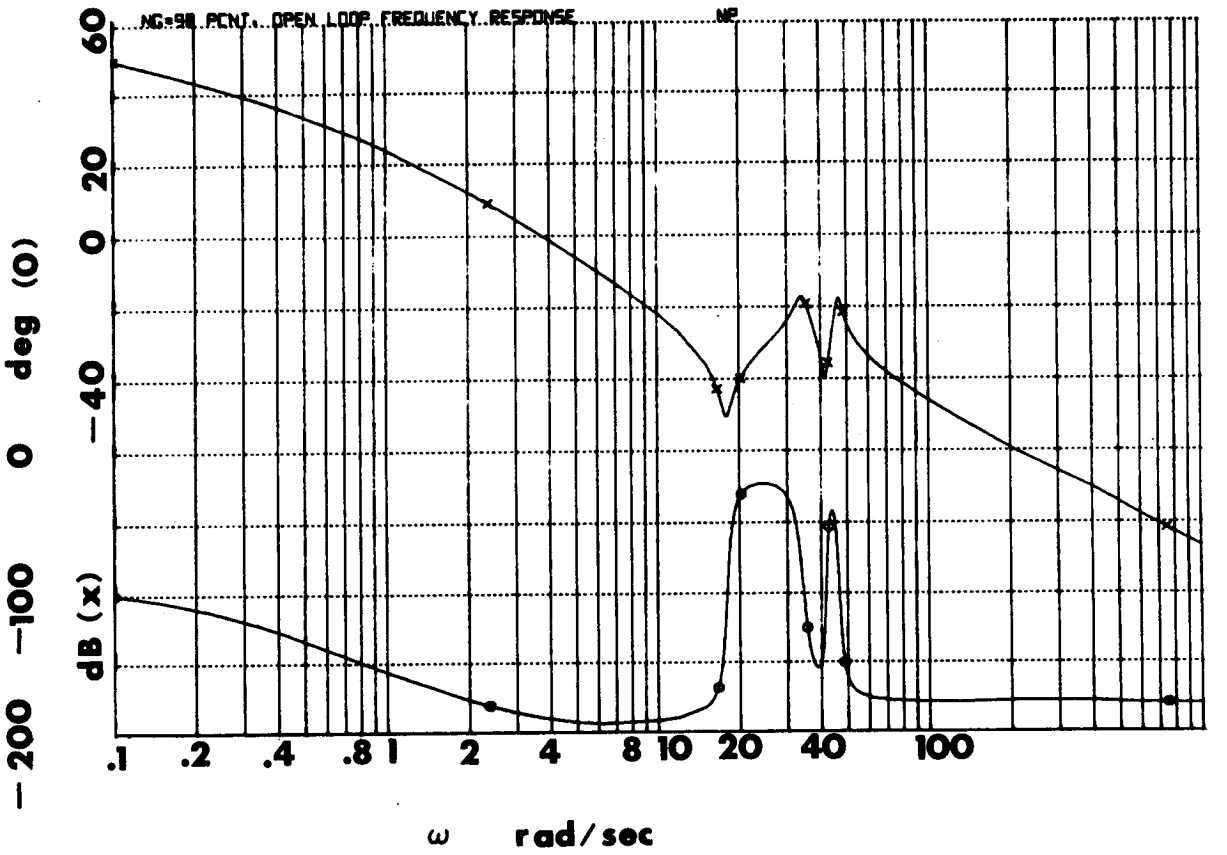


Figure 2.56 Bode Plot of Westland WG30 Rotor System Frequency Response from d(WF)/dt Input to Np Output.

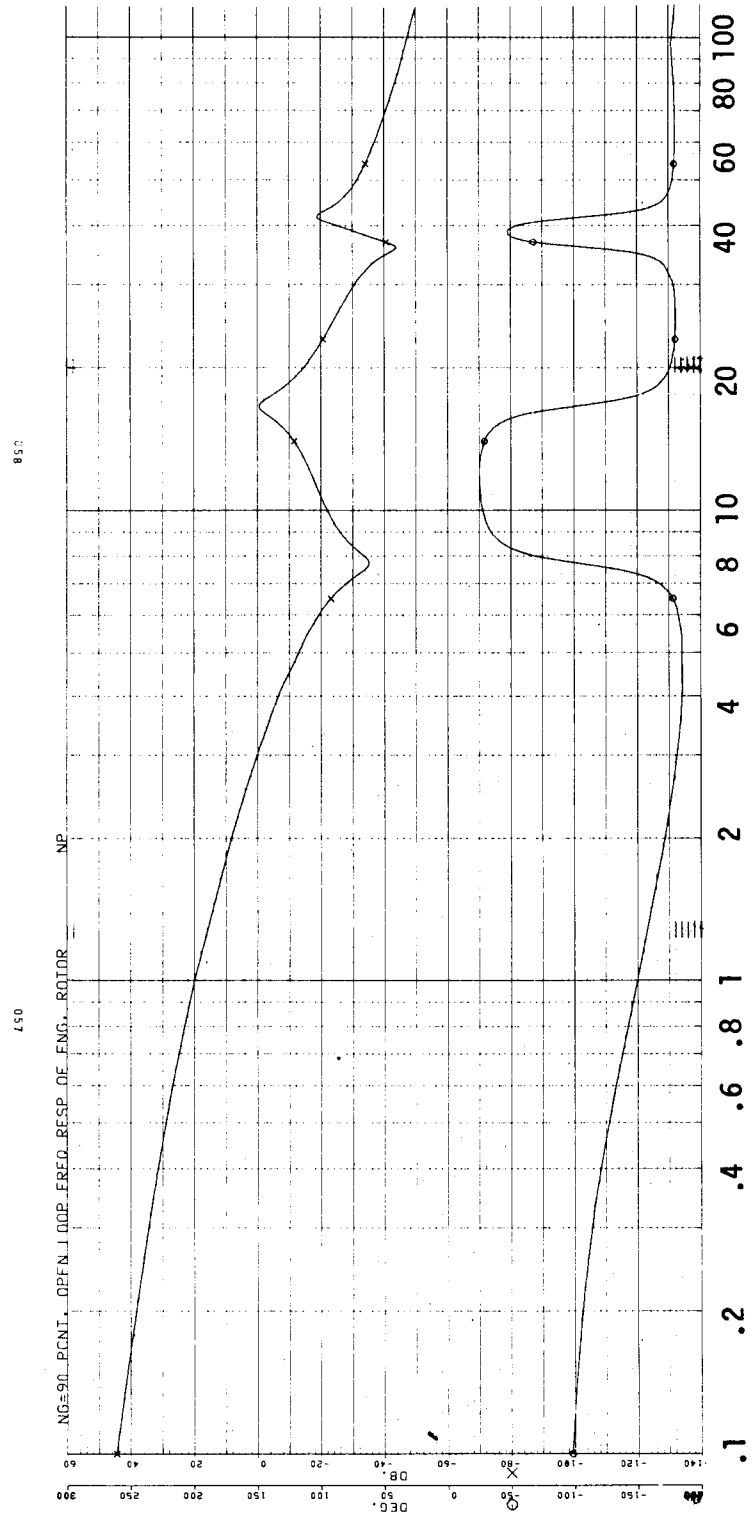


Figure 2.57 Bode Plot of Hughes Rotor System Frequency Response from d(WF)/dt Input to Np Output.

rotor natural frequency and a resonant peak at the tail rotor natural frequency. The Black Hawk and Hughes systems have the peaks in the same frequency range, except the Hughes main rotor peak is less damped and, therefore, more pronounced. The Westland system has the main rotor resonance at a higher frequency compared to the Hughes and Black Hawk systems.

The Black Hawk LQR gains and Kalman Filter were used with the Westland WG30 and Hughes rotor systems. The frequency response of the Westland system with the Black Hawk power turbine governor is shown in Figure 2.58. The excitation is WF to the engine and the response is demanded WF as shown in Figure 2.24. The antiresonance before the first resonant peak was reduced considerably, but the phase margin is reduced to near zero degrees. The effect of adding a lead compensator to increase phase margin is shown in Figure 2.59. The lead compensator has the undesirable effect of increasing the resonant peaks. Lowering the gain to get 6dB attenuation of the peaks lowers the bandwidth to around 3 rad/sec, reducing the effectiveness of the power turbine governor. The frequency response of the Black Hawk power turbine governor with the Hughes rotor system is shown in Figure 2.60. The excitation is WF to the engine and the response is demanded WF as shown in Figure 2.24. The main rotor resonant peak is not reduced as much as was the Black Hawk resonant peak. A gain reduction to attenuate the resonant peaks would reduce the bandwidth too much for the governor to be more effective than the T700 baseline governor. It is possible that different LQR governors could be designed for each rotor system and then a compromise made to make the control transferable among different rotor systems.

## 2.4 Dynamometer Design

The LQR power turbine governor designed for the Black Hawk rotor system was also evaluated in the frequency and time domains using a dynamometer load for test cell operation. The goal was to be able to transfer the engine between the airframe and the test cell with no modification to the control laws. This has not been achieved, although only the coefficients of a lead compensator need to be changed.

The LQR power turbine governor designed for the Black Hawk rotor system was evaluated in the frequency domain with a dynamometer load. This response is shown in Figure 2.61 for the engine at 90% Ng. The model used for the dynamometer is shown in Figure 2.62. The frequency response shows no resonant peaks since the dynamometer does not contain the same dynamic characteristics of a helicopter rotor system. The phase margin was reduced to about 12 degrees and is insufficient to maintain stability on a real engine. Lead compensation was added at 5 rad/sec to increase the phase margin to 56 degrees with 6 dB gain margin. Figure 2.63 is a Bode plot of the LQR governor with the dynamometer load with the lead compensator added. This lead compensator has its peak phase contribution one decade above the peak phase lead of the

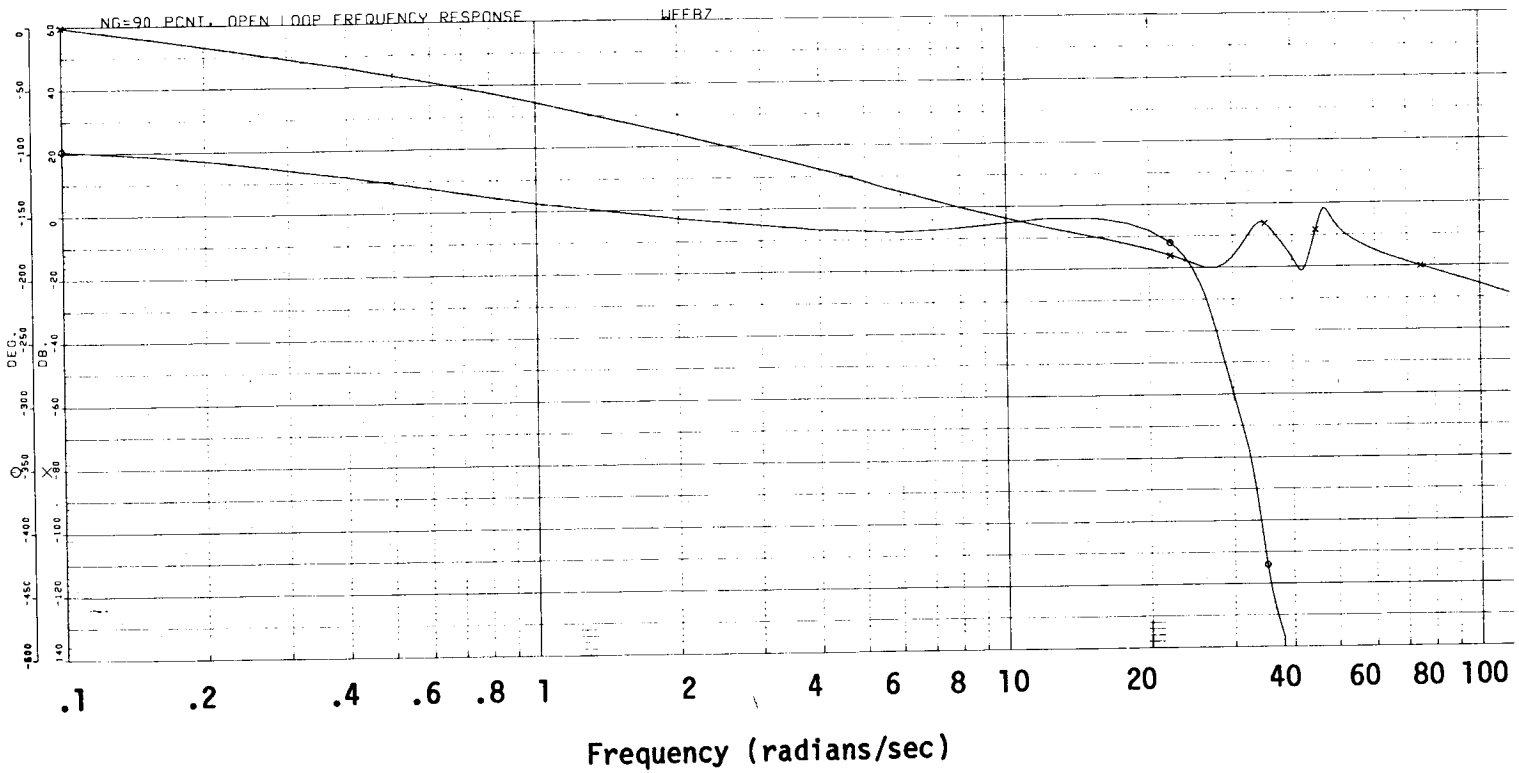


Figure 2.58 Bode Plot of Black Hawk LQR Np Governor with Westland WG30 Rotor System. No Dynamic Compensation Added.

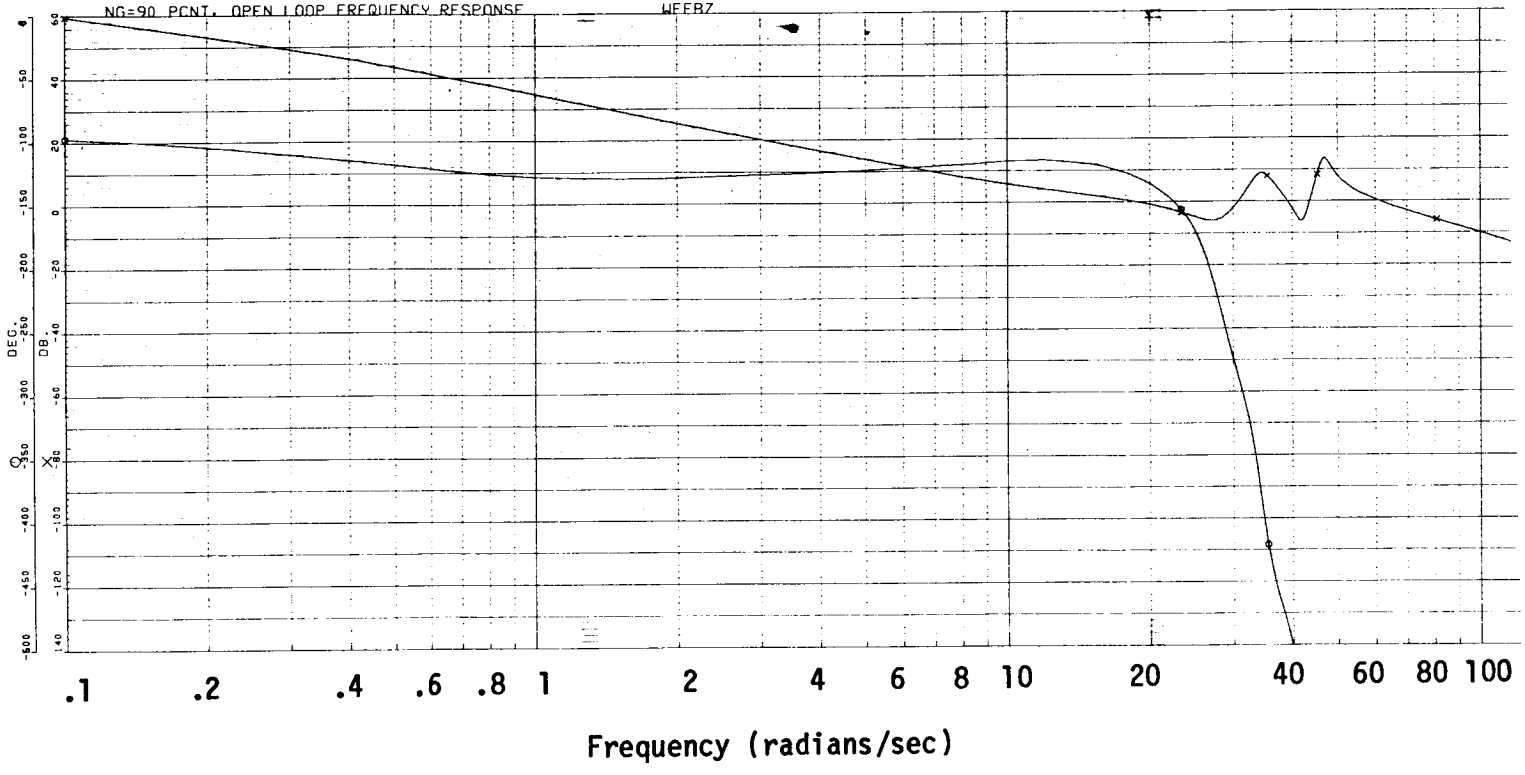


Figure 2.59 Bode Plot of Black Hawk LQR Np Governor with Westland WG30 Rotor System. Lead Compensation Added.

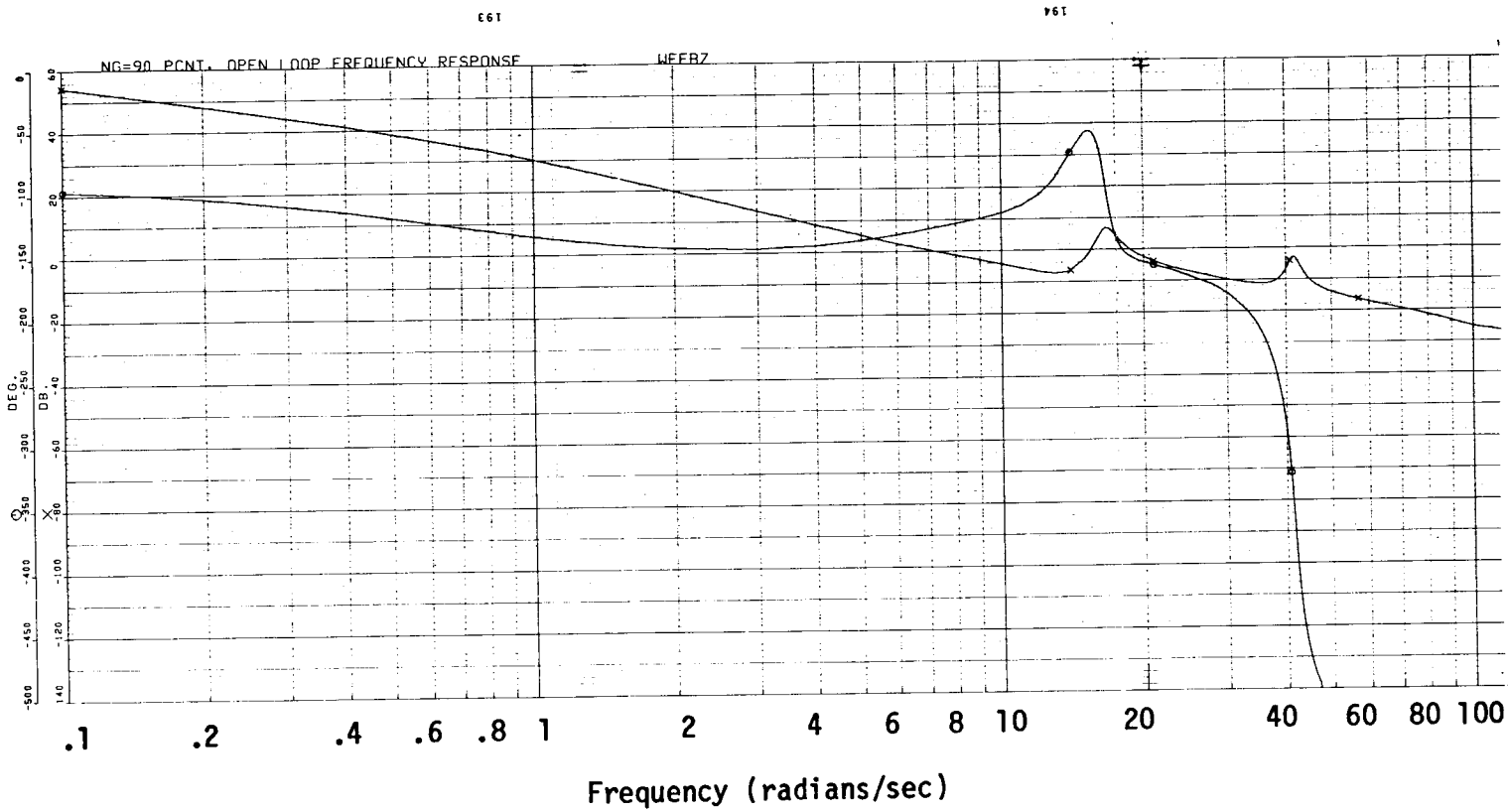


Figure 2.60 Bode Plot of Black Hawk LQR Np Governor with Hughes Rotor System. No Dynamic Compensation Added.

ORIGINAL PAGE IS
OF POOR QUALITY

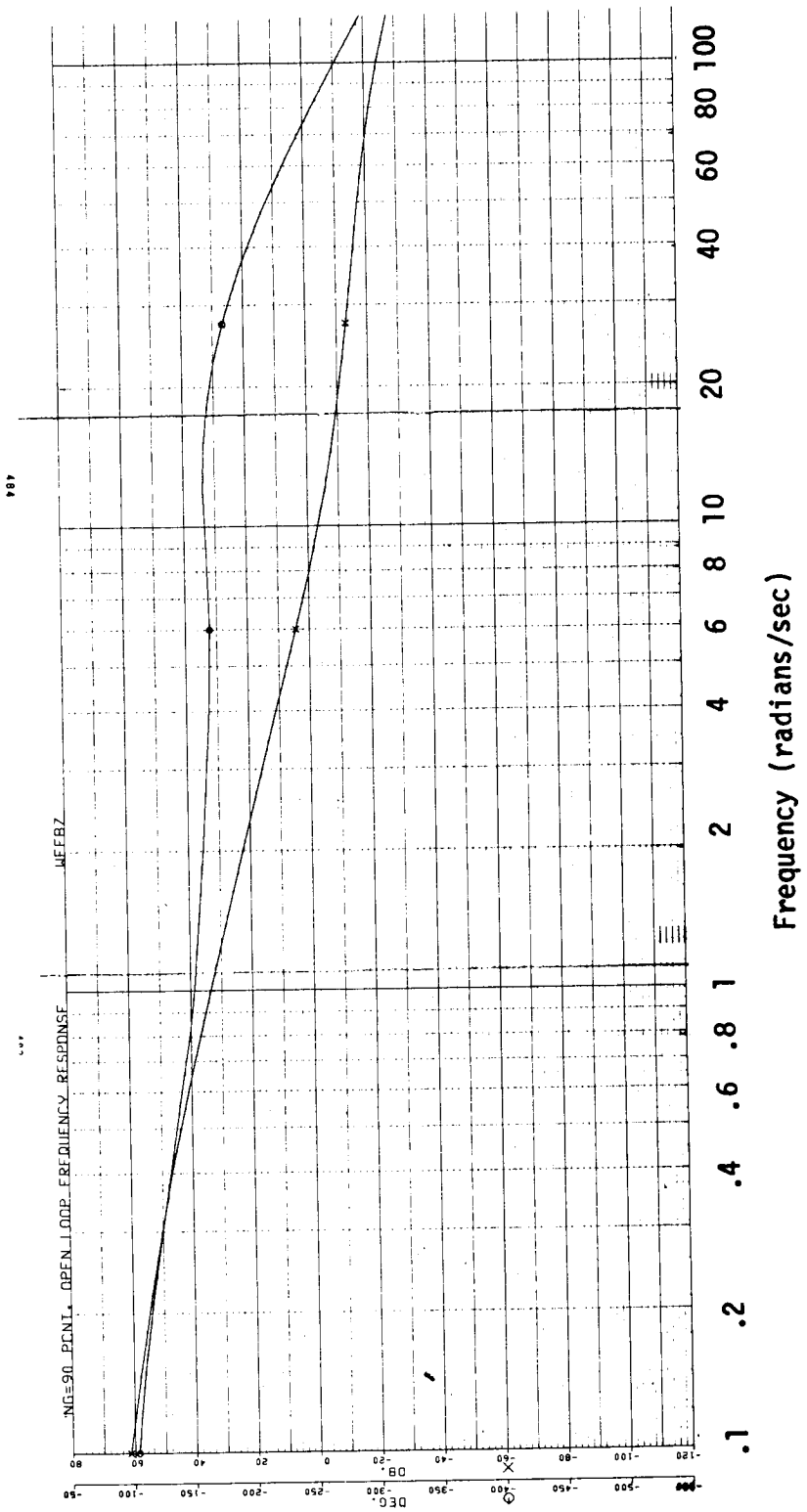


Figure 2.61 Bode Plot of Black Hawk LQR Np Governor with Dynamometer. No Dynamic Compensation Added.

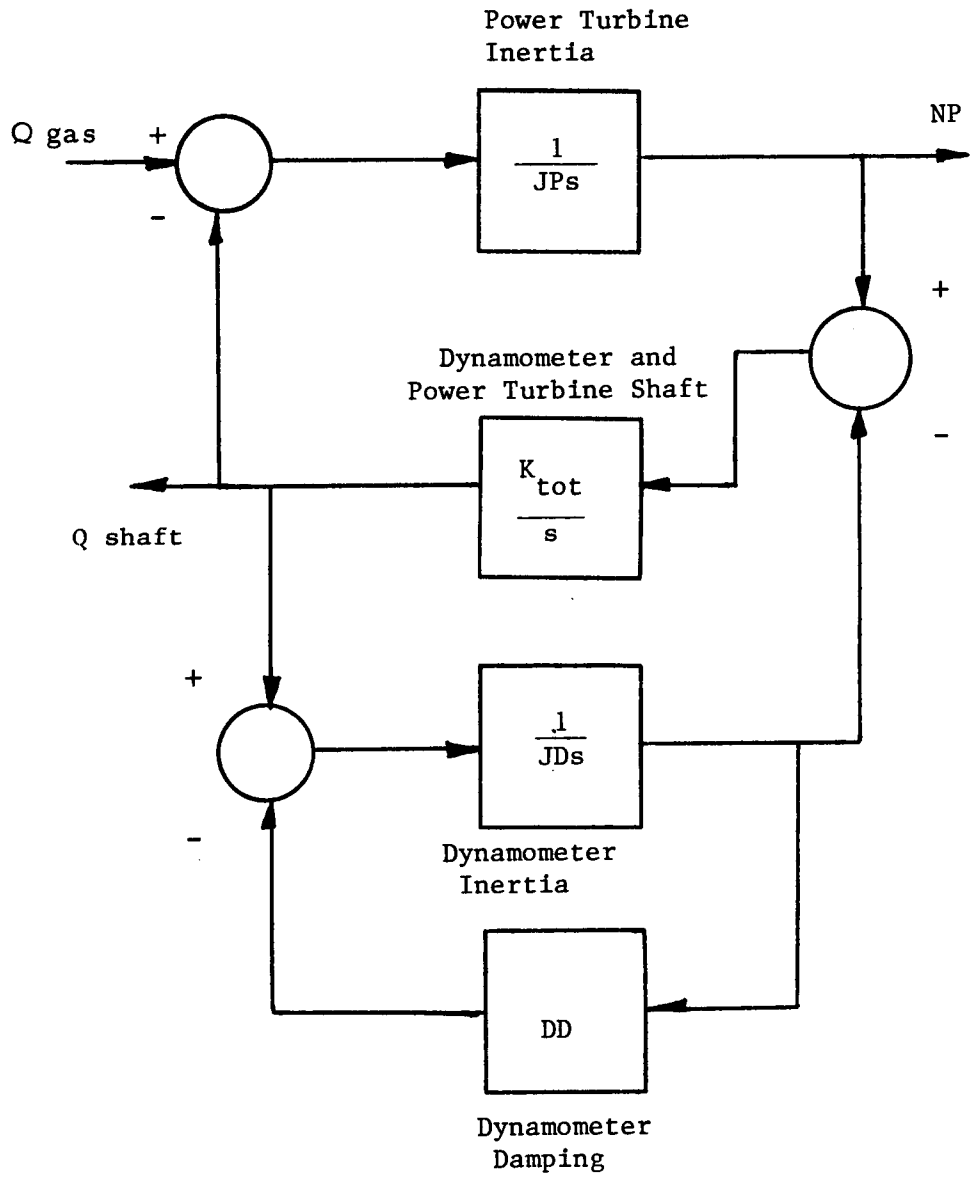


Figure 2.62 Simplified Dynamometer Model.

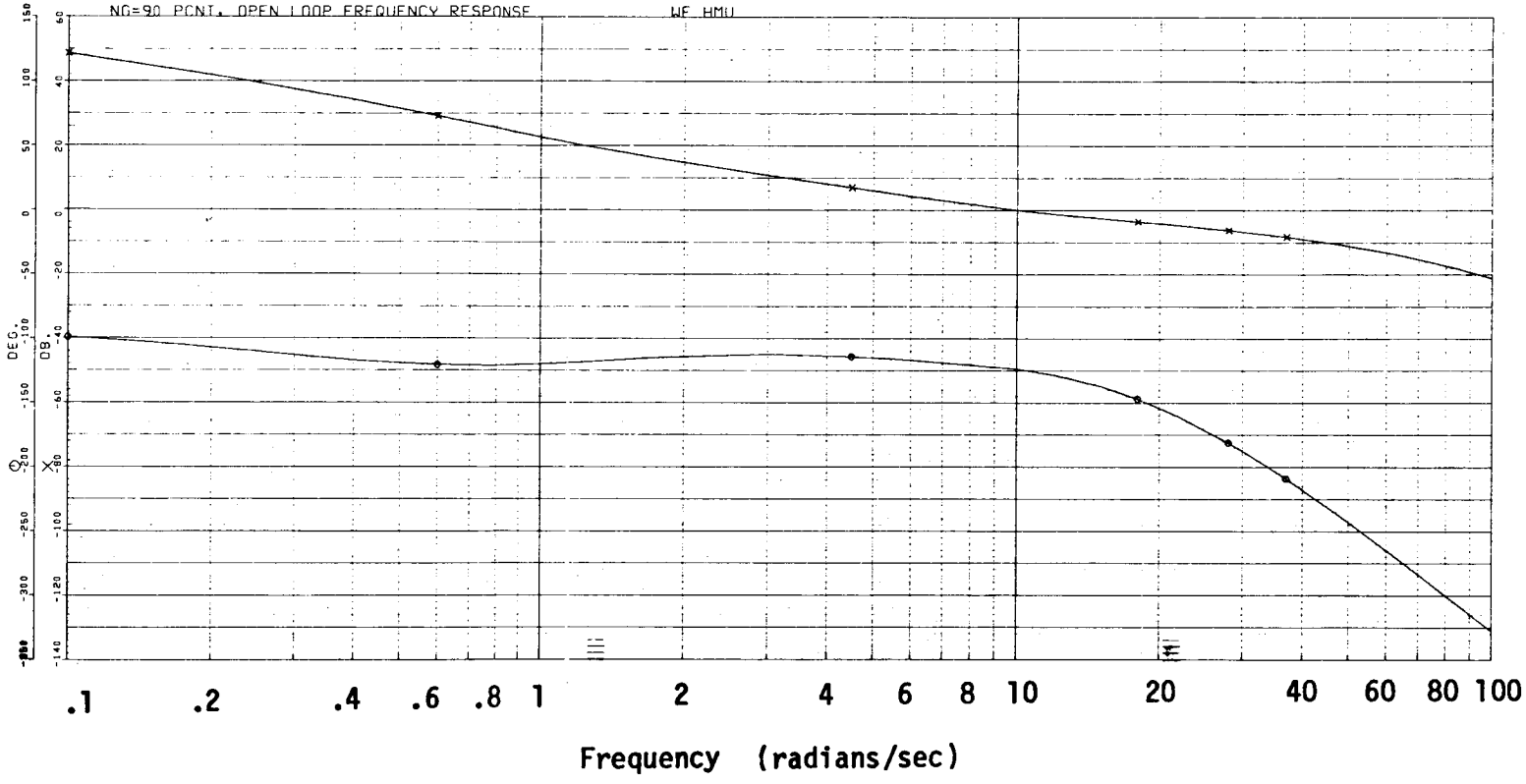


Figure 2.63 Bode Plot of Black Hawk LQR Np Governor with Dynamometer. 60° Phase Lead Added at 5 rad/sec.

Black Hawk compensator at 0.5 rad/sec. The lead compensator for the Black Hawk helicopter rotor system was primarily added to counteract the effect of the heat soak model in the T700 nonlinear DISCUS model. As described in Section 2.3.2.5 the lag contributed by the heat soak model may be excessive. If this is true, it may be possible to use one lead compensator for both the Black Hawk system and the dynamometer system.

### 2.4.1 Results of Dynamometer Simulations

The LQR power turbine governor was analyzed in the time domain using the GE nonlinear DISCUS model of the T700 engine with the dynamometer model. Four collective-pitch-angle transients were simulated for comparison of the LQR governor with the baseline T700 governor. Two of the transients were compensated with the load demand spindle (LDS) as described in Section 2.1.11, and two of the transients were not compensated with LDS.

The load on the engine with the uncompensated controller was changed with collective pitch angle, but the LDS was maintained constant at the starting level. This causes the load on the engine to change with no feed-forward information going to the control. The two compensated transients were an acceleration caused by a 0%-70% collective pitch angle burst in 0.5 sec and a deceleration caused by a 70%-0% collective pitch chop in 0.5 sec. This is a change of about 700 shaft horsepower.

The uncompensated transients were an acceleration caused by a 40%-70% collective pitch angle burst in 0.1 sec and a deceleration caused by a 70%-40% collective pitch angle chop in 0.1 sec. This is a 488 shaft horsepower change. All transients were done with and without the model of the heat sink, since the accuracy of the model is in question. The system was designed, however, as though the heat sink model were accurate because this is the safer approach.

Figures 2.64 and 2.65 show the 0%-70% collective pitch burst compensated with LDS for the LQR and T700 baseline governors, respectively. These simulations do not include the heat sink. Figures 2.66 and 2.67 show the same transient with the heat sink for the LQR and T700 baseline, respectively. The 70%-0% collective pitch chops compensated with LDS with no heat sink model are shown in Figure 2.68 for the LQR and Figure 2.69 for the T700 baseline. The same chop with a heat sink model is shown in Figure 2.70 for the LQR and Figure 2.71 for the T700 baseline.

Figures 2.72 and 2.73 show the 40%-70% collective pitch burst compensated with LDS for the LQR and T700 baseline governors, respectively. These simulations do not include the heat sink. Figures 2.74 and 2.75 show the same transient with the heat sink for the LQR and T700 baseline, respectively. The 70%-40% collective pitch chops compensated with LDS with no heat sink model are shown in Figure 2.76 for the LQR and Figure 2.77 for the T700 baseline. The same

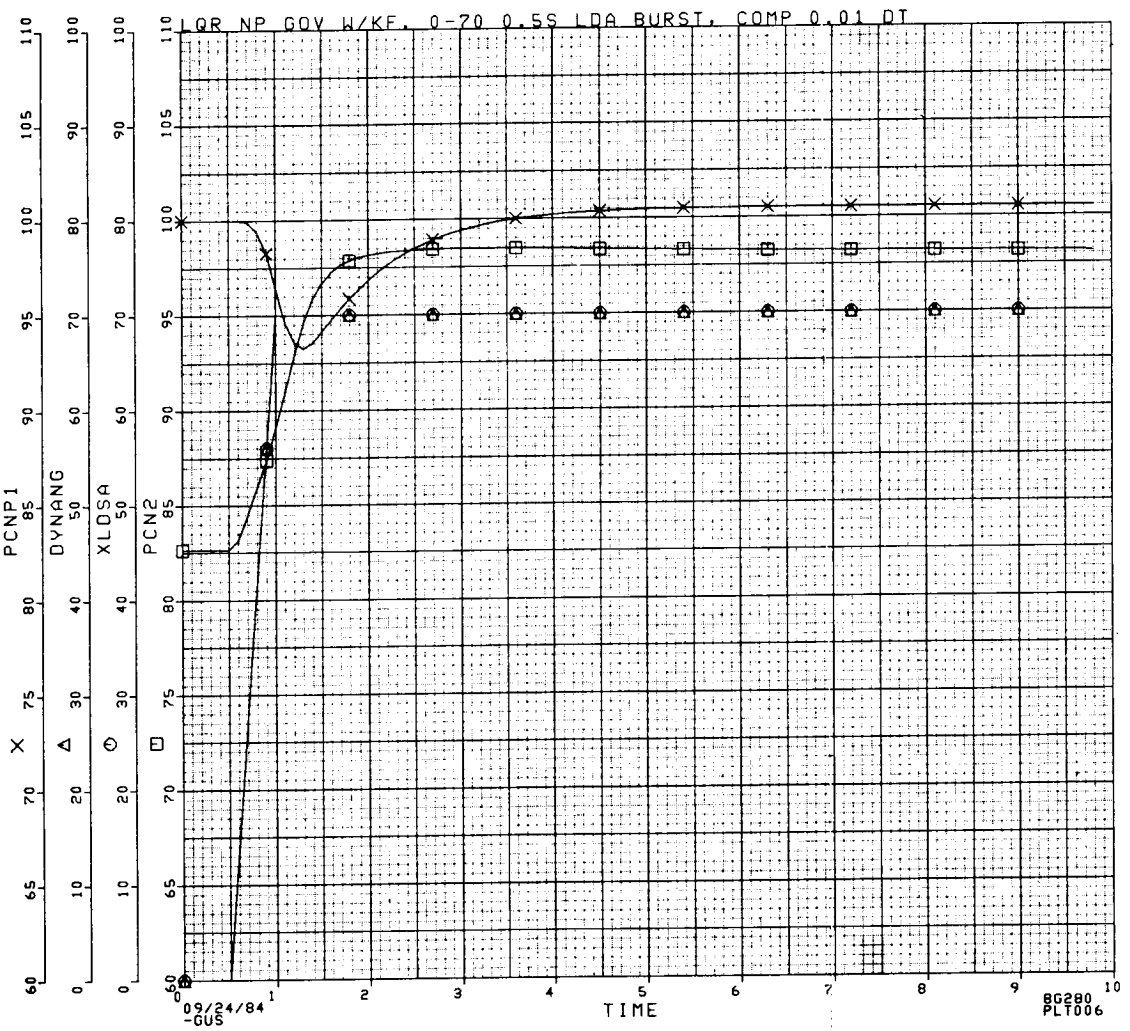


PCNP1: NP (%)
PCN2: NG (%)
XLDSA: Load demand spindle (LDS) anticipation to control
DYNANG: Load demand of dynamometer

Figure 2.64 LQR Np Governor with Dynamometer. 0% - 70% Collective Pitch Burst Compensated with LDS. No Heat Sink Model. 0.5 Sec Transient.

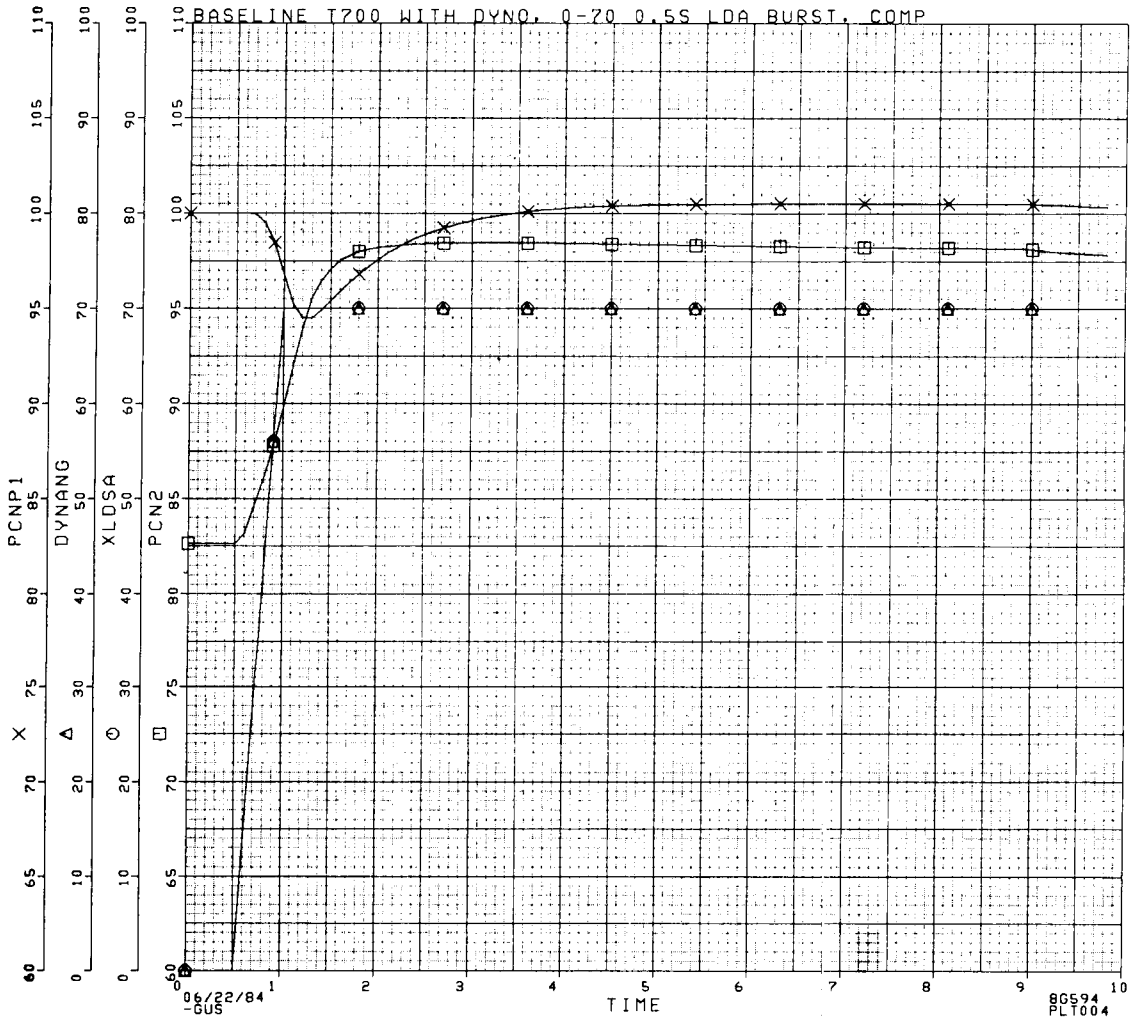


PCNP1: NP (%)
PCN2: NG (%)
XLDSA: Load demand spindle (LDS) anticipation to control
DYNANG: Load demand of dynamometer

Figure 2.65 T700 Baseline Np Governor with Dynamometer. 0% - 70% Collective Pitch Burst Compensated with LDS. No Heat Sink Model. 0.5 Sec Transient.

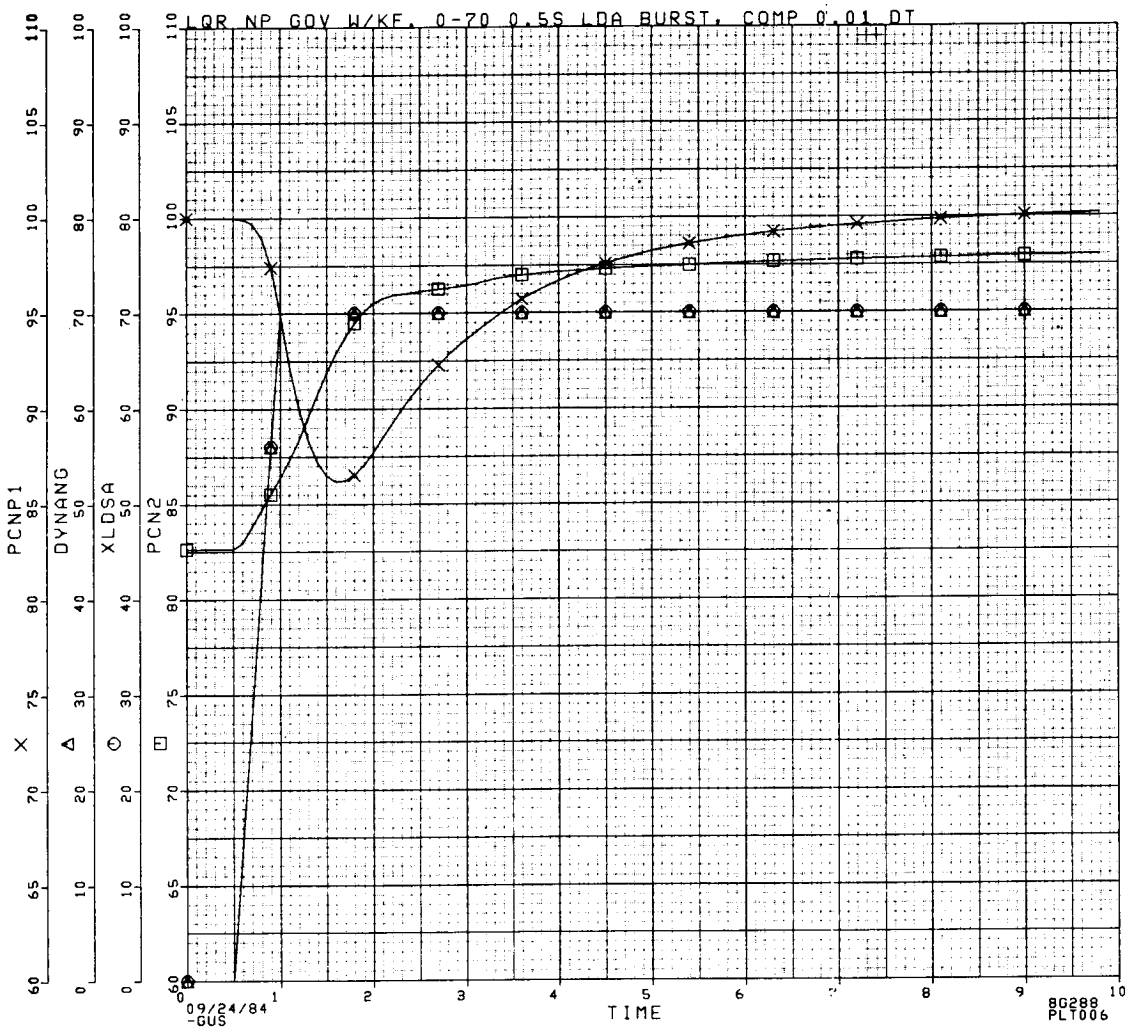


PCNP1: NP (%)
PCN2: NG (%)
XLDSA: Load demand spindle (LDS) anticipation to control
DYNANG: Load demand of dynamometer

Figure 2.66 LQR Np Governor with Dynamometer. 0% - 70% Collective Pitch Burst Compensated with LDS. Heat Sink Included. 0.5 Sec Transient.

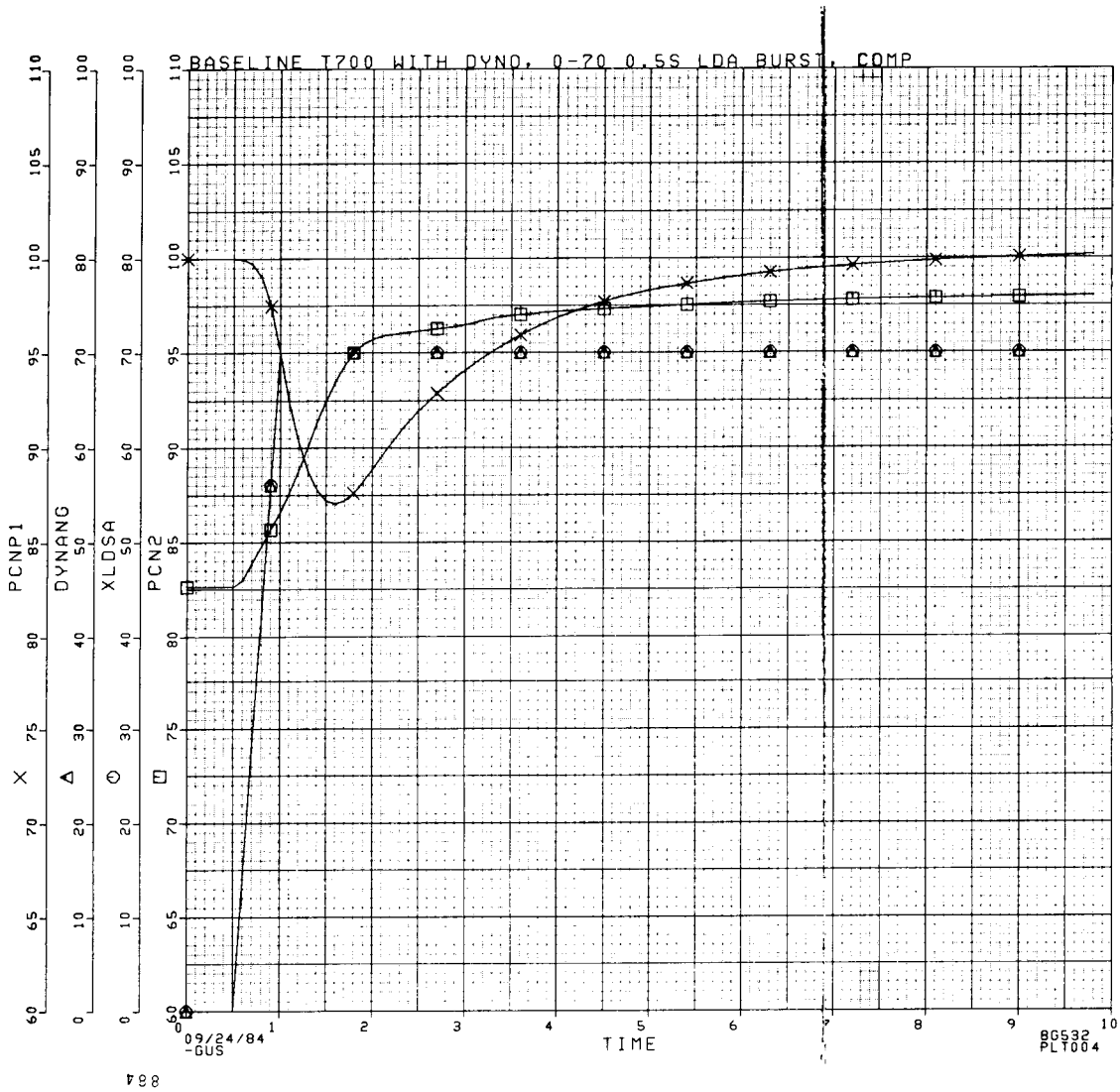


PCNP1: NP (%)
PCN2: NG (%)
XLDSA: Load demand spindle (LDS) anticipation to control
DYNANG: Load demand of dynamometer

Figure 2.67 T700 Baseline Np Governor with Dynamometer. 0% - 70% Collective Pitch Burst Compensated with LDS. Heat Sink Included. 0.5 Sec Transient.

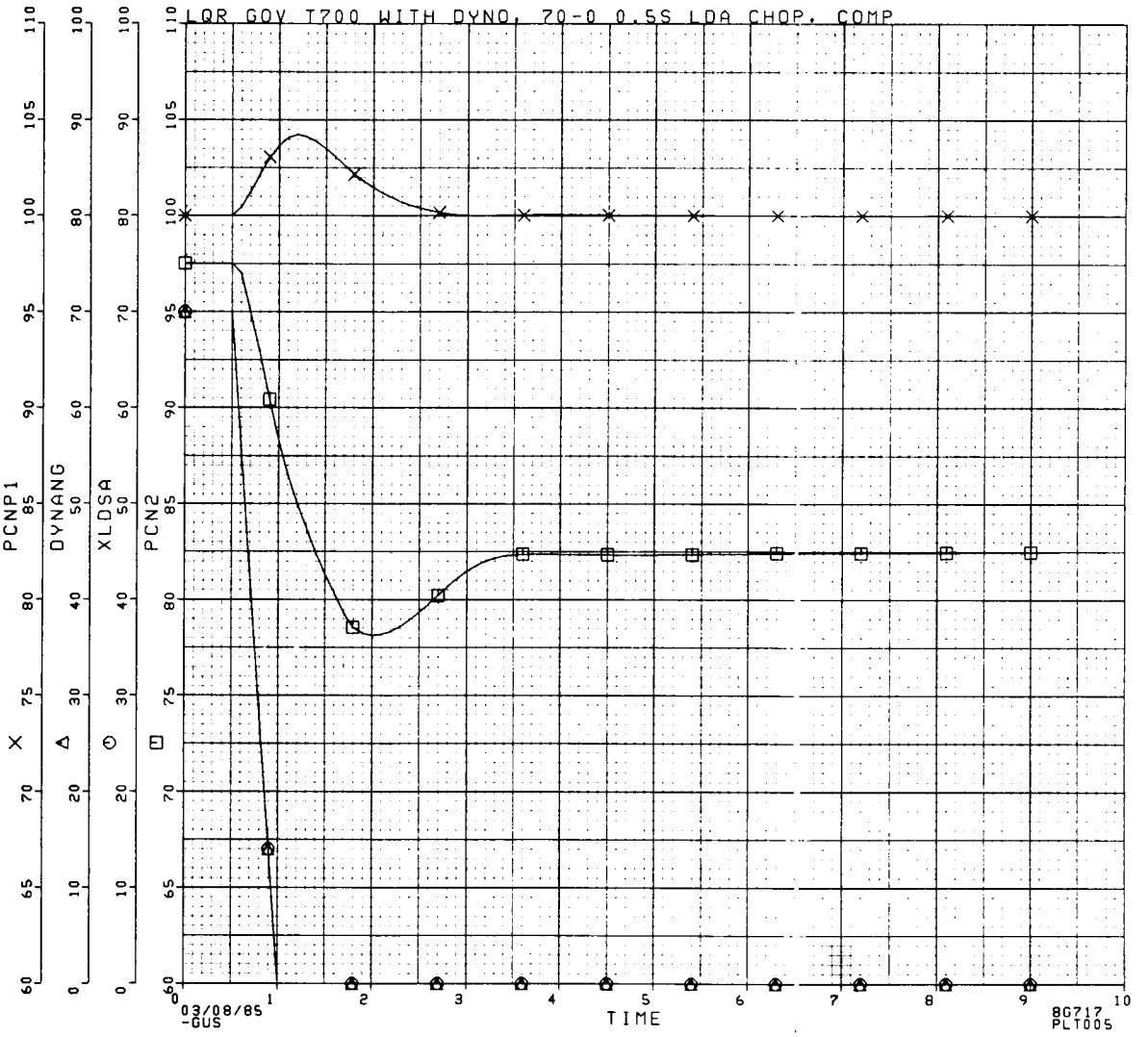


PCNP1: NP (%)
PCN2: NG (%)
XLDSA: Load demand spindle (LDS) anticipation to control
DYNANG: Load demand of dynamometer

Figure 2.68 LQR Np Governor with Dynamometer. 70% - 0% Collective Pitch Chop Compensated with LDS. No Heat Sink Model. 0.5 Sec Transient.

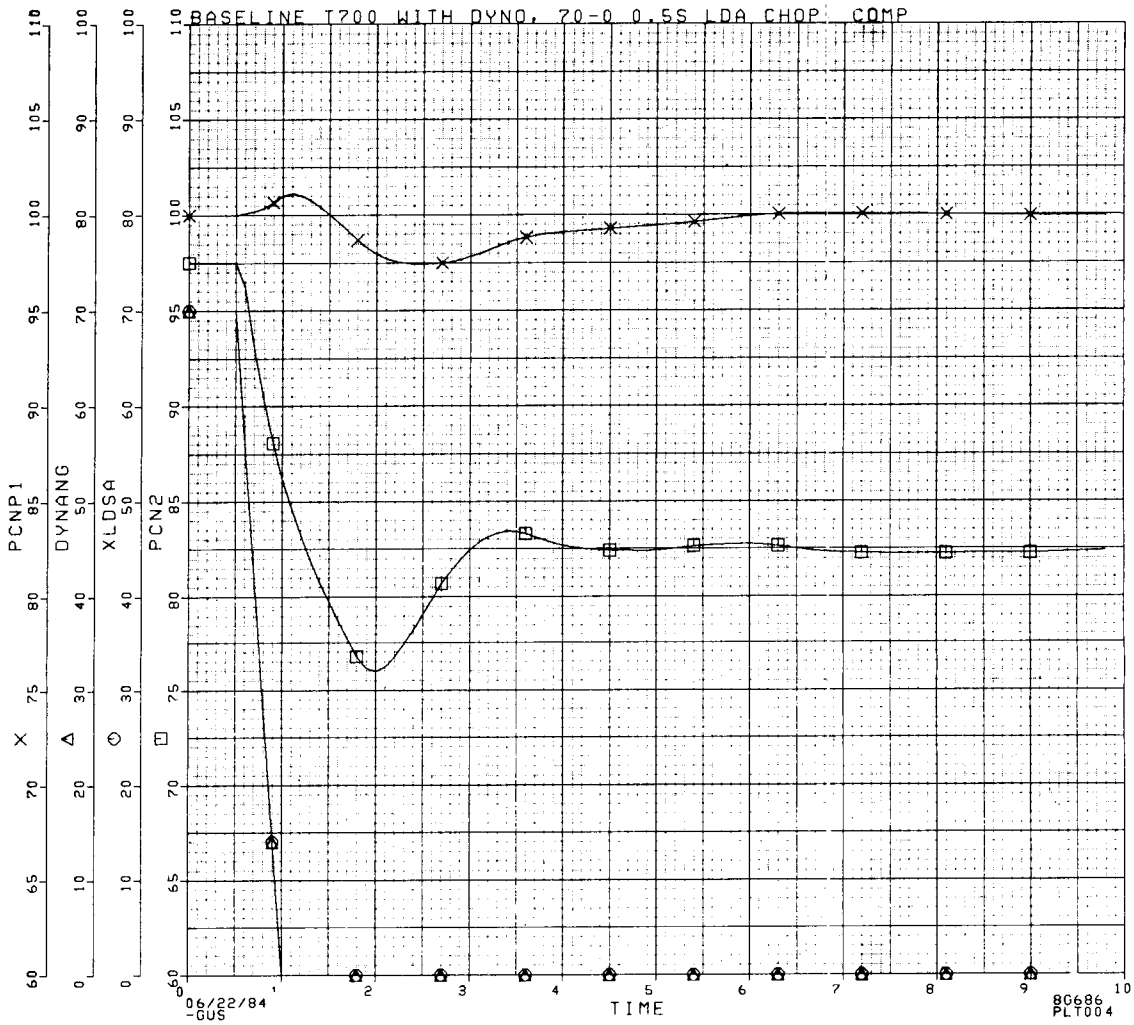


PCNP1: NP (%)
PCN2: NG (%)
XLDSA: Load demand spindle (LDS) anticipation to control
DYNANG: Load demand of dynamometer

Figure 2.69 T700 Baseline Np Governor with Dynamometer. 70% - 0% Collective Pitch Chop Compensated with LDS. No Heat Sink Model. 0.5 Sec Transient.

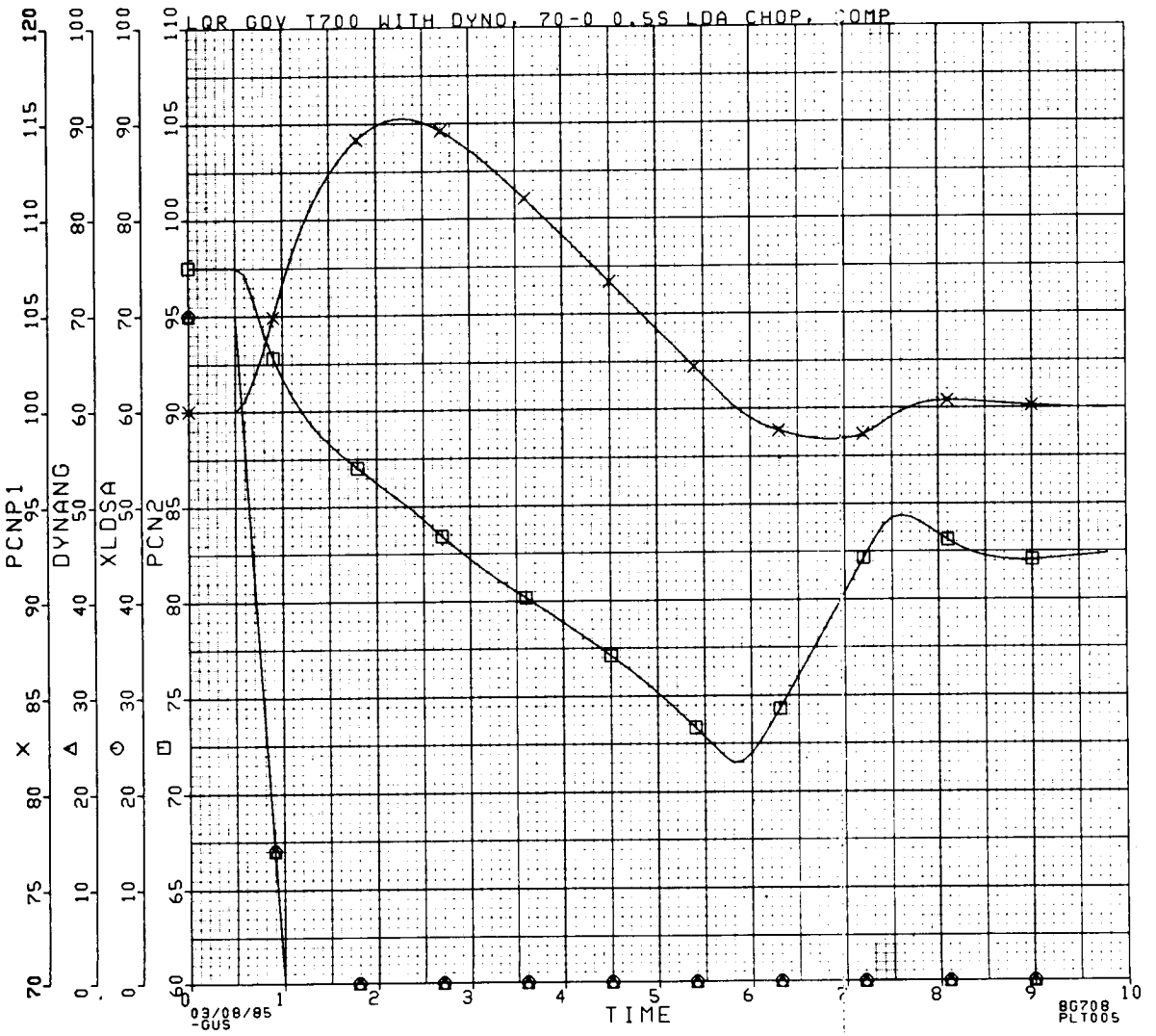


PCNP1: NP (%)
PCN2: NG (%)
XLDSA: Load demand spindle (LDS) anticipation to control
DYNANG: Load demand of dynamometer

Figure 2.70 LQR Np Governor with Dynamometer. 70% - 0% Collective Pitch Chop Compensated with LDS. Heat Sink Included. 0.5 Sec Transient.

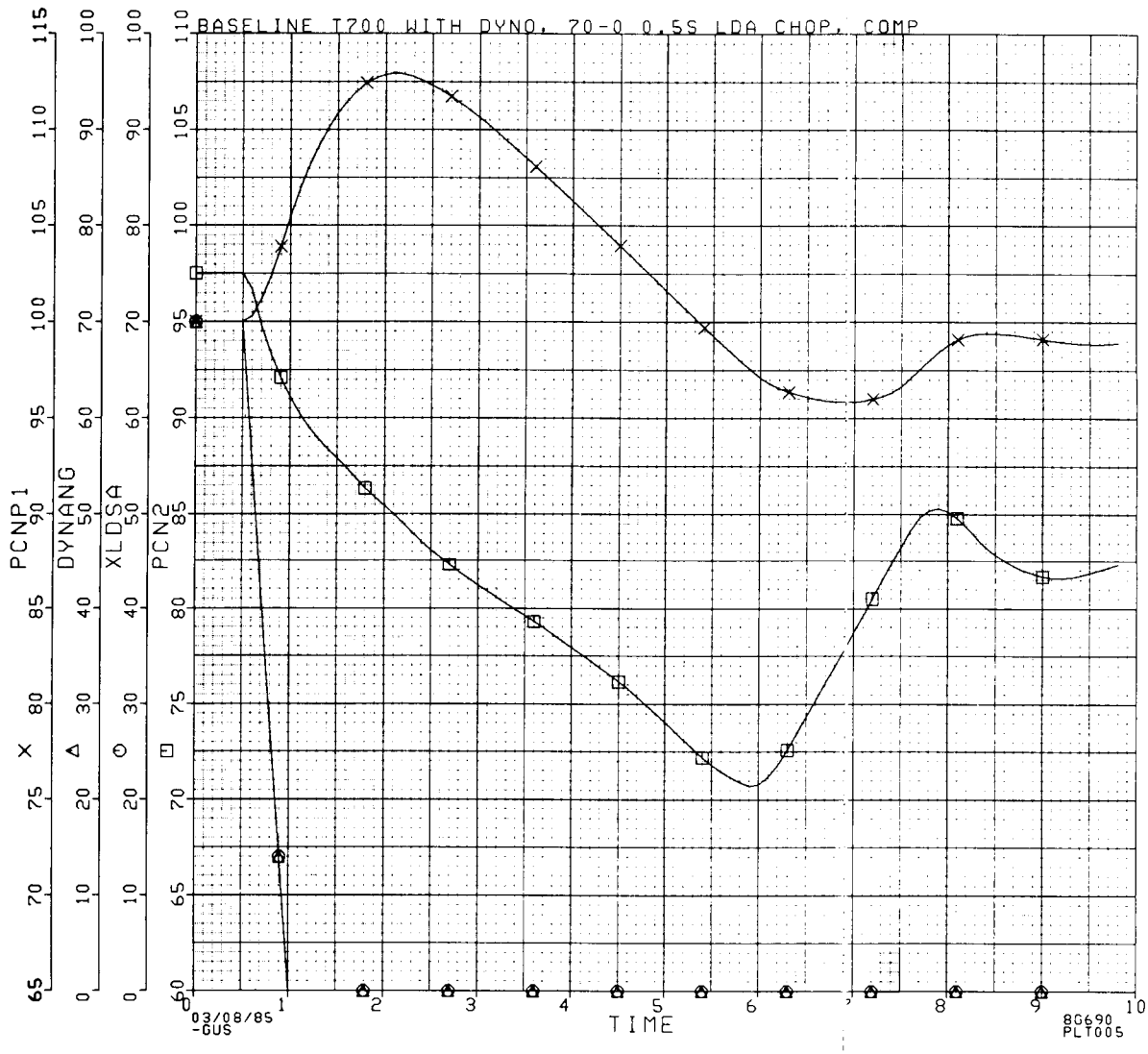


PCNP1: NP (%)
PCN2: NG (%)
XLDSA: Load demand spindle (LDS) anticipation to control
DYNANG: Load demand of dynamometer

Figure 2.71 T700 Baseline Np Governor with Dynamometer. 70% - 0% Collective Pitch Chop Compensated with LDS. Heat Sink Included. 0.5 Sec Transient.

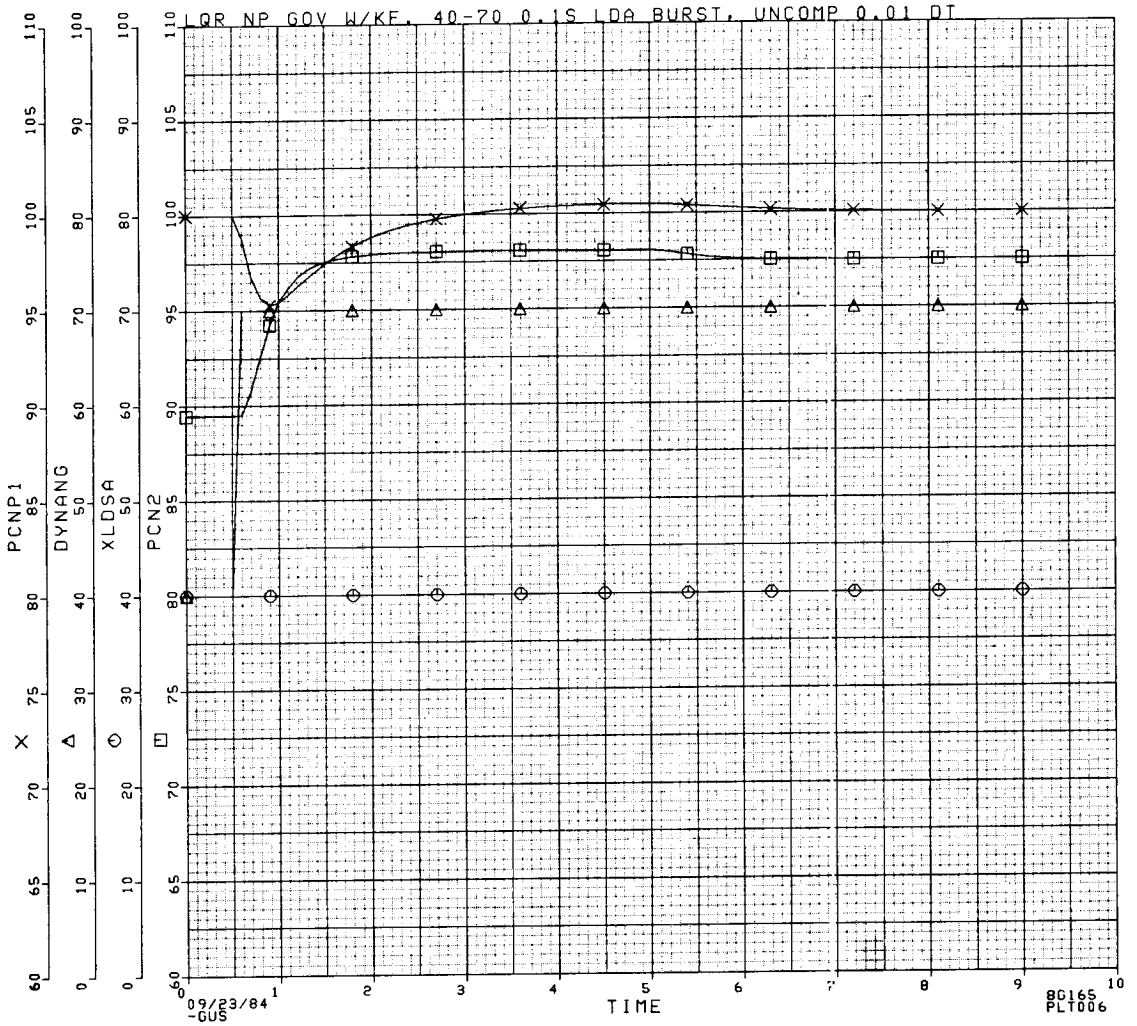


PCNP1: NP (%)
PCN2: NG (%)
XLDSA: Load demand spindle (LDS) anticipation to control
DYNANG: Load demand of dynamometer

Figure 2.72 LQR Np Governor with Dynamometer. 40% - 70% Collective Pitch Burst not Compensated with LDS. No Heat Sink Model. 0.1 Sec Transient.

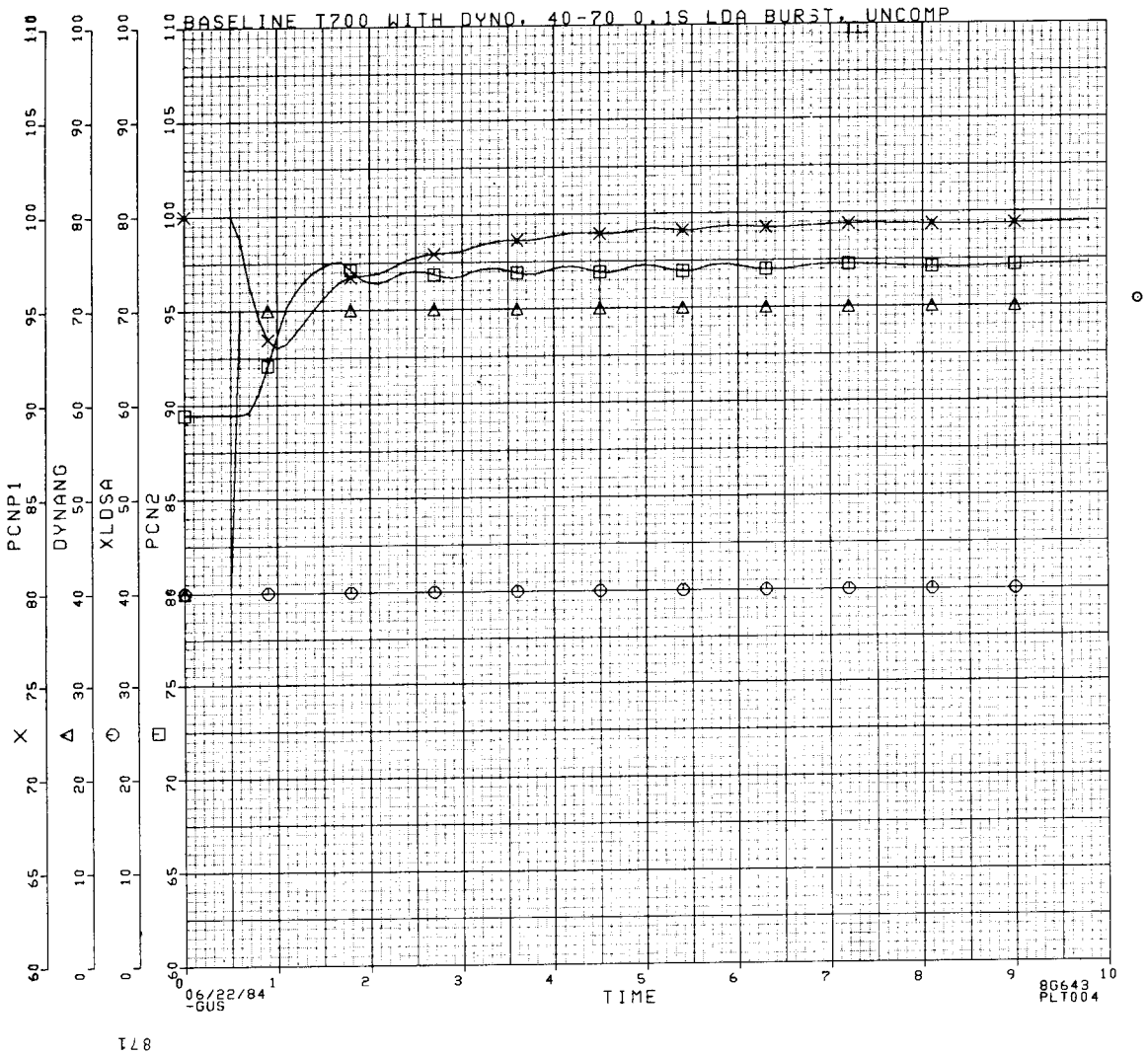


PCNP1: NP (%)
PCN2: NG (%)
XLDSA: Load demand spindle (LDS) anticipation to control
DYNANG: Load demand of dynamometer

Figure 2.73 T700 Baseline Np Governor with Dynamometer. 40% - 70% Collective Pitch Burst not Compensated with LDS. No Heat Sink Model. 0.1 Sec Transient.

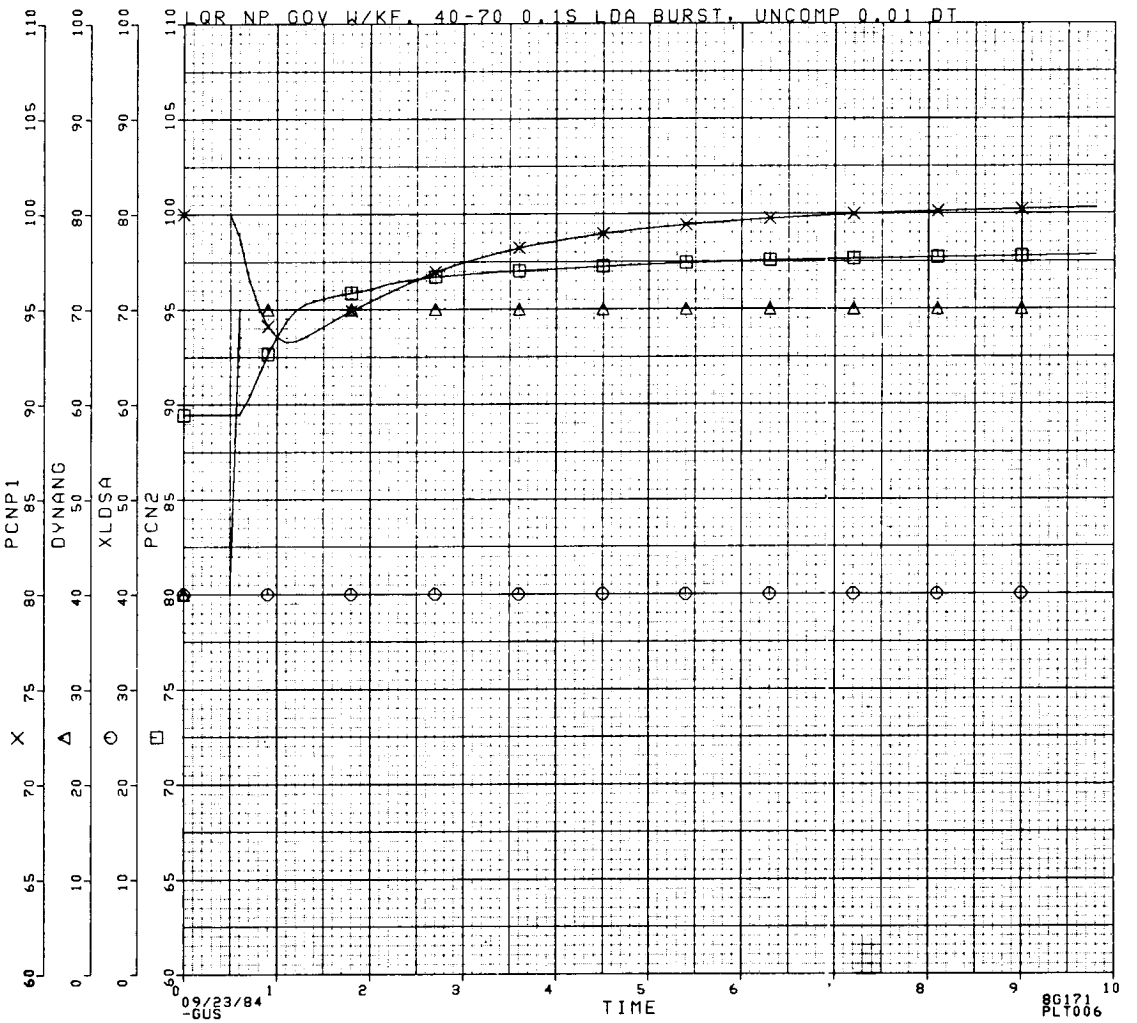


PCNP1: NP (%)
PCN2: NG (%)
XLDSA: Load demand spindle (LDS) anticipation to control
DYNANG: Load demand of dynamometer

Figure 2.74 LQR Np Governor with Dynamometer. 40% - 70% Collective Pitch Burst not Compensated with LDS. Heat Sink Included. 0.1 Sec Transient.

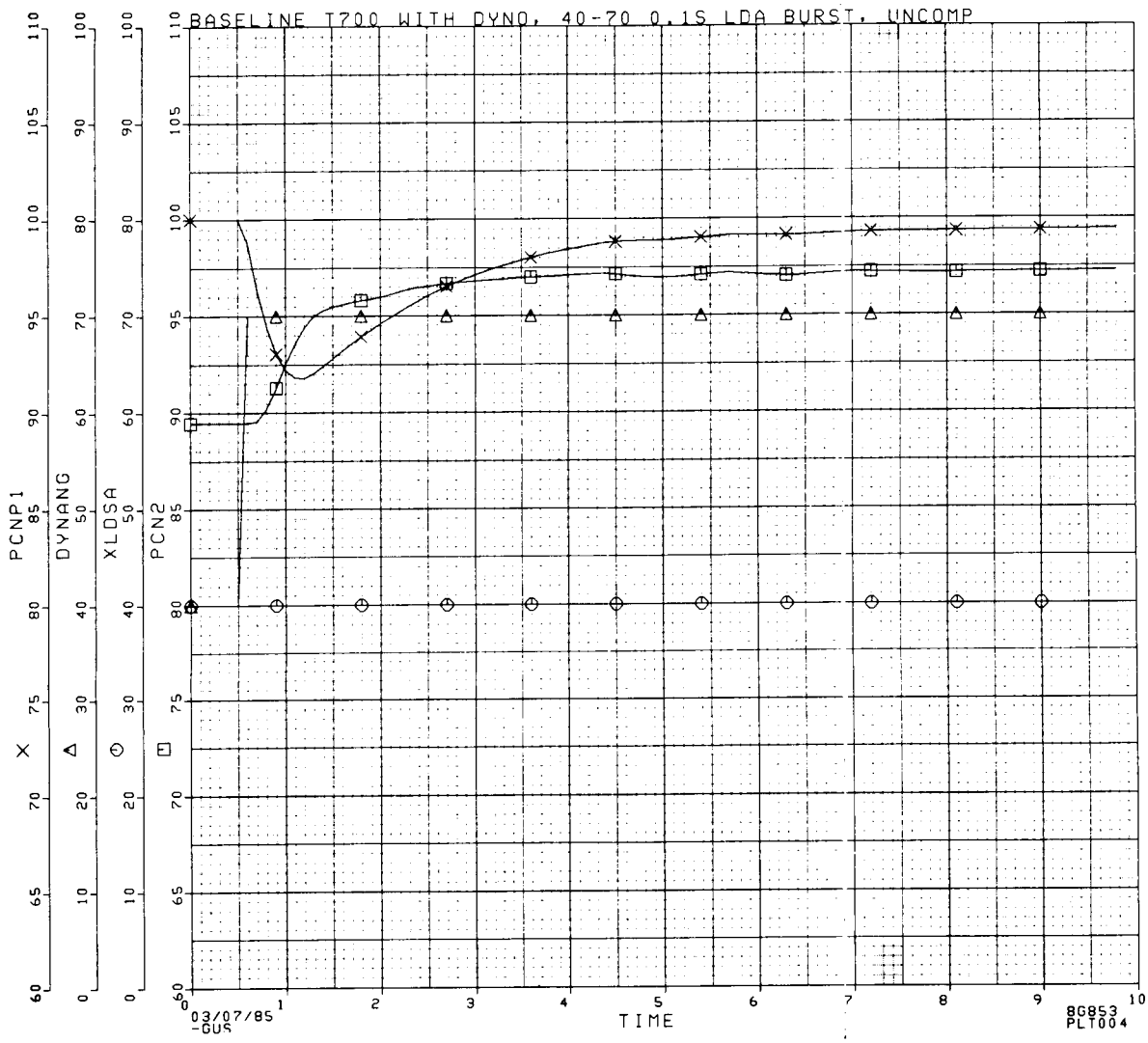


PCNP1: NP (%)
PCN2: NG (%)
XLDSA: Load demand spindle (LDS) anticipation to control
DYNANG: Load demand of dynamometer

Figure 2.75 T700 Baseline Np Governor with Dynamometer. 40% - 70% Collective Pitch Burst not Compensated with LDS. Heat Sink Included. 0.1 Sec Transient.

ORIGINAL PAGE IS
OF POOR QUALITY

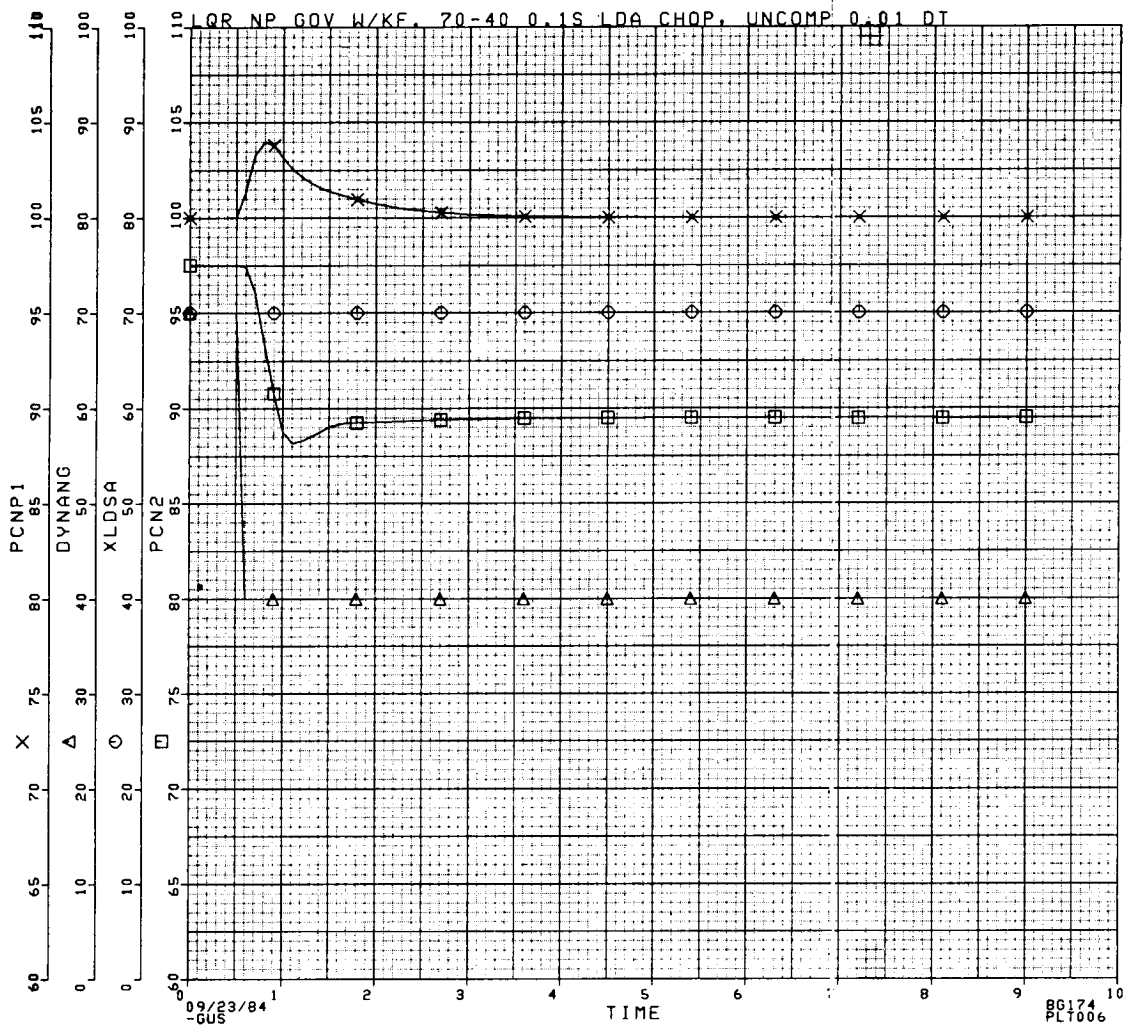


PCNP1: NP (%)
PCN2: NG (%)
XLDSA: Load demand spindle (LDS) anticipation to control
DYNANG: Load demand of dynamometer

Figure 2.76 LQR Np Governor with Dynamometer. 70% - 40% Collective Pitch Chop not Compensated with LDS. No Heat Sink Model. 0.1 Sec Transient.

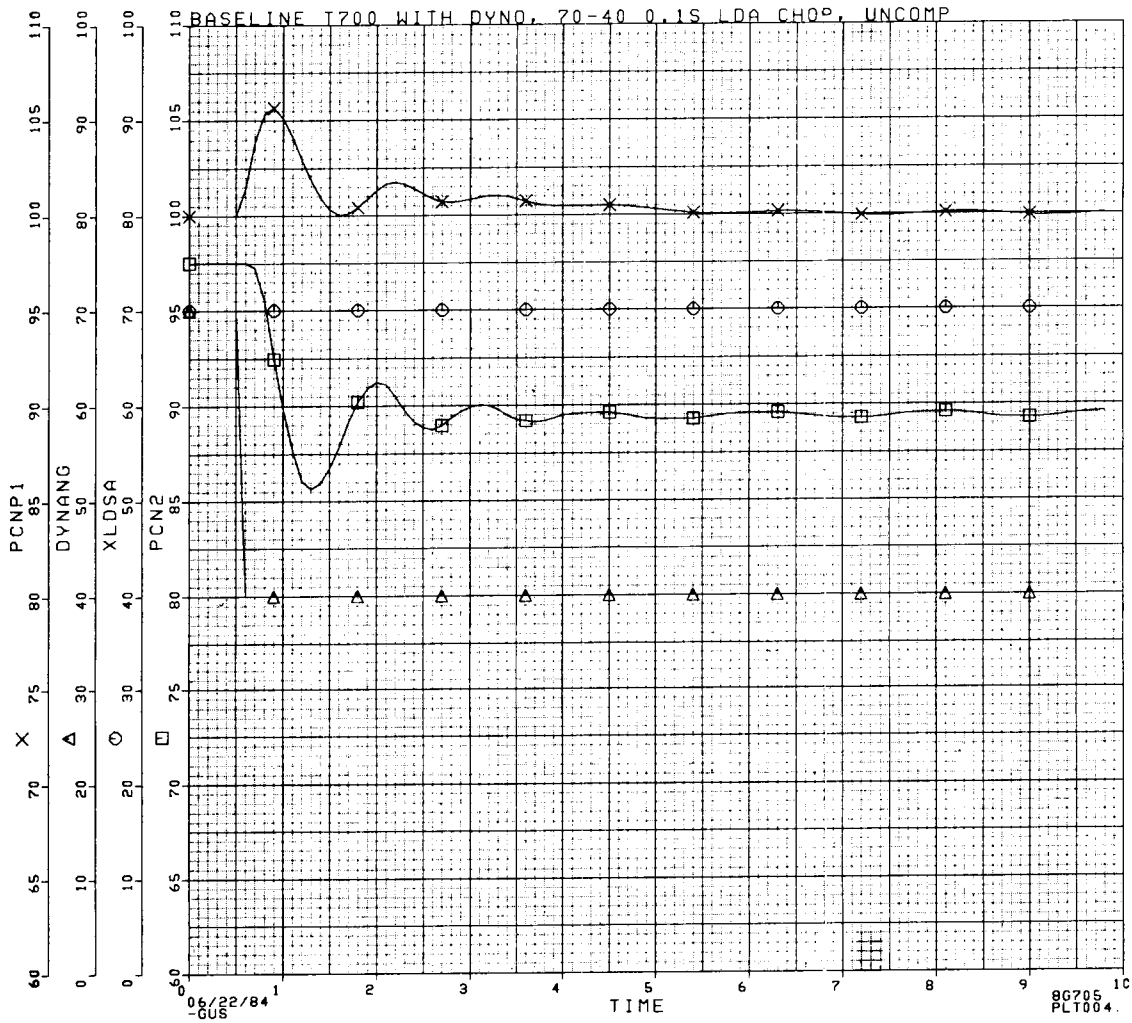


PCNP1: NP (%)
PCN2: NG (%)
XLDSA: Load demand spindle (LDS) anticipation to control
DYNANG: Load demand of dynamometer

Figure 2.77 T700 Baseline Np Governor with Dynamometer. 70% - 40% Collective Pitch Chop not Compensated with LDS. No Heat Sink Model. 0.1 Sec Transient.

chop with a heat sink model is shown in Figure 2.78 for the LQR and Figure 2.79 for the T700 baseline. Table 2.2 Summarizes the above results.

The performance of the LQR power turbine governor with the dynamometer is not consistently better than the T700 baseline system with the dynamometer. This is not unexpected since the governor was designed for use with a Black Hawk rotor system and not for use with a dynamometer.

Table 2.2. Comparison of Droop and Overshoot of T700 Baseline and LQR Np Governors with Dynamometer

| Event | Droop (-) or Overshoot (+) | |
|---|---|---|
| | T700 Baseline | LQR |
| 1. 40% - 70% beta*, uncompensated,** 0.1 sec | | |
| - with no heat sink | -6.96% | -4.73% |
| - with heat sink | -8.21% | -6.71% |
| 2. 70% - 40% beta, uncompensated, 0.1 sec | | |
| - with no heat sink | +5.66% | +3.98% |
| - with heat sink | +7.34% | +6.01% |
| 3. 0% - 70% beta, compensated**, 0.5 sec | | |
| - with no heat sink | -5.51% | -5.75% |
| - with heat sink | -12.96% | -13.82% |
| 4. 70% - 0% beta, compensated, 0.5 sec | | |
| - with no heat sink | +1.14%/-2.57% | +4.24% |
| - with heat sink | +12.93% | +15.28% |

* beta is collective pitch angle
** compensated or uncompensated with LDS

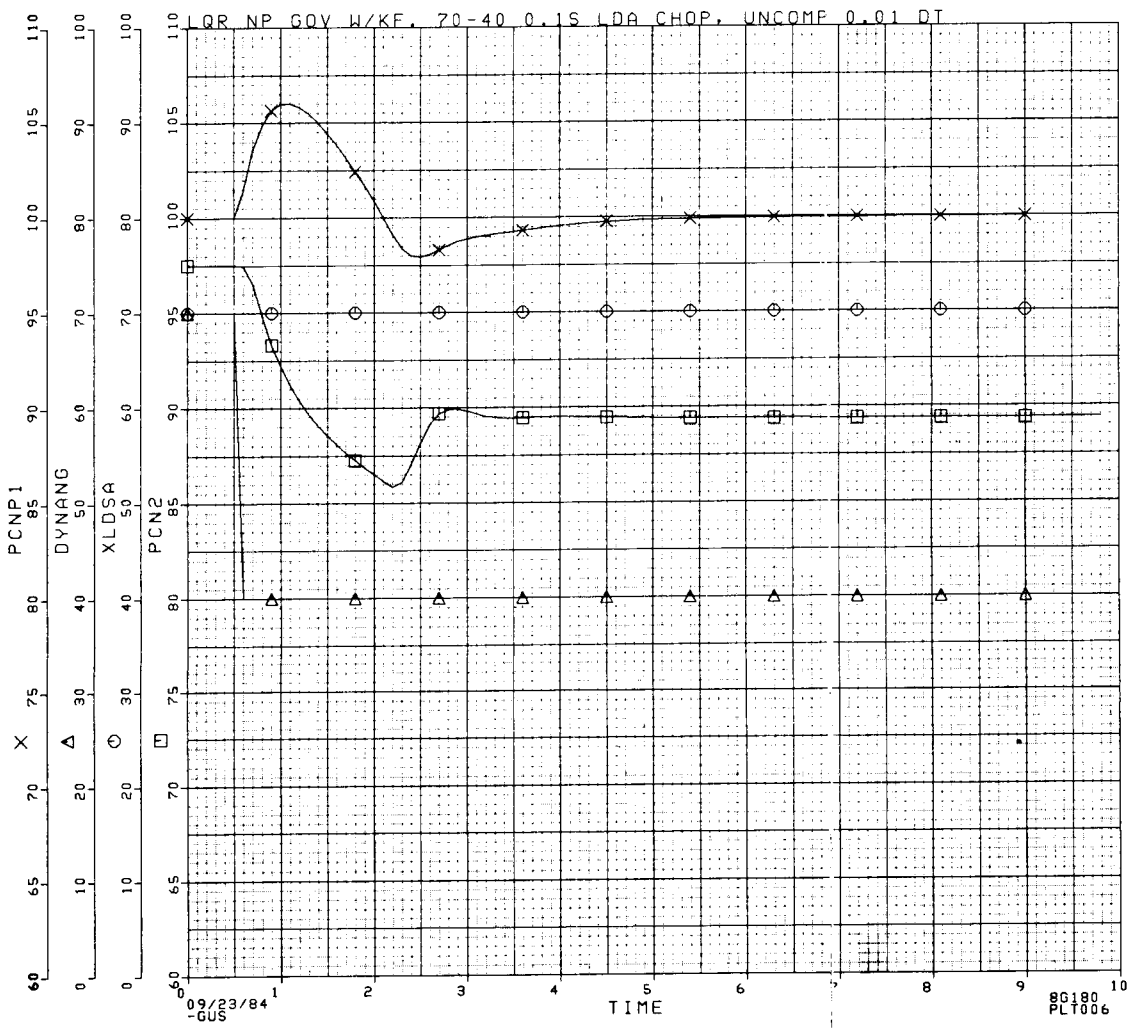


PCNP1: NP (%)
PCN2: NG (%)
XLDSA: Load demand spindle (LDS) anticipation to control
DYNANG: Load demand of dynamometer

Figure 2.78 LQR Np Governor with Dynamometer. 70% - 40% Collective Pitch Chop not Compensated with LDS. Heat Sink Included. 0.1 Sec Transient.

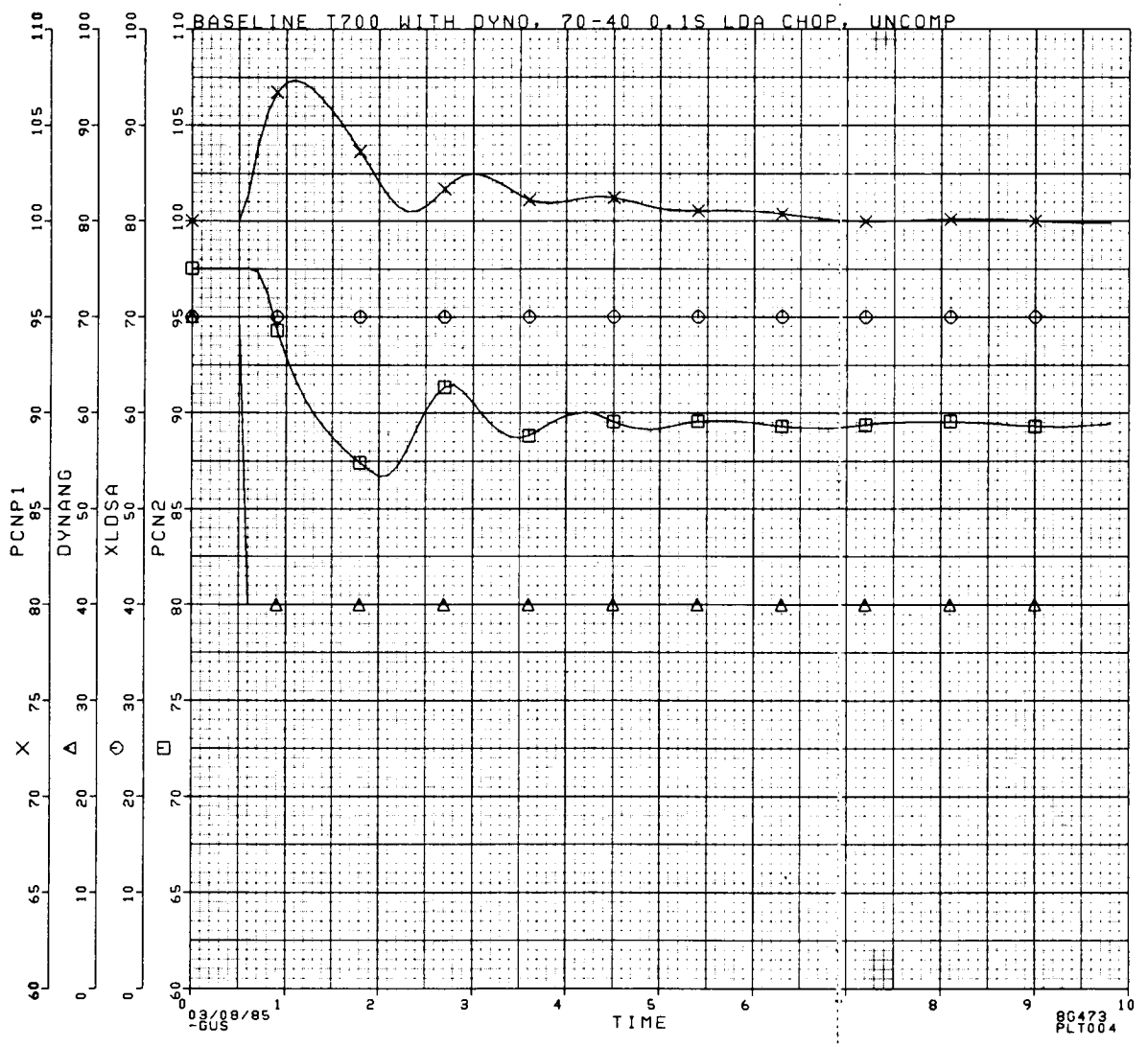


PCNP1: NP (%)
PCN2: NG (%)
XLDSA: Load demand spindle (LDS) anticipation to control
DYNANG: Load demand of dynamometer

Figure 2.79 T700 Baseline Np Governor with Dynamometer. 70% - 40% Collective Pitch Chop not Compensated with LDS. Heat Sink Included. 0.1 Sec Transient.

## 2.5 Use of Variable Geometry and Fuel Flow to Control Np

The simultaneous use of compressor variable geometry, VG, and fuel flow, WF, to control power turbine speed, NP, was researched to determine any performance improvements over the use of WF alone to control NP. A block diagram of this system is shown in Figure 2.1. This system is a multi-input-multi-output (MIMO) system with WF and VG as inputs and NP and VG as outputs. Because of the multiple inputs, standard Bode plot analysis is not strictly valid although singular value techniques may be used. These techniques are detailed in Ref. 15, and a brief synopsis of their use is given below.

### 2.5.1 Singular Values

For a MIMO system, each output is in general affected by every input, and conversely each input generally affects every output. Only for a decoupled system does one input affect one and only one output. Because of the coupling, gain and phase margin criteria from Bode techniques cannot be used for MIMO systems with the confidence of "guaranteed" stability that they imply for single-input-single-output (SISO) systems. Singular value techniques combined with the LQR method provide the engineer with powerful design and analysis tools for MIMO systems. This section discusses some of these methods.

Singular values will not be defined, but their properties and use will be explained. Singular value plots are analogous to the magnitude plot of a standard Bode plot. The magnitude curve of a Bode plot for a SISO system is identical to the singular value plot of the system. The Bode magnitude plot gives the amount of amplification or attenuation that an output exhibits for a sinusoidal input at a given frequency. Singular value plots also show the amplification and attenuation of the output for a given input, except now the inputs and outputs are vectors. The input and output vectors have as elements the individual inputs and outputs, respectively. This can be visualized for a two-input, two-output system as shown in Figure 2.80. The vectors directions $\gamma$ and $\psi$ are defined by the ratio of the elements. For a MIMO system, the input-output relationship is given by:

$$\underline{Y}(s) = \underline{H}(s)\,\underline{U}(s)$$

where $\underline{Y}(s)$ is the Laplace transform of each element of the output vector, $\underline{U}(s)$ is the Laplace transform of each element of the input vector, and $\underline{H}(s)$ is the plant transfer function matrix in s relating each output to each input. $\underline{H}(s)$ is a transformation or mapping of $\underline{U}(s)$ into $\underline{Y}(s)$, and the maximum and minimum singular value curves quantify the maximum and minimum amplification, respectively, of the input vector by the system described by $H(s)$. This is shown schematically in Figure 2.81. Direction of the vector is not preserved in this transformation. For a SISO system, there is only one singular value curve versus frequency, and it is the same as the magnitude of the Bode plot.

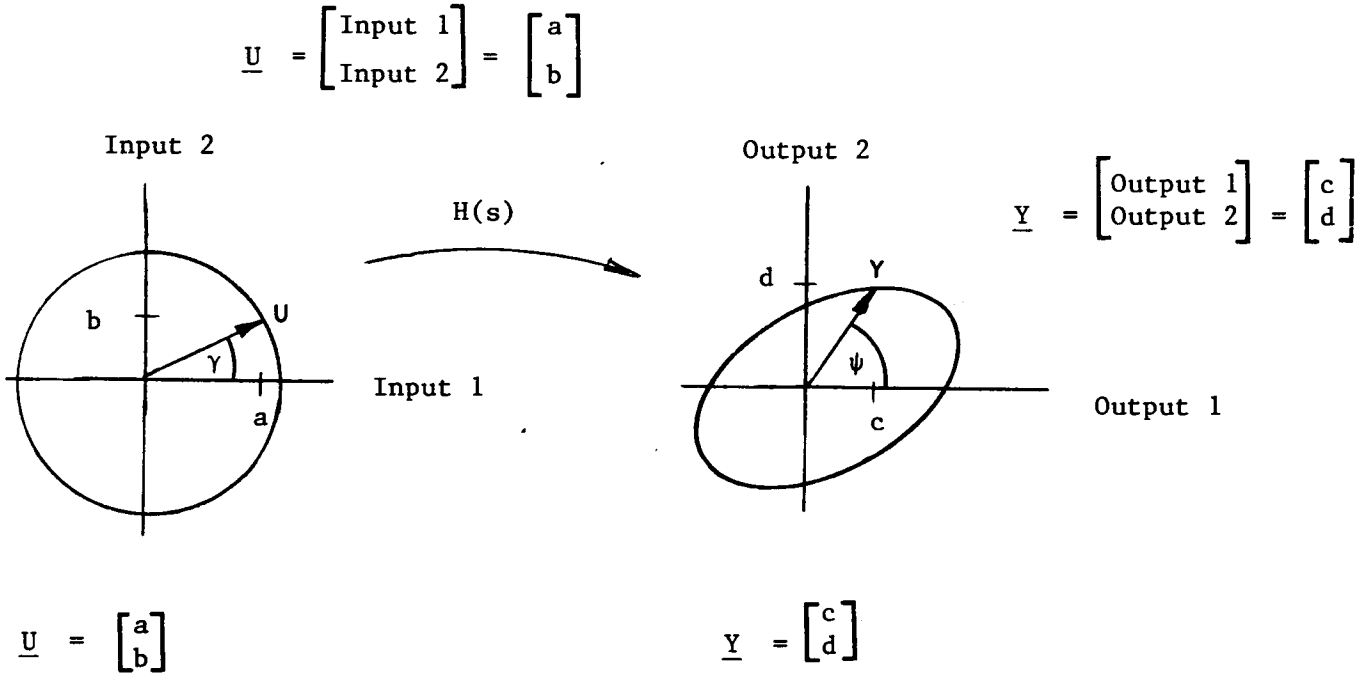


Figure 2.80 Definition of Input and Output Vector Angles (Directions) for a Two-Input, Two-Output System.

Figure 2.81 Schematic Showing a Mapping of the Input Vector Through the Transfer Function Matrix.

For a system designed using the LQR method, 60° phase margin and -6dB, + $\infty$ gain margin are guaranteed. The gain change or the phase change can occur in each loop separately or all loops simultaneously and the system will remain stable. There is no guarantee, however, if the gain and phase changes occur simultaneously. This is consistent with single-input-single-output gain and phase margin definitions. The singular value (magnitude) plot can be used to design for performance since stability is "guaranteed." The desirable loop shapes for singular value plots are similar to those for the Bode magnitude plot: high loop gain at low frequencies for good command following, and disturbance rejection at those frequencies, a sufficiently-high crossover frequency for adequate speed of response, and sufficient attenuation at high frequency for noise filtering. A crossover rate of about -20dB/decade is guaranteed by the LQR method and is implied by the stability margins. The only additional requirement when there are two magnitude curves on one plot is that the minimum curve should be large where amplification is desirable, and the maximum curve should be small where attenuation is desired. A typical singular value plot is shown in Figure 2.82a.

A design using VG and WF as inputs and NP and VG as outputs showed that the best performance by frequency response specifications occurred when the minimum and maximum singular values converged to one. This plot is shown in Figure 2.82b. [This is not the same as a SISO system that only have one singular value curve. The above system has two curves that are equal.] Since the two curves are the same, the amplification is the same for any ratio of WF and VG inputs as long as the magnitude of the vector is constant. This is equivalent to saying that the amplification is independent of input vector direction. This implies that choosing on input vector consisting of a certain WF with a VG magnitude of zero gives the same performance as a vector with any other combination of Wf and VG inputs. Since this is so, WF alone can be used to get good performance, and VG does not improve performance. Therefore, the variable geometry was discarded as a method of improving NP governing. VG is scheduled open-loop as a function of corrected gas generator speed as is done in the baseline T700 control.

## 2.6 Sequence of Parameter Sampling

The Kalman Filter algorithm, as programmed, estimates the helicopter main rotor angular velocity, NMR, one sampling period ahead of the measurements that it uses for the computations. Because of this, the parameters should be sampled just before or just after the new fuel flow level has been output to the engine, that is, before the parameters have been affected significantly by the new WF level. The value of estimated main rotor angular velocity that is to be used in the computation of WF should not be the newly computed value based on the new measurements, but rather, the previously computed value.

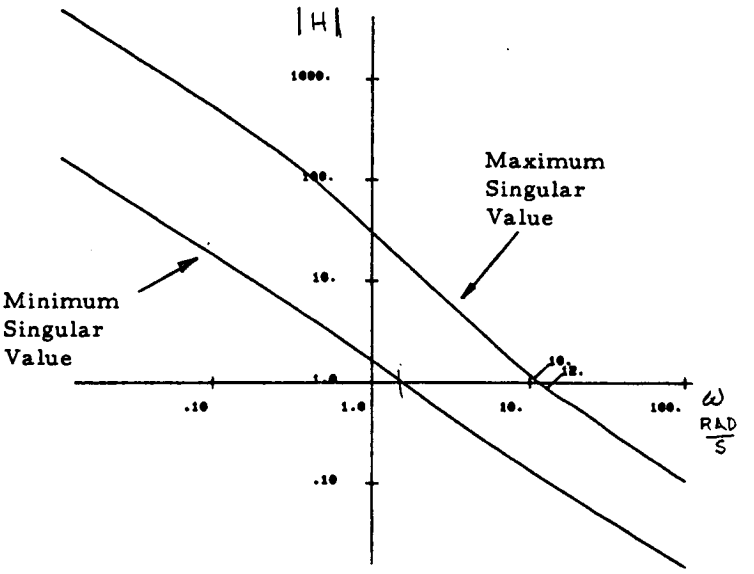


Figure 2.82a Typical Singular Value Plot for a Two-Input, Two-Output System with Integral Augmentation.

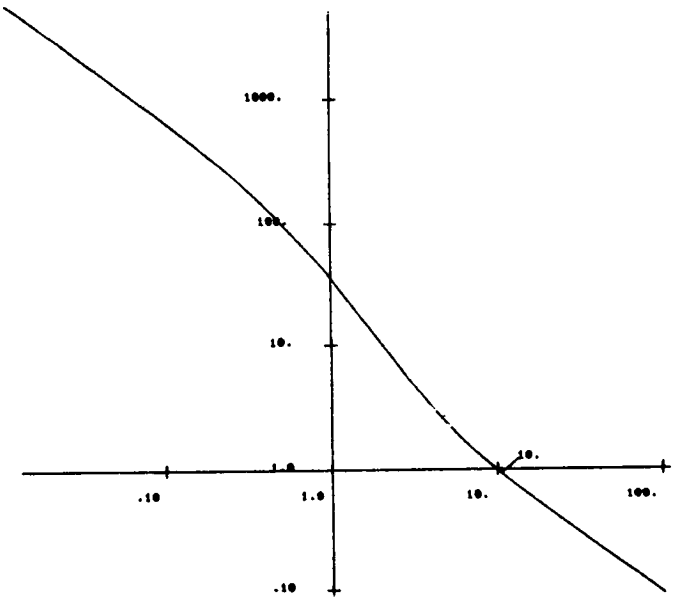


Figure 2.82b Singular Value Plot for VG-Input Analysis.

## 2.7 Effect on Rotor Droop of Deviations from the Design Model

The LQR power turbine governor was first designed for an ideal system where helicopted main-rotor blade velocity and torque states were measured, HMU dynamics were neglected, antialias filters were excluded, and the heat sink model was excluded. As the design progressed, the deviations from the ideal were taken into account as described in Section 2.3.2. The effect on rotor droop of each of these deviations in summarized in Table 2.3. The transient used for comparison was a 40% - 70%, 0.1 sec burst not compensated with LDS.

Table 2.3. Effect on Droop of Approximations to the Ideal Model

| Case: | | Peak Droop |
|---|---|---|
| Ideal Case: | | |
| (1) | Actual NMR<br>Actual QMR<br>No HMU dynamics<br>No heat sink model<br>No lead compensation<br>No anti- alias filters | 0.73% |
| Changes: | | |
| (2) | Shaft torque used to approximate QMR | 0.98% |
| (3) | KF used to estimate NMR | 1.15% |
| (4) | Shaft torque and estimated NMR | 1.56% |
| (5) | Shat torque, estimated NMR, and antialias filters | 1.44% |
| (6) | Shaft torque, estimated NMR, antialias filters, and HMU dynamics | 1.33% |
| (7) | Shaft, torque, estimated NMR, antialias filters, HMU dynamics, and lead compensator | 1.62% |
| (8) | Shaft torque, estimated NMR, antialias filters, HMU dynamics, lead compensator, and heat sink model | 2.31% |

## 2.8 Results

The LQR power turbine governor was analyzed in the time domain using the GE nonlinear DISCUS model of the T700 engine. Four collective-pitch-angle transients were simulated for comparison of the LQR governor with the baseline T700 governor. Two of the transients were compensated with the load demand spindle (LDS) as described in Section 2.1.11, and two of the transients were not compensated with LDS.

The load on the engine with the uncompensated controller was changed with collective pitch angle, but the LDS was maintained constant at the starting level. This causes the load on the engine to change with no feed-forward information going to the control. The two compensated transients were an acceleration caused by a 0%-70% collective pitch angle burst in 0.5 sec and a deceleration caused by a 70%-0% collective pitch angle chop in 0.5 sec. This is a change of about 700 shaft horsepower.

The uncompensated transients were an acceleration caused by a 40%-70% collective pitch angle burst in 0.1 sec and a deceleration caused by a 70%-40% collective pitch angle burst in 0.1 sec. This is a 483 shaft horsepower change. All transients were done with and without the model of the heat sink, since the accuracy of the model is in question (Section 2.3.2.5). The system was designed, however, as though the heat sink model were accurate because this is the safer approach.

Figures 2.83 and 2.84 show the 0%-70% collective pitch burst compensated with LDS for the LQR and T700 baseline governors, respectively. These simulations do not include the heat sink. Figures 2.85 and 2.86 show the same transient with the heat sink for the LQR and T700 baseline, respectively. The 70%-0% collective pitch chops compensated with LDS with no heat sink model are shown in Figure 2.87 for the LQR and Figure 2.88 for the T700 baseline. The same chop with no heat sink model is shown in Figure 2.89 for the LQR and Figure 2.90 for the T700 baseline.

Figures 2.91 and 2.92 show the 40%-70% collective pitch burst compensated with LDS for the LQR and T700 baseline governors, respectively. These simulations do not include the heat sink. Figures 2.93 and 2.94 show the same transient with the heat sink for the LQR and T700 baseline, respectively. The 70%-40% collective pitch chops compensated with LDS with no heat sink model are shown in Figure 2.95 for the LQR and Figure 2.96 for the T700 baseline. The same chop with no heat sink model is shown in Figure 2.97 for the LQR and Figure 2.98 for the T700 baseline. Tabe 2.4 summarizes the above results.


PCNP1: NP (%)
PCN2: NG (%)
XLDSA: Load demand spindle (LDS) anticipation to control.
DYNANG: Load demand due to collective pitch.

Figure 2.83 LQR Np Governor with Black Hawk Rotor. 0% - 70% Collective Pitch Burst Compensated with LDS. No Heat Sink Model. 0.5 Sec Transient.

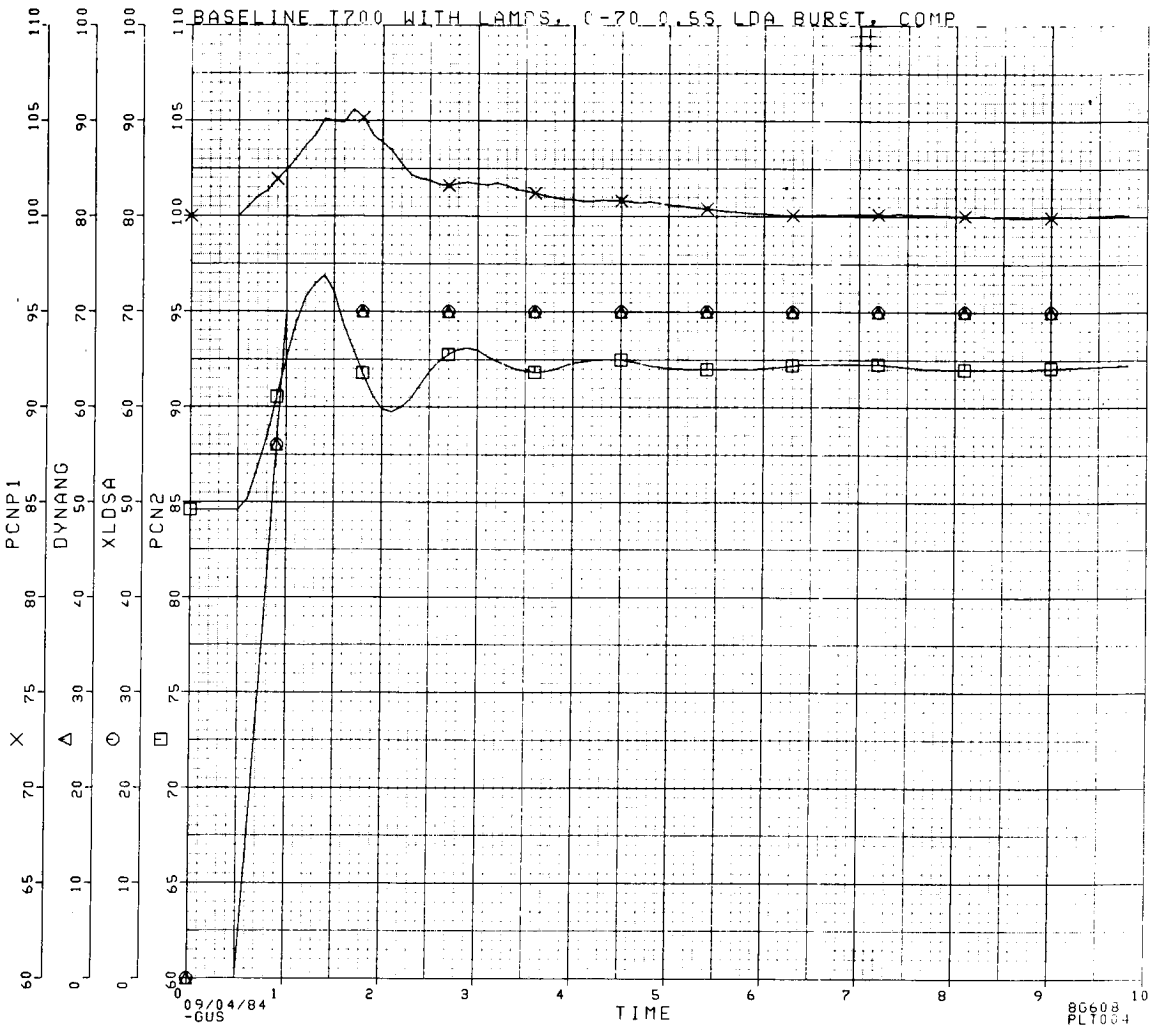


PCNP1: NP (%)
PCN2: NG (%)
XLDSA: Load demand spindle (LDS) anticipation to control.
DYNANG: Load demand due to collective pitch.

Figure 2.84 T700 Baseline Np Governor with Black Hawk Rotor. 0% - 70% Collective Pitch Burst Compensated with LDS. No Heat Sink Model. 0.5 Sec Transient.

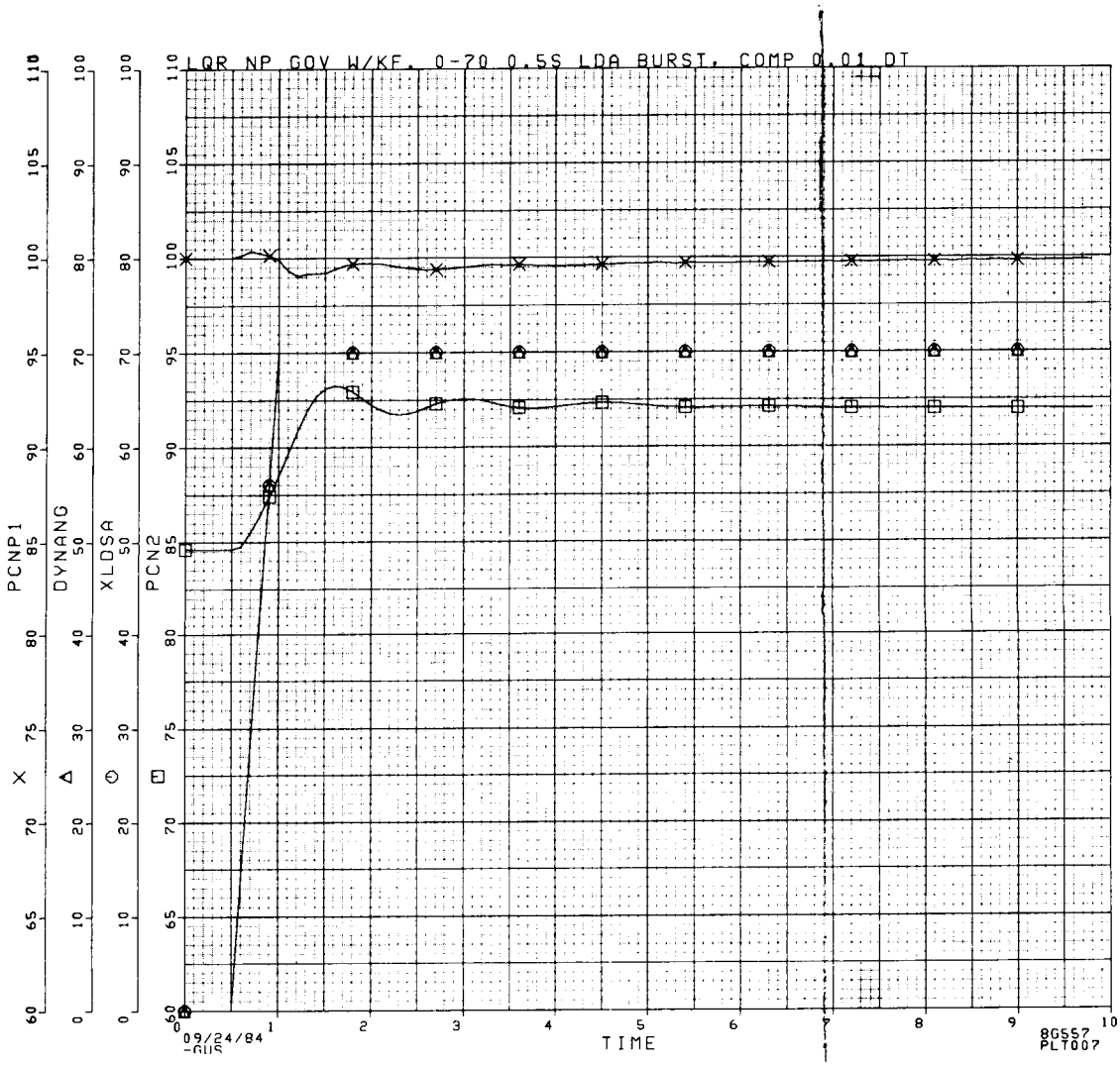


PCNP1: NP (%)
PCN2: NG (%)
XLDSA: Load demand spindle (LDS) anticipation to control.
DYNANG: Load demand due to collective pitch.

Figure 2.85 LQR Np Governor with Black Hawk Rotor. 0% - 70% Collective Pitch Burst Compensated with LDS. Heat Sink Included. 0.5 Sec Transient.

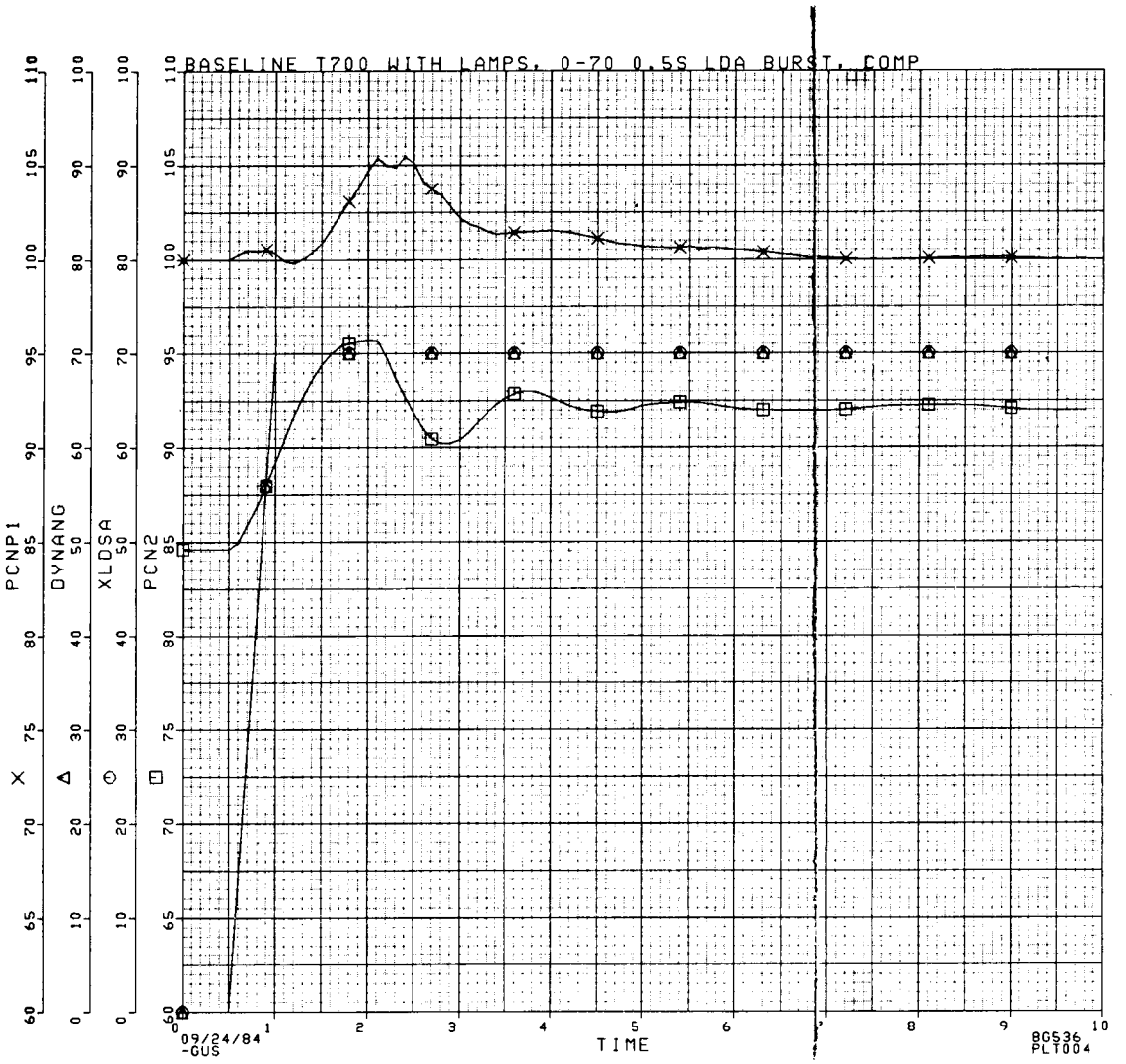


PCNP1: NP (%)
PCN2: NG (%)
XLDSA: Load demand spindle (LDS) anticipation to control.
DYNANG: Load demand due to collective pitch.

Figure 2.86 T700 Baseline Np Governor with Black Hawk Rotor. 0% - 70% Collective Pitch Burst Compensated with LDS. Heat Sink Included. 0.5 Sec Transient.

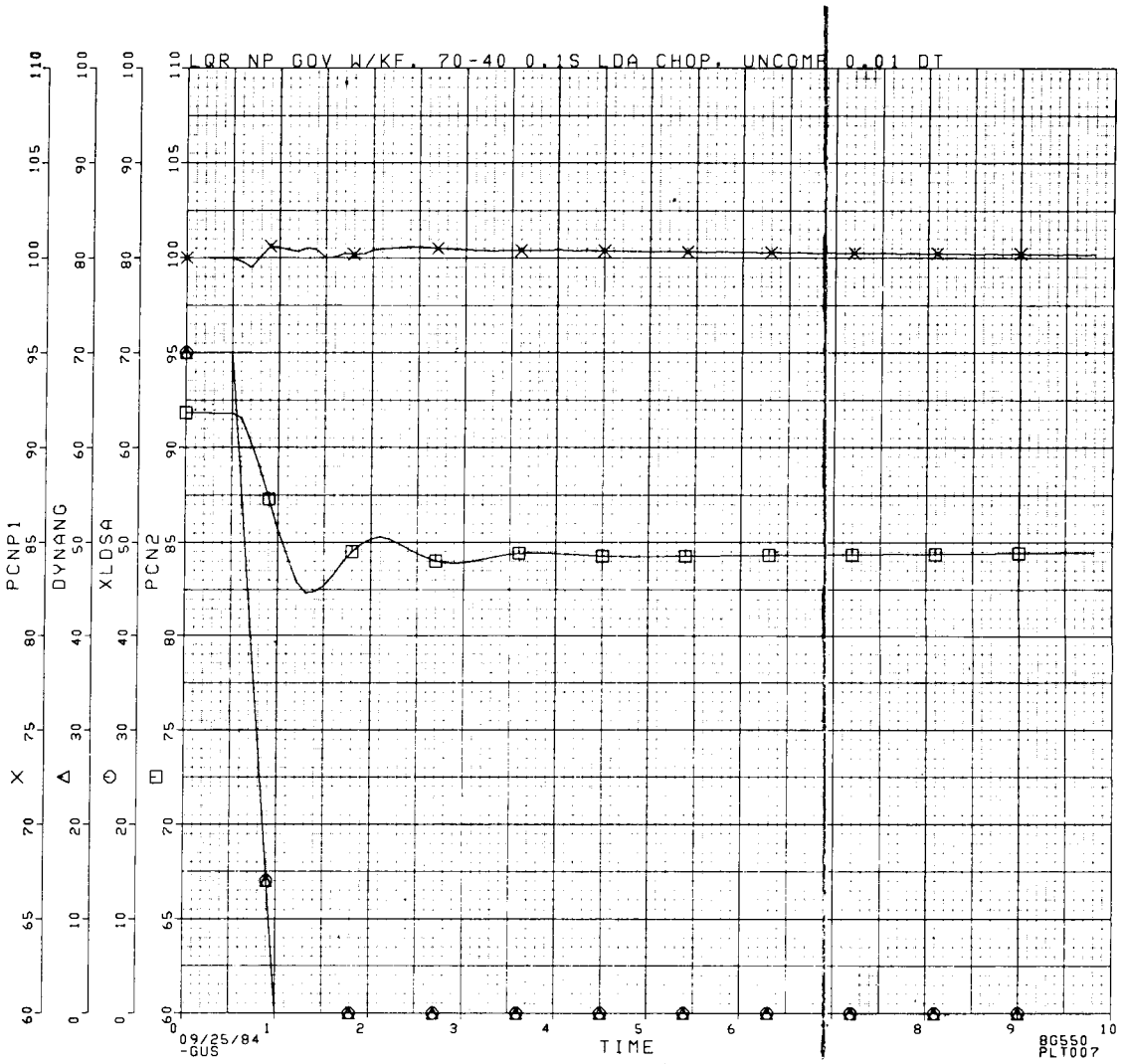


PCNP1: NP (%)
PCN2: NG (%)
XLDSA: Load demand spindle (LDS) anticipation to control.
DYNANG: Load demand due to collective pitch.

Figure 2.87 LQR Np Governor with Black Hawk Rotor. 70% - 0% Collective Pitch Chop Compensated with LDS. No Heat Sink Model. 0.5 Sec Transient.

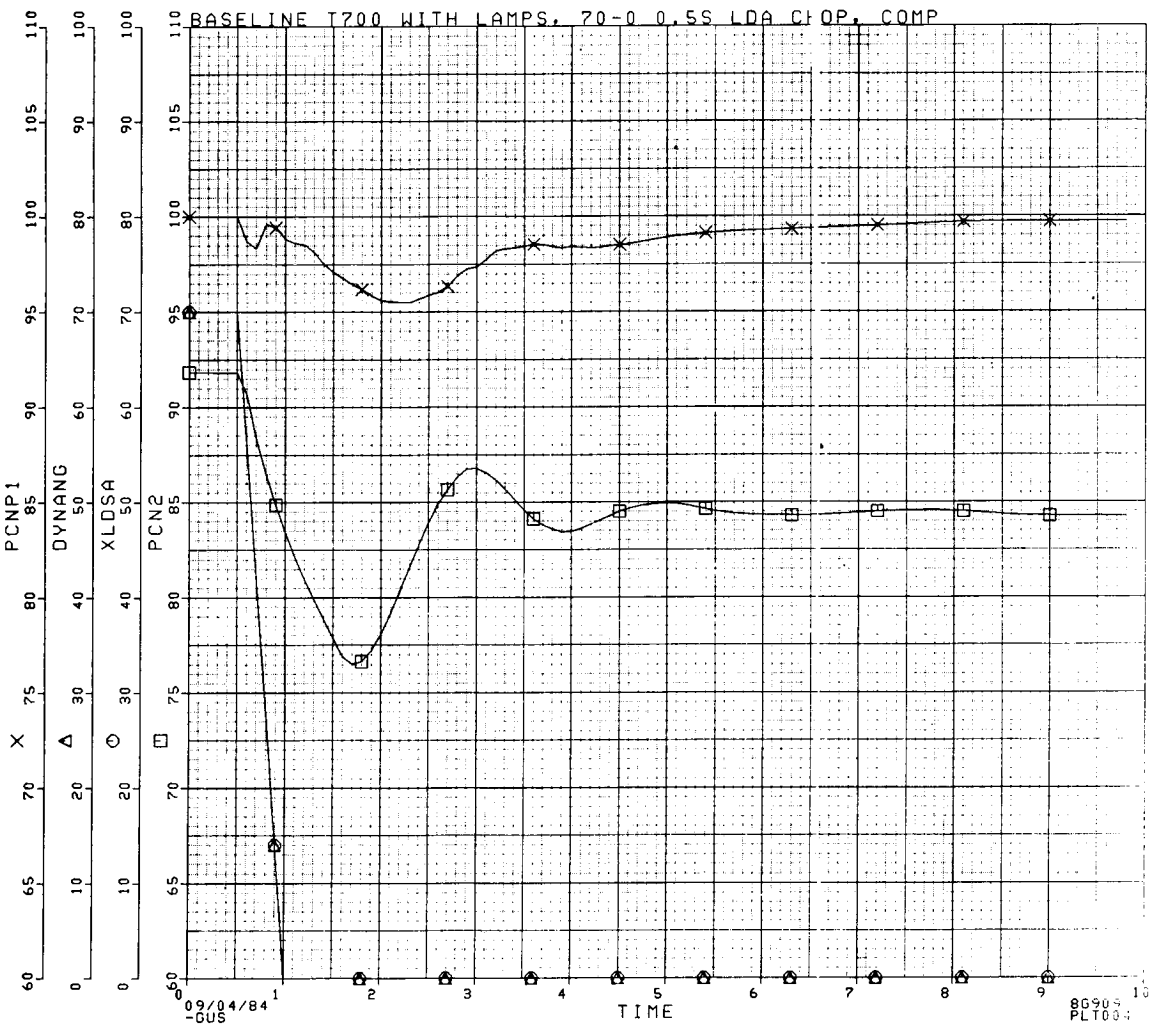


PCNP1: NP (%)
PCN2: NG (%)
XLDSA: Load demand spindle (LDS) anticipation to control.
DYNANG: Load demand due to collective pitch.

Figure 2.88 T700 Baseline Np Governor with Black Hawk Rotor. 70% - 0% Collective Pitch Chop Compensated with LDS. No Heat Sink Model. 0.5 Sec Transient.

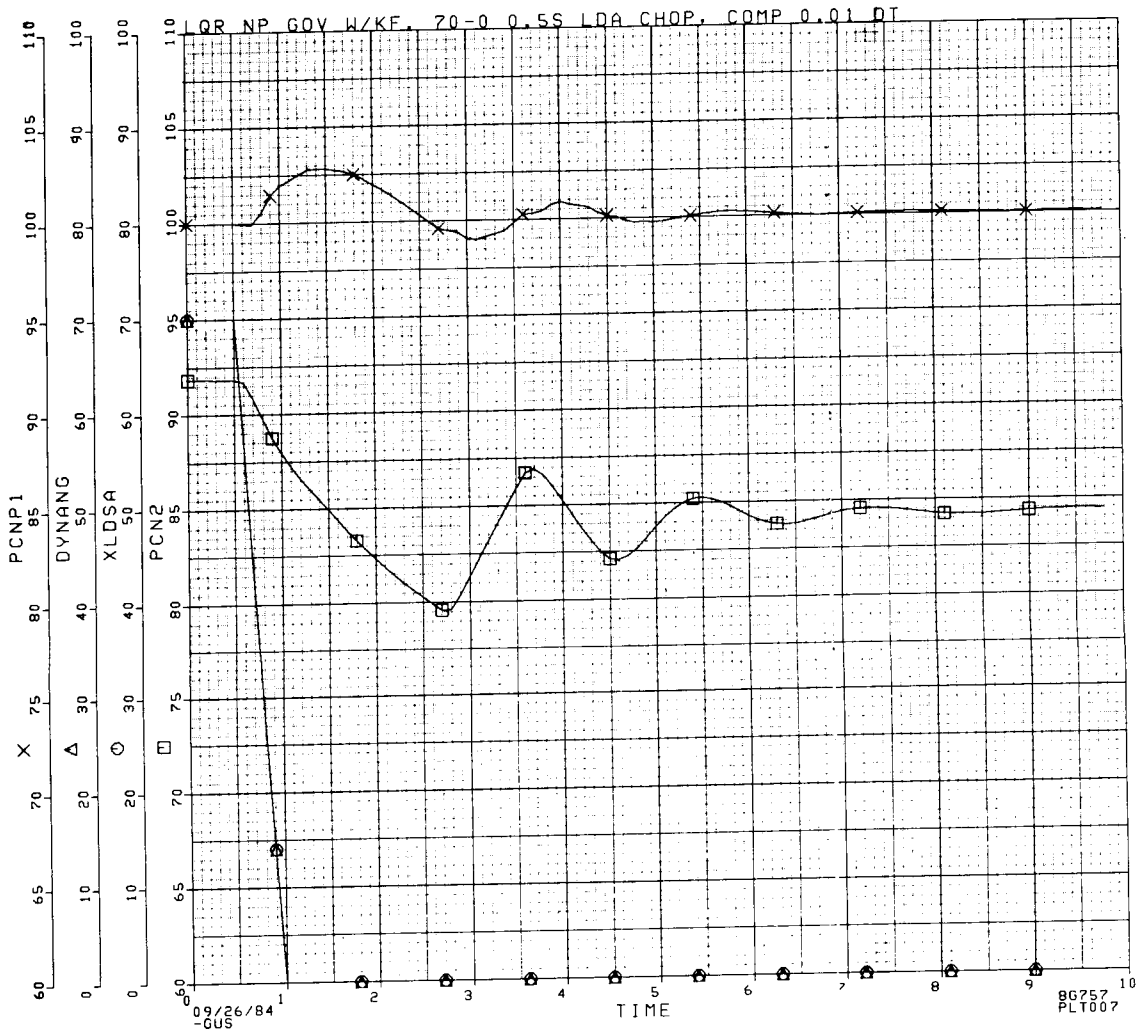


PCNP1: NP (%)
PCN2: NG (%)
XLDSA: Load demand spindle (LDS) anticipation to control.
DYNANG: Load demand due to collective pitch.

Figure 2.89 LQR Np Governor with Black Hawk Rotor. 70% - 0% Collective Pitch Chop Compensated with LDS. Heat Sink Included. 0.5 Sec Transient.

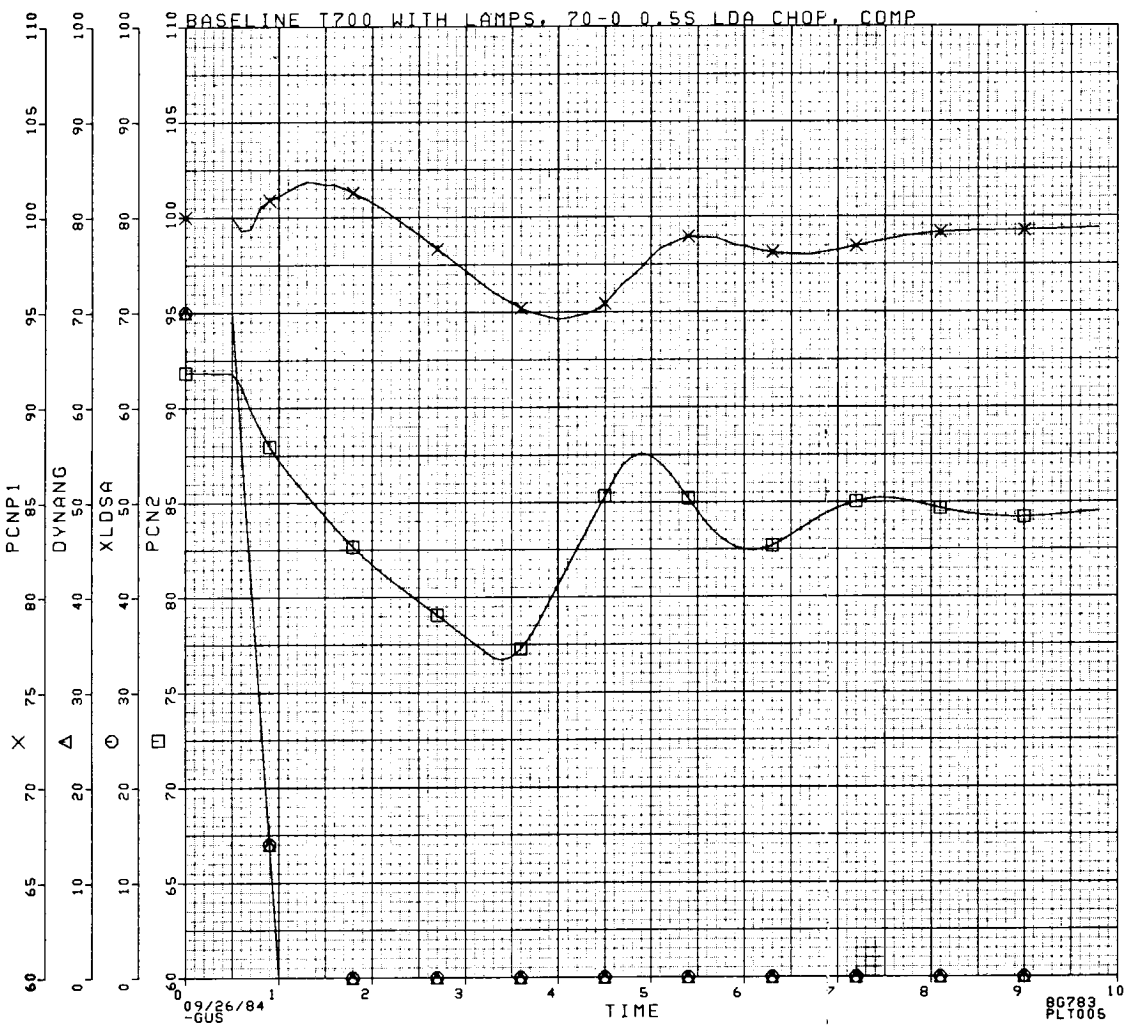


PCNP1: NP (%)
PCN2: NG (%)
XLDSA: Load demand spindle (LDS) anticipation to control.
DYNANG: Load demand due to collective pitch.

Figure 2.90 T700 Baseline Np Governor with Black Hawk Rotor. 70% - 0% Collective Pitch Chop Compensated with LDS. Heat Sink Included. 0.5 Sec Transient.

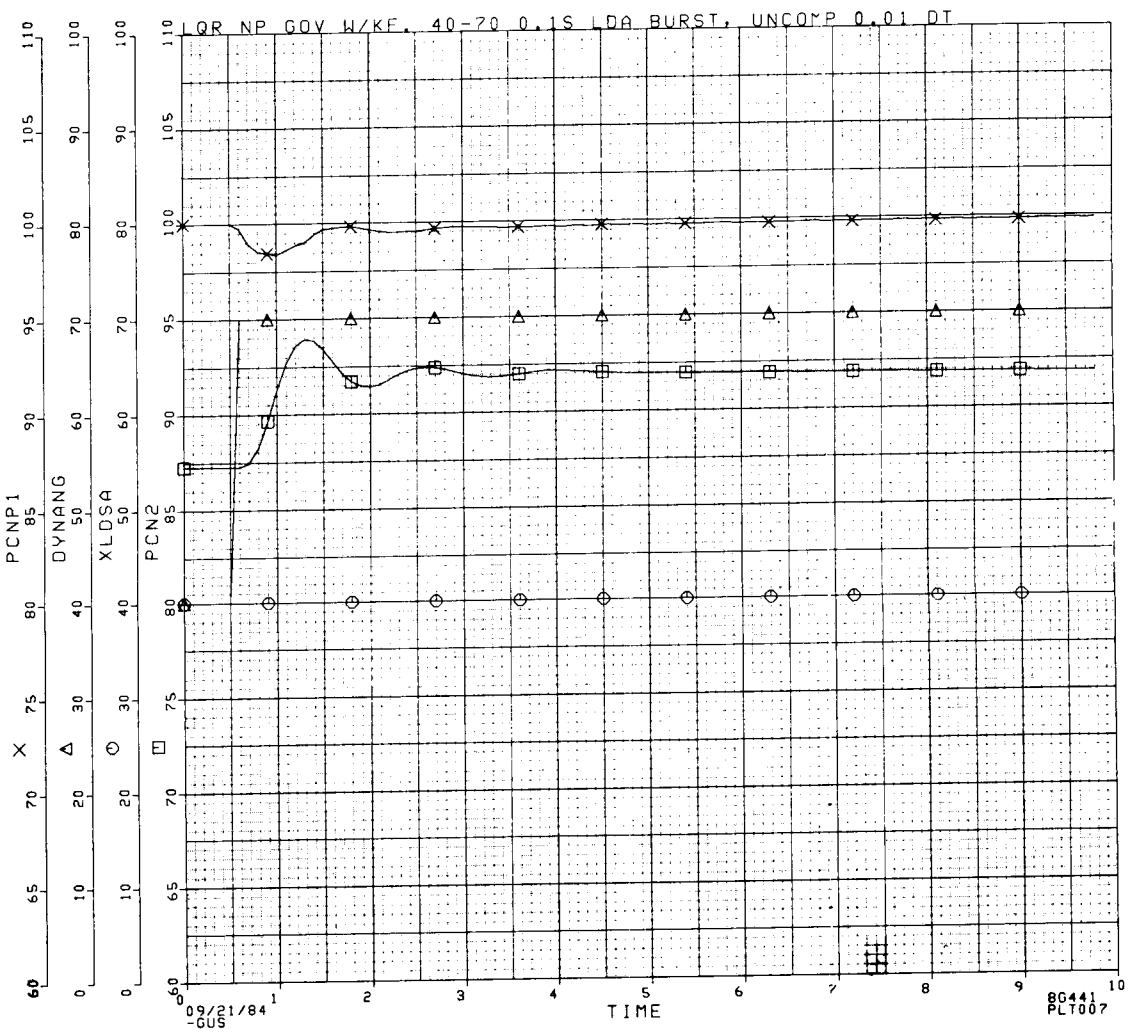


PCNP1: NP (%)
PCN2: NG (%)
XLDSA: Load demand spindle (LDS) anticipation to control.
DYNANG: Load demand due to wind gust, constant collective pitch

Figure 2.91 LQR Np Governor with Black Hawk Rotor. 40% - 70% Collective Pitch Burst not Compensated with LDS. No Heat Sink Model. 0.1 Sec Transient.

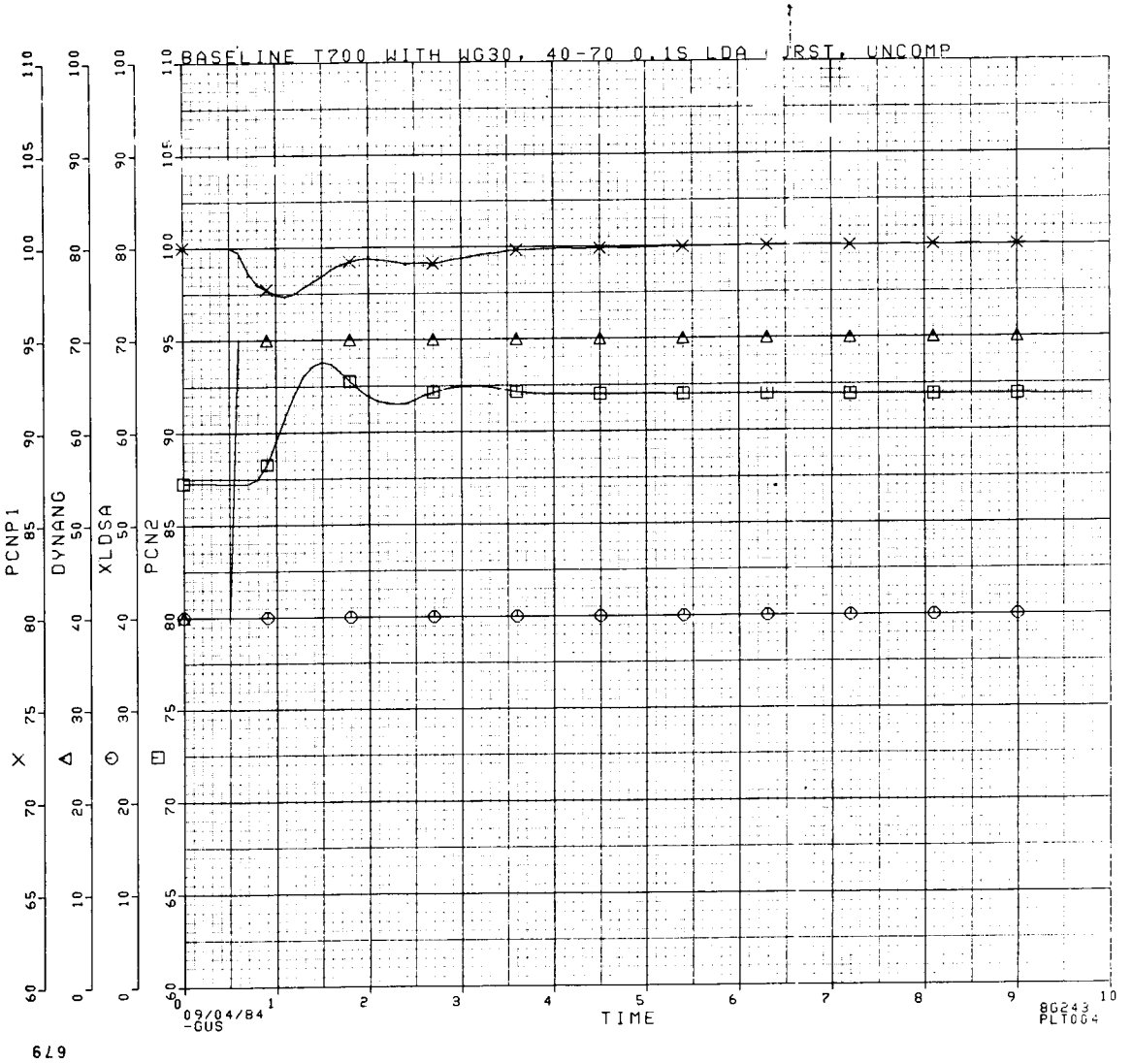


PCNP1: NP (%)
PCN2: NG (%)
XLDSA: Load demand spindle (LDS) anticipation to control.
DYNANG: Load demand due to wind gust, constant collective pitch

Figure 2.92

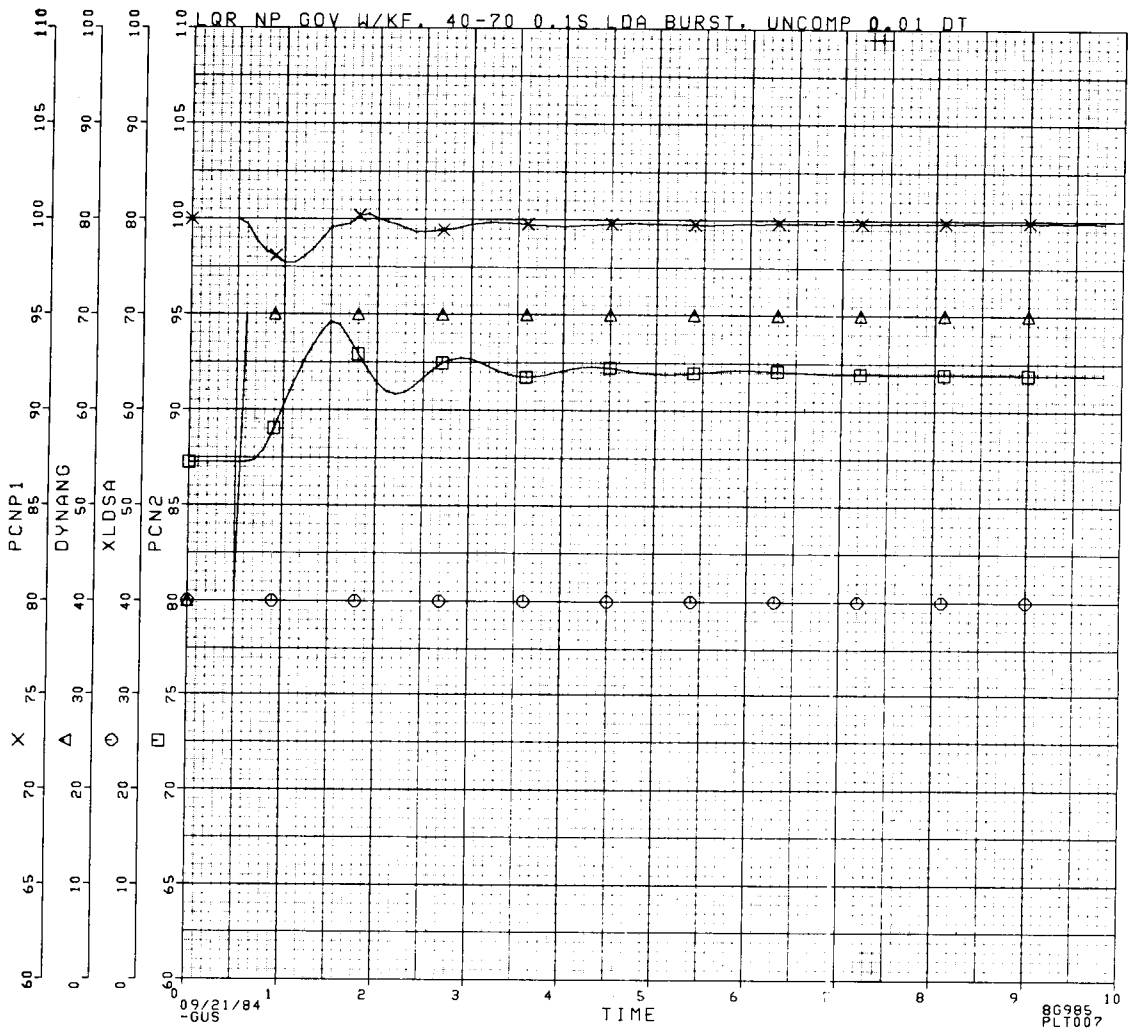


PCNP1: NP (%)
PCN2: NG (%)
XLDSA: Load demand spindle (LDS) anticipation to control.
DYNANG: Load demand due to wind gust, constant collective pitch

Figure 2.93 LQR Np Governor with Black Hawk Rotor. 40% - 70% Collective Pitch Burst not Compensated with LDS. Heat Sink Included. 0.1 Sec Transient.

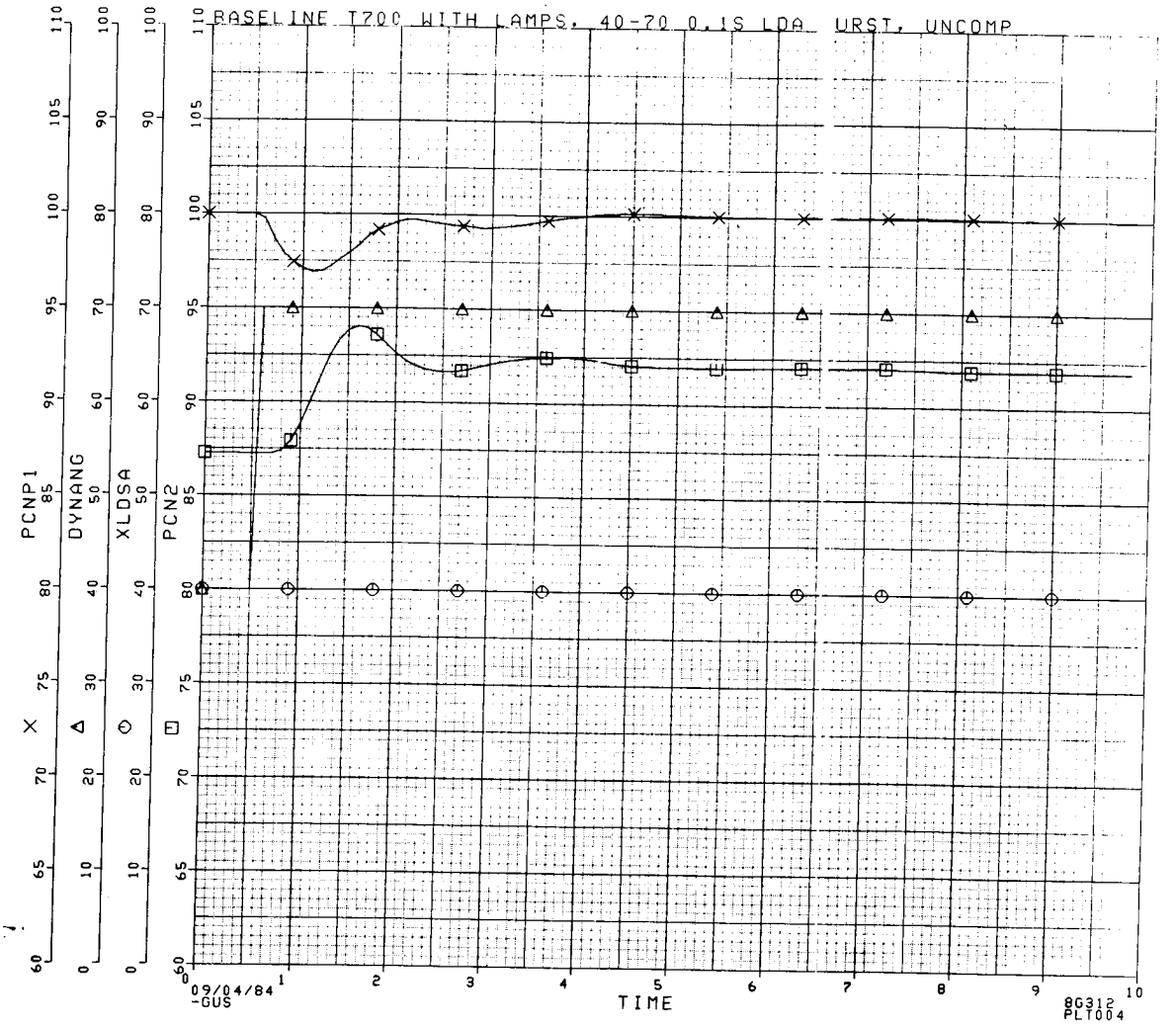


PCNP1: NP (%)
PCN2: NG (%)
XLDSA: Load demand spindle (LDS) anticipation to control.
DYNANG: Load demand due to wind gust, constant collective pitch

Figure 2.94 T700 Baseline Np Governor with Black Hawk Rotor. 40% - 70% Collective Pitch Burst not Compensated with LDS. Heat Sink Included. 0.1 Sec Transient.


PCNP1: NP (%)
PCN2: NG (%)
XLDSA: Load demand spindle (LDS) anticipation to control.
DYNANG: Load demand due to wind gust, constant collective pitch

Figure 2.95 LQR Np Governor with Black Hawk Rotor. 70% - 40% Collective Pitch Chop not Compensated with LDS. No Heat Sink Included. 0.1 Sec Transient.

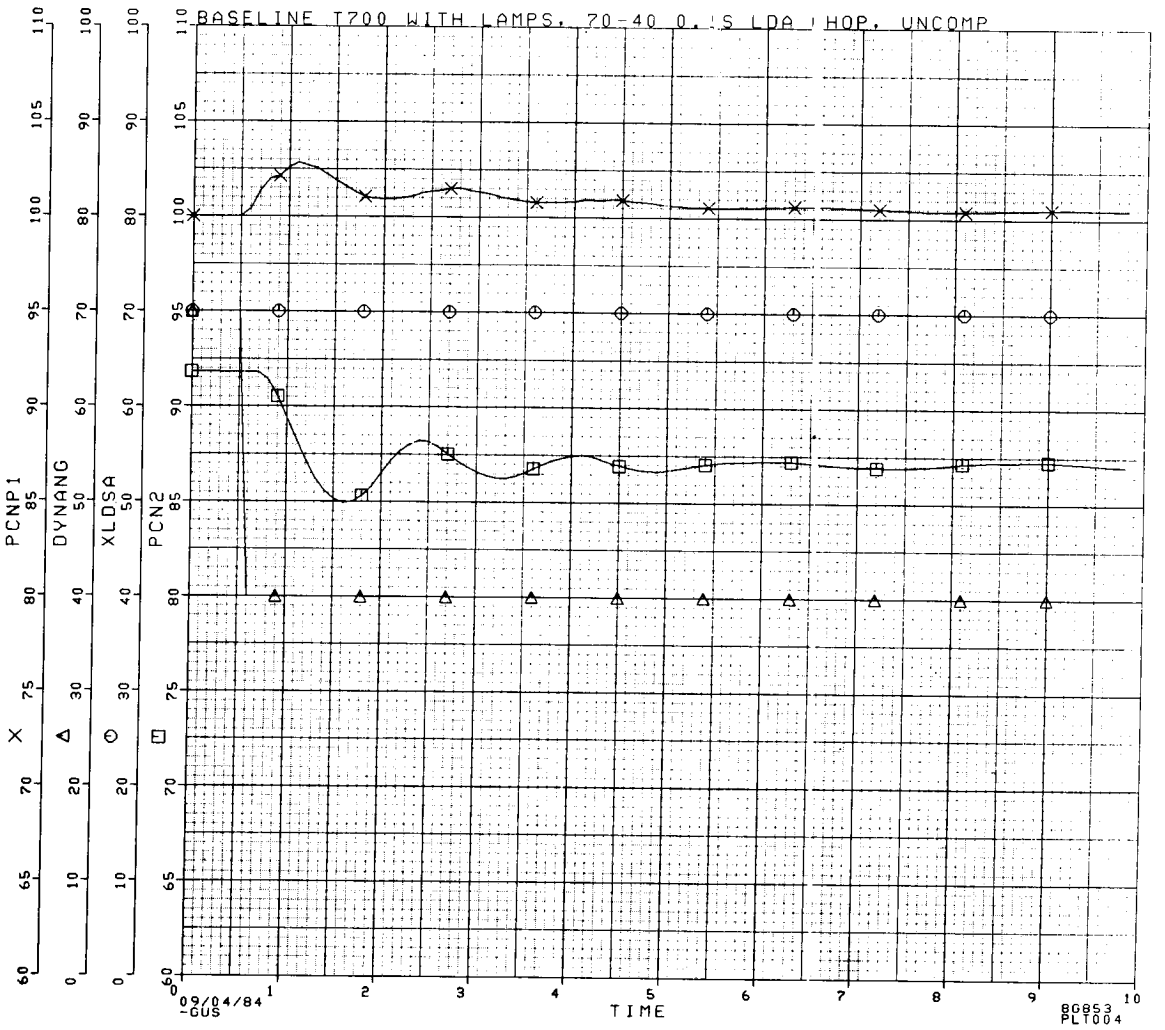


PCNP1: NP (%)
PCN2: NG (%)
XLDSA: Load demand spindle (LDS) anticipation to control.
DYNANG: Load demand due to wind gust, constant collective pitch

Figure 2.96 T700 Baseline Np Governor with Black Hawk Rotor. 70% - 40% Collective Pitch Chop not Compensated with LDS. No Heat Sink Included. 0.1 Sec Transient.

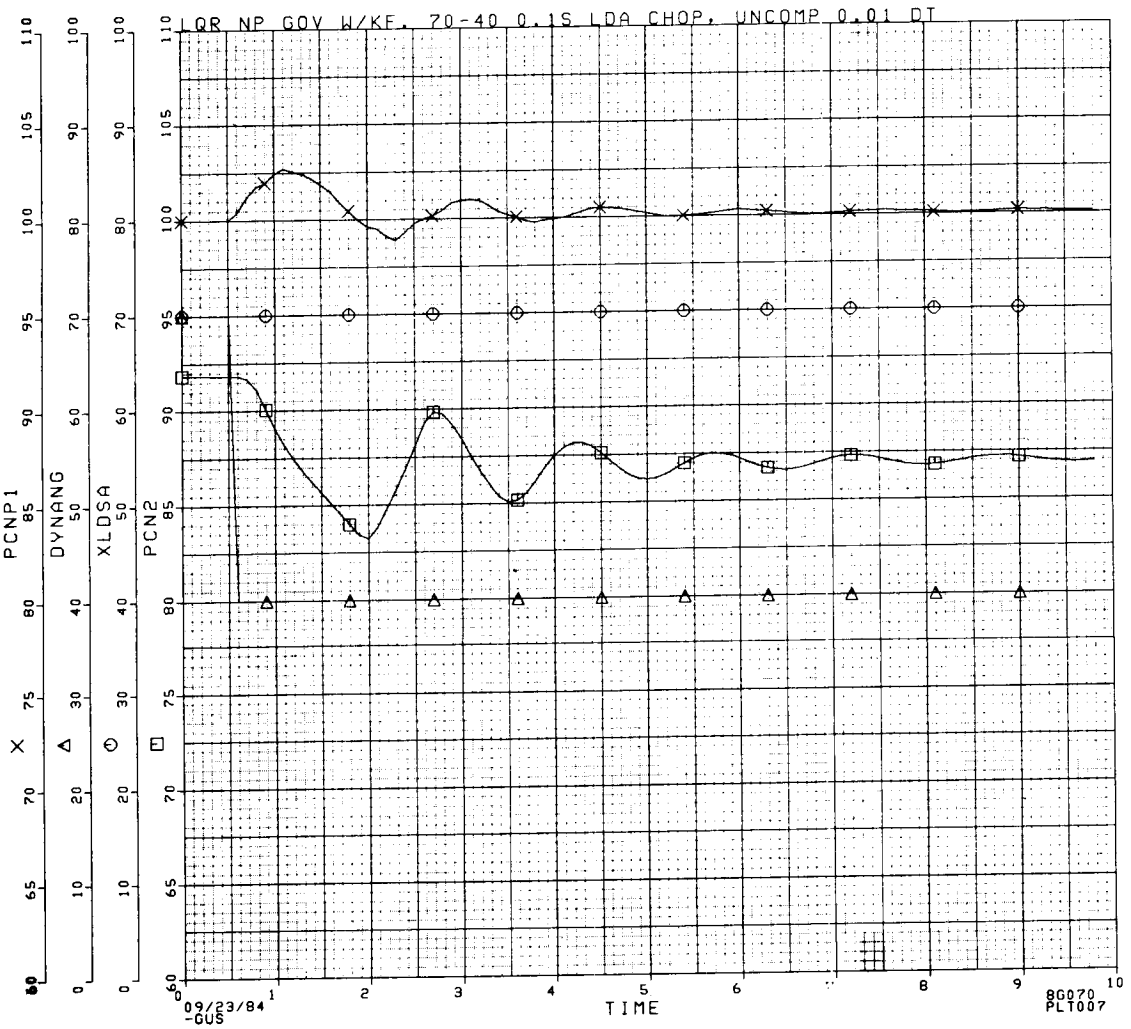


PCNP1: NP (%)
PCN2: NG (%)
XLDSA: Load demand spindle (LDS) anticipation to control.
DYNANG: Load demand due to wind gust, constant collective pitch

Figure 2.97 LQR Np Governor with Black Hawk Rotor. 70% - 40% Collective Pitch Chop not Compensated with LDS. Heat Sink Included. 0.1 Sec Transient.

ORIGINAL PAGE IS
OF POOR QUALITY

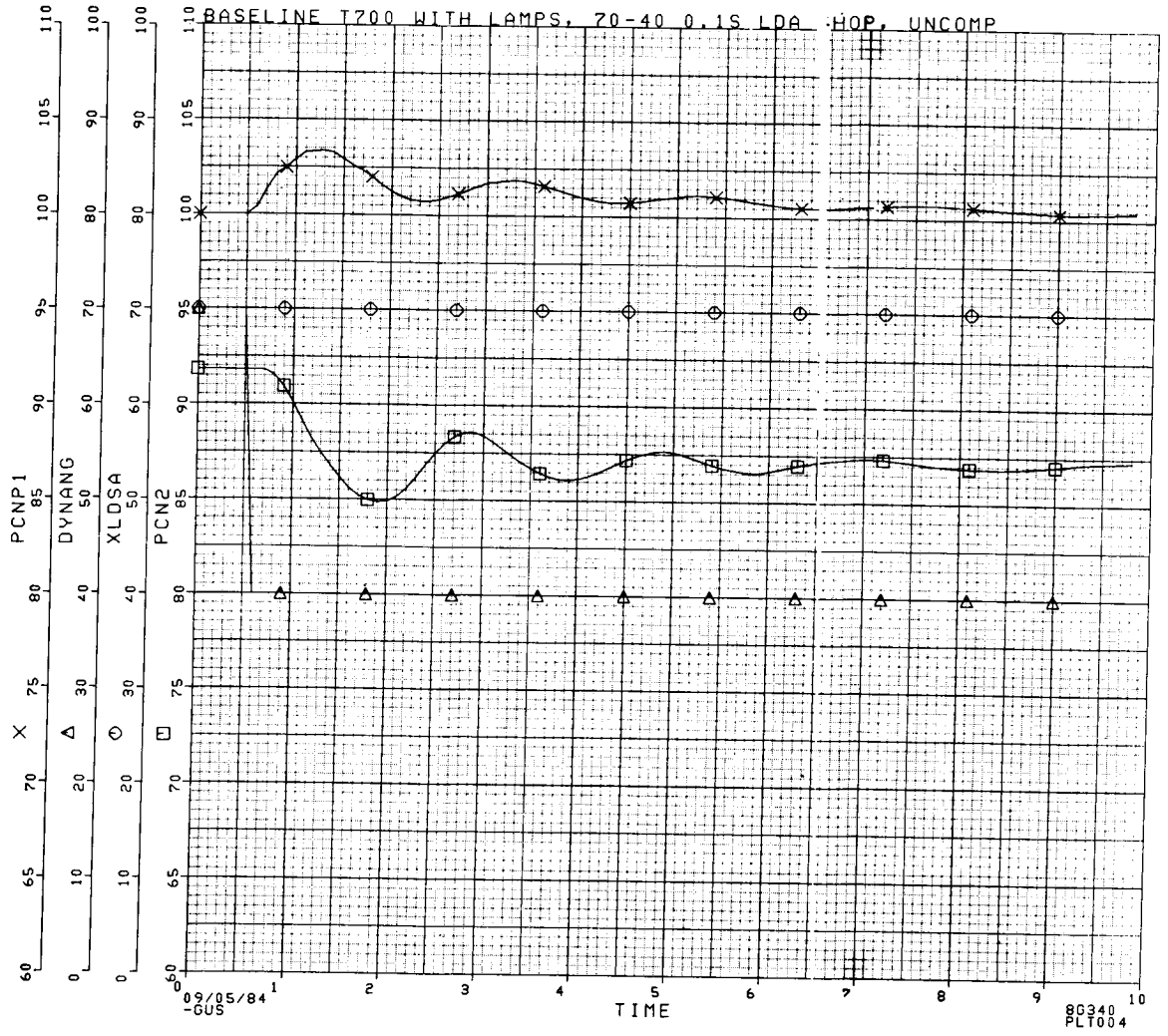


PCNP1: NP (%)
PCN2: NG (%)
XLDSA: Load demand spindle (LDS) anticipation to control.
DYNANG: Load demand due to wind gust, constant collective pitch

Figure 2.98 T700 Baseline Np Governor with Black Hawk Rotor. 70% - 40% Collective Chop Burst not Compensated with LDS. Heat Sink Included. 0.1 Sec Transient.

Table 2.4. Comparison of Droop and Overshoot of T700 Baseline and LQR Np Governors with Black Hawk Rotor

| Event | Droop (-) or Overshoot (+) | |
|---|---|---|
| | T700 Baseline | LQR |
| 1. 40% - 70% beta*, uncompensated**, 0.1 sec | | |
| - with no heat sink | -2.67% | -1.62% |
| - with heat sink | -3.09% | -2.31% |
| 2. 70% - 40% beta, uncompensated, 0.1 sec | | |
| - with no heat sink | +2.83% | +1.64% |
| - with heat sink | +3.37% | +2.70% |
| 3. 0% - 70% beta, compensated**, 0.5 sec | | |
| - with no heat sink | +5.10% | +0.71%/-0.74% |
| - with heat sink | +5.38% | -0.79% |
| 4. 70% - 0% beta, compensated, 0.5 sec | | |
| - with no heat sink | -4.50% | 0.60% |
| - with heat sink | +1.87%/-5.35% | +2.82% |

* beta is collective pitch angle
** compensated or uncompensated with LDS

The effect of the Kalman Filter on rotor droop was assessed by simulating a transient using the actual main rotor speed and a transient using the estimated main rotor speed. These simulations have no heat sink model, antialias filters, ZOH model, or HMU model. The transient was a 40%-70% uncompensated collective pitch angle burst in 0.1 sec. Rotor droop on the transient with the Kalman Filter increased from 0.98% droop to 1.56% droop. This is a large but acceptable effect. Figure 2.99 is the transient with the actual main rotor speed and Figure 2.100 is the transient with the estimated main rotor speed. Figure 2.101 shows how estimated main rotor speed tracks actual main rotor speed for a typical transient.

The gain and phase margin results of the frequency domain analysis were tested for one transient in the time domain by separately doubling the gain and adding phase lag at unity gain through a time delay. Doubling the gain is equivalent to raising the magnitude plot 6dB. The time transient was a 40%-70% collective pitch angle burst in 0.1 sec with no LDS compensation. The time response for the system with doubled loop gain is shown in Figure 2.102. The system is only slightly less stable indicating there is gain margin in excess of 6dB. Table 2.1 shows there should be a minimum of 10dB gain margin. A delay of 0.08 sec was added to the system to assess phase margin. The delay has unity gain and contributes 45° phase lag at 10 rad/sec. 45° phase margin is a minimum acceptable margin for stability. The time response is shown in Figure 2.103. The system is less stable, but still settles down, indicating a minimum of 45° phase margin.

The LQR Np governor shows about a 37% reduction in droop and overshoot for the transients not compensated with LDS and about an 85% reduction for transients compensated with LDS. The uncompensated transients are a good indication of controller performance because there is no anticipation of load demand going to the control. The controller must respond after the disturbance has occurred. If one knows the characteristics of the disturbance before it occurs, one can design feed forward compensation to minimize the effects of that disturbance. For the compensated transients shown in the figures, the LQR substantially reduces droop using a very simple LDS compensation. The compensation is not in the form of dynamic leads and lags but in the form of approximate reference schedules that vary with LDS. Engine testing and simulations with more accurate vehicle models are necessary to verify these results.

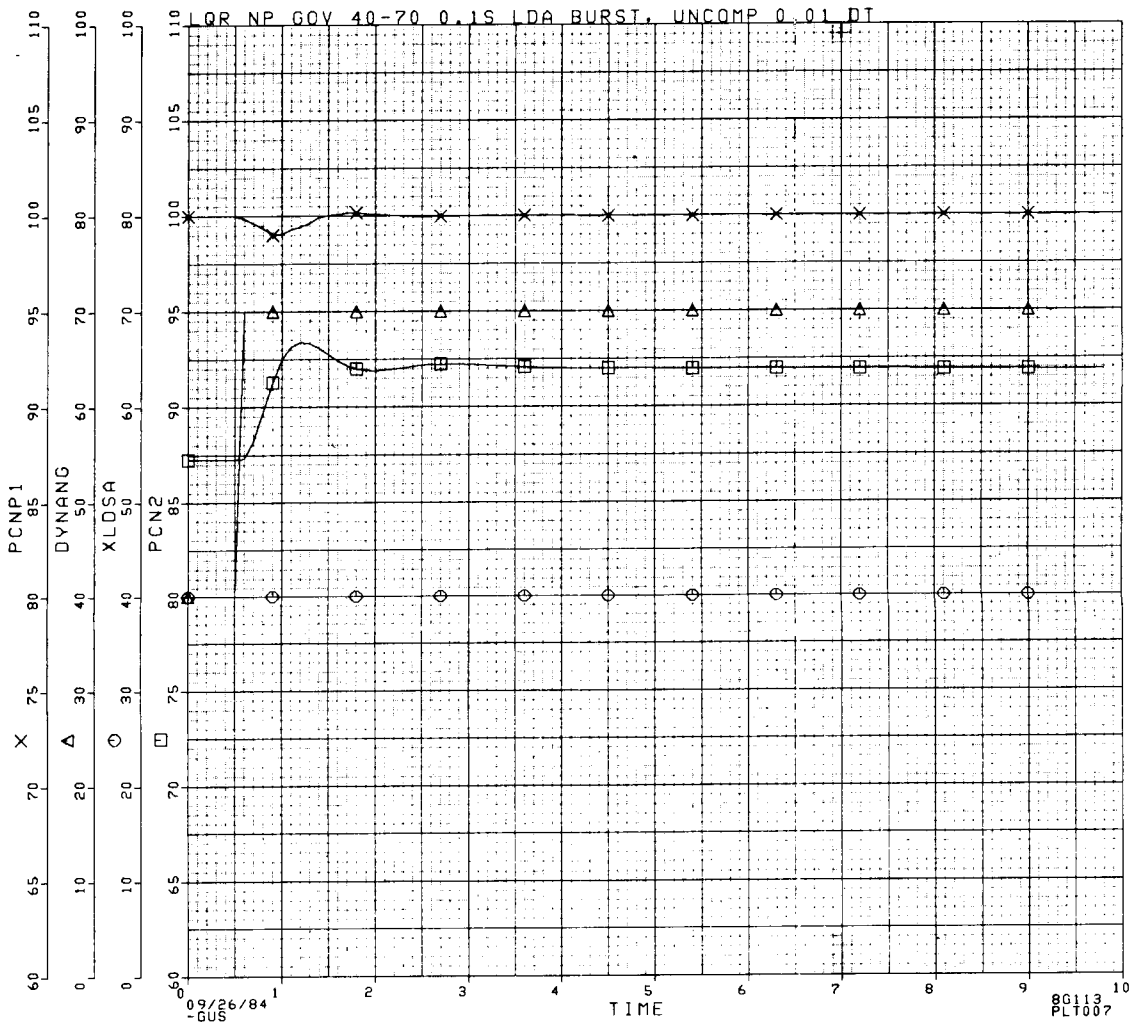


PCNP1: NP (%)
PCN2: NG (%)
XLDSA: Load demand spindle (LDS) anticipation to control.
DYNANG: Load demand due to wind gust, constant collective pitch

Figure 2.99 Effect of Using Actual Main Rotor Velocity in LQR Governor. 40% - 70% Collective Pitch Angle Burst in 0.1 Sec Uncompensated with LDS. No Heat Sink, No ZOH, No Anti-Alias Filters, No HMU Model.

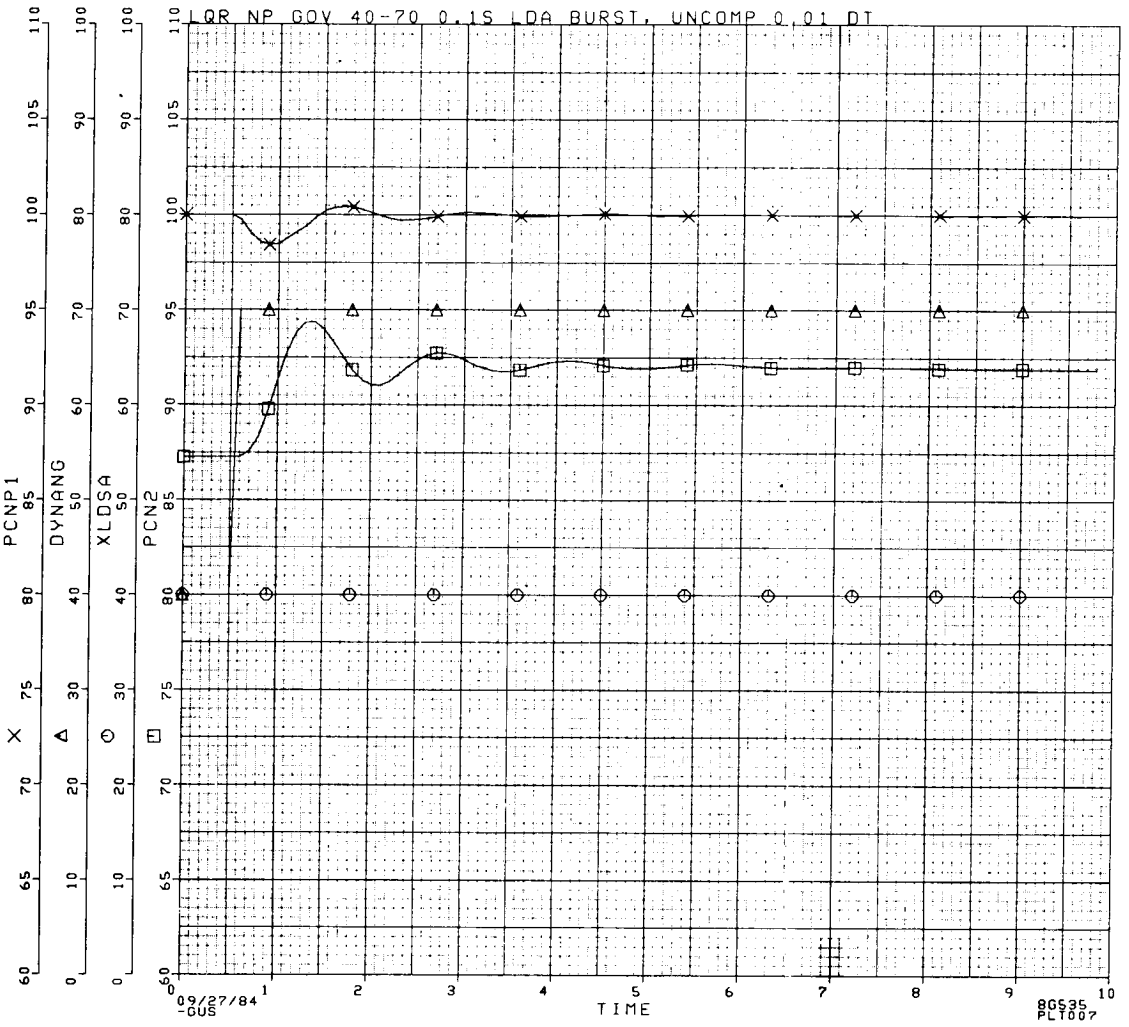


PCNP1: NP (%)
PCN2: NG (%)
XLDSA: Load demand spindle (LDS) anticipation to control.
DYNANG: Load demand due to wind gust, constant collective pitch

Figure 2.100 Effect of Using Estimated Main Rotor Velocity in Place of Actual Main Rotor Velocity (see Figure 99).

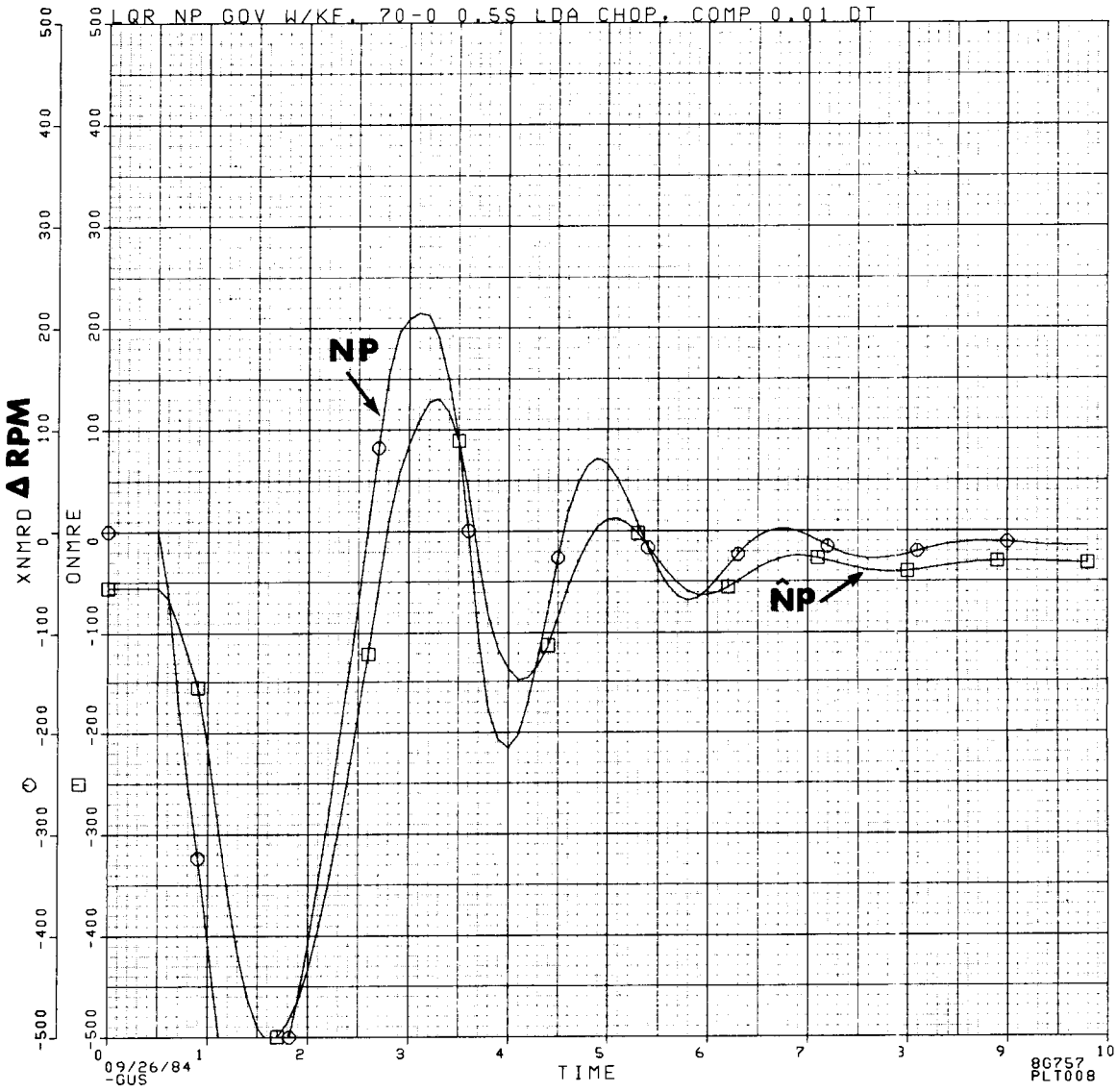


Figure 2.101 Tracking of Estimated Main Rotor Velocity with Actual Main Rotor Velocity in Kalman Filter for Typical Transient.

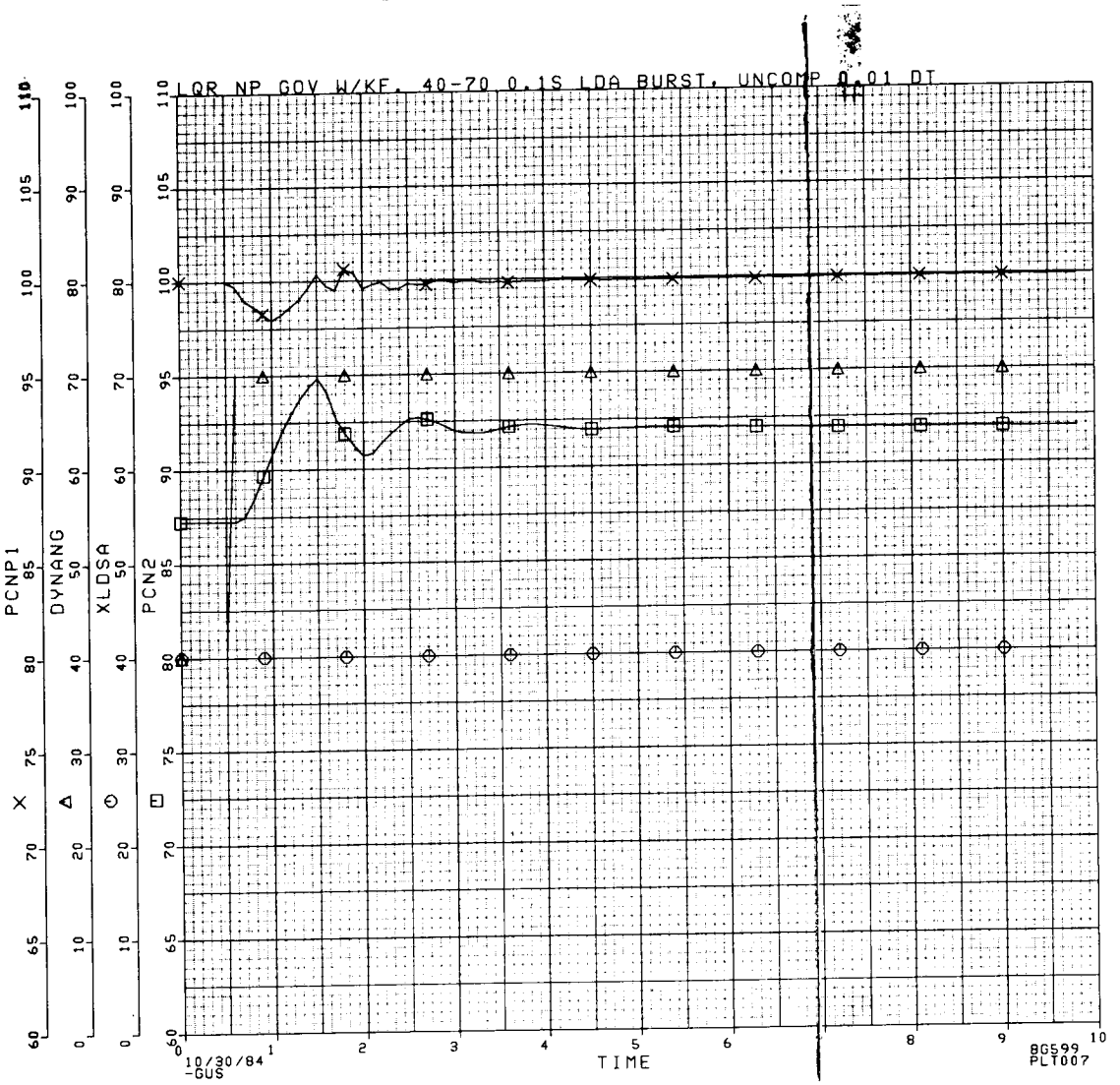


PCNP1: NP (%)
PCN2: NG (%)
XLDSA: Load demand spindle (LDS) anticipation to control.
DYNANG: Load demand due to wind gust, constant collective pitch

Figure 2.102 Effect of Doubling Loop Gain of Controller for 40% - 70% Collective Pitch Angle Burst in 0.1 Sec Uncompensated with LDS.

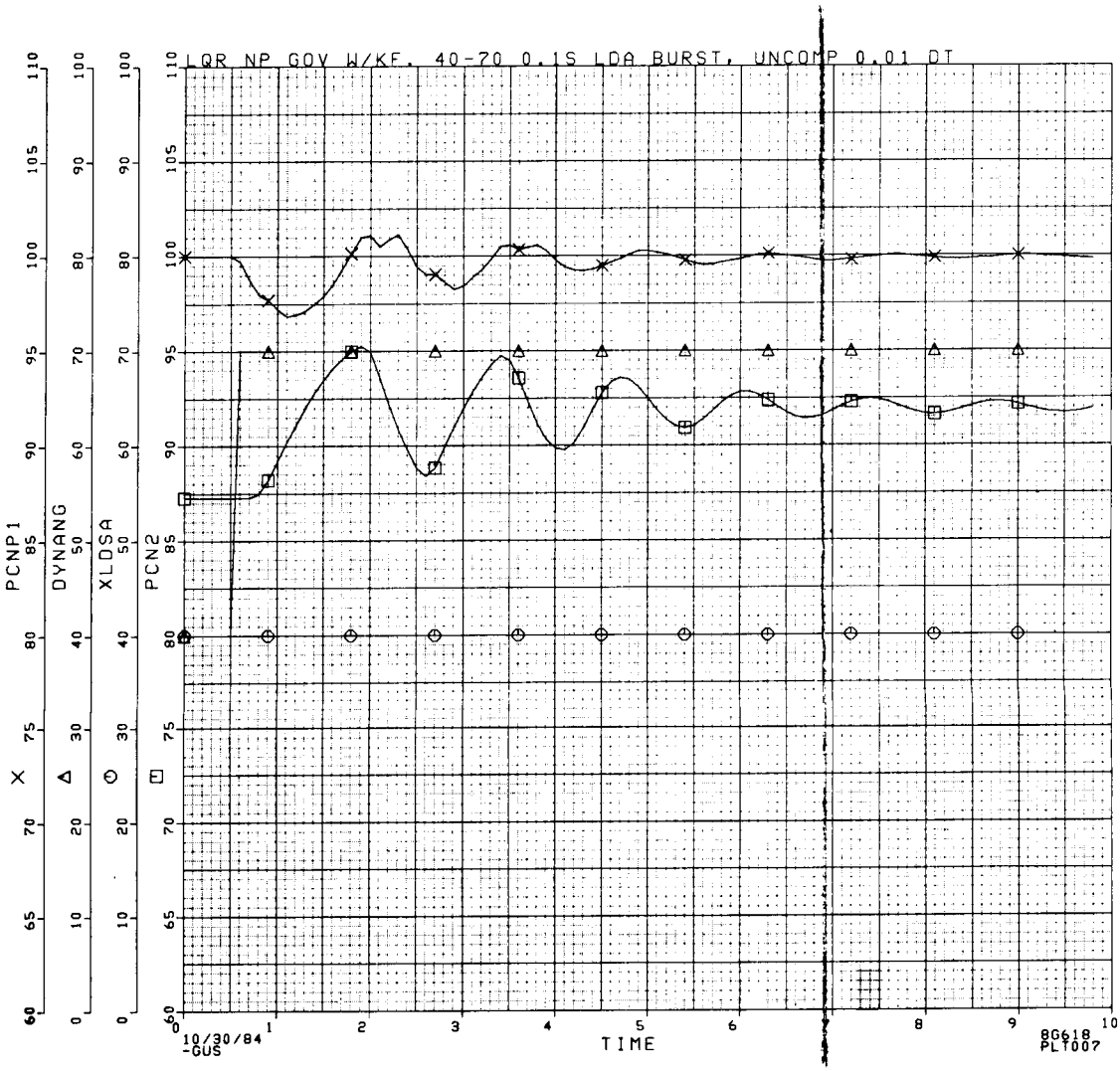


PCNP1: NP (%)
PCN2: NG (%)
XLDSA: Load demand spindle (LDS) anticipation to control.
DYNANG: Load demand due to wind gust, constant collective pitch

Figure 2.103 Effect of Adding 45° Phase Lag at 10 rod/sec to System for 40% - 70% Collective Pitch Angle Burst in 0.1 Sec Uncompensated with LDS.

## 3.0 Introduction: Linear Model Identification

Accurate information concerning the dynamic behavior, or frequency response, of gas turbine engines is essential for the design of high performance engine controls. Engine controls, evaluated in the time domain, are designed in the frequency domain using digital computer engine models. Empirical engine data provides a benchmark for checking the validity of the basic engine models. Discrepancies between experimental and analytical engine frequency responses indicate areas of uncertainty in the control system design and help to identify areas of potential improvement in the engine computer models.

Traditional methods of obtaining engine frequency response, such as discrete sinewave testing, are time consuming processes. The sinewave stimulates a single frequency in the engine, and is correlated with the output response to obtain some measure of attenuation and phase shift. Measuring the frequency response characteristics of the engine at several frequency points can take anywhere between two days to a week including setup and instrumentation validation. This process must be repeated for each engine operating point of interest. Substantial time and cost savings could be realized, however, with a more efficient means of gathering frequency response data.

Pseudo-random binary noise (PRBN) frequency response testing is used as an alternative to traditional frequency response testing methods. The use of a random signal that, by definition, contains a wide range of frequencies, speeds the acquisition of frequency response data. With the PRBN testing technique, a range of frequencies in the bandwidth of interest is injected simultaneously into the engine, as opposed to individually with sinewave testing. Theoretically, only one period of the PRBN signal is needed to excite all the engine dynamics in the PRBN range of frequencies. For gas turbine applications, the effective PRBN period is approximately one minute, providing the potential to considerably reduce the test cell time required to obtain engine data. The frequency response is derived from the engine data using analytical correlation techniques. This analysis is easily performed off-line with a digital computer, effectively reducing the amount of data reduction required compared with sinewave testing.

R. V. Cottington and C. B. Pease (Ref. 16) have demonstrated successful dynamic response testing of gas turbines using a PRBN testing technique in conjunction with spectral analysis. A number of engines were analyzed using this method, and results compared very well with sinewave testing data.

The objective of the PRBN testing of the NASA T700 engine was to illustrate the use of PRBN testing as an accurate and expedient method of obtaining engine frequency response data compared to traditional methods such as discrete sinewave frequency response testing. The PRBN method also allows the evaluation of existing linear models by comparing model and engine frequency responses. In addition, the PRBN technique lends itself to creating linear engine models by fitting reduced-order models to engine data and identifying

engine partial derivatives. Evaluating linear engine model responses and partials in this manner will reveal areas of potential improvement and provide more accurate engine models.

A PRBN signal superimposed on a steady-state fuel flow command signal was injected into the fuel flow actuator. Engine input (fuel flow, WF) and output (gas generator speed, NG, and power turbine speed, NP) time series data were analyzed by an off-line digital computer used to recover the engine frequency response through separate spectral analysis and maximum likelihood (ML) model identification techniques. NASA-supplied sinewave test points were used to evaluate the PRBN test results. A reduced-order model was obtained from the ML results, and engine partial derivatives were identified and compared to those of a linear engine model.

## 3.1 Procedure

### 3.1.1. PRBN Test

The following procedure details the equipment and techniques used to conduct the PRBN testing of the NASA YT700 engine.

#### 3.1.1.1 Hardware

The hardware required for the engine tests include:

- Two consoles within the Hybrid Computer Simulation Facility.
- The microprocessor control, Engine Monitoring and Control (EMAC), unit.
- An interface unit to act as a feedback "loop closer" and to drive electrohydraulic servo valves.
- A YT700 engine.
- A modified YT700 control (ref. contract NAS3-22763).
- An engine loading device (i.e. eddy current dynamometer).
- A sea level static test stand.
- An analog computer (TR48) to schedule engine loading and other calculations as required.

#### 3.1.1.2 Data Acquisition

Data from engine tests performed at the Engine Components Research Laboratory (ECRL) was recorded as follows:

- Steady-state data was recorded on the Lewis central steady-state system (ESCORT) and on the Microcomputer Interactive Data System (MINDS).

- Transient data was recorded on visicorders, on the Lewis central analog system, and on safety tape.

#### 3.1.1.3 Test Matrix

The PRBN test was performed with the following engine configurations:

- Variable geometry (VG) system locked at steady-state scheduled position.

- 90% Ng power point.

- EMAC fuel flow command locked.

- 5 Hz PRBN signal imposed on steady-state fuel flow command signal.

The PRBN signal amplitude was approximately 20% peak to peak of the steady-state command signal. The test period was approximately 9 minutes long with data sampled at 200 Hz (200 samples/sec). The test was performed at sea level static conditions.

#### 3.1.1.4 Data Reduction

The middle 5 minutes of engine data were used in the analysis to avoid any start-up or shutdown transients. All statistical analyses were performed with IDPAC software (Ref. 17).

### 3.2 Analysis

#### 3.2.1. Time Series Analysis

Figure 3.1 shows the PRBN command, WF, NG, and NP signals for a representative data sample slice. Since the PRBN command signal and consequently WF, NG, and NP exhibit random behavior, the correlation between the engine input and outputs is obtained through statistical analysis. An underlying assumption made in this analysis is that the engine is operating at steady state in the sense that the statistical properties of the time series are stationary or independent of absolute time. This assumption is tested by comparing the individual statistical properties of several consecutive minutes of data in the following analysis. Also implicit in the analysis is the

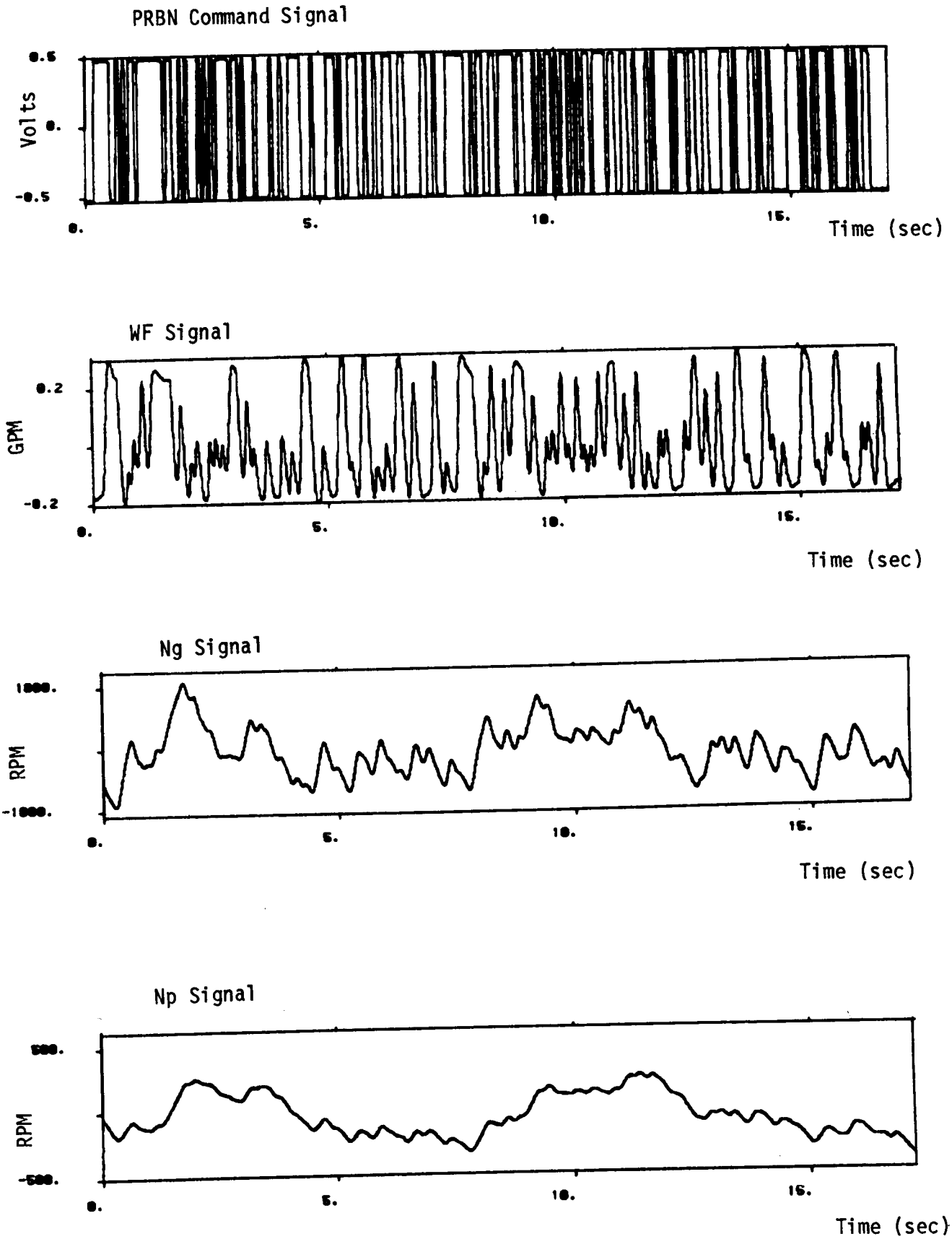


Figure 3.1 Engine Data Slice.

assumption that the engine data is ergodic; i.e., the statistical properties of the data are independent of the particular sample. The statistics for the same engine under the same conditions, therefore, should be identical. The ergodic assumption cannot be tested, however, with only one time series sample.

### 3.2.2 Frequency Response

The statistical properties of the engine data show the correlation between the engine input and outputs. The cross-spectrum $\gamma_{xy}(\omega)$ of the engine input and outputs and the autospectrum $\gamma_{xx}(\omega)$ of the engine input give a measure of the attenuation and phase shift between input and outputs. The cross and auto spectra are obtained from the statistical properties of the engine data. The engine frequency response transfer function $H(\omega)$ is

$$H(\omega) = \gamma_{xy}(\omega) / \gamma_{xx}(\omega) \quad . \tag{3.1}$$

The statistical properties and spectral analysis of the engine data are explained in detail in the following analysis.

### 3.2.3 Statistical Properties

The statistical properties of the engine data are obtained for a representative one minute time slice. Comparison of several minutes of time series data verifies the stationary process assumptions made.

#### 3.2.3.1 Autocovariance Function

The autocovariance function (ACVF) $\rho_{xx}(\tau)$ of a stochastic stationary process x(t) is the mean or expected value of the product of the centered processes x(t) and $x(t + \tau)$ so that

$$\rho_{xx}(\tau) = E\left\{[x(t) - m_x][x(t + \tau) - m_x]\right\} \tag{3.2}$$

where E denotes expected value, $\tau$ is the lag or difference between two instants of time t1 and t2 during the process, and $m_x$ is the mean value of x(t). The ACVF shows how the dependence or correlation between adjacent values of f(t) changes with the lag $\tau$. A discrete time estimate of the ACVF used in the IDPAC computer software is expressed as

$$R_{xx}(\tau) = \frac{1}{N} \sum_{t=1}^{N-\tau} [x_t - \bar{x}][x_{t+\tau} - \bar{x}] \tag{3.3}$$

$\tau = 0, 1, .. (N-1)$

where N is the number of discrete data samples and $\bar{x}$ is the sample mean. The sample mean $\bar{x}$ is

$$\bar{x} = \frac{1}{N} \sum_{t=1}^{N} X_t \tag{3.4}$$

An appreciation of the significance of the ACVF is obtained by considering the normalized ACVF $r_{xx}(\tau)$ where

$$r_{xx}(\tau) = R_{xx}(\tau)/\sigma_x^2 \tag{3.5}$$

and $\sigma_x^2$ is the variance of the function x(t). The value of the normalized ACVF lies between the limits -1 and +1, which correspond to 100% negative and 100% positive correlation, respectively.

3.2.3.2 Cross Covariance Function

The cross covariance function (CCVF) $\rho_{xy}(\tau)$ of a stochastic stationary process with input x(t) and output y(t) is

$$\rho_{xy} = E\left|[x(t) - m_x][y(t+\tau) - m_y]\right| \tag{3.6}$$

The cross covariance function indicates how the correlation between the input and output change with a shift in relative time $\tau$. A discrete time estimate of the ACVF is expressed as

$$R_{xy}(\tau) = \frac{1}{N}\sum_{t=1}^{N-\tau}[x_t - \bar{x}][y_{t+\tau} - \bar{y}] \qquad \tau = -(N-1),..,0,..,(N-1) \tag{3.7}$$

The normalized CCVF $r_{xy}(\tau)$ is

$$r_{xy}(\tau) = R_{xy}(\tau)/(\sigma_x \sigma_y) \tag{3.8}$$

where $\sigma_x$ and $\sigma_y$ are the standard deviations of x(t) and y(t), respectively.

3.2.3.3 Statistical Properties of the PRBN Signal

Figure 3.2a shows the normalized autocovariance function for a representative one minute sample of the PRBN command signal. The normalized ACVF for an ideal white noise signal (i.e. a signal containing an infinite range of frequencies) is equal to unity for $\tau$ equal to zero (i.e. it is perfectly correlated with itself) and is equal to zero elsewhere. The normalized autocovariance function shown in Figure 3.2a is, therefore, an approximation to that of ideal white noise. Figure 3.2b shows $r_{xx}(\tau)$ of five consecutive one-minute samples of engine data.

3.2.3.4 Statistical Properties of Fuel Flow Signal

Figure 3.3a shows the normalized ACVF for a representative one minute sample of the fuel flow signal WF. Figure 3.3b shows the normalized ACVF of five consecutive one-minute samples of engine data.

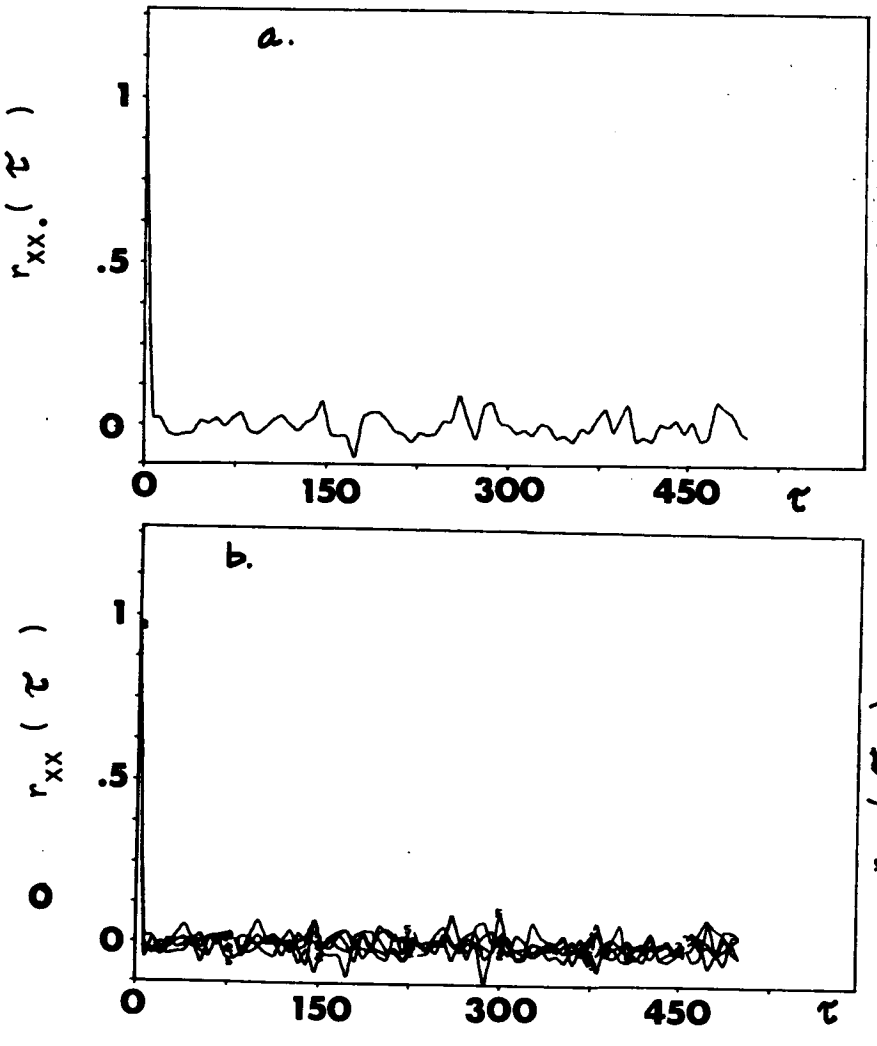


Figure 3.2 Normalized ACVF For PRBN Command Signal.

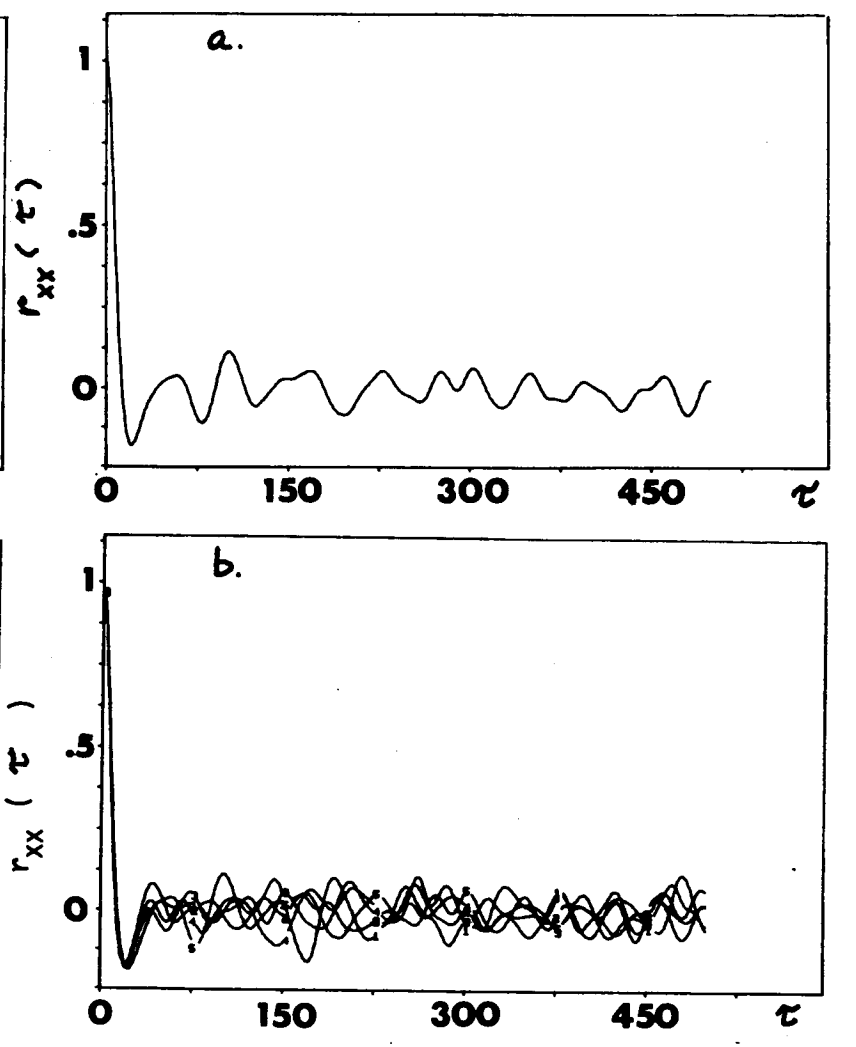


Figure 3.3 Normalized ACVF For WF Signal.

### 3.2.3.5 Statistical Properties of NG Signal

Figure 3.4a shows the normalized ACVF for a one minute sample of the NG signal. Figure 3.4b shows the normalized ACVF of five consecutive samples of engine data. Figure 3.5 shows the normalized CCVF between the input WF and output NG for a one minute sample.

### 3.2.3.6 Statistical Properties of Np Signal

Figure 3.6a shows the normalized ACVF for a one minute Np signal sample. Figure 3.6b shows the normalized ACVF of five consecutive one-minute samples of engine data. Figure 3.7 shows the normalized CCVF between WF and Np for the one minute sample.

The statistical properties of the engine input and outputs of several consecutive one-minute samples are quite similar, supporting the stationary process assumptions made.

## 3.2.4 Spectral Analysis

### 3.2.4.1 Autospectrum

The autospectrum $\gamma_{XX}(\omega)$ of x(t) is the Fourier transform of the ACVF $R_{XX}(\tau)$ where

$$\gamma_{XX}(\omega) = \frac{1}{2\pi}\int_{-\infty}^{\infty} R_{XX}(\tau)\, e^{-i\omega\tau}\, d\tau \qquad (3.9)$$

The autospectrum is the frequency decomposition of x(t). A smoothed spectral estimate of the autospectrum used in the IDPAC computer software is

$$S_{XX}(\omega) = \frac{T}{\pi}\left\{R_{XX}(0) + 2\sum_{\tau=1}^{L} R_{XX}(\tau)\,\mathrm{COS}\,(\omega\ T\ \tau)\, W_{BH}(\tau)\right\} \qquad (3.10)$$

where $W_{BH}(\tau)$ is a Blackman-Harris window and T is the sample period. The intent of the window is to introduce an equalizing effect in the estimated autospectrum. Increasing the number of lags decreases the "width" of the window and gives the spectral estimate more resolution.

The autospectrum of a one minute PRBN sample is shown in Figure 3.8. An ideal white noise signal has a uniform spectral density over all frequencies. Figure 3.8 shows that the PRBN signal has a uniform spectral density over the frequency range of 0.1 to 40 rad/sec. The PRBN signal is referred to as band-limited white noise in this region. Figure 3.9 shows the autospectrum of WF for a one minute sample.

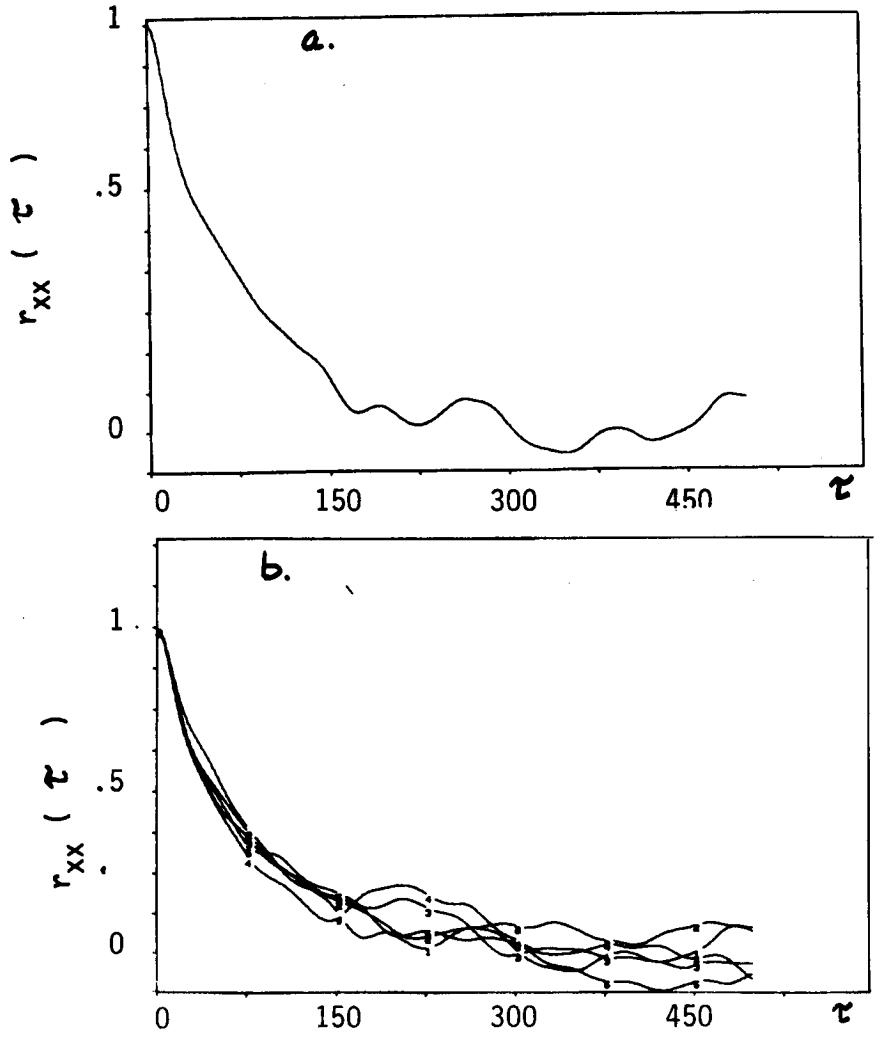


Figure 3.4 Normalized ACVF for NG Signal.

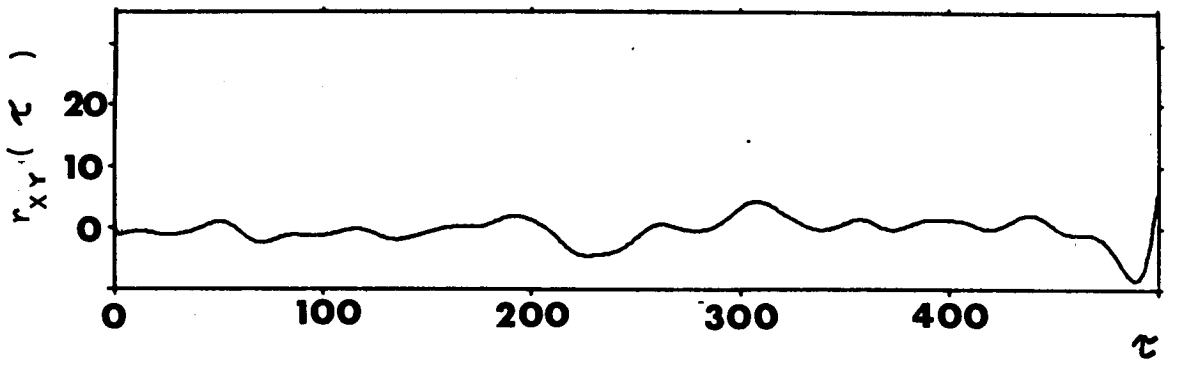


Figure 3.5 Normalized CCVF for WF-NG.

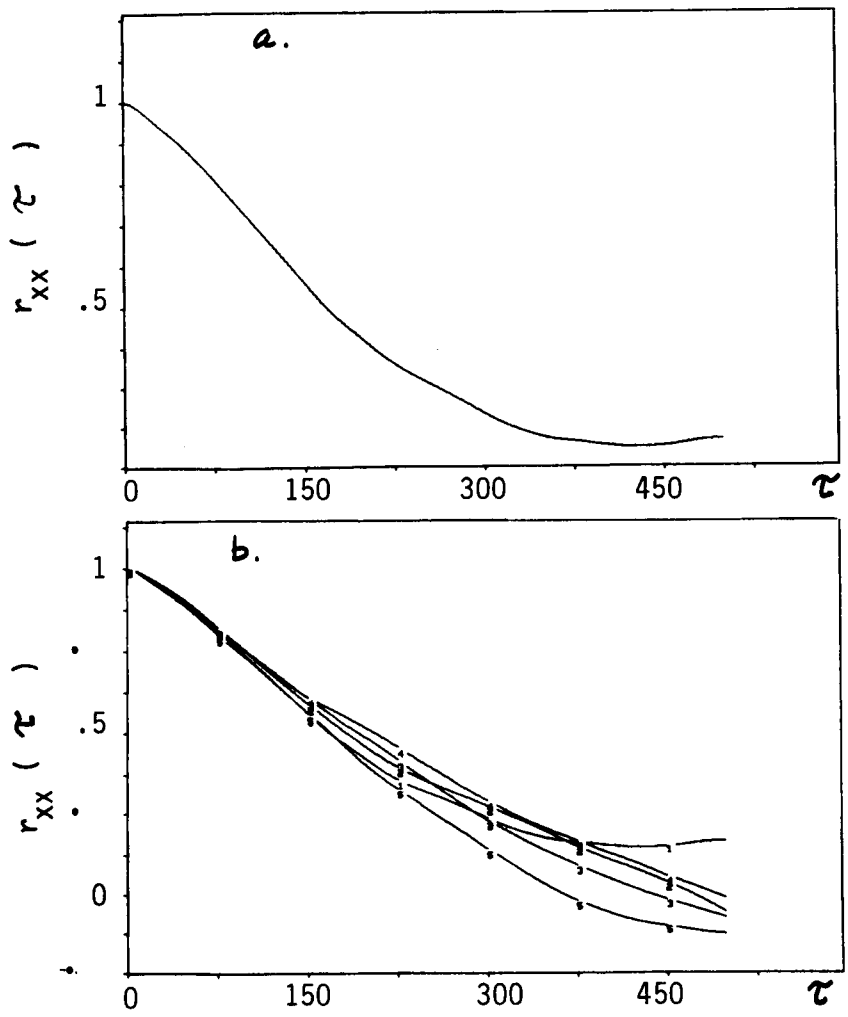


Figure 3.6 Normalized CCVF for Np Signal.

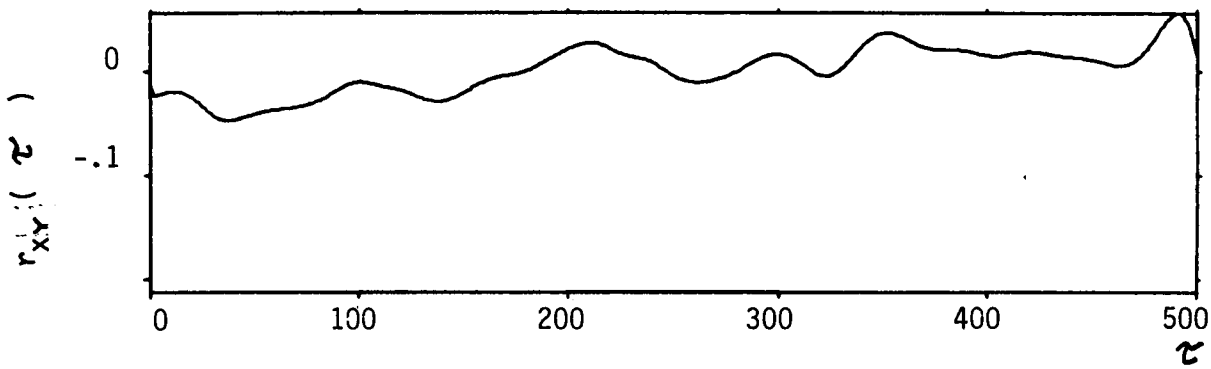


Figure 3.7 Normalized CCVF for WF-Np.

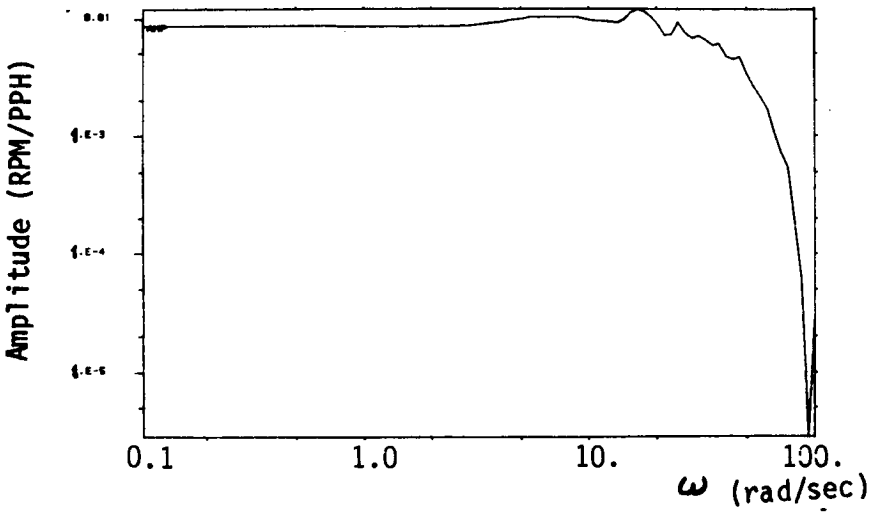


Figure 3.8 PRBN Autospectrum.

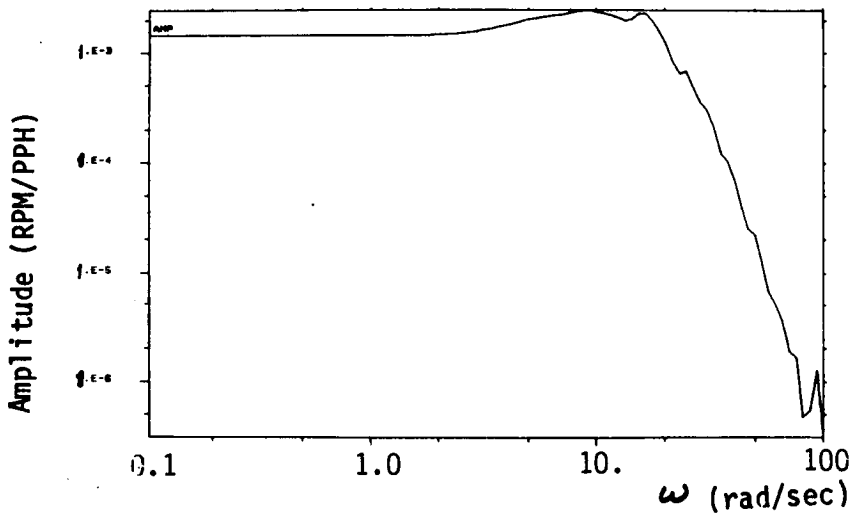


Figure 3.9 WF Autospectrum.

3.2.4.2 Cross-Spectrum

The cross-spectrum $\gamma_{xy}(\omega)$ relating the input x(t) and output y(t) of an arbitrary process is the Fourier transform of the CCVF $R_{xy}(\tau)$ where

$$\gamma_{xy}(\omega) = \frac{1}{2\pi}\int_{-\infty}^{\infty} R_{xy}(\tau)\, e^{-i\omega\tau}\, d\tau \quad . \tag{3.11}$$

The IDPAC computer software uses a smoothed spectral estimate of the cross-spectrum, $S_{xy}(\omega)$, obtained by dividing the CCVF into even and odd functions $Ev(\tau)$ and $O(\tau)$, respectively, where

$$EV(\tau) = 1/2\,[R_{xy}(\tau) + R_{xy}(-\tau)] \tag{3.12}$$

and

$$O(\tau) = 1/2\,[R_{xy}(\tau) - R_{xy}(-\tau)] \tag{3.13}$$

Equations (3.12) and (3.13) are used to compute the real and imaginary parts of the Fourier transform, $RS(\omega)$ and $IS(\omega)$, respectively, which are

$$RS(\omega) = \frac{T}{\pi}\left[EV(0) + 1/2 \sum_{\tau=1}^{L} EV(\tau)\, COS(\omega T \tau)\, W_{BH}(\tau)\right] \tag{3.14}$$

and

$$IS(\omega) = \frac{2T}{\pi} \sum_{\tau=1}^{L} [O(\tau)\, SIN(\omega T \tau)\, W_{BH}(\tau)]. \tag{3.15}$$

The magnitude of the transform is

$$\left|S_{xy}(\omega)\right| = \left\{[RS(\omega)]^2 + [IS(\omega)]^2\right\}^{1/2} \tag{3.16}$$

and the phase angle is

$$\measuredangle S_{xy}(\omega) = -\tan^{-1}[IS(\omega)/RS(\omega)]. \tag{3.17}$$

The cross-spectrum of WF and NG is shown in Figure 3.10. Figure 3.11 shows the cross-spectrum of WF and NP.

The frequency response $H(\omega)$ of NG versus WF, and NP versus WF is obtained by dividing the cross and auto spectra where

$$H(\omega) = S_{xy}(\omega)/S_{xx}(\omega). \tag{3.18}$$

The frequency response of NG versus WF is shown in Figure 3.12. Figure 3.13 shows the frequency response of NP versus WF.

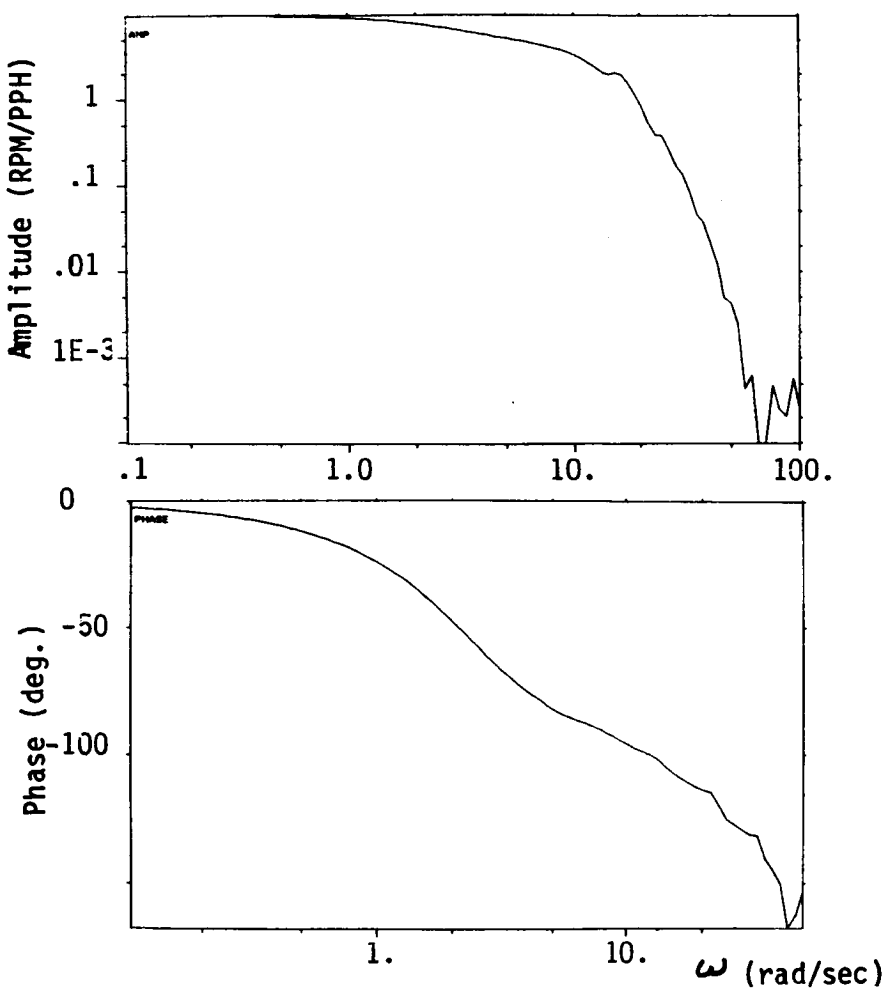


Figure 3.10 WF-NG Cross-Spectrum.

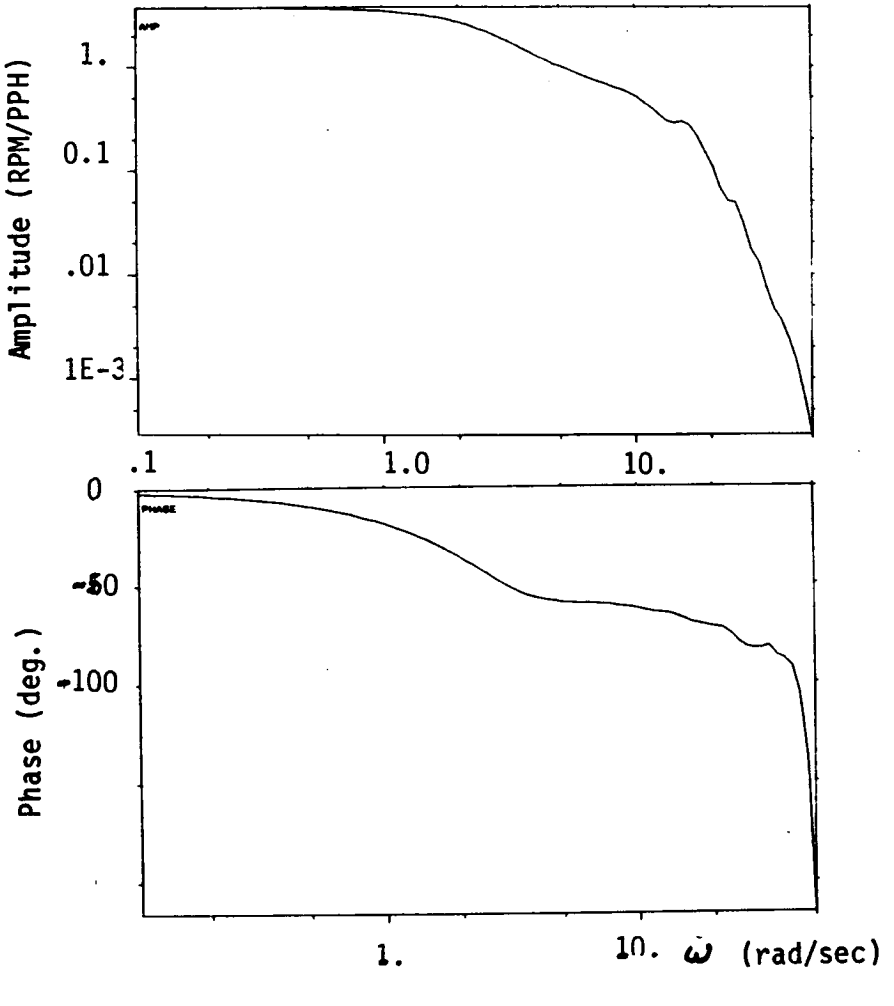


Figure 3.11 WF-Np Cross-Spectrum.

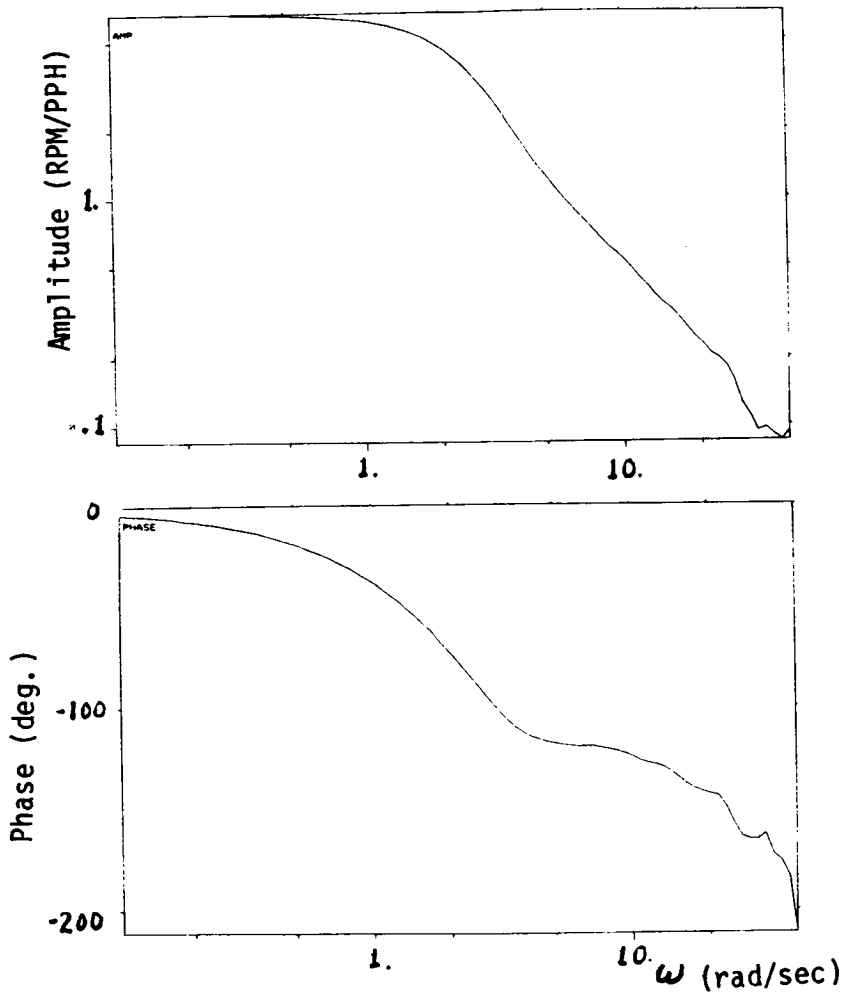


Figure 3.13 Np/WF Frequency Response (Spectral Analysis).

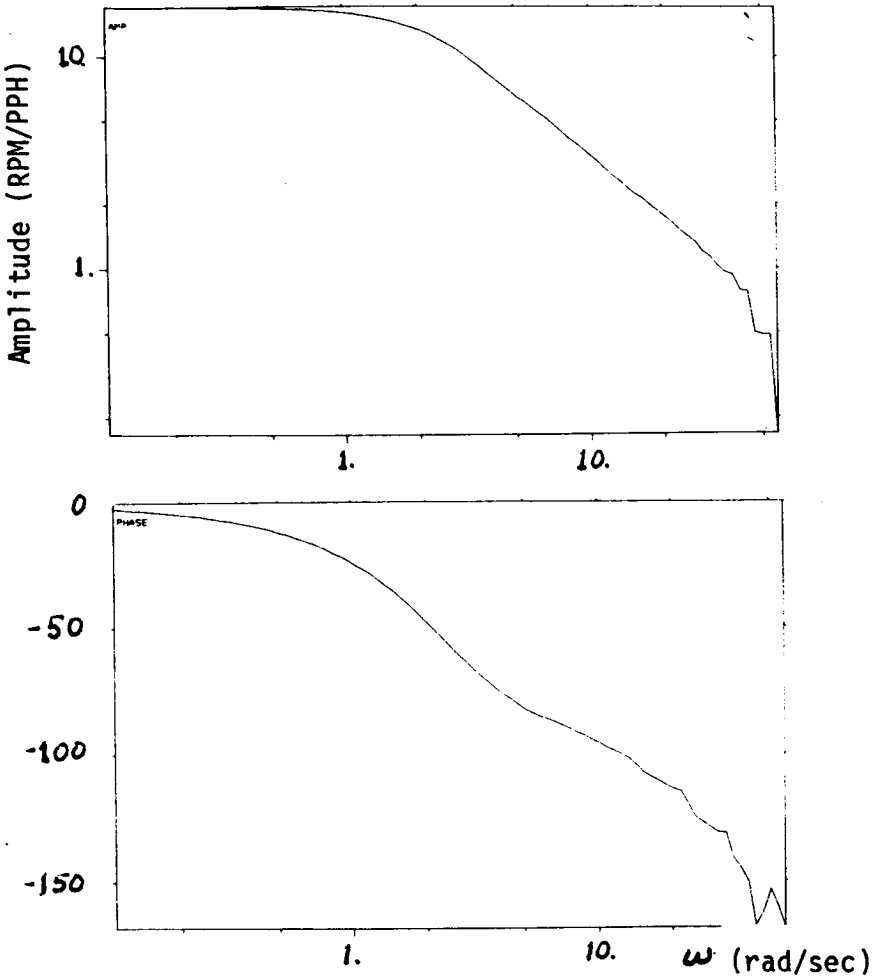


Figure 3.12 NG/WF Frequency Response (Spectral Analysis).

### 3.2.5 Maximum Likelihood Model Identification

Model identification techniques are used as an alternate method of obtaining the frequency response of the T700 engine from the time series data. An optimal model of the engine was identified using a maximum likelihood (ML) model identification algorithm. The ML estimate of a multi-input, single output system is of the form

$$A(z^{-1})\, y(\tau) = \sum_{i=1}^{n} B_i\,(z^{-1})\, X_i\,(t) + \lambda\, C(z)^{-1} e(t) \qquad (3.19)$$

Subject to minimizing the loss function

$$V(\theta) = \frac{1}{2} \sum_{i=1}^{N} e^{2}\,(t) \qquad (3.20)$$

where
- $A$ = characteristic polynomial
- $y(t)$ = system output
- $B_i$ = input polynomial coefficients
- $Z^{-1}$ = Z transform unit delay
- $X_i$ = system inputs
- $n$ = number of inputs
- $\lambda$ = lambda
- $C$ = residual polynomial
- $e(t)$ = residual

$$\theta = (a_1, \ldots, a_n, b_1, \ldots, b_{1m}, \ldots, b_{n1}, \ldots, b_{nm}, c_1, \ldots, c_n)$$

The residuals in equation (3.19) can be visualized as noise corrupting the output of a deterministic model. The use of the ML algorithm was chosen so as to handle the general case where the residuals are correlated. The problem is solved by estimating the parameters in $\theta$ subject to minimizing equation (3.20) and providing the maximum likelihood estimate of $\lambda$ by

$$\lambda^2 = \frac{2}{N} V(\theta) \qquad (3.21)$$

where $\theta$ is the minimum point of V.

The best ML estimate for the NG/WF model was determined to be of eighth order. Software limitations prevented the identification of higher order models.

The accuracy of the model was evaluated by testing the residuals of equation (3.20). The normalized ACVF of the eighth order model residuals is shown in Figure 3.14a. The normalized CCVF of the input WF and the residuals for the eigth order model is shown in Figure 3.14b. For an ideal model, the residuals

should be white noise; i.e., the normalized autocorrelation function should be equal to unity for $\tau$ equal to zero, and zero elsewhere. The CCVF between the input and residuals should be zero everywhere; i.e., the input and the output noise are uncorrelated. The figures contain a 5% tolerance band indicating the region inside which the estimates of the residual correlations should lie if the input and residuals are independent, or uncorrelated.

The best ML estimate for the NP/WF model was limited to eighth order, also. The normalized ACVF for the eighth order NP/WF model is shown in Figure 3.15a. Figure 3.15a shows the normalized CCVF between the input and residuals for the eigth order NP/WF model.

### 3.2.5.1 Model Frequency Response

The transfer function of the ML model is

$$H_{ML}(\omega) = \frac{\sum_{i=i}^{n} B_i (z^{-1})}{A(z^{-1})} \qquad (3.22)$$

The frequency response of $H_{ML}(\omega)$ for the NG/WF eighth order model is shown in Figure 3.16. Figure 3.17 shows the frequency response of $H_{ML}(\omega)$ for the NP/WF model. Figure 3.18 compares the ML model and spectral analysis results for NG/WF. Figure 3.19 compares the ML model and spectral analysis results for NP/WF. Discrepancies are seen between the engine frequency responses obtained through spectral analysis and those obtained by model identification techniques. The magnitudes of the spectral analysis frequency responses are consistently lower those that of the maximum likelihood results. Jenkins and Watts (Ref. 18) show that the smoothed spectral density is considerably underestimated for a relatively low number of lags, $\tau$. Software limitations restrict the maximum number of lags to 500. For a one minute sample slice of 12,000 data points (200 Hz sampling rate) the maximum number of lags is only 4% of the number of data points compared to a recommended 5% to 20%. The magnitude, break frequency and, consequently, the phase of the frequency responses are quite biased under these conditions.

### 3.2.5.2 NASA Discrete Frequency Data

Table 3.1 lists the magnitude and phase of the engine discrete frequency test points supplied by NASA. Figure 3.20 compares the magnitude and phase of the discrete frequency points and ML model for NG/WF. Figure 3.21 compares the magnitude and phase of the NASA data and the ML model for NP/WF.

The ML model frequency response compares very well with the NASA discrete frequency points for both NG/WF and NP/WF.

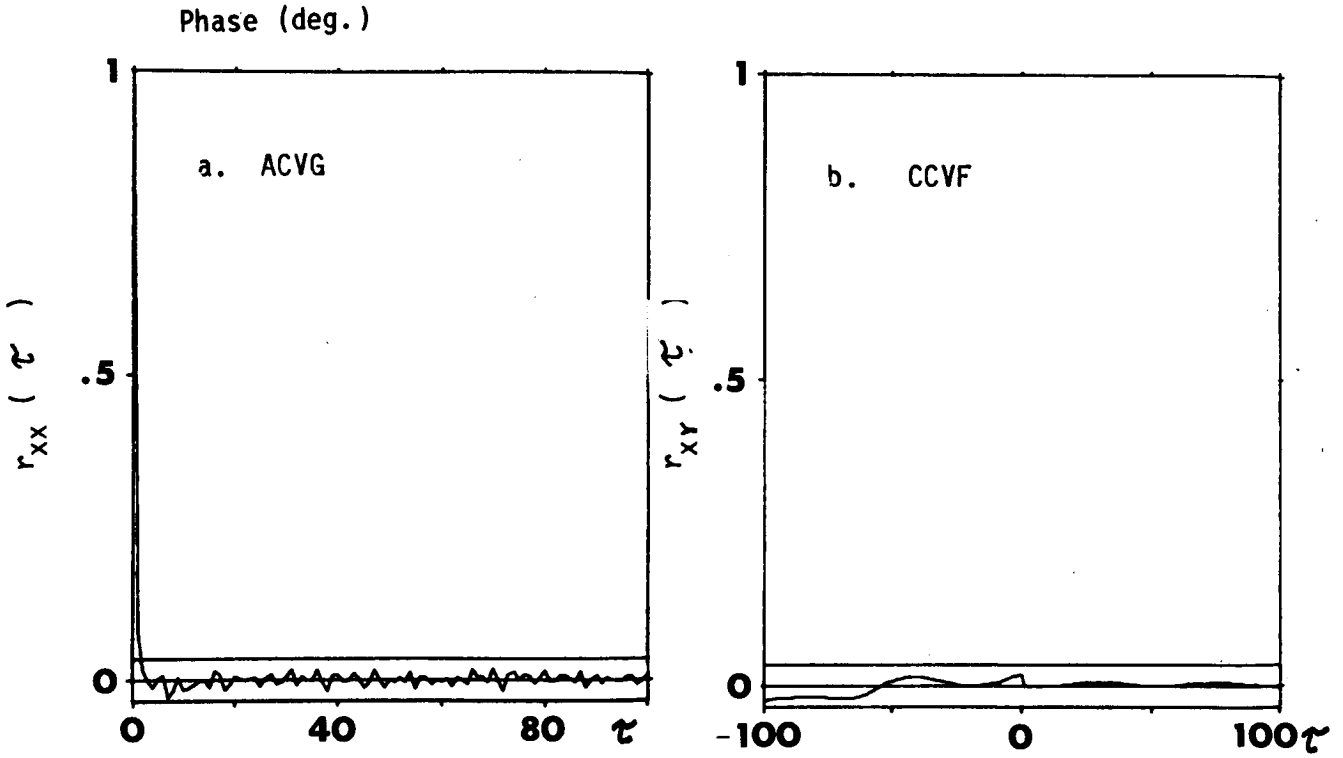


Figure 3.14 NG/WF Model Residuals.

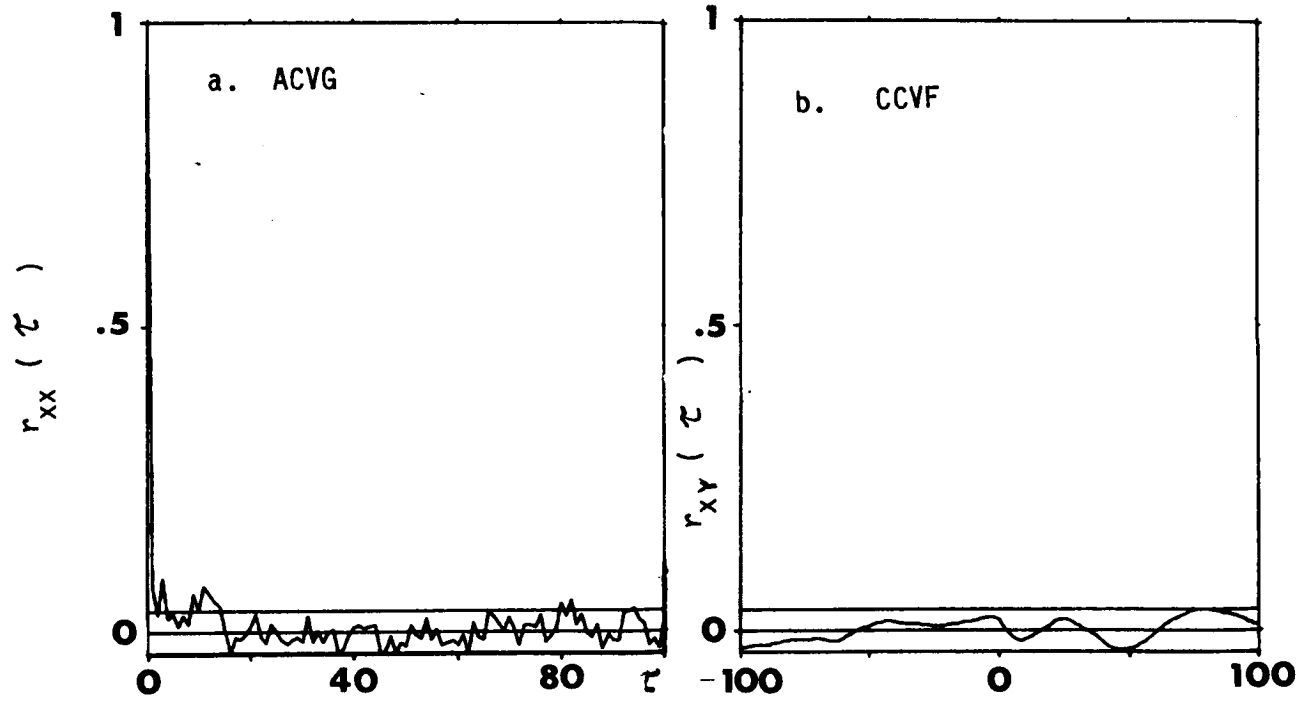


Figure 3.15 Np/WF Model Residuals.

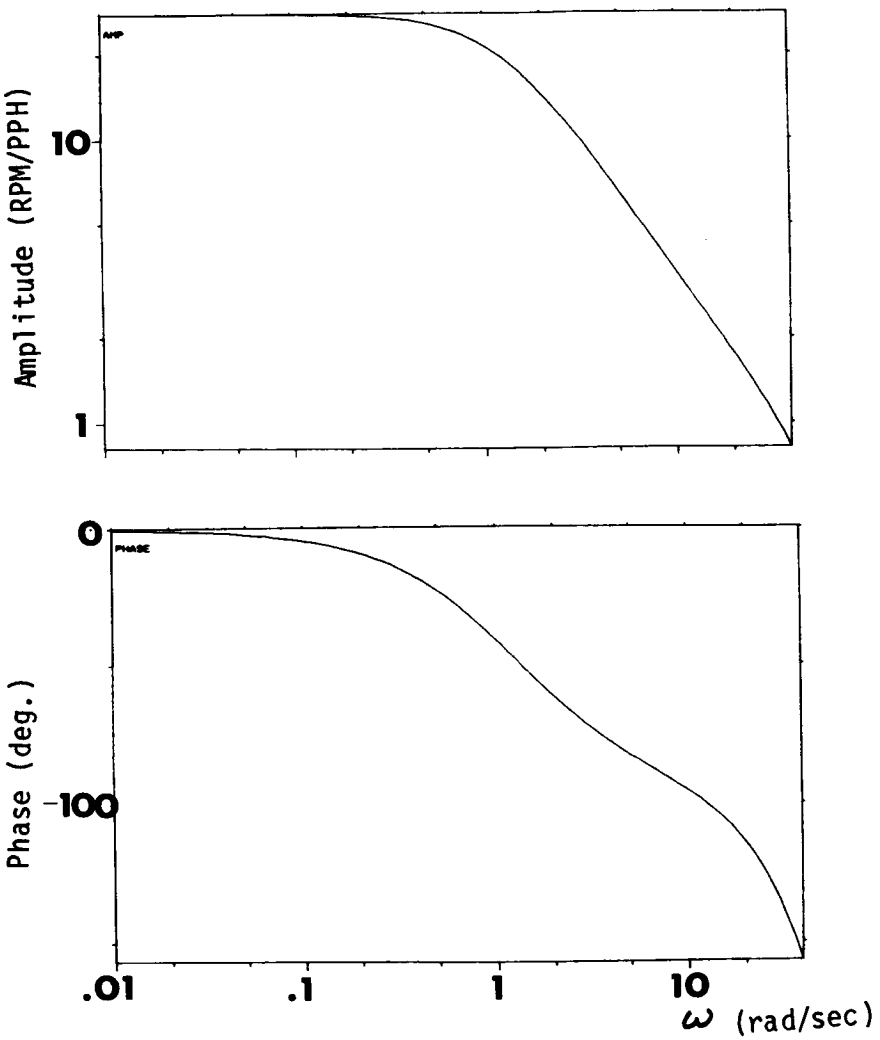


Figure 3.16 NG/WF ML Model Frequency Response.

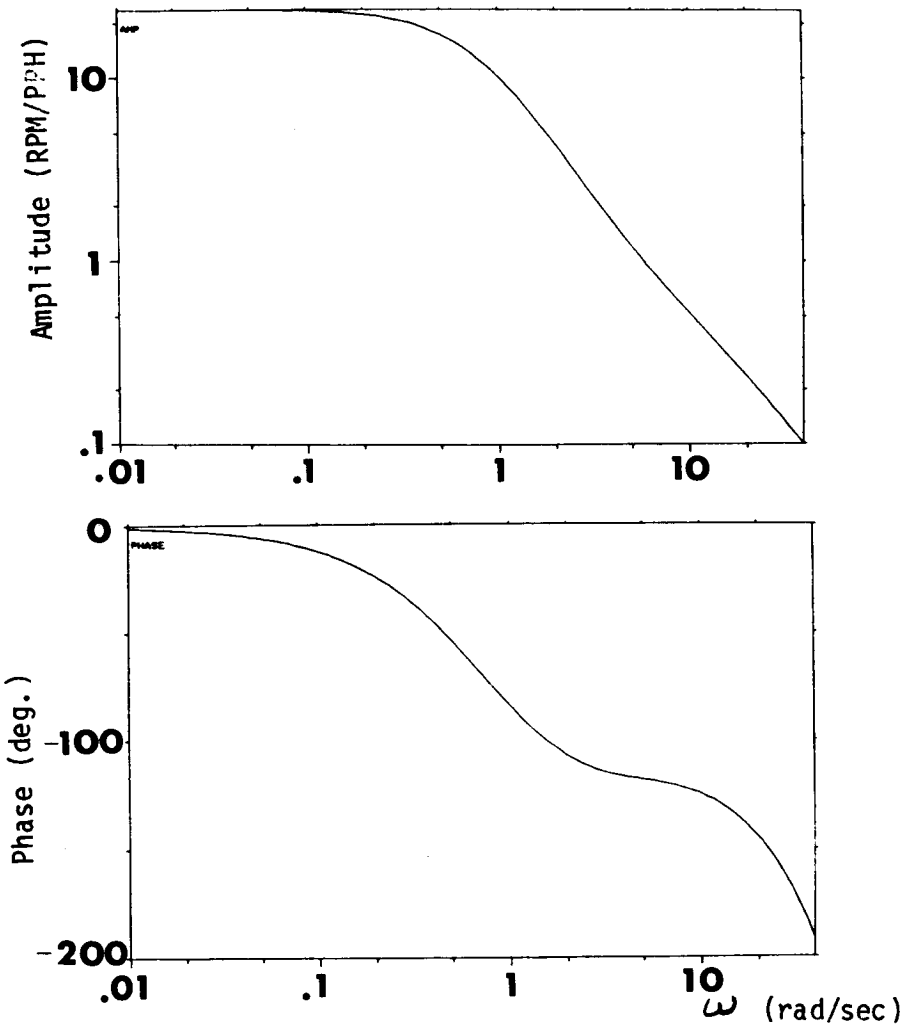


Figure 3.17 Np/WF ML Model Frequency Response.

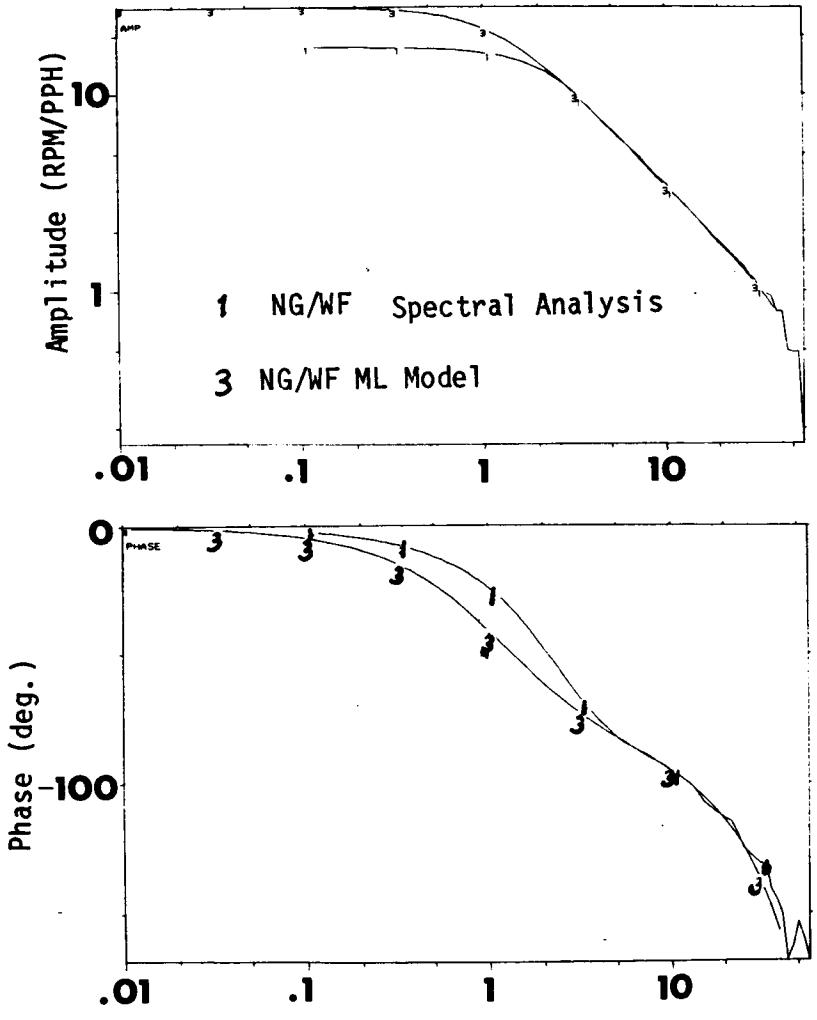


Figure 3.18 NG/WF Frequency Response Comparison.

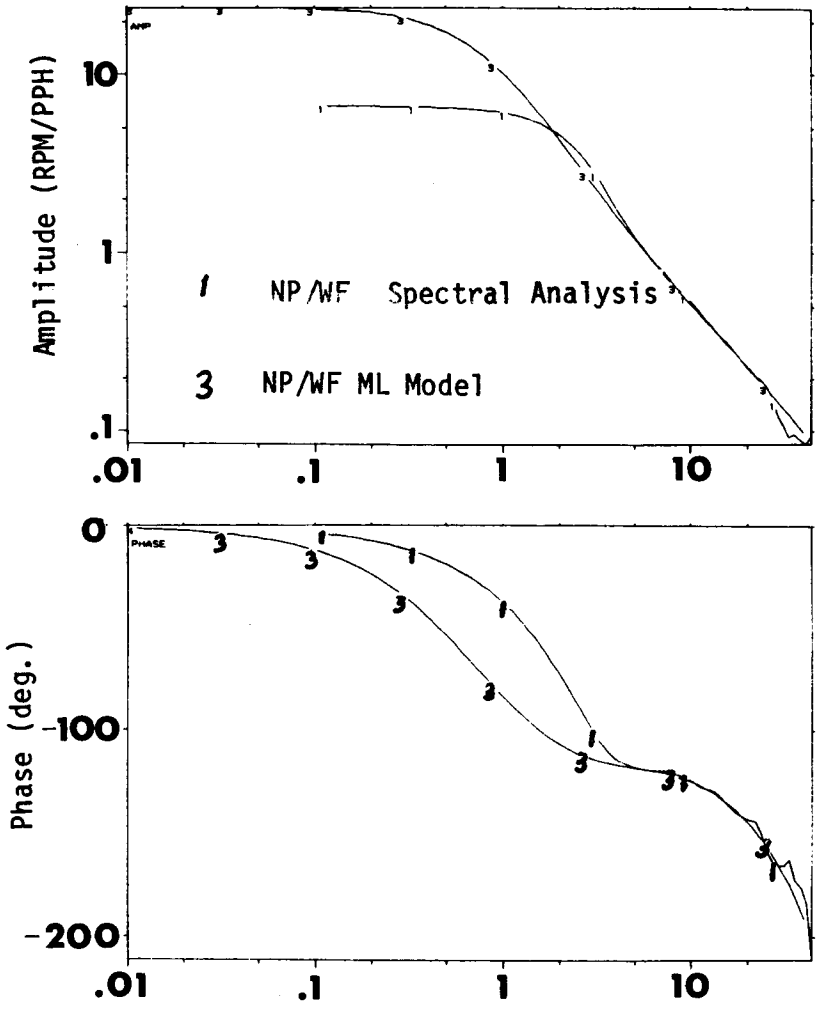


Figure 3.19 Np/WF Frequency Response Comparison.

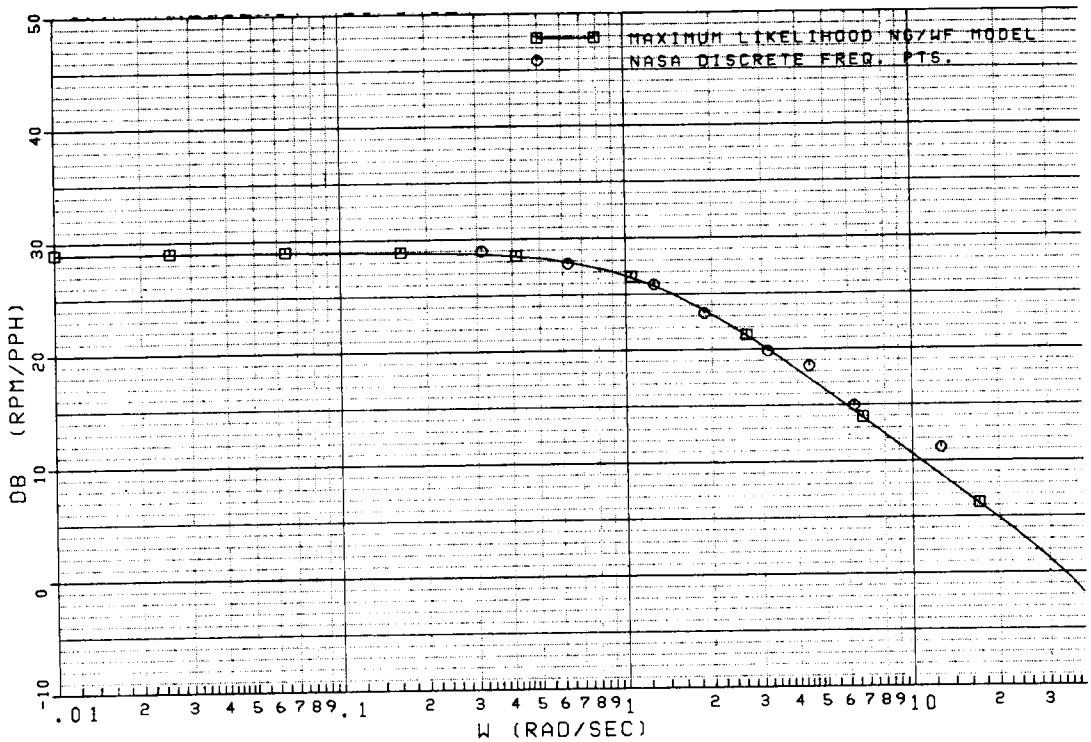


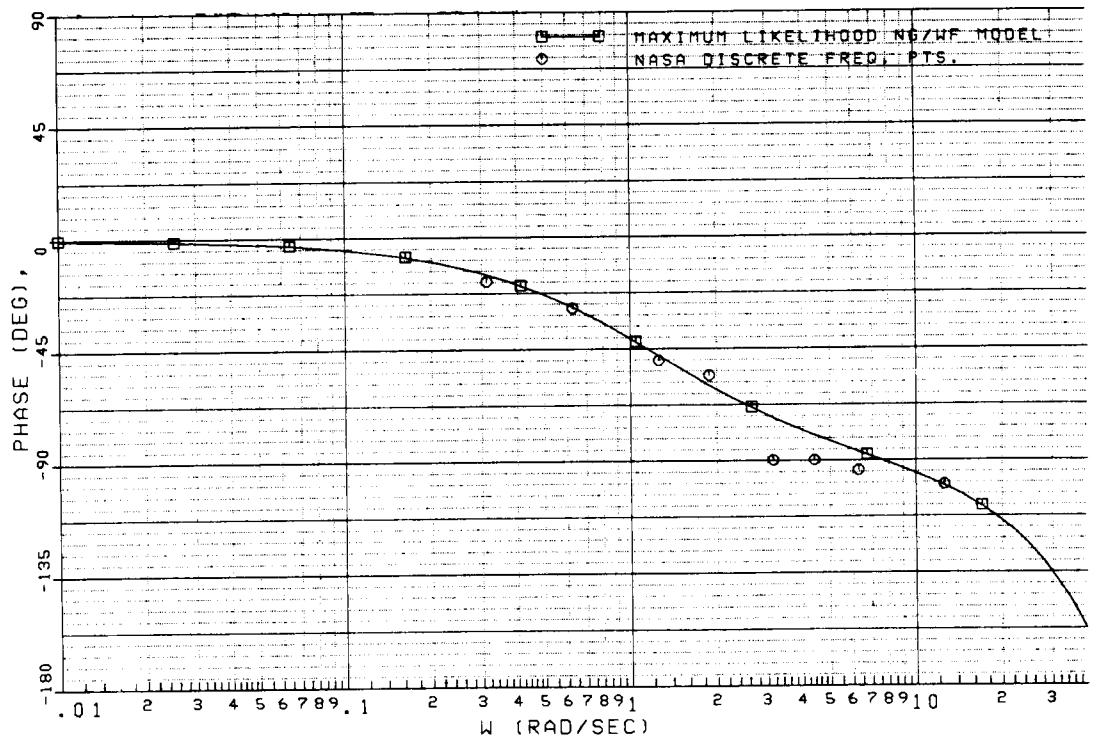


Figure 3.20 NG/WF Frequency Response.

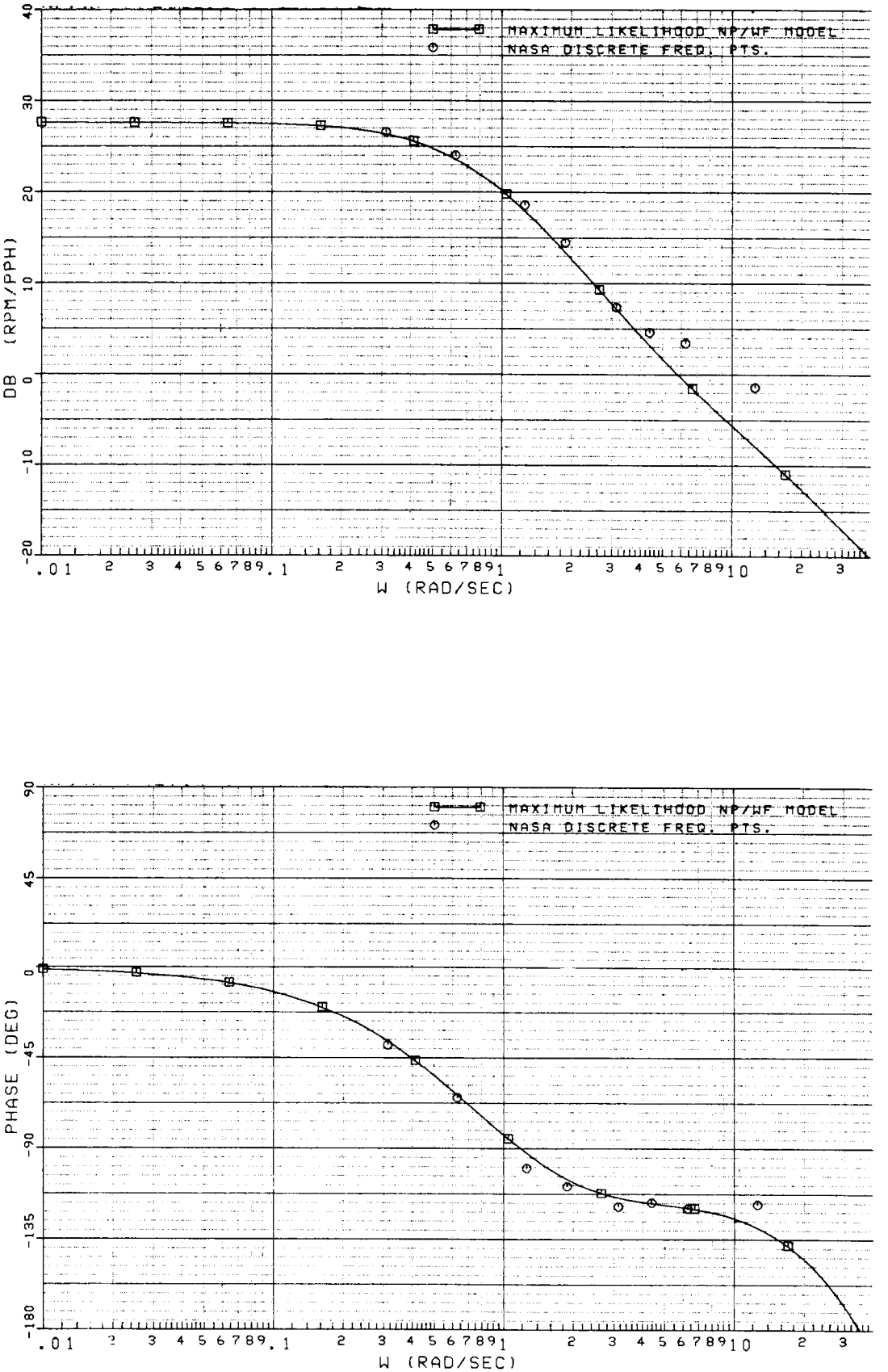


Figure 3.21 Np/WF Frequency Response.

### 3.2.5.3 Identifying Partial Derivatives

Reduced order models were obtained from the ML frequency response data and compared to the simplified linear engine model, shown in Figure 3.22, in order to identify engine partial derivatives.

Table 3.1 NASA Discrete Frequency Data

| W(rad/sec) | Gain, RPM/PPH (dB) | | Phase (degrees) | |
|---|---|---|---|---|
| | NG/WF | NP/WF | NG/WF | NP/WF |
| 0.314 | 28.9 | 26.5 | -10.0 | -39.0 |
| 0.628 | 27.7 | 24.0 | -29.0 | -65.0 |
| 1.257 | 25.8 | 18.5 | -50.0 | -100.0 |
| 1.885 | 23.2 | 14.5 | -56.0 | -109.0 |
| 3.142 | 19.8 | 7.3 | -90.0 | -119.0 |
| 4.392 | 18.4 | 4.6 | -90.0 | -117.0 |
| 6.283 | 14.9 | 3.4 | -94.0 | -120.0 |
| 12.566 | 11.2 | -1.5 | -100.0 | -118.0 |

#### 3.2.5.3.1 $\Delta$ NG/ $\Delta$ WF

Figure 3.23 compares the gain and phase of the linear model and eighth order ML model of NG/WF. There is less than a 3db difference in magnitude and approximately 10 degrees difference in phase at 10 rad/sec.

The state-space equation for NG derived from Figure 3.22 is

$$\Delta\dot{NG} = \frac{1}{JG}\left(\frac{\partial QG}{\partial NG}\right)\Delta NG + \frac{1}{JG}\left(\frac{\partial QG}{\partial WF}\right)\Delta WF \qquad (3.23)$$

Note that all partials in $\partial$ VG are neglected since the engine is tested with locked variable geometry. The partial derivatives in the linear model were calculated using locked VG. The effects of PS3 and T45 are also neglected since the corresponding dynamics are assumed to be fast compared to QG and QPT dynamics.

The Laplace transform transfer function for $\Delta$NG/ $\Delta$ WF derived from equation (3.23) is

$$\frac{\Delta NG}{\Delta WF} = \frac{\frac{1}{JG}\left(\frac{\partial QG}{\partial WF}\right)}{\left(s - \frac{1}{JG}\left(\frac{\partial QG}{\partial NG}\right)\right)} \qquad (3.24)$$

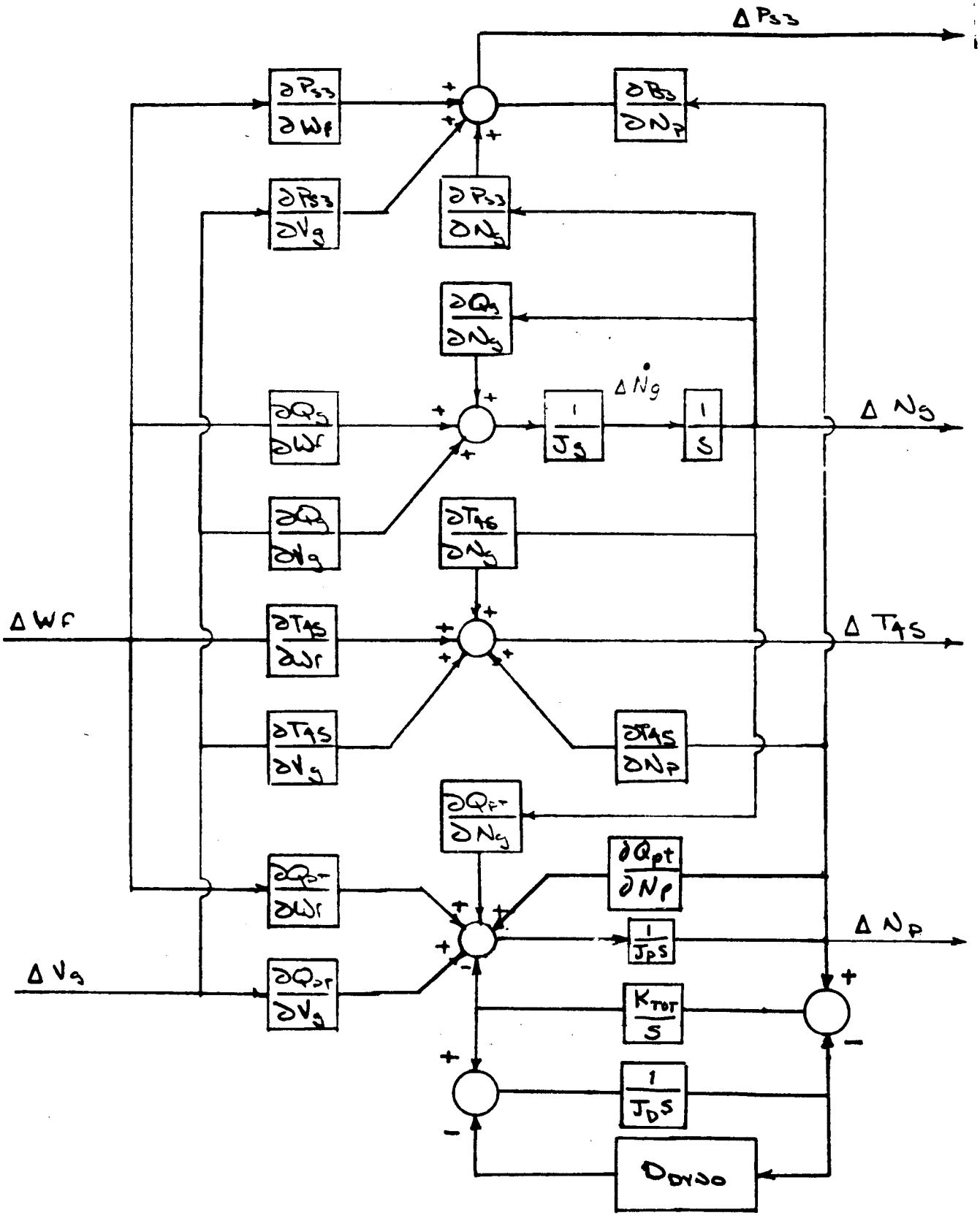


Figure 3.22 Linear Engine Model.

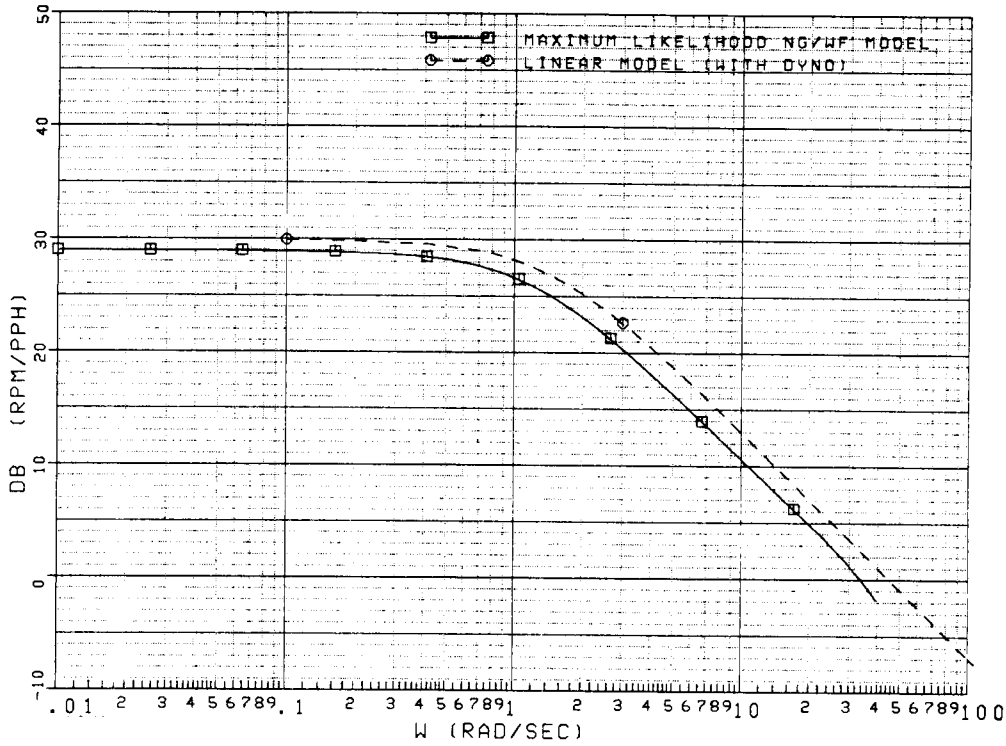


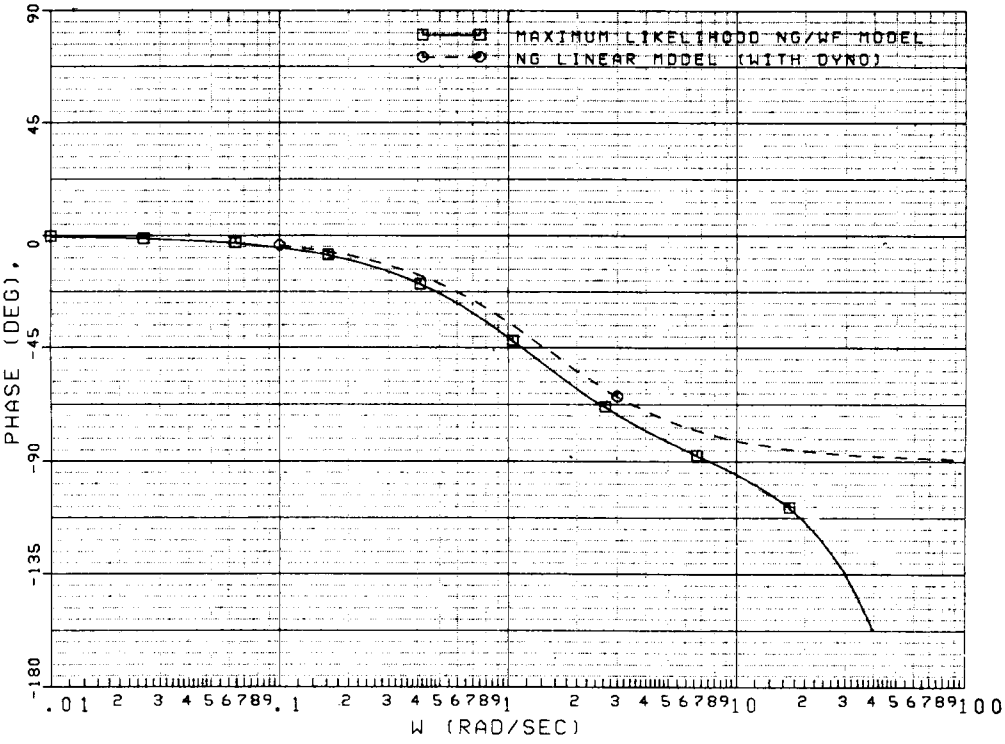


Figure 3.23 NG/WF Frequency Response.

where JG is the gas turbine inertia;

$$JG = 0.00466 \text{ ft. lb. sec/RPM} \tag{3.25}$$

A reduced order Laplace transform transfer function for the NG/WF ML model is computed from the frequency response data using an iterative curve-fitting program that minimizes the gain and phase error between the computed and actual frequency response data. The identified NG/WF transfer function, restricted to a first order model fit, is

$$\frac{\Delta NG}{\Delta WF} = \frac{30.09}{(s + 1.075)} \tag{3.26}$$

The partials $\partial QG/\partial WF$ and $\partial QG/\partial NG$ are identified by equating equations (3.25) and (3.26). Table 3.2 compares the identified partials with the computer generated linear model partials. The identified and linear model partial derivatives compare fairly well.

Table 3.2. NG/WF Partials (92% NG)

| Partial | Identified | Linear Model |
|---|---|---|
| $\frac{\partial QG}{\partial NG}$ $\frac{(ft.lb)}{(RPM)}$ | -0.0050 | -0.0067 |
| $\frac{\partial QG}{\partial WF}$ $\frac{(ft.lb)}{(RPM)}$ | +0.14 | +0.21 |

3.2.5.3.2 $\Delta NP/\Delta WF$

Figure 3.24 compares the gain and phase, of the $\Delta NP/\Delta WF$ linear model and eigth order ML model for NP/WF. The linear model frequency response diverges from that of the ML model at higher frequencies. There is approximately 4 db difference in magnitude and over 30 degrees difference in phase at 10 rad/sec.

The state-space equation for NP derived from Figure 22 is

$$\dot{\Delta NP} = \frac{1}{(JPT + JD)} \frac{\partial QPT}{\partial NG} \Delta NG + \frac{1}{(JPT + JD)} \left[\frac{\partial QPT}{\partial NP} - D_{dyno}\right] \Delta NP \tag{3.27}$$

where JD is the dynamometer inertia,

$$JD = 0.0371 \frac{\text{ft.lb sec}}{\text{RPM}} \tag{3.28}$$

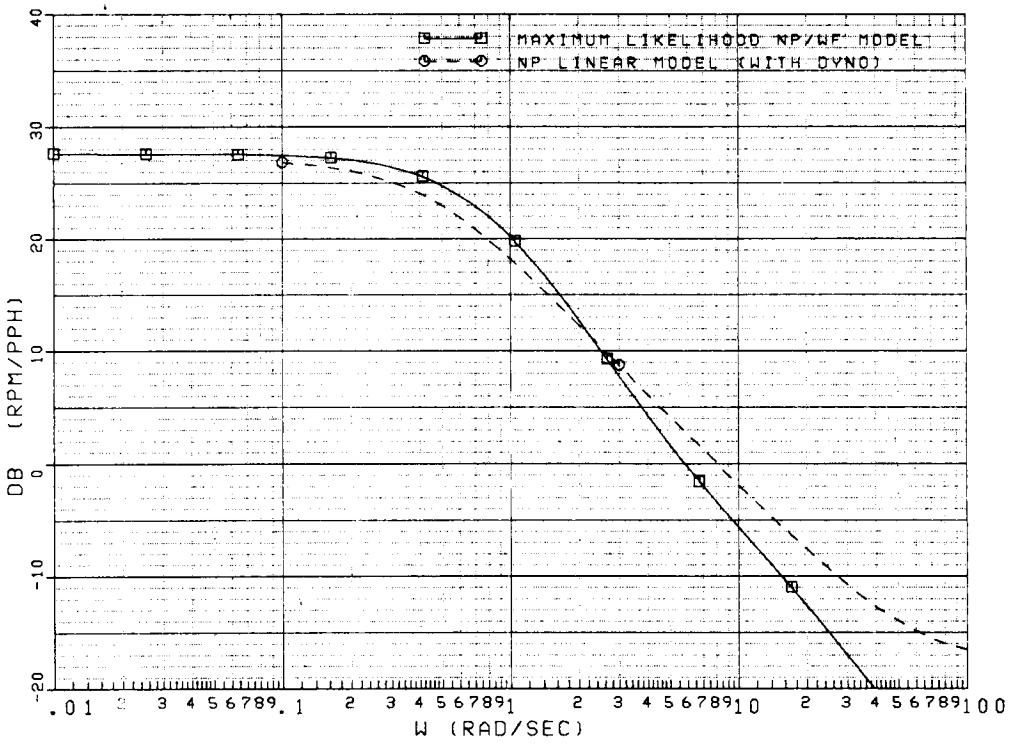


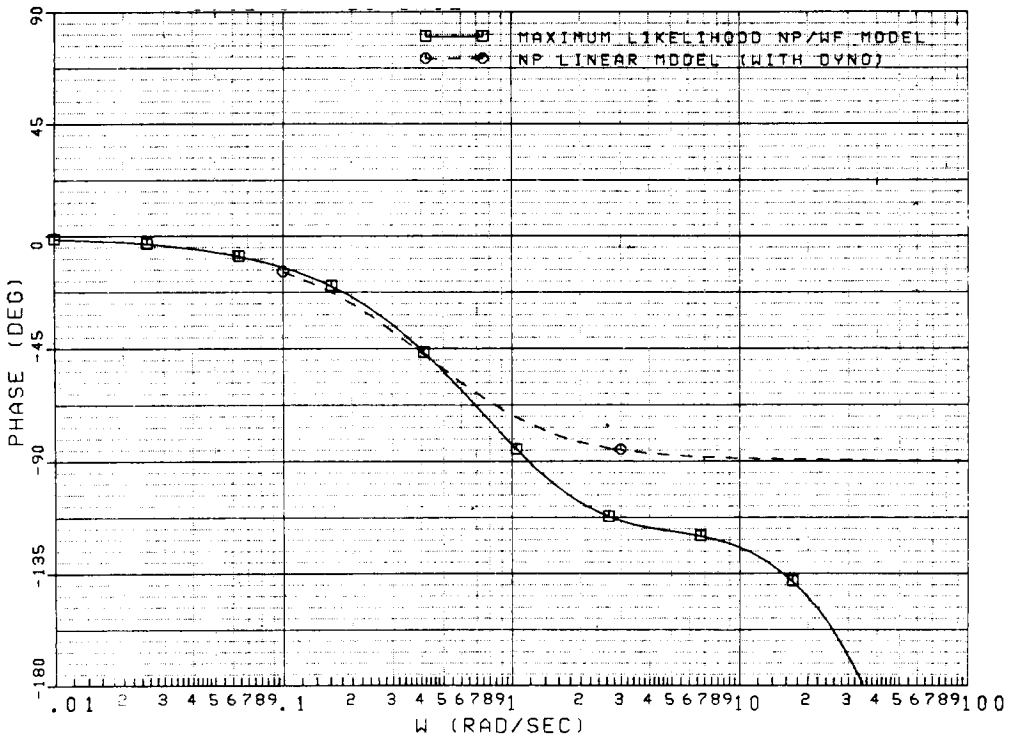


Figure 3.24 Np/WF Frequency Response.

and JPT is the power turbine inertia,

$$JPT = 0.0108 \frac{ft.lb\ sec}{RPM} \tag{3.29}$$

The dynamometer damping, D dyno, is

$$D_{dyno} = 0.0089 \frac{ft.lb}{RPM} \tag{3.30}$$

Note that the dynamometer model was further simplified by assuming an infinite power turbine/dynamometer shaft stiffness $K_{tot}$. The dynamometer and power turbine inertias are, consequently, lumped together.

The Laplace transform transfer function for $\Delta NP/\Delta WF$ derived from equation (3.27) is

$$\frac{\Delta NP}{\Delta WF} = \frac{\left(\frac{1}{JT}\ \frac{\partial QPT}{\partial WF}\right)s - \left[\frac{1}{J_T J_G}\left(\frac{\partial QG}{\partial NG}\ \frac{\partial QPT}{\partial WF} - \frac{\partial QPT}{\partial NG}\ \frac{\partial QG}{\partial WF}\right)\right]}{\left(s - \frac{1}{JG}\ \frac{\partial QG}{\partial NG}\right)\left(s - \frac{1}{JT}\left(\frac{\partial QPT}{\partial NP} - D_{dyno}\right)\right)} \tag{3.31}$$

where JT is the lumped dynometer/power turbine inertia.

$$JT = JPT + JD. \tag{3.32}$$

The NP/WF transfer function obtained from a second-order fit of the ML frequency response data is

$$\frac{\Delta NP}{\Delta WF} = \frac{(0.0021)\ s + 64.26}{(s + 0.3702)(s + 9.66)} \tag{3.33}$$

The remaining engine partial derivatives are obtained by equating equations (3.31) and (3.33). Table 3.3 contains the partials derived from NP/WF.

Table 3.3 NP/WF Partials (92% NG)

| Partial | Identified | Linear Model |
|---|---|---|
| $\frac{\partial QPT(ft.lb)}{\partial WF\ (RPM)}$ | $+1.01 \times 10^{-4}$ | +0.35 |
| $\frac{\partial QPT(ft.lb)}{\partial NP\ (RPM)}$ | -0.47 | -0.009 |
| $\frac{\partial QPT(ft.lb)}{\partial NG\ (RPM)}$ | +0.089 | +0.0017 |

Table 3.3 indicates that there is a very poor correlation between the identified NP/WF partials and the linear model partials.

Since the NP/WF ML model and linear model frequency responses didn't compare well past 1 rad/sec, a poor correlation between the identified partials and linear model partials was expected. The divergence of the linear model response from that of the actual engine is attributed, in part, to the linear model dynamometer representation.

## 4.0 Introduction: Variable Geometry Off-Schedule Modeling

The design of high performance turboshaft engine control systems focuses on modern control and adaptive control techniques which improve overall helicopter performance and reduce pilot workload. Some adaptive control feature concepts under current investigation at General Electric are aimed at improving engine transient response through control of the engine variable geometry (VG).

The conventional control system design procedure involves the use of detailed engine computer models during preliminary design efforts. In order to adequately design and implement control systems based on modified VG control schedules and algorithms, VG off-design performance must be validated in the engine models.

The objective of this study was to investigate the compressor variable geometry off-angle effects through analysis of the NASA YT700 engine test data. Off-schedule VG data were used to validate the L0023J DISCUS T700 engine transient computer model.

Steady-state test data were obtained with the nominal VG schedule, 6 degrees off-schedule in the open direction, and 6 degrees off-schedule in the closed direction conditions. The performance data were compared with data obtained from T700 transient model simulations.

### 4.1 Procedure

#### 4.1.1 Off-Design VG Test

The following procedure details the equipment and techniques used to conduct the off-design VG testing of the NASA YT700 engine.

##### 4.1.1.1 Hardware

The hardware required for the engine tests include:

- The microprocessor control, Engine Monitoring and Control (EMAC), unit.
- An interface unit to act as a feedback "loop closer" and to drive electrohydraulic servo valves.
- A YT700 engine (207214-34).
- A modified YT700 control (ref. contract NAS3-22763).

- An engine loading device (i.e., eddy current dynamometer).
- A sea level static test stand.
- An analog computer to schedule engine loading and other calculations as required.

4.1.1.2 Data Acquisition

Steady-state data from engine tests performed at the Engine Components Research Laboratory (ECRL) was recorded on the Lewis Central steady-state system (ESCORT) and on the Microcomputer Interactive Data System (MINDS).

4.1.1.3 Test Matrix

Engine performance data were recorded with VG off schedule by 0 degrees (nominal), 6 degrees in the open direction, 6 degrees in the closed direction, 3 degrees in the open direction, and 3 degrees in the closed direction.

1. Nominal schedule performance. The following procedure was used to conduct engine testing on the nominal VG schedule.
   a. Advance LDS to achieve a minimum of 92% corrected core speed ($NG/\sqrt{\theta}$) and hold for 10 minutes.
   b. Advance LDS to maximum load (slowly), hold for 5 minutes, and take steady-state reading.
   c. Advance LDS (very slowly) to achieve the following corrected speeds and take steady-state readings:
      - Maximum (approximately 95%)
      - 93%
      - 90%
      - 86%
      - 83%
      - 78% (VG schedule break point)
      - 73%

2. Off-schedule (6 degrees in open direction).

   a. Advance to 95% NG/$\sqrt{\theta}$ and stabilize for 5 minutes. Reset stage 1 VG to 6 degrees open from nominal. Record data.

   b. Repeat procedure 1.c. for 6 degrees off-schedule (open).

3. Off-schedule (6 degrees in closed direction).

   a. Advance to maximum power and stabilize for 5 minutes. Reset stage 1 VG to 6 degrees closed from nominal. Record data.

   b. Repeat procedure 1.c. for 6 degrees off-schedule (closed).

4. Repeat parts 2. and 3. for 3 degrees open and 3 degrees closed.

## 4.2 Analysis

### 4.2.1 Analysis of Off-Angle HPVG Steady State Calibrations

Figures 4.1-4.5 show differences between model predictions (L0023J) and the STEP engine data compressor performance for nominal, 6° closed, and 6° open Stage 1 variable vane deviations. Lynn pre-shipment performance is also shown.

Figures 4.1 shows that the compressor flow at speed is quite low relative to prediction (approximately 10%). This is attributed to the fact that tip clearances were deliberately increased for the last three axial stages in order to avoid stall problems from the anticipated severe testing. The NASA flow at speed was about 3% high relative to the Lynn calculation. This difference results from Lynn using the measured P2 for performance calculations while NASA used the calculated P2. The calculated P2 agrees with cycle predictions (as it should), and it is believed that the measured P2 is high because of pressure profiles. Figure 4.6 shows comparisons between measured and predicted compressor corrected flow after the prediction flow is debited by 10%. The measured versus the predicted off angle effects now agree quite closely.

Figures 4.2 and 4.3 show that the measured pressure ratio is extremely high for both the axial and overall compressor. Measurement errors are suspected since the compressor would be close to stall at these pressure ratio levels.

Figures 4.4 and 4.5 show axial and overall efficiency trends. The measured overall efficiency is 3-4 points higher than prediction while the axial efficiency has about the same level. Both exhibit different off angle effects from prediction. Since pressure measurement errors are suspected, modeling changes did not seem warranted.

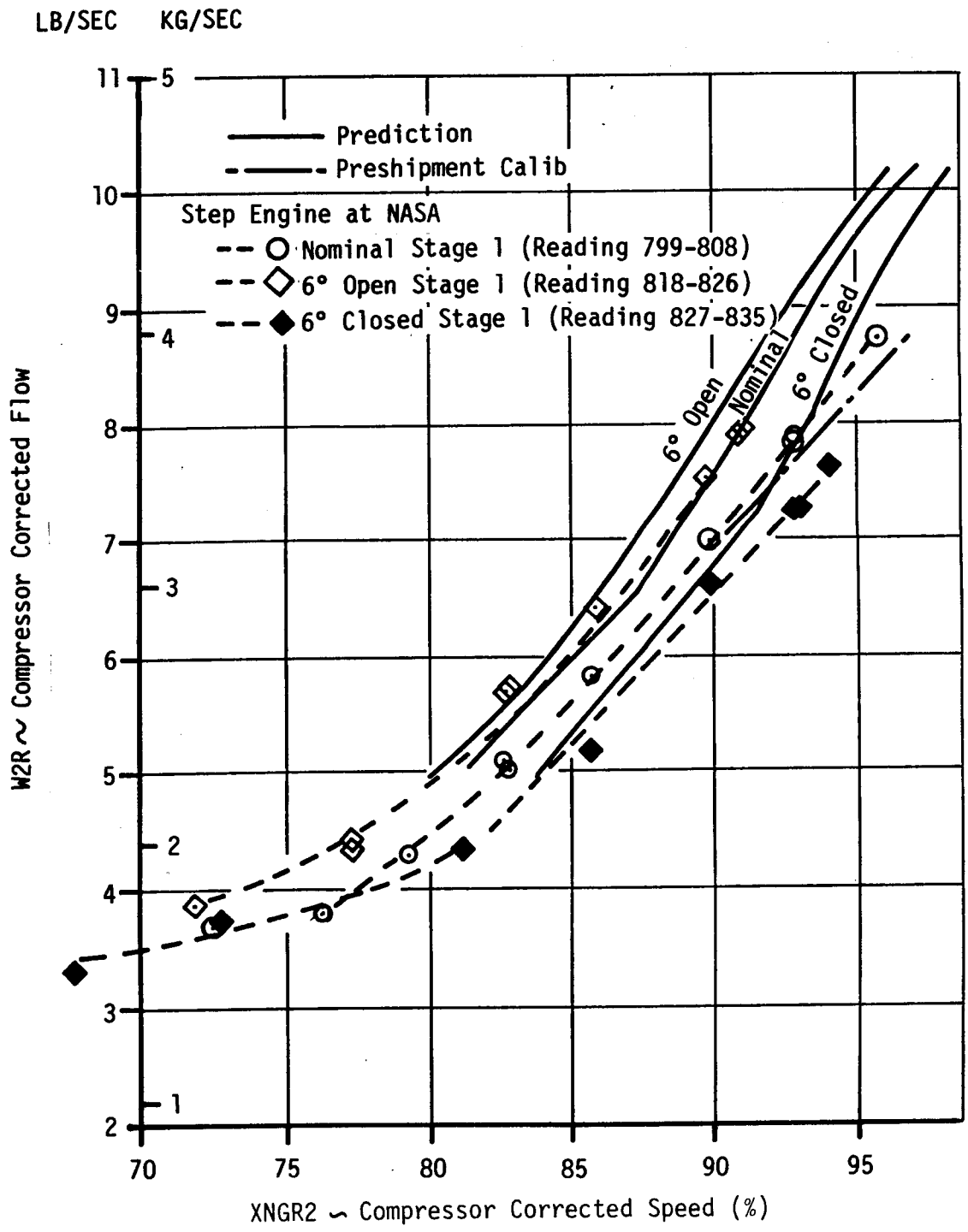


Figure 4.1 Compressor Corrected Flow vs. Compressor Corrected Speed.

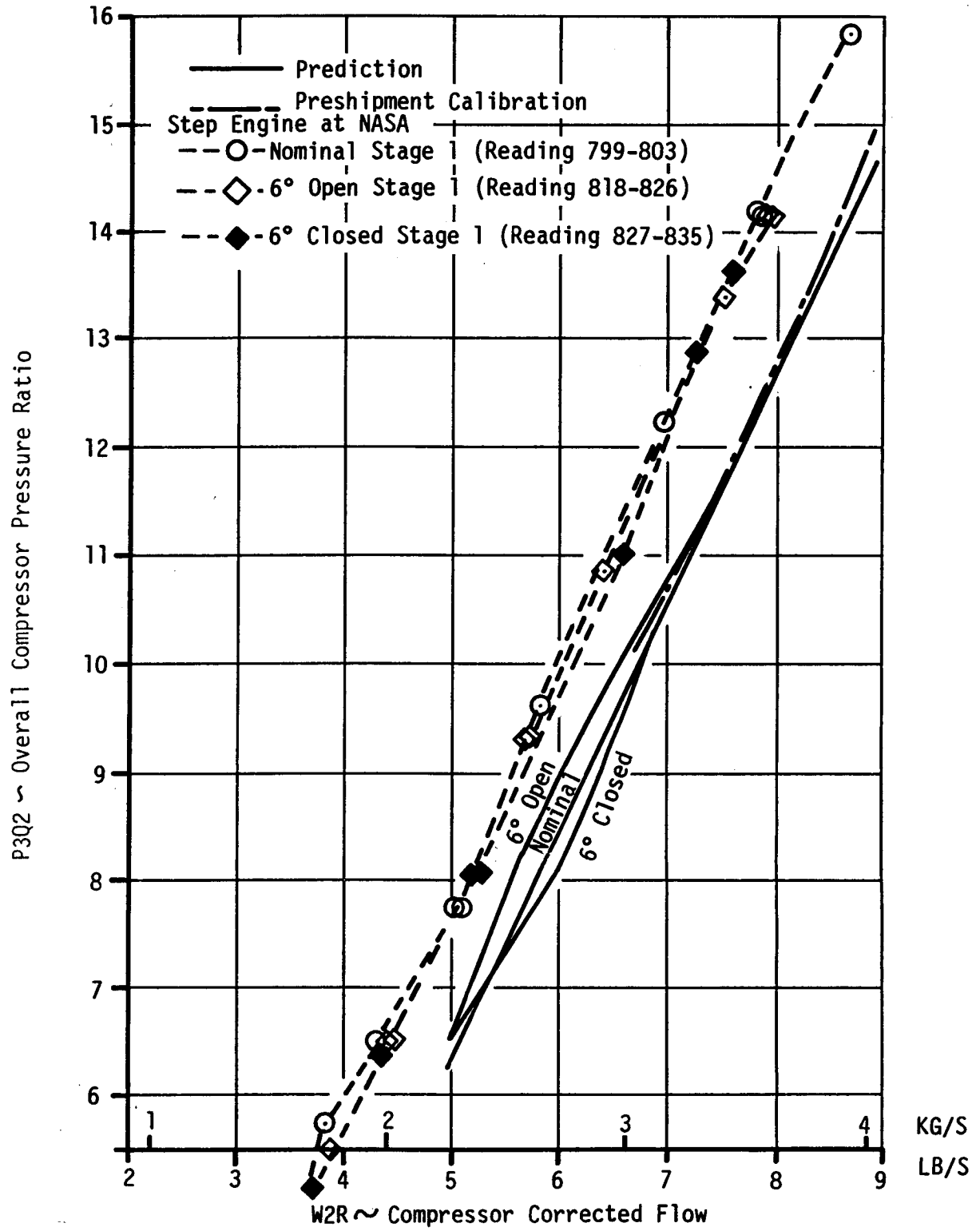


Figure 4.2 Overall Compressor Pressure Ratio vs. Compressor Corrected Flow.

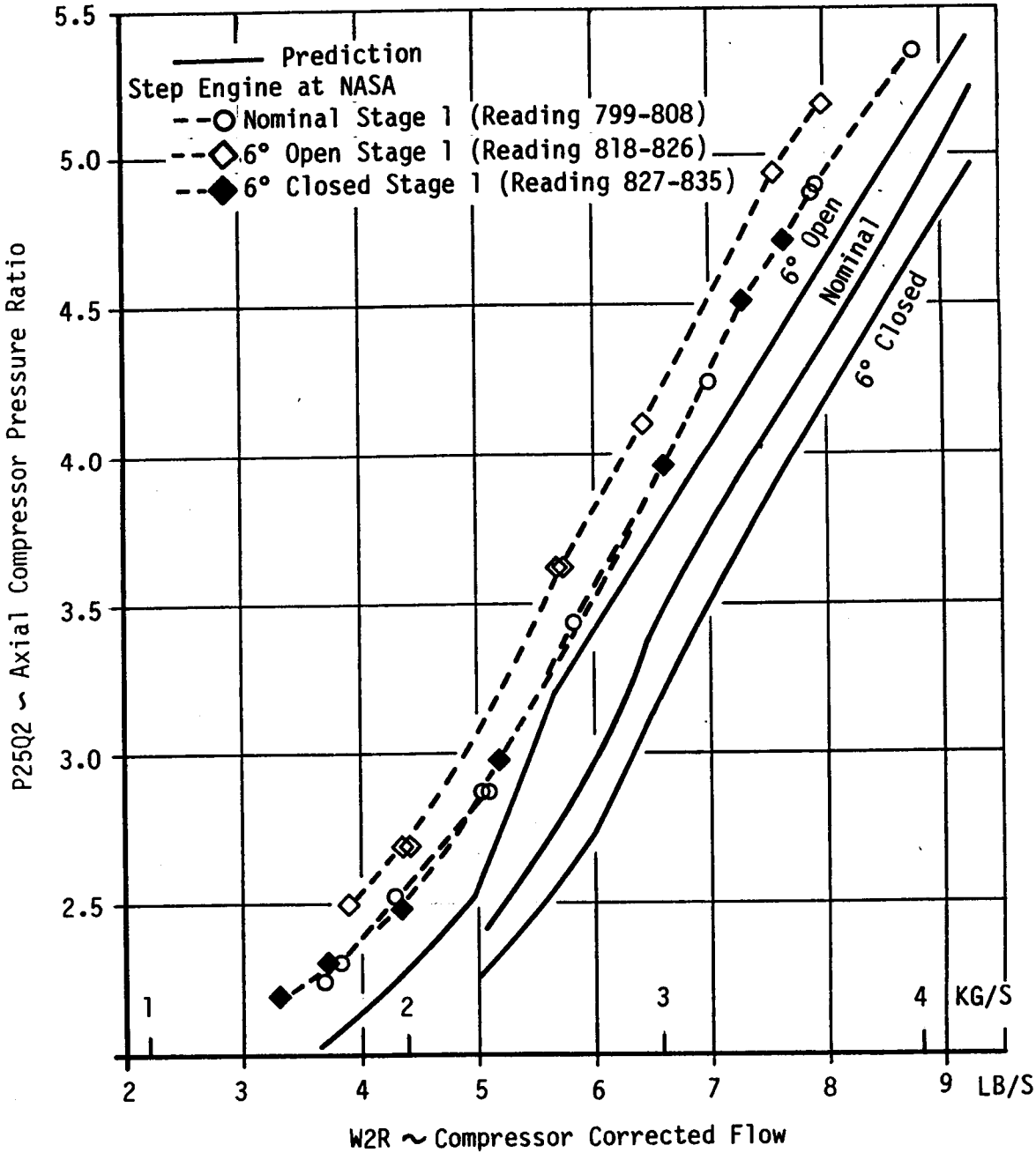


Figure 4.3 Axial Compressor Ratio vs. Compressor Corrected Flow.

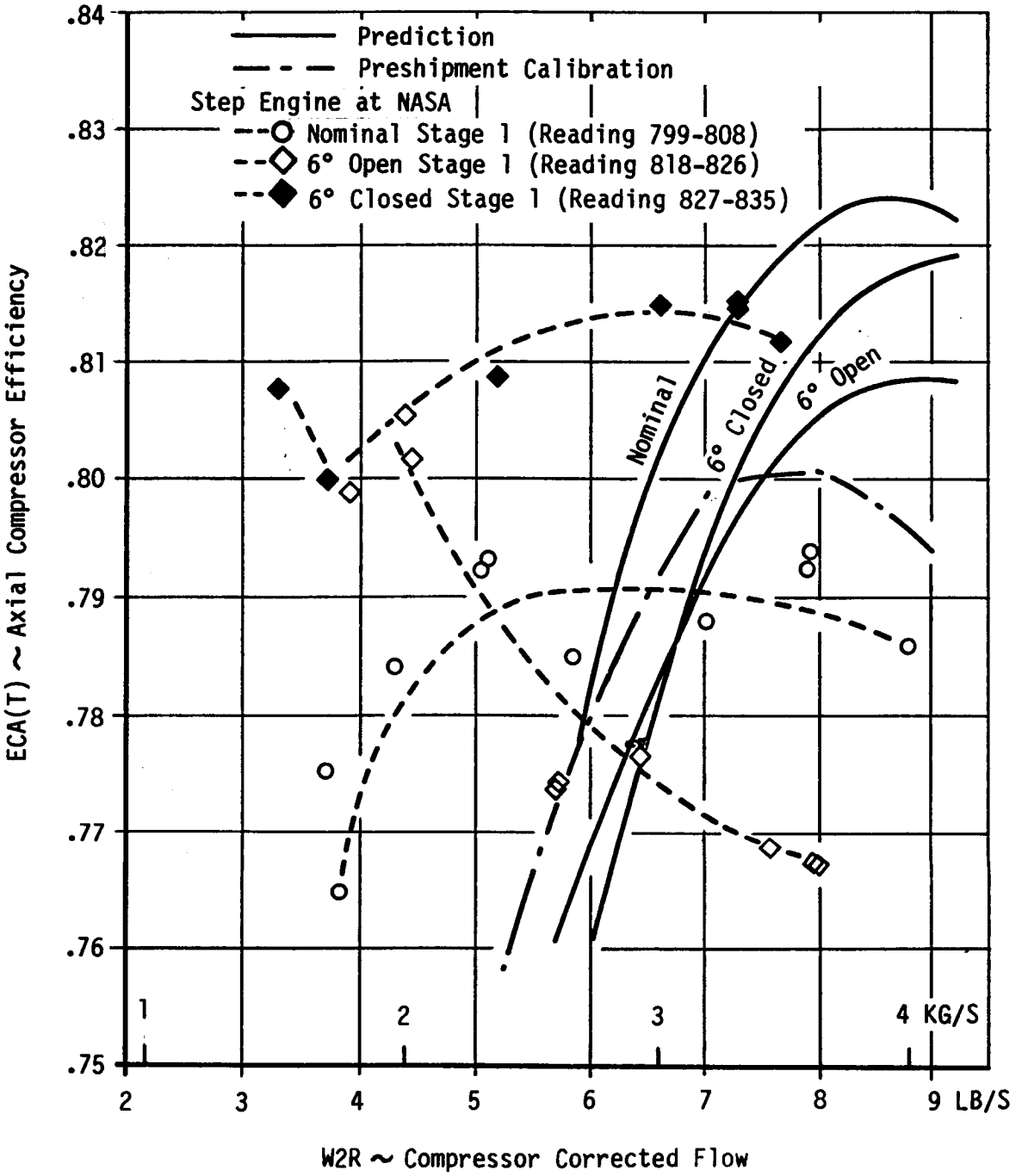


Figure 4.4 Axial Compressor Efficiency vs. Compressor Corrected Flow.

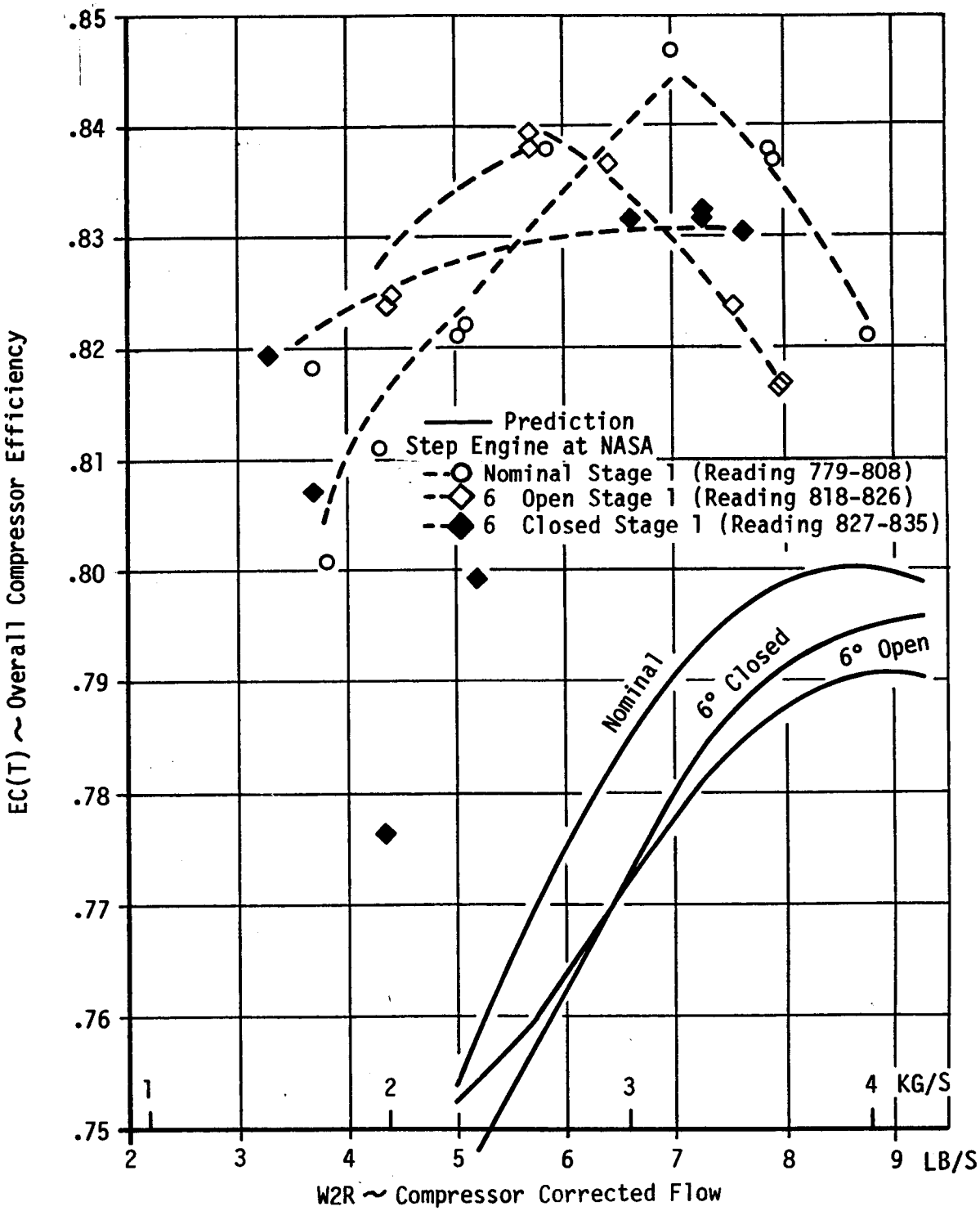


Figure 4.5 Overall Compressor Efficiency vs. Compressor Corrected Flow.

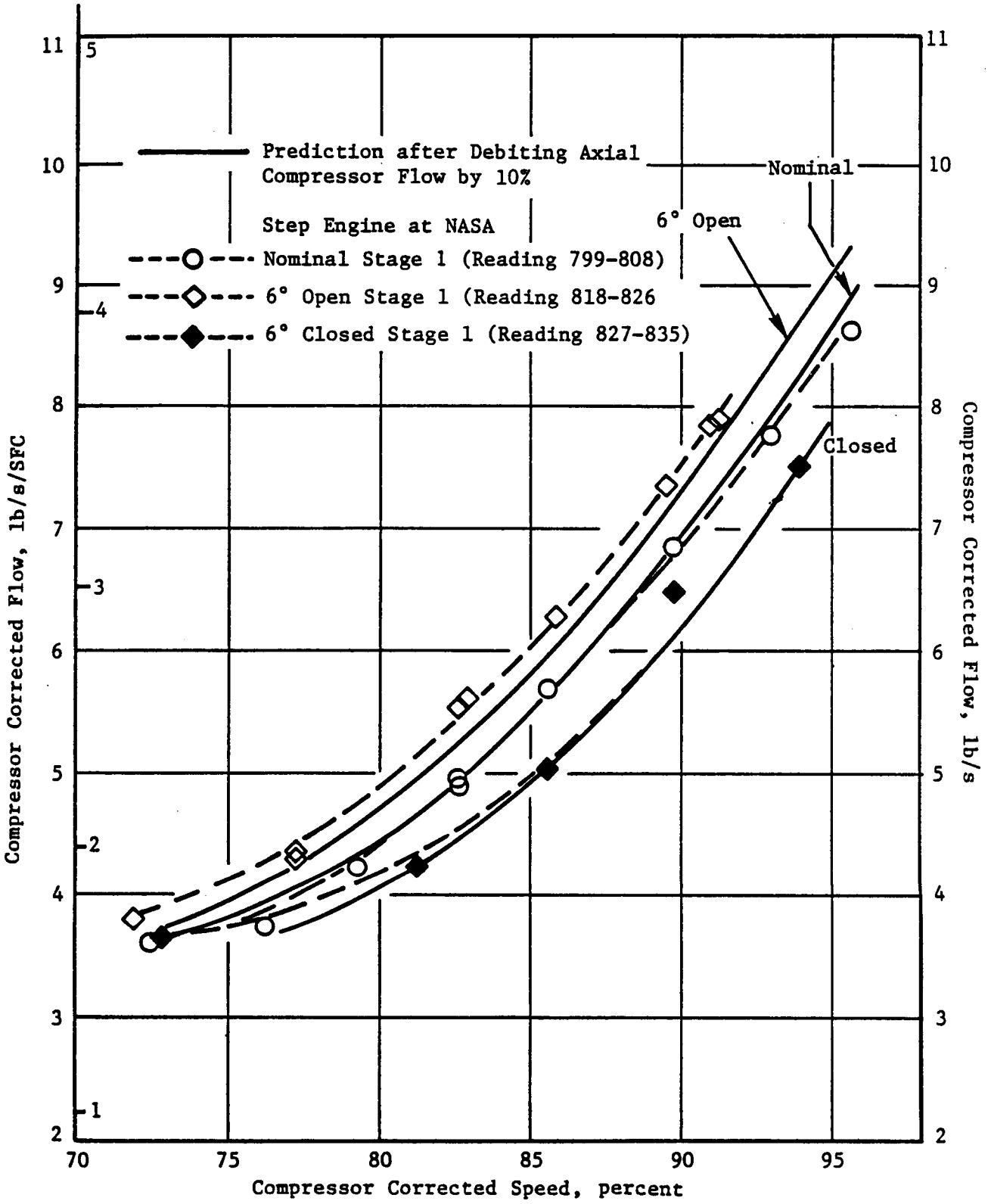


Figure 4.6 Compressor Corrected Flow vs. Compressor Corrected Speed.

Since NASA suspected a possible leak in the scanivalve PS3 reference pressure (which would cause the apparent PS3 to be high), it was decided to use the PS1G PS3 transducer measurement to reduce the data. Figures 4.7 and 4.8 show overall compressor ratio and overall compressor efficiency using these measurements. This makes much closer agreement relative to prediction. Also, the HPT nozzle flow function level looks much closer to that expected for a "YT" Black Hawk nozzle as shown in Figure 4.9.

Note that the calculated flow function dips by up to 5% at low speeds. This dip correlates with the same speed as the starting bleed valve. An overboard leak in the starting bleed valve flow (approximately 50%) could explain this phenomenon.

### 4.2.2 Hysteresis Effects

Figure 4.10 shows that maximum stage 1 hysteresis is about 4-6 degrees. The flow difference of 8-10% as shown in Figure 4.11 is consistent with the flow difference observed in Figure 4.7 lending creditability to the 4-6 degree hysteresis. T700 experience would predict maximum hysteresis of 3-4 degrees for a nominal engine.

### 4.2.3 Starting Bleed/Anti-icing Bleed Flow Fraction

Figure 4.12 shows the stage 1 effect on starting bleed as a function of compressor corrected speed. This curve is required for data reduction. When off-schedule variable vanes are employed, the flow fraction changes with variable vane changes because the bleed valve and variable vanes work off the same actuator. The NASA data reduction already includes a bleed fraction schedule as a function of speed and variable vane bias (supplied by GE) but this curve is a refinement.

## 5.0 Conclusions

### 5.1 Modern Control Power Turbine Governor

A high performance power turbine speed governor was designed for a recent technology turboshaft engine coupled to an advanced, articulated helicopter rotor system. Modern control system design techniques were used to obtain a higher-bandwidth system than previously achievable. The Linear Quadratic Regulator (LQR) technique was used to design the governor, and a Kalman Filter (KF) was included in the control system to estimate the helicopter main rotor blade velocity used in the LQR governor. The effect of the LQR governor in the frequency domain is to attenuate the resonant peak caused by the interaction of the helicopter main rotor and the power turbine. The LQR governor provides adequate phase and gain margins for good stability and robustness. The resonant peak attenuation, combined with large phase margin, allows the system gain to be higher and results in the increased bandwidth.

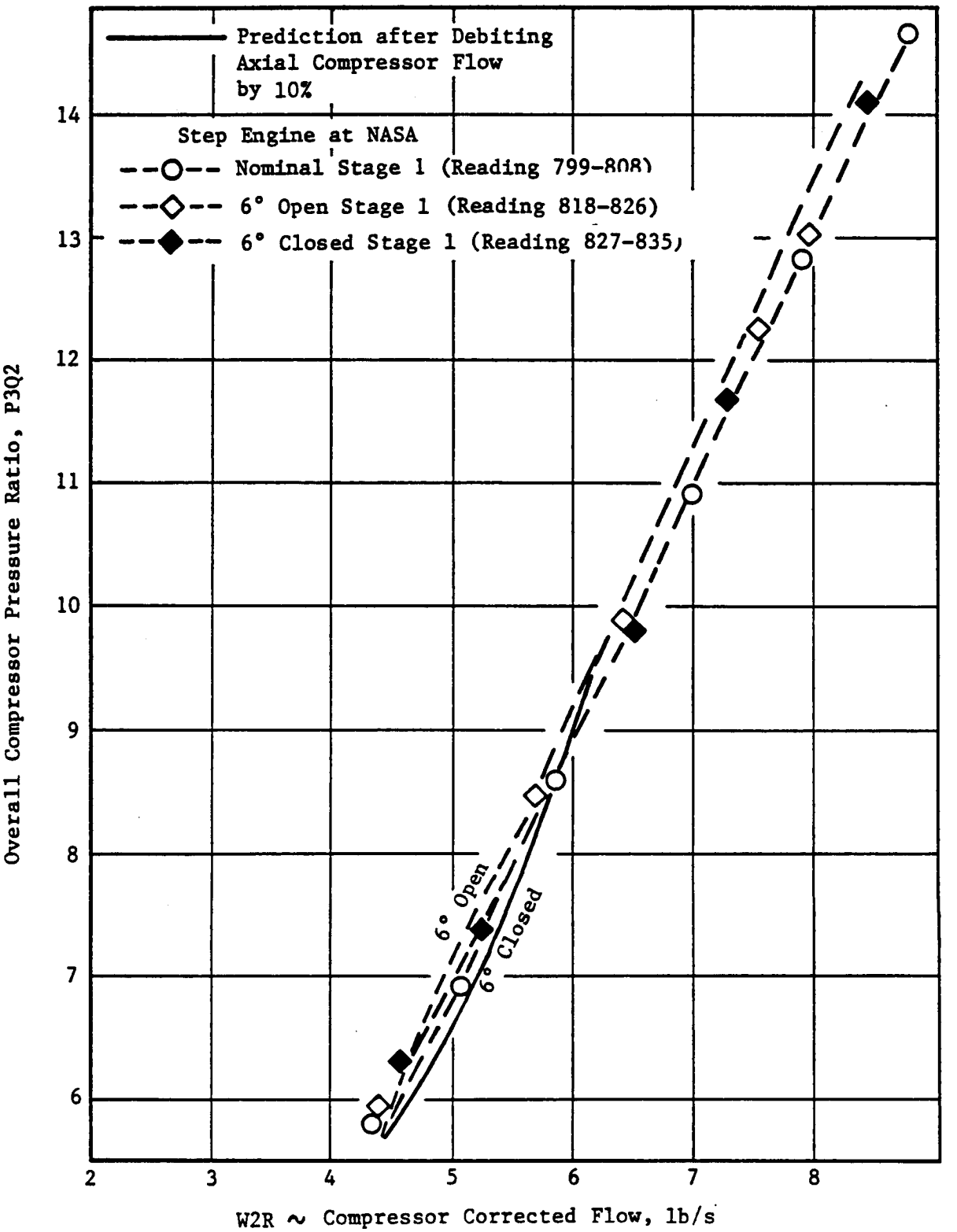


Figure 4.7 Overall Compressor Pressure Ratio vs. Compressor Corrected Flow.

C-3

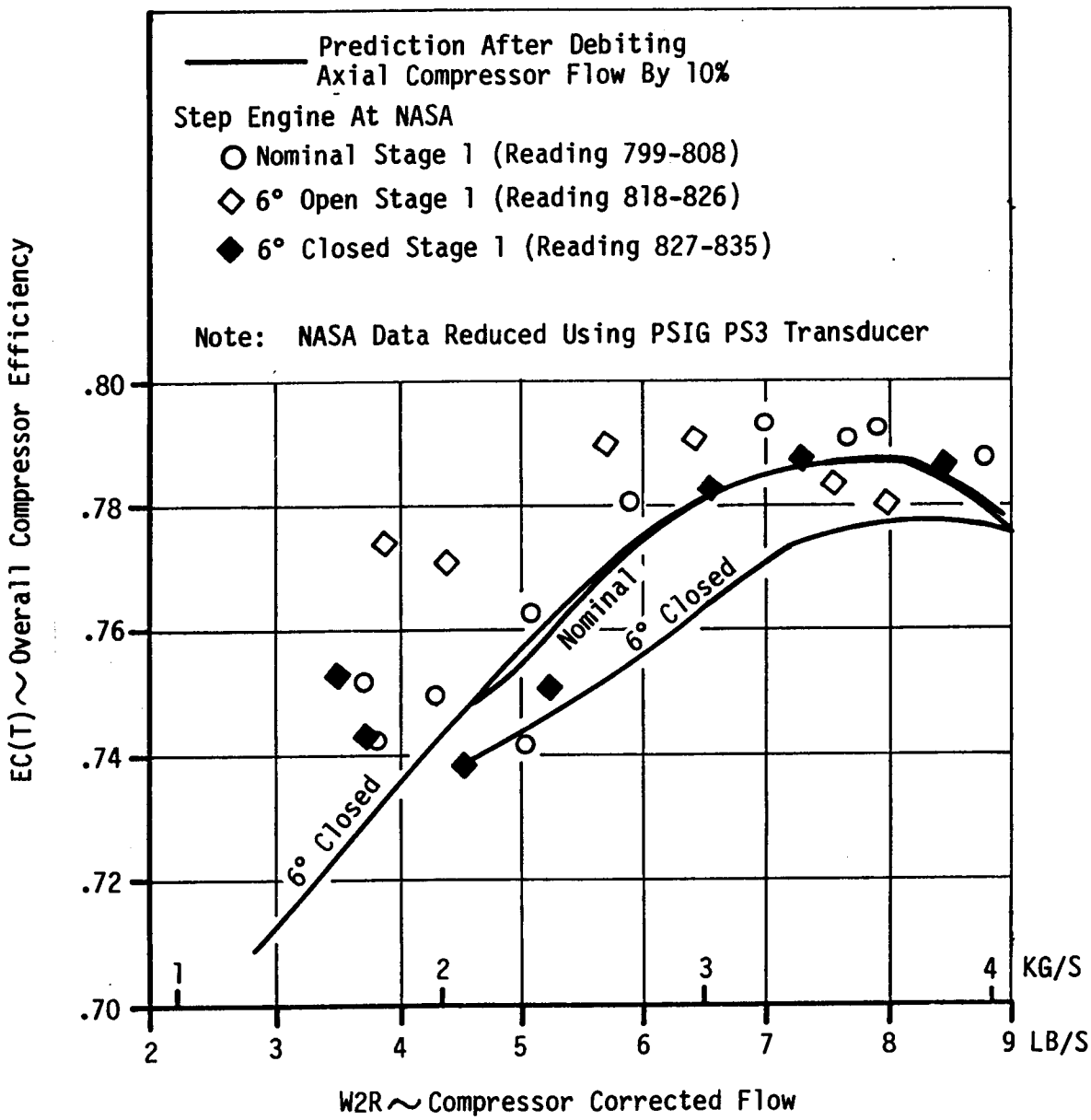


Figure 4.8 Overall Compressor Efficiency vs. Compressor Corrected Flow.

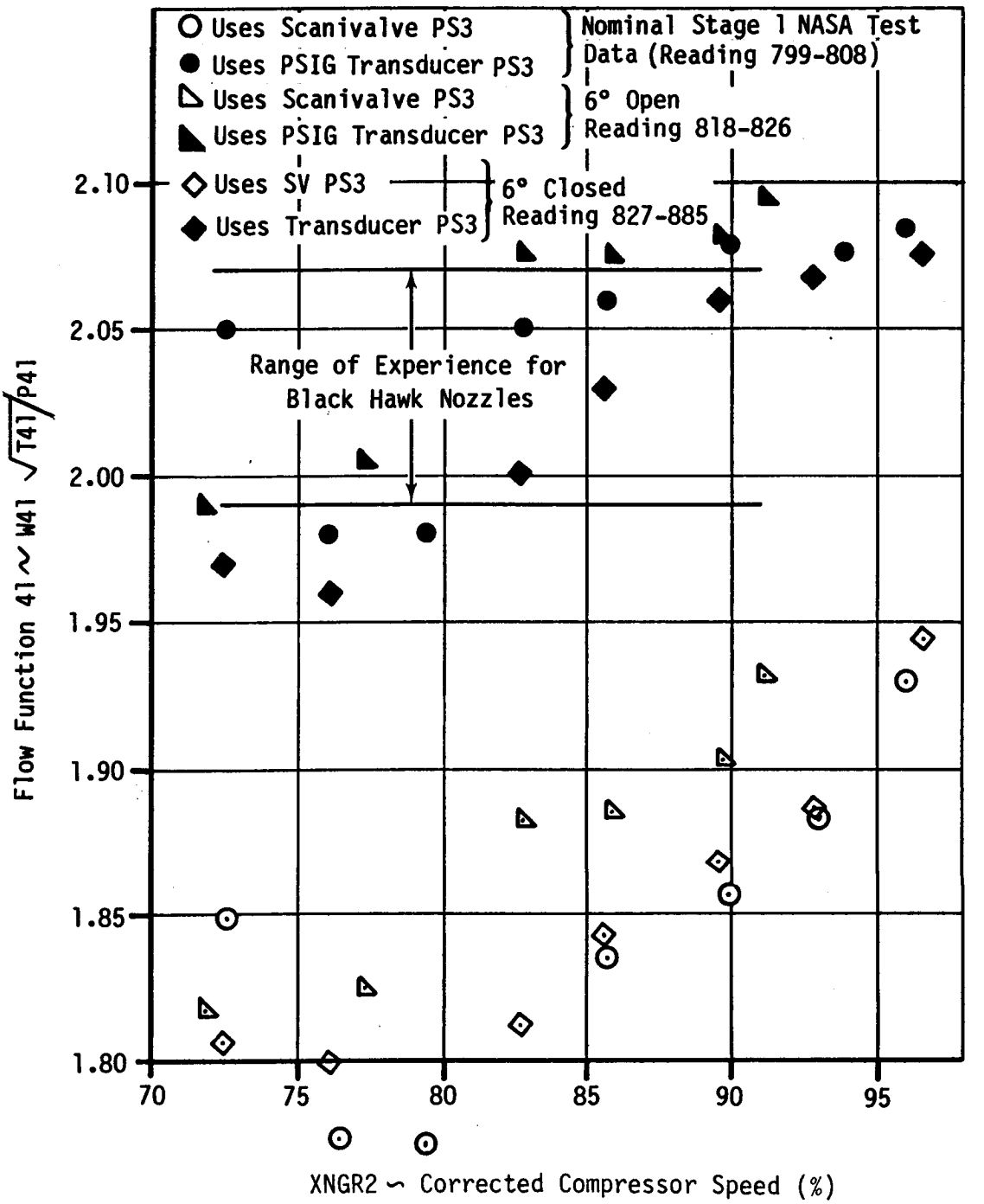


Figure 4.9 Flow Function 41 vs. Corrected Compressor Speed.

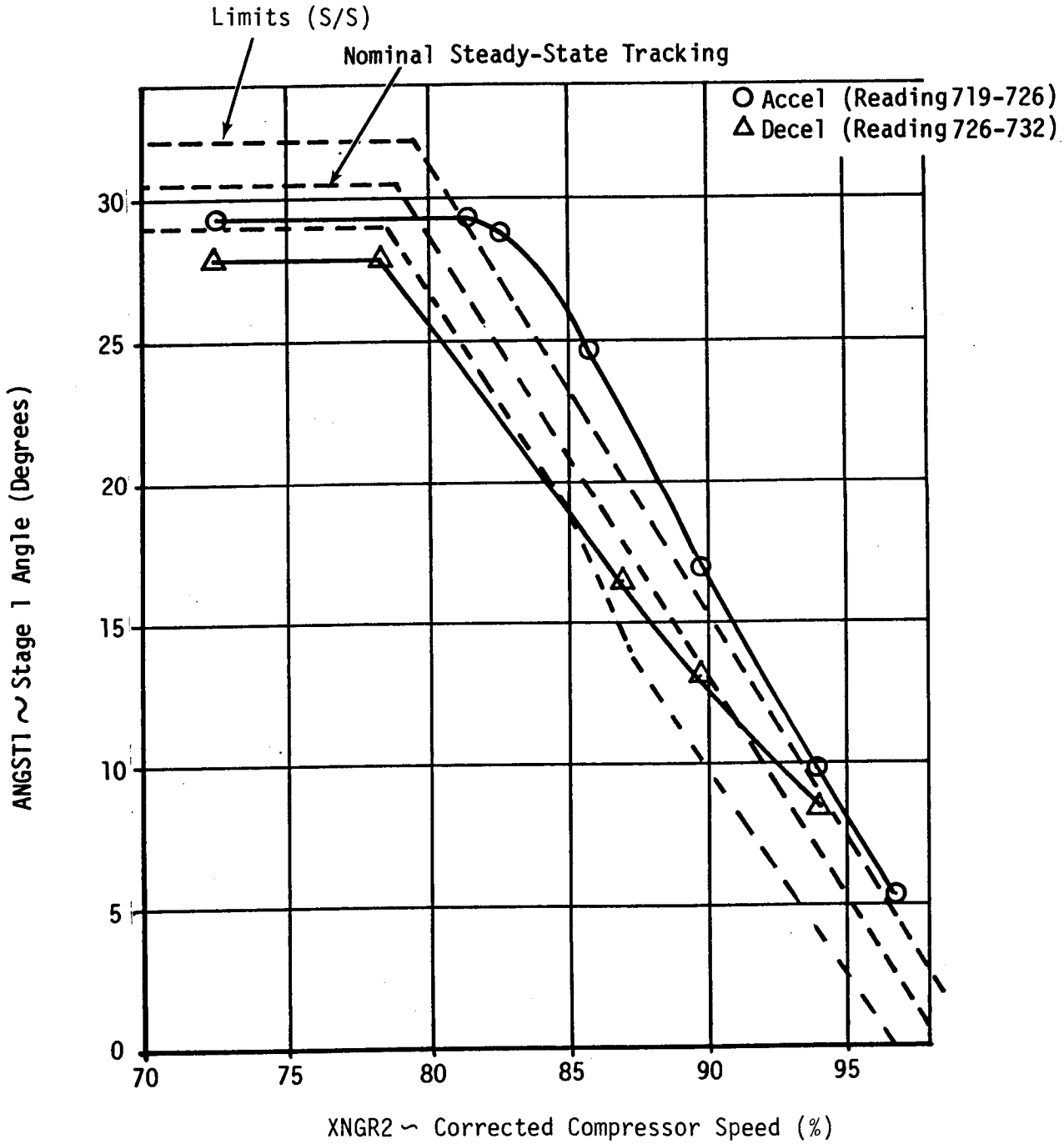


Figure 4.10 Stage 1 Angle vs. Corrected Compressor Speed.

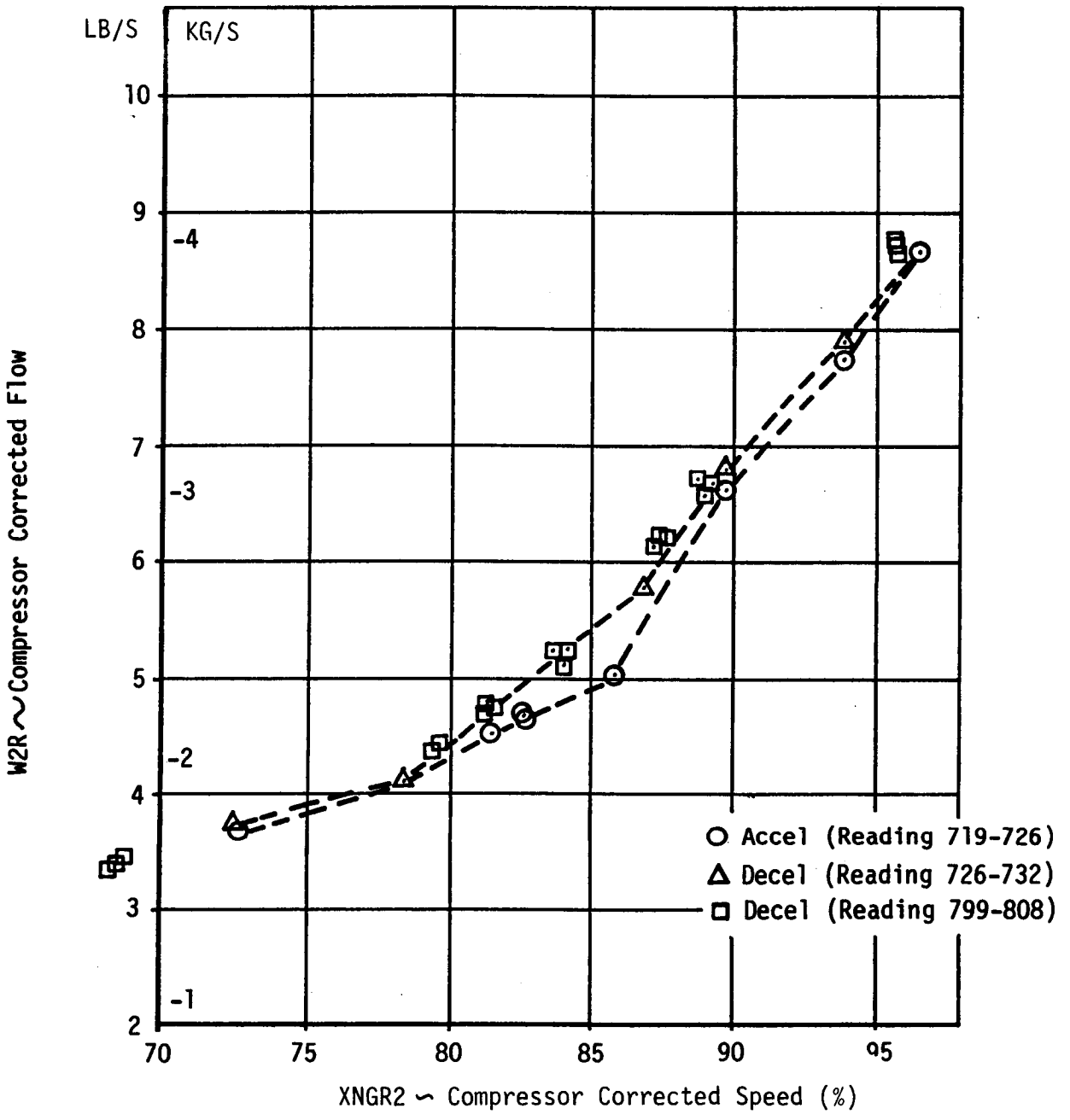


Figure 4.11 Compressor Corrected Flow vs. Compressor Corrected Speed.

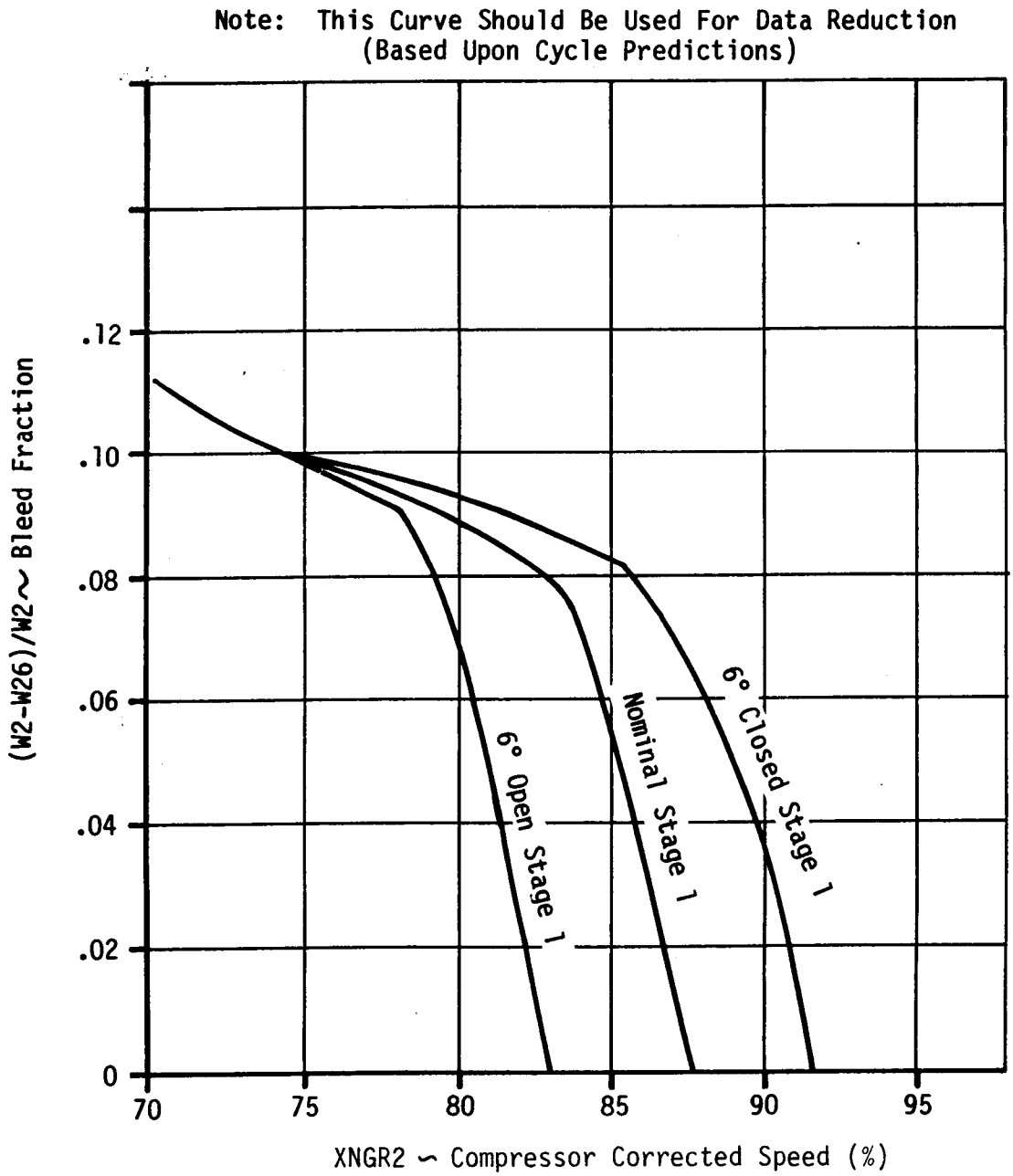


Figure 4.12 Bleed Fraction vs. Compressor Corrected Speed.

The higher bandwidth translates directly into better performance in the time domain. Two load bursts and two load chops were simulated to compare the LQR governor to the current, baseline governor. The simulations were done with a full nonlinear engine model and a simplified helicopter rotor model. One burst and one chop were a 490 shaft horsepower change in demand in 0.1 s with no anticipation of the change in demand going to the controller. This would simulate a wind gust load or a cyclic pitch change with constant collective pitch. The LQR governor reduced power turbine speed droop and overshoot up to 25%. The other burst and chop were a 700 shaft horsepower change in demand in 0.5 sec caused by a change in collective pitch. The collective pitch demand was fed into the control as anticipation to help reduce power turbine speed droop and overshoot. For these transients, the droop and overshoot was reduced up to 35%.

The LQR power turbine governor was analyzed with two other helicopter rotor systems. The two systems are the Westland WG30 and the Hughes systems. The LQR governor was designed for the Black Hawk rotor system. No modifications were made to the governor when the rotor system was changed, because the goal was to have one controller that would be installation independent. The LQR controller did not attenuate the main rotor resonant peak on either the Westland or the Hughes systems as effectively as it attenuated the Black Hawk resonant peak. This may be due to the sharpness of the resonant peaks of these systems compared to the Black Hawk system. Because the resonant peak is not attenuated sufficiently, the system gain must be dropped to obtain 6dB gain margin, and the system bandwidth will decrease. The final bandwidth is about the same as the baseline governor and no significant performance improvement can be expected. It is likely that a different LQR governor could be designed for each rotor system. Analysis could be done to determine if a compromise system could perform well on any of the three rotor systems with few or no modifications.

The LQR governor with the Black Hawk rotor system was analyzed in the frequency domain to determine the effect of having one engine inoperative, and the effect of reducing the lag-hinge damping to zero. The one-engine-inoperative situation did not adversely affect stability margins and lowered the bandwidth of the system from about 8-10 rad/sec to about 5 rad/sec. The LQR governor did not attenuate the main rotor resonant peak when the lag-hinge damping was reduced to zero. Performance degradation and instability could result in this situation. It is possible that a LQR governor could be designed to perform well in this situation and in the normal-damping situation. Active control of the variable geometry was studied as a way of helping fuel flow control rotor droop. A frequency response analysis showed that fuel flow was sufficient to control power turbine speed and there was no advantage to using variable geometry. Variable geometry was left to be controlled open loop as a function of corrected gas generator speed.

Significant improvements in speed governing were achieved by the LQR governor, but engine testing and additional simulations are necessary to gain confidence that the controller will perform as expected in flight test. Engine testing is scheduled for the LQR governor with a dynamometer. The primary goals of this testing program are to verify that the controller will govern power turbine speed and to validate the analysis done in the time and frequency domains. The time simulations of the LQR governor with a dynamometer load did not show consistent improvement over the baseline governor. Performance is not critical for this test, however, since the governor was designed for a helicopter rotor system and was only made stable for test cell operation. Performance was not optimized for a dynamometer load. Other tests that should be done prior to flight test are time simulations with an accurate, nonlinear helicopter rotor system model and tie-down tests with a helicopter.

## 5.2 Linear Model Identification

Pseudo-Random Binary Noise (PRBN) testing of a NASA YT700 engine was performed to illustrate the use of PRBN testing as an accurate and expedient method of engine frequency response data compared to traditional testing methods. Separate spectral analysis and maximum likelihood (ML) model identification techniques were used to recover engine frequency response characteristics from engine test data.

### 5.2.1 Spectral Analysis

Discrepancies were seen between the engine frequency response data obtained through spectral analysis and NASA discrete sine wave test data. The magnitude of the spectral analysis results is consistently lower than that of engine frequency response. The smoothed spectral density is considerably underestimated for a relatively low number of time lags $\tau$ used in the spectral analysis algorithms. Software limitations restrict the maximum number of lags to 500. For a one minute sample slice of 12,000 data points (200 Hz sampling rate) the maximum number of lags is only 4% of the number of data points compared to a recommended 5% to 20%. The magnitude, break frequency and, consequently, the phase of the frequency responses are quite biased under these conditions.

The results of the spectral analysis were useful, however, in verifying the white noise approximations made concerning the PRBN signal, and the stationary assumptions made concerning the engine test. Spectral analysis results were also used to verify the accuracy of the ML identified models by testing the residuals.

### 5.2.2 Maximum Likelihood Model Identification

The ML frequency response data compared well with the NASA discrete frequency points used as the benchmark for evaluating the ML identified frequency responses. The ML model for NG/WF compared very well with the NASA test data. The model residuals are white noise with a 95% degree of confidence, verifying the accuracy of the ML model.

The ML model residuals for Np/WF, however, are not white noise with a 95% degree of confidence. A better correlation could be achieved with a higher order ML model. Software limitations restrict the identification to an eigth order model, however. The slight divergence between the ML frequency response data and discrete frequency points for Np/WF could be attributed, in part, to the less than optimal Np/WF model.

### 5.2.3 Linear Models

A linear model of the T700 engine was compared to a reduced-order engine model obtained from the ML results in order to evaluate the accuracy of the linear model.

#### 5.2.3.1 NG/WF

The linear model compares well with the ML model for NG/WF. There is less than a 3db difference in magnitude, and approximately a 10 degree difference in phase at 10 rad/sec. An additional lag appears in the engine frequency response at approximately 30 rad/sec. These higher frequency dynamics are neglected in the linear model. Physically, these dynamics could be attributed to a lag from fuel flow introduction to torque produced at the gas generator due to the compressibility of air.

The correlation between the linear model and the engine (represented by the ML model frequency response) is adequate in the frequency range of interest. Consequently, no further investigation into the source of these higher frequency dynamics is warranted.

#### 5.2.3.2 Np/WF

The linear model compares well with the ML model out to approximately 1 rad/sec for Np/WF. Higher frequency dynamics produce considerably more phase lag than is indicated by the linear model. The divergence of the linear model response from that of the actual engine is attributed, in part, to the linear model dynamometer representation. The contribution of the dynamometer damping to the phase lag observed in the engine may be inadequately modeled. Consequently, additional work could be focused on identifying the actual dynamometer frequency response using techniques similar to those outlined in this report. The accuracy of the linear model at higher frequencies becomes significant when implementing high performance Np governors, and a better

understanding of the dynamometer transient characteristics is essential to the model accuracy. Other higher frequency dynamics in the engine not accounted for in the linear model, may be contributing to the discrepancies between the ML and linear model.

## 5.3 Variable Geometry Off-Schedule Model Validation

A T700 engine was tested at NASA-Lewis for the purpose of investigating compressor variable guide vane (stage 1) off angle effects.

Steady-state test data of the variable geometry (VG) was obtained with the nominal VG schedule, 6 degrees off-schedule in the open direction, and 6 degrees off-schedule in the closed direction conditions. This performance data was compared with data obtained from T700 transient model simulations.

Analysis of the off-schedule VG steady-state test data indicates that the original model of the VG contained in the T700 DISCUS transient deck is adequate and should not be altered.

The data showed that current compressor flow/speed off angle effects modeling is adequate but that validity of NASA STEP engine measurements required for compressor pressure ratio and efficiency calculations are suspect, thus precluding proper analysis of these effects. Also, improved data reduction calculations of bleed fractions to account for off angle effects were used.

Appendix I. Comparison of Simplified and Complex Rotor System Bode Plots for Black Hawk, Hughes, and Westland WG30.

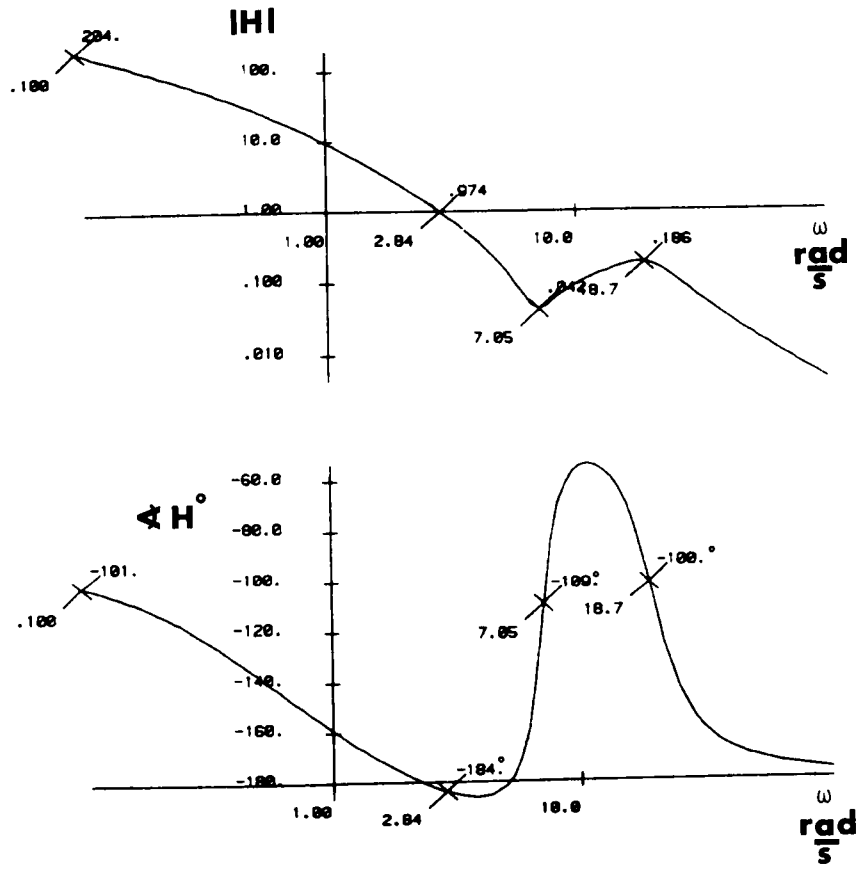


Figure I.1 Bode Plot of Black Hawk Rotor System Frequency Response from d(WF)/dt Input to Np Output. Simplified Rotor System.

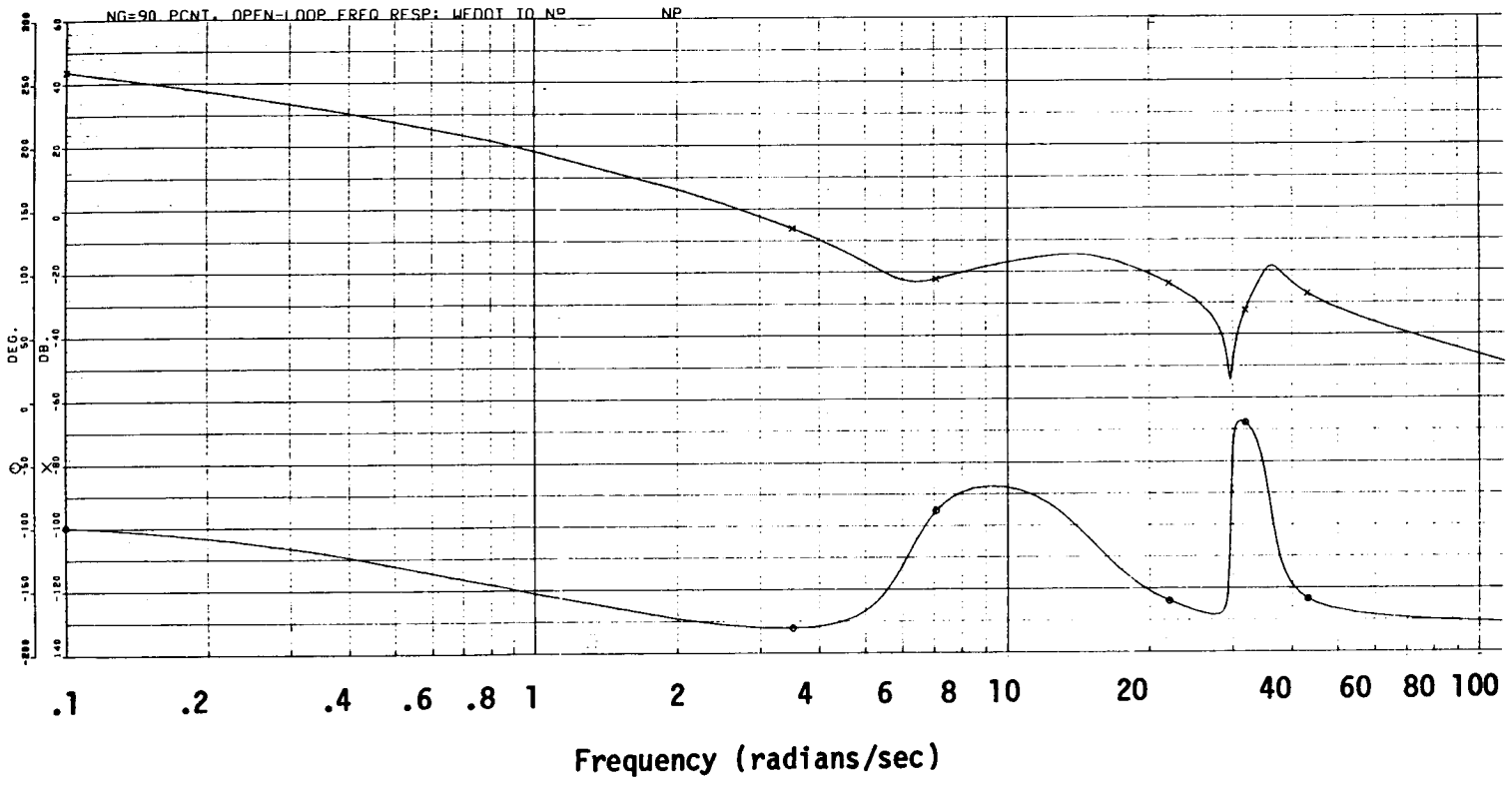


Figure I.2 Bode Plot of Black Hawk Rotor System Frequency Response from d(WF)/dt Input to Np Output. Complex Rotor System.

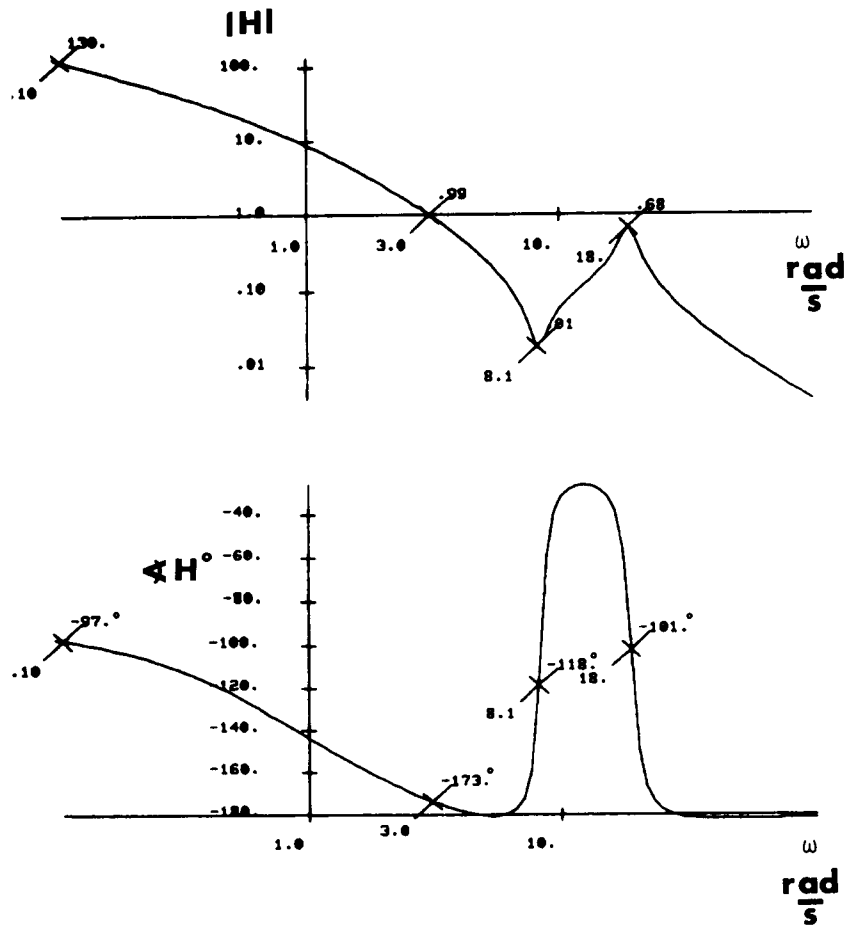


Figure I.3 Bode Plot of Hughes Rotor System Frequency Response from d(WF)/dt Input to Np Output. Simplified Rotor System.

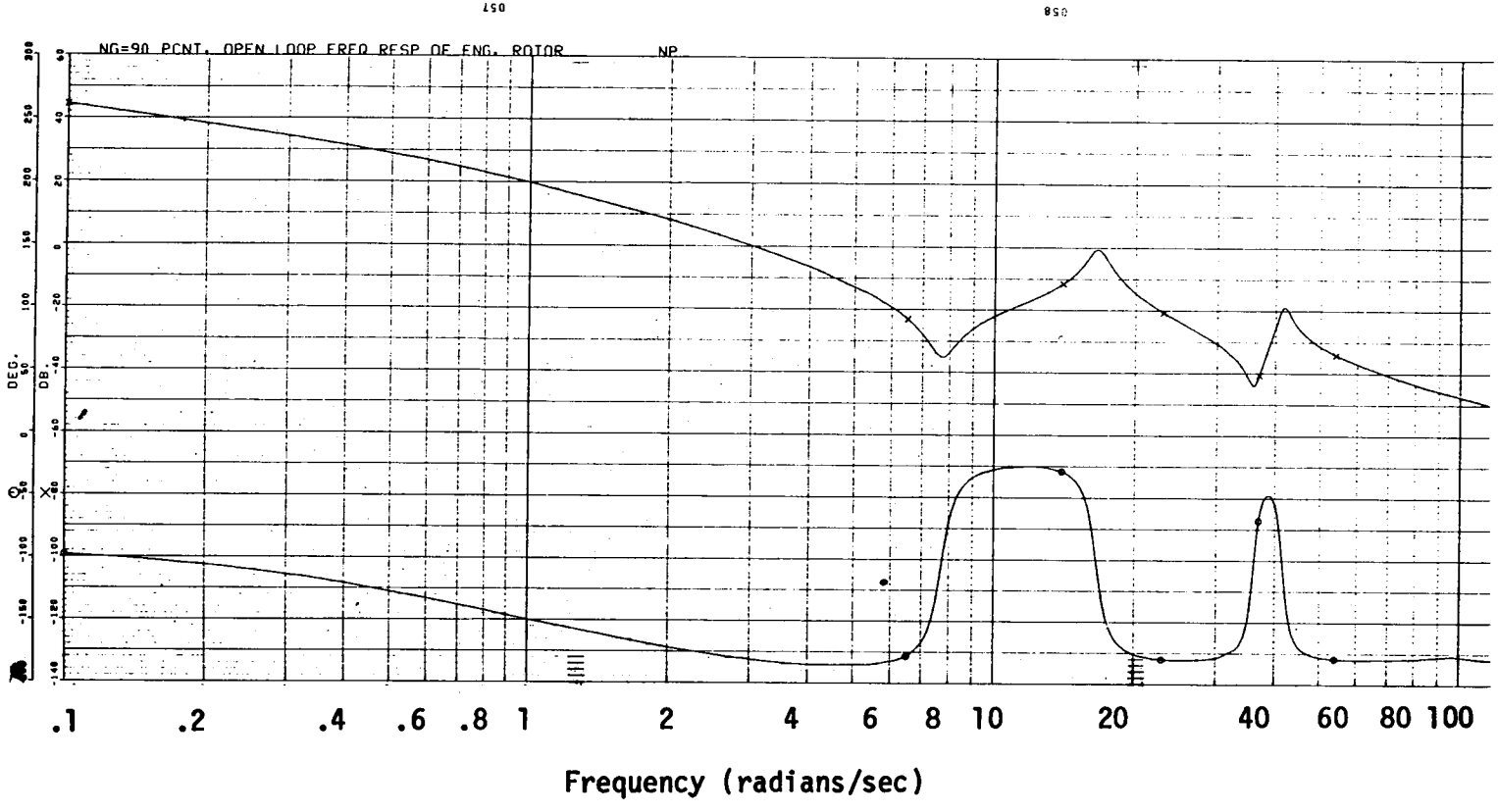


Figure I.4 Bode Plot of Hughes Rotor System Frequency Response from d(WF)/dt Input to Np Output. Complex Rotor System.

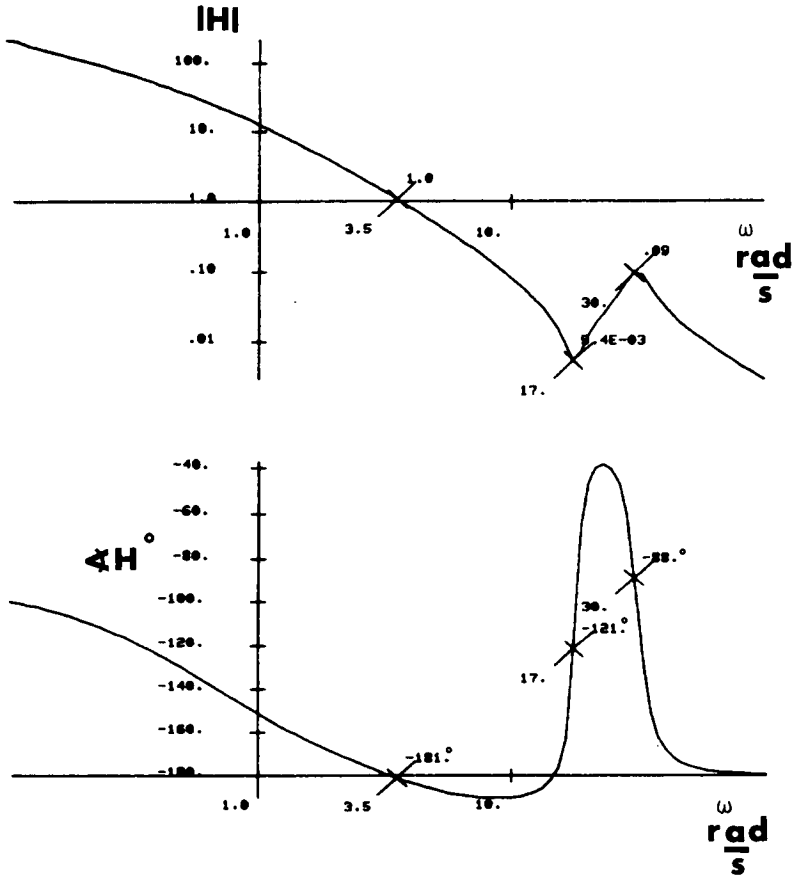


Figure I.5 Bode Plot of Westland and WG30 Rotor System Frequency Response from d(WF)/dt Input to Np Output. Simplified Rotor System.

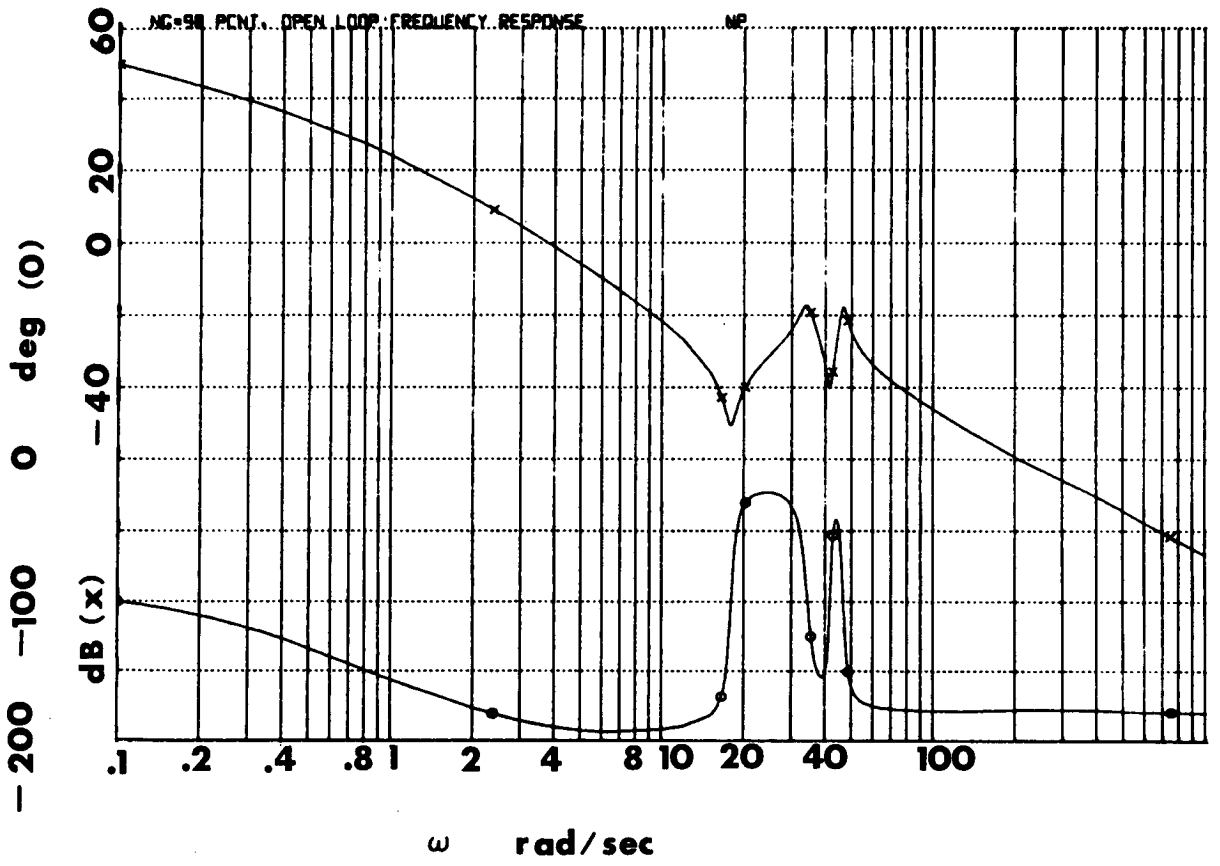


Figure I.6 Bode Plot of Westland WG30 Rotor System Frequency Response from d(WF)/dt Input to Np Output. Complex Rotor System.

## Appendix II. Engine and Black Hawk Helicopter System Parameters.

Table II.1 Unbalanced Torque Partial Derivatives for T700

| Case | | 1 | 2 | 3 | 4 | 5 | 6 | |
|---|---|---|---|---|---|---|---|---|
| | | F/I | | | | IRP | | Units |
| Ng | | 73.7 | 83.0 | 90.0 | 95 | 97.2 | 100.0 | % |
| Np | | 20900 | 20900 | 20900 | 20900 | 20900 | 20900 | RPM |
| Wf | | 156 | 219 | 420 | 687 | 772 | 831 | PPH |
| T4.5 | | 1387 | 1439 | 1611 | 1887 | 1968 | 2054 | °R |
| Ps3 | | 69 | 96 | 165.7 | 224 | 241 | 255 | PSIA |
| SHP | | 0 | 155 | 763 | 1494 | 1709 | 1822 | SHP |
| Q | | 0 | 40.8 | 200.8 | 393.2 | 450.0 | 479.4 | FT-LB |
| δA/δB | | | | | | | | |
| A | B | | | | | | | |
| Qg | Ng | -.0025 | -.0090 | -.017 | -.029 | -.011 | -.0068 | FT-LB/RPM |
| Qp | Ng | +.0022 | +.012 | +.029 | +.042 | +.011 | +.0050 | FT-LB/RPM |
| T4.5 | Ng | -.034 | -.063 | -.066 | -.070 | +.0073 | +.0070 | °R/RPM |
| Ps3 | Ng | +.0037 | +.0093 | +.016 | +.020 | +.0045 | +.0020 | PSI/RPM |
| Qg | Np* | -.00035 | +.0001 | -.00070 | -.001 | -.0010 | -.0009 | /RPM |
| Qp | Np | -.0041 | -.0060 | -.0090 | -.014 | -.015 | -.015 | |
| T4.5 | Np* | +.0019 | - | +.0019 | +.002 | +.002 | +.0019 | |
| Ps3 | Np* | - | - | - | - | - | - | |
| Qg | Wf | +.26 | +.24 | +.21 | +.18 | +.17 | +.165 | /PPH |
| Qp | Wf | +.25 | +.29 | +.35 | +.35 | +.36 | +.35 | |
| T4.5 | Wf | +4.68 | +3.27 | +1.87 | +1.45 | +1.31 | +1.29 | |
| Ps3 | Wf | +.070 | +.070 | +.082 | +.076 | +.077 | +.076 | |
| OPEN Qg | VG | +.37 | +1.46 | +2.65 | +3.05 | +1.33 | +.43 | /DEG |
| Qp | VG | -.22 | -1.82 | -4.00 | -4.90 | -1.02 | -.27 | |
| T4.5 | VG | +1.4 | +7.80 | +7.40 | +6.60 | -1.40 | -.60 | |
| Ps3 | VG | -.24 | -1.34 | -2.05 | -2.13 | -.33 | -.09 | |
| CLOSED Qg | VG | +.30 | +1.92 | +4.18 | +6.19 | +1.99 | +.32 | /DEG |
| Qp | VG | -.24 | -2.65 | -7.33 | -10.16 | -1.69 | -.21 | |
| T4.5 | VG | +4.8 | +14.40 | +17.30 | +14.30 | -1.30 | -.50 | |
| Ps3 | VG | -.43 | -1.98 | -3.85 | -4.42 | -.60 | -.06 | |

*Neglect these terms as they are close to deck tolerance.

Table II.2 Typical VTOL Rotor Constants - Black Hawk

System Parameters

| Parameters | Units | Values | | | Units |
|---|---|---|---|---|---|
| **Moments of Inertia** | | | | | |
| JG Gas Generator | FT-LB $\frac{SEC^2}{RAD}$ | .0445 | X $\frac{2\pi}{60}$ | .00466 | $\frac{FT\text{-}LB\text{-}SEC}{RPM}$ |
| JPT Power Turbine | ↓ | .062 | ↓ | .00649 | ↓ |
| JT Transmission | | .0334 | | .0035 | |
| JMR Main Rotor | | 1.0531 | | .1103 | |
| JTR Tail Rotor | | .0514 | | .00538 | |
| **Spring Constants** | | | | | |
| KMR Main Rotor | FT-LB/RAD | 50.28 | | 5.265 | $\frac{FT\text{-}LB}{RPM\text{-}SEC}$ |
| KTR Tail Rotor | | 60.12 | | 6.296 | |
| **Damping** | | | | | |
| DMR Main Rotor | FT-LB $\frac{SEC}{RAD}$ | 1.38 Min. | | .1445 | $\frac{FT\text{-}LB}{RPM}$ |
| DAM Aero-Main | ↓ | .4775 | ↓ | .05 | ↓ |
| DAT Aero-Tail | | .0191 | | .002 | |

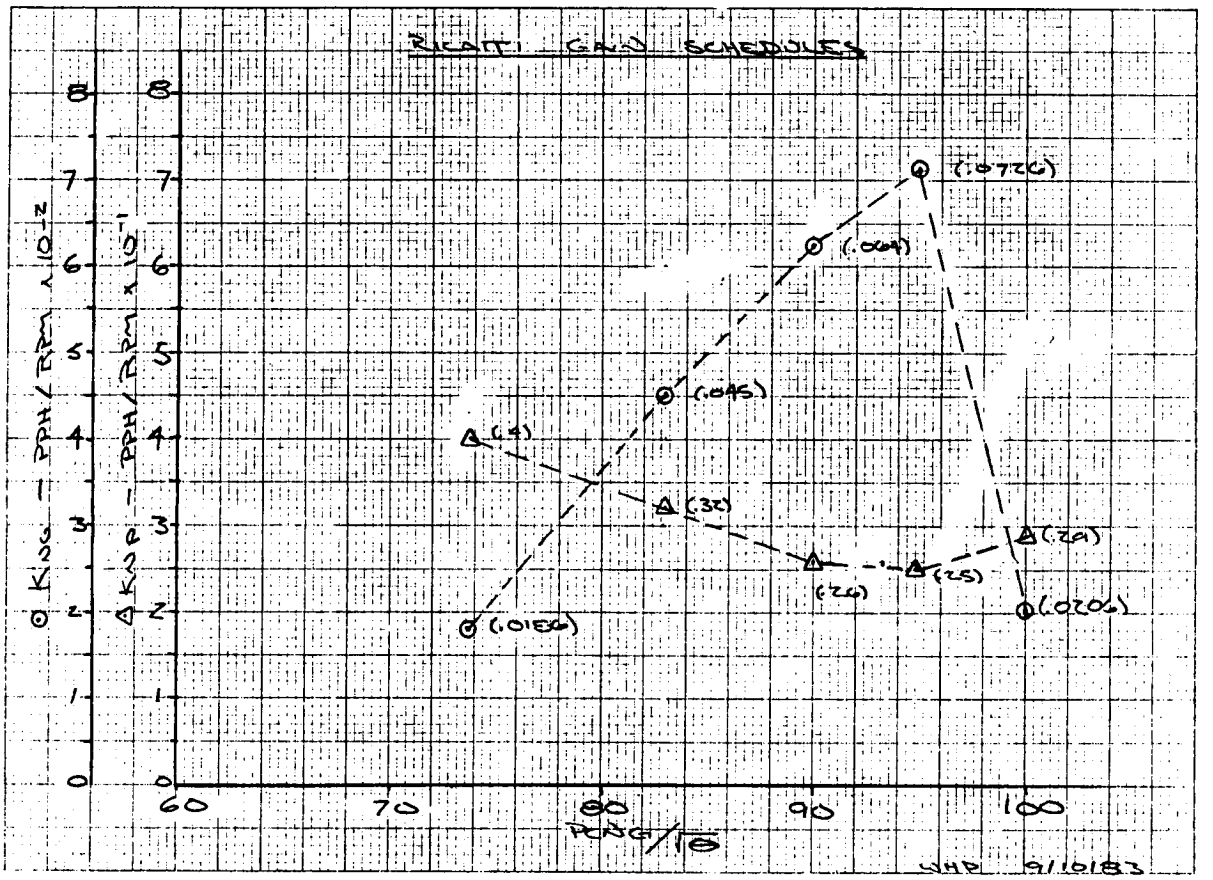


Figure II.1 LQR Gains vs. % NG/$\sqrt{\theta}$ for NG and Np.

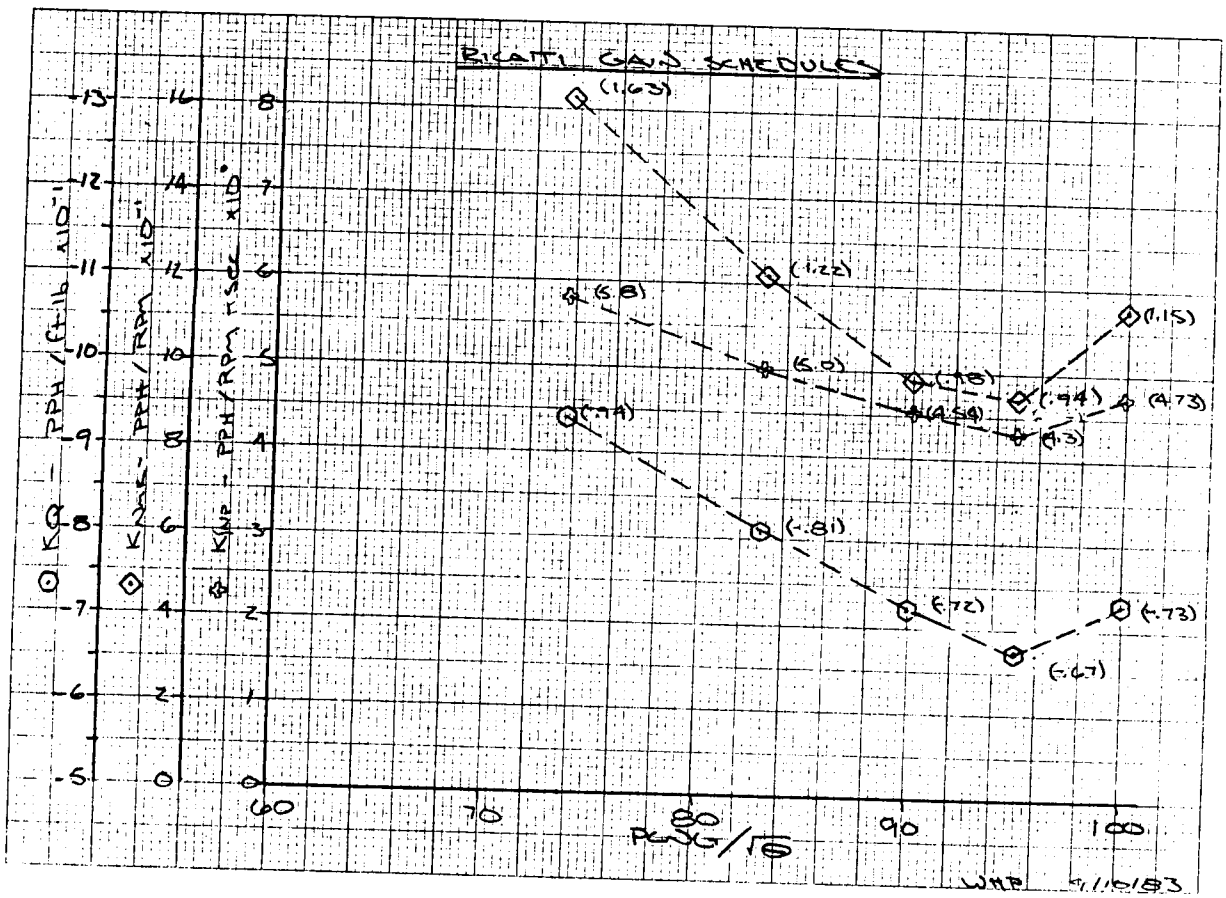


Figure II.2 LQR Gains vs. % NG/$\sqrt{\theta}$ for Q Shaft, NMR, and $\int$ Np.

## Nomenclature - Section 2

| | |
|---|---|
| A, B, C | System Weighting Matrices |
| E | Expected value |
| G | LQR gain matrix |
| $\overline{H}(s)$ | Transfer function |
| I | Identity matrix |
| $\overline{J}$ | LQR cost functional |
| K | Kalman filter gain matrix |
| $\overline{KF}$ | Kalman filter |
| LDS | Load demand spindle |
| LH | Transformed LQR gain matrix |
| $\overline{LQR}$ | Linear quadratic regulator |
| NG | Gas generator speed |
| NMR | Helicopter main rotor blade velocity |
| NP | Power turbine speed |
| Q | LQR state weighting matrix |
| $\overline{QMR}$ | Helicopter rotor torque state |
| Q Shaft | Engine shaft torque |
| R | LQR input weighting matrix |
| $\overline{S}$ | Solution of Algebraic Ricatti equation |
| $\overline{s}$ | Laplace operator, pole location in s-plane |
| T | Sampling period (sec) |
| U | System input vector |
| $\overline{V1}$ | Kalman filter process noise variance matrix |
| $\overline{V2}$ | Kalman filter measurement noise variance matrix |
| $\overline{WF}$ | Fuel flow |
| X | System state matrix |
| Y | System output matrix |
| $\overline{z}$ | Pole location in z-plane |
| $\alpha$ | Scalar multiplier on KF measurement noise variance matrix |
| $\gamma$ | Input vector angle |
| $\theta$ | Lag hinge angle |
| $\tau$ | Time constant |
| $\Phi$ | State transition matrix |
| $\psi$ | Output vector angle |
| $\wedge$ | Estimated |

## Nomenclature - Sections 3 & 4

| | |
|---|---|
| A | Characteristic polynomial |
| Bi | Input polynomial coefficient |
| C | Residual polynomial |
| Ddyno | Dynamometer damping |
| E | Expected value |
| EV | Even function |
| H | Transfer function |
| $H_{ML}$ | Maximum likelihood model transfer function |
| IS | Imaginary part of $S_{xy}$ |
| JD | Dynamometer inertia |
| JG | Gas turbine inertia |
| JP | Power turbine inertia |
| JT | Lumped power turbine/dynamometer inertia |
| N | Number of discrete data samples |
| NG | Gas turbine speed |
| NP | Power turbine speed |
| O | Odd function |
| QG | Available gas torque |
| QP | Available power turbine torque |
| $R_{xx}$ | Autocovariance function discrete time estimate |
| $R_{xy}$ | Cross-covariance function discrete time estimate |
| RS | Real part of $S_{xy}$ |
| $S_{xx}$ | Smoothed spectral estimate of cross-spectrum |
| T | Sample period |
| V | Loss function |
| $W_{BH}$ | Blackman-Harris window |
| WF | Fuel flow |
| e | Residual |
| $m_x$ | Mean value of x |
| $m_y$ | Mean value of y |
| n | Number of inputs |
| $r_{xx}$ | Normalized autocovariance function |
| $r_{xy}$ | Normalized cross-covariance function |
| s | Complex variable |
| x | Stochastic stationary process input |
| $\bar{x}$ | Sample mean of x |
| y | Stochastic stationary process output |
| $z^{-1}$ | Z-transform |
| $\partial$ | Partial derivative |
| $\gamma_{xx}$ | Autospectrum |
| $\gamma_{xy}$ | Cross-spectrum |
| $\lambda$ | Lambda |
| $\rho_{xx}$ | Autocovariance function |
| $\rho_{xy}$ | Cross-covariance function |
| $\theta$ | Loss function parameter |
| $\tau$ | Lag - difference between two time periods |
| $\omega$ | Frequency (rad/sec) |
| $\phi$ | Temperature correction factor |

## References


[1]Kuczynski, W.A. and others, "The Influence of Engine/Fuel Control Design on Helicopter Dynamics and Handling Qualities," Journal of the American Helicopter Society, Vol. 25, No. 2, April 1980.

[2]Corliss, L.D. "A Helicopter Handling Qualities Study of the Effects of Engine Response Characteristics, Height Control Dynamics, and Excess Power on Nap-of-the-Earth Operations," Presented at the AHS/NASA Specialists Meeting on Helicopter Handling Qualities, Palo Alto, California, April 1982.

[3]Dehoff, R.C. and Hall, W.E., "Optimal Control of Turbine Engines," Journal of Dynamic Systems, Measurements, and Control, Vol. 101, June 1979.

[4]Zeller, J., Lehtinen, B., and Merrill, W., "The Role of Modern Control Theory in the Design of Controls for Aircraft Turbine Engines," NASA TM-82815, Jan. 1982.

[5]Michael, G.J. and Farrar, F.A., "Development of Optimal Control Modes for Advanced Technology Propulsion Systems," Report No. AD 767425, United Aircraft Research Labs, East Hartford, CT, August 1973.

[6] ---------,"An Analytical Method for the Synthesis of Nonlinear Multivariable Feedback Control," Report No. AD 762797,----------, June 1973.

[7]Pisano, A.D., "Control System for Gas Turbine Engine," U.S. Patent No. 4,276,744, Filed Sept. 1979.

[8]Curran, J.J., "T700 Fuel and Control System," Presented at the 29th Annual National Forum of the American Helicopter Society, May 1973.

[9]Kwakernaak, H., and Sivan, R., Linear Optimal Control Systems. New York: Wiley-Interscience, 1972.

[10]Athans, M., "The Role and Use of the Stochastic Linear-Quadratic-Gaussian Problem in Control System Design," IEEE Trans. on Automatic Control, Vol. AC-16, No. 6, Dec. 1971.

[11]Sellers, J.F., Baez, A.N., and Bobula, G.A., "Army/NASA Small Turboshaft Engine Digital Controls Research Program," NASA TM-82979, Nov. 1982.

[12]Michael, G.J. and Farrar, F.A., "An Analytical Method for the Synthesis of Nonlinear Multivariable Feedback Control," Report No. AD-762797, United Aircraft Research Labs, East Hartford, CT, June 1973.

[13]Franklin, G.F., and Powell, J.D., Digital Control of Dynamic Systems, Reading, MA: Addison-Wesley, 1980.

References - Continued

[14]Gessow, A., and Myers, G.C., Jr. Aerodynamics of the Helicopter. New York: Frederick Ungar, 1952.

[15]Lehtomaki, N.A., Sandell, N.R., Jr., and Athans, M, "Robustness Results in Linear-Quodratic Gaussian Based Multivariable Control Designs," IEEE Trans. on Automatic Control, Vol. AC-26, No. 1, February 1981.

[16]Cottington, R.V., Pease, C.B. "Dynamic Response Testing of Gas Turbines." Journal of Engineering for Power, Paper No. 78-GT-31, 1977.

[17]Wieslander, J., IDPAC Commands - User's Guide. Lund Institute of Technology, Department of Automatic Control. Lund, Sweden, 1980

[18]Jenkins, W., Spectral Analysis and Its Applications. New York: Holden-Day, 1968.

| 1. Report No. | 2. Government Accession No. | 3. Recipient's Catalog No. |
|---|---|---|
| CR175046 | | |

| 4. Title and Subtitle | 5. Report Date |
|---|---|
| The Design of a Turboshaft Speed Governor Using Modern Control Techniques | February 1986 |
| | 6. Performing Organization Code |

| 7. Author(s) | 8. Performing Organization Report No. |
|---|---|
| G. de los Reyes<br>D. R. Gouchoe | |
| | 10. Work Unit No. |

| 9. Performing Organization Name and Address | 11. Contract or Grant No. |
|---|---|
| General Electric Company<br>Aircraft Engine Business Group<br>Lynn, MA 01910 | NAS3-22763 |
| | 13. Type of Report and Period Covered<br>Final Report<br>9/30/82 thru 2/20/85 |

| 12. Sponsoring Agency Name and Address | 14. Sponsoring Agency Code |
|---|---|
| National Aeronautics and Space Administration<br>Lewis Research Center<br>21000 Brookpark Road<br>Cleveland, OH 44135 | |

15. Supplementary Notes

PROJECT MANAGER: William Costakis, Rotorcraft Section, Propulsion Systems Division, NASA Lewis Research Center, Cleveland, Ohio

16. Abstract

The three objectives of this research program were: To verify the model of off-schedule compressor variable geometry in the T700 turboshaft engine nonlinear model; to evaluate the use of the pseudo-random binary noise (PRBN) technique for obtaining engine frequency response data; and to design a high-performance power turbine speed governor using modern control methods. Reduction of T700 engine test data generated at NASA Lewis Research Center indicated that the off-schedule variable geometry effects were accurate as modeled. Analysis also showed that the PRBN technique combined with the maximum likelihood model identification method produced a Bode frequency response that was as accurate as the response obtained from standard sinewave testing methods. The frequency response substantially verified the accuracy of linear models consisting of engine partial derivatives and used for design. A power turbine governor was designed using the Linear Quadratic Regulator (LQR) method of full state feedback control. A Kalman Filter observer was used to estimate helicopter main-rotor blade velocity. Compared to the baseline T700 power turbine speed governor, the LQR governor reduced droop up to 25% for a 490 shaft horsepower transient in 0.1 sec simulating a wind gust, and up to 85% for a 700 shaft horsepower transient in 0.5 sec simulating a large collective pitch angle transient.

| 17. Key Words (Suggested by Author(s)) | 18. Distribution Statement |
|---|---|
| Turboshaft Engine, Linear Quadratic Regulator, Kalman Filter, Observer, Pseudo-Random Binary Noise, Model Identification, T700 | UNCLASSIFIED<br>GENERAL RELEASE<br>Star Category: 01, 05, 08, 09 |

| 19. Security Classif. (of this report) | 20. Security Classif. (of this page) | 21. No. of pages | 22. Price* |
|---|---|---|---|
| unclassified | unclassified | 219 | |

*For sale by the National Technical Information Service, Springfield, Virginia 22161